N° d'ordre NNT : 2024ISAL0014

THÈSE de DOCTORAT DE L'INSA DE LYON
membre de l'Université de Lyon

École doctorale N°34
Matériaux de Lyon

Spécialité de doctorat : Matériaux

Soutenue publiquement le 01/02/2024, par :
Florian Steinhilber

On the use of X-ray computed tomography to investigate the influence of surface integrity on the fatigue properties of additively manufactured Ti64

Devant le jury composé de :

Fabien Szmytka	Professeur associé	ENSTA Paris	Rapporteur
Sabine Rolland du Roscoat	Maître de Conférences	3SR	Rapporteur
Stefano Beretta	Professeur	PoliMI	Examinateur
Jean-Yves Buffière	Professeur	INSA LYON	Directeur de thèse
Rémy Dendievel	Professeur	Grenoble INP	Co-encadrant
Guilhem Martin	Maître de Conférences	Grenoble INP	Co-encadrant
Victor Chastand	Ingénieur	Dassault Aviation	Invité

Cette thèse est accessible à l'adresse : https://theses.insa-lyon.fr/publication/2024ISAL0014/these.pdf
© [F. Steinhilber], [2024], INSA Lyon, tous droits réservés

Cette thèse est accessible à l'adresse : https://theses.insa-lyon.fr/publication/2024ISAL0014/these.pdf
© [F. Steinhilber], [2024], INSA Lyon, tous droits réservés

INSTITUT NATIONAL DES SCIENCES APPLIQUÉES LYON

Département de la Formation par la Recherche et des Études Doctorales (**FEDORA**)

Bâtiment INSA direction, 1er étage
37, av. J. Capelle
69621 Villeurbanne Cédex
fedora@insa-lyon.fr

Référence : TH1077_STEINHILBER Florian

L'INSA Lyon a mis en place une procédure de contrôle systématique via un outil de détection de similitudes (logiciel Compilatio). Après le dépôt du manuscrit de thèse, celui-ci est analysé par l'outil. Pour tout taux de similarité supérieur à 10%, le manuscrit est vérifié par l'équipe de FEDORA. Il s'agit notamment d'exclure les auto-citations, à condition qu'elles soient correctement référencées avec citation expresse dans le manuscrit.

Par ce document, il est attesté que ce manuscrit, dans la forme communiquée par la personne doctorante à l'INSA Lyon, satisfait aux exigences de l'Etablissement concernant le taux maximal de similitude admissible.

Cette thèse est accessible à l'adresse : https://theses.insa-lyon.fr/publication/2024ISAL0014/these.pdf
© [F. Steinhilber], [2024], INSA Lyon, tous droits réservés

Cette thèse est accessible à l'adresse : https://theses.insa-lyon.fr/publication/2024ISAL0014/these.pdf
© [F. Steinhilber], [2024], INSA Lyon, tous droits réservés

Département FEDORA – INSA Lyon - Ecoles Doctorales

SIGLE	ECOLE DOCTORALE	NOM ET COORDONNEES DU RESPONSABLE
E D 206 CHIMIE	**CHIMIE DE LYON** https://www.edchimie-lyon.fr Sec. : Renée EL MELHEM Bât. Blaise PASCAL, 3e étage secretariat@edchimie-lyon.fr	**M. Stéphane DANIELE** C2P2-CPE LYON-UMR 5265 Bâtiment F308, BP 2077 43 Boulevard du 11 novembre 1918 69616 Villeurbanne directeur@edchimie-lyon.fr
E D 341 E2M2	**ÉVOLUTION, ÉCOSYSTÈME, MICROBIOLOGIE, MODÉLISATION** http://e2m2.universite-lyon.fr Sec. : Bénédicte LANZA Bât. Atrium, UCB Lyon 1 Tél : 04.72.44.83.62 secretariat.e2m2@univ-lyon1.fr	**Mme Sandrine CHARLES** Université Claude Bernard Lyon 1 UFR Biosciences Bâtiment Mendel 43, boulevard du 11 Novembre 1918 69622 Villeurbanne CEDEX e2m2.codir@listes.univ-lyon1.fr
E D 205 EDISS	**INTERDISCIPLINAIRE SCIENCES-SANTÉ** http://ediss.universite-lyon.fr Sec. : Bénédicte LANZA Bât. Atrium, UCB Lyon 1 Tél : 04.72.44.83.62 secretariat.ediss@univ-lyon1.fr	**Mme Sylvie RICARD-BLUM** Laboratoire ICBMS - UMR 5246 CNRS - Université Lyon 1 Bâtiment Raulin - 2ème étage Nord 43 Boulevard du 11 novembre 1918 69622 Villeurbanne Cedex Tél : +33(0)4 72 44 82 32 sylvie.ricard-blum@univ-lyon1.fr
E D 34 EDML	**MATÉRIAUX DE LYON** http://ed34.universite-lyon.fr Sec. : Yann DE ORDENANA Tél : 04.72.18.62.44 yann.de-ordenana@ec-lyon.fr	**M. Stéphane BENAYOUN** Ecole Centrale de Lyon Laboratoire LTDS 36 avenue Guy de Collongue 69134 Ecully CEDEX Tél : 04.72.18.64.37 stephane.benayoun@ec-lyon.fr
E D 160 EEA	**ÉLECTRONIQUE, ÉLECTROTECHNIQUE, AUTOMATIQUE** https://edeea.universite-lyon.fr Sec. : Philomène TRECOURT Bâtiment Direction INSA Lyon Tél : 04.72.43.71.70 secretariat.edeea@insa-lyon.fr	**M. Philippe DELACHARTRE** INSA LYON Laboratoire CREATIS Bâtiment Blaise Pascal, 7 avenue Jean Capelle 69621 Villeurbanne CEDEX Tél : 04.72.43.88.63 philippe.delachartre@insa-lyon.fr
E D 512 INFOMATHS	**INFORMATIQUE ET MATHÉMATIQUES** http://edinfomaths.universite-lyon.fr Sec. : Renée EL MELHEM Bât. Blaise PASCAL, 3e étage Tél : 04.72.43.80.46 infomaths@univ-lyon1.fr	**M. Hamamache KHEDDOUCI** Université Claude Bernard Lyon 1 Bât. Nautibus 43, Boulevard du 11 novembre 1918 69 622 Villeurbanne Cedex France Tél : 04.72.44.83.69 direction.infomaths@listes.univ-lyon1.fr
E D 162 MEGA	**MÉCANIQUE, ÉNERGÉTIQUE, GÉNIE CIVIL, ACOUSTIQUE** http://edmega.universite-lyon.fr Sec. : Philomène TRECOURT Tél : 04.72.43.71.70 Bâtiment Direction INSA Lyon mega@insa-lyon.fr	**M. Etienne PARIZET** INSA Lyon Laboratoire LVA Bâtiment St. Exupéry 25 bis av. Jean Capelle 69621 Villeurbanne CEDEX etienne.parizet@insa-lyon.fr
E D 483 ScSo	**ScSo**[1] https://edsciencessociales.universite-lyon.fr Sec. : Mélina FAVETON Tél : 04.78.69.77.79 melina.faveton@univ-lyon2.fr	**M. Bruno MILLY** (INSA : J.Y. TOUSSAINT) Univ. Lyon 2 Campus Berges du Rhône 18, quai Claude Bernard 69365 LYON CEDEX 07 Bureau BEL 319 bruno.milly@univ-lyon2.fr

[1] ScSo : Histoire, Géographie, Aménagement, Urbanisme, Archéologie, Science politique, Sociologie, Anthropologie

Cette thèse est accessible à l'adresse : https://theses.insa-lyon.fr/publication/2024ISAL0014/these.pdf
© [F. Steinhilber], [2024], INSA Lyon, tous droits réservés

Cette thèse est accessible à l'adresse : https://theses.insa-lyon.fr/publication/2024ISAL0014/these.pdf
© [F. Steinhilber], [2024], INSA Lyon, tous droits réservés

Remerciements

Cette thèse aura représenté pour moi, au-delà du projet scientifique, trois années importantes et une formidable source d'évolution sur le plan personnel. A toutes les personnes qui ont rendu cette expérience unique, riche en apprentissages et un très beau souvenir pour toute la suite, je tiens à leur dire de tout cœur merci.

Merci d'abord à mes formidables encadrants de thèse qui m'ont accompagné tout du long, et qui m'ont aidé à faire mes premiers pas dans ce beau domaine qu'est la recherche. Merci de m'avoir soutenu dans mes démarches et les voies que j'ai voulu emprunter, qui devaient pourtant vous sembler assez obscures par moment... tout en m'aidant à me replacer parfois pour m'éviter de m'égarer dans l'infinité des possibles.

Mon choix de faire cette thèse s'est décidé je pense que tu t'en souviens Jean-Yves dans les combles d'une maison à la campagne en plein confinement Covid-19, pendant un échange par visio. Quelques dizaines de minutes, cela aura été suffisant pour voir toute la simplicité, bienveillance et autres qualités qui font de toi un excellent encadrant de thèse, en plus d'une belle personne qui est source d'inspiration et de bonne humeur pour tout le monde. Cette simplicité aura eu raison d'un bout de mon trop de sérieux et de rigidité, et ce n'est pas peu dire ! Merci pour tous les échanges que l'on a pu avoir, au coin d'un tableau blanc ou d'une tasse de chicorée.

Guilhem, je pense que j'ai rarement eu l'occasion de travailler avec une personne aussi fiable, constante et efficace (pense à prendre du temps pour toi aussi !). Que ce soit lors de notre mésaventure sur les superalliages base Nickel ou plus récemment, tu as toujours répondu présent et proposé ton aide quand il y en avait besoin... alors que ton emploi du temps bien rempli aurait facilement pu t'en dissuader. Merci aussi pour tes retours détaillés et toujours pertinents, qui ont forgé aussi mes qualités scientifiques durant ces trois années.

Rémy, cela fait un moment maintenant que l'on se connait, et j'ai apprécié de t'avoir autant en tant que professeur (et responsable du département SIM :)), encadrant de projet qu'encadrant de thèse. À y réfléchir, mes questionnements qui frôlaient parfois la métaphysique des matériaux ont peut-être dû te faire poser quelques questions ou avoir des sueurs froides lorsque tu as appris que tu allais m'encadrer pour trois ans au complet :) En espérant que ma ténacité qui frôlait parfois l'entêtement n'aura pas dépassé votre limite d'endurance, et qu'au final ces trois années ont été pour toi une bonne expérience comme elles l'ont été pour moi. Tes jeux de mot aussi subtils que bien placés ont toujours su créer de beaux moments lors de nos réunions d'avancement, desquelles je garde de très bons souvenirs. Vous formez une très belle équipe, qui j'espère aura l'occasion de vivre encore d'autres aventures au cœur des mystères de la fatigue...

Cette thèse est accessible à l'adresse : https://theses.insa-lyon.fr/publication/2024ISAL0014/these.pdf
© [F. Steinhilber], [2024], INSA Lyon, tous droits réservés

Une thèse étant loin d'être une aventure solitaire, un grand nombre de personnes m'ont soutenu et aidé à porter ce travail bien plus loin que je ne l'aurais pu seul. Au-delà des aspects technique et scientifique, je suis heureux d'avoir pu échanger avec chacun de vous le long du chemin.

Merci Quentin, cela a réellement été une chance de pouvoir travailler en complémentarité avec toi. D'abord pour tes grandes qualités humaines ; à la fois posé et attentionné, tu as vraiment le cœur sur la main. Ta rigueur scientifique, ton esprit d'initiative et ta capacité à marier milieux académique et industriel ont été source d'inspiration et je pense autant de clés de réussite pour la suite de ton parcours. Au plaisir de se refaire une randonnée au cœur du Pilat :)

Joël, je me demande bien comment je m'en serais sorti au beau milieu de mes lignes de code si tu n'avais pas été là ! Merci pour tes explications, ta patience et les débogages sur lesquels tu m'as aidé... pour certains c'est sûr que je n'en serais pas arrivé à bout seul ! Tu peux être fier d'avoir initié un fervent utilisateur de Python :) Linux, ça reste à voir ;) Au-delà de l'aspect technique, merci pour nos discussions philosophiques sur la société et tout le reste, toujours de beaux moments source de réflexions.

Je ne pourrais pas parler de programmation sans mentionner aussi l'aide que tu m'as apporté, David. Sans elle la mesure de courbure 3D serait peut-être restée une perspective lointaine, et m'aurait sinon donné bien du fil à retordre ! Cela fait plaisir d'avoir pu faire cette collaboration ; un bon exemple de comment partager son savoir peut aider et éviter bien difficultés à une personne qui a encore tout à apprendre dans le domaine !

Merci également sur cette thématique à Sylvain et Pierre-Antoine, qui m'ont apporté leur aide et répondu à mes questions pour faire mes débuts dans le monde de la programmation. Si coder a eu sa part de défis tout le long de ma thèse, je crois qu'on peut dire que les essais de fatigue ne sont pas en reste non plus. Merci Justine Papillon, Théophile ou encore Pascal Reynaud pour m'avoir aidé sur ce chemin. Merci Justine Papillon et Jérôme aussi pour votre aide en tomographie, pour toute votre gentillesse et écoute, vous formez une super équipe et l'équipe métal est bien chanceuse de vous avoir !

Plus largement, j'aimerais remercier l'ensemble des personnes que j'ai pu rencontrer au laboratoire MatéIS, l'un des endroits les plus inspirants où il m'a été donné de travailler. Merci à tous mes cobureaux : Masato et Amin, Sébastien et Maureen, Louis Lesage, Justine Taurines et Théophile... Merci pour l'ambiance inspirante et la bonne humeur pendant ces trois années, qui m'aidaient quand j'étais trop pris par les difficultés techniques et que je pouvais en perdre de vue l'essentiel. Une pensée en particulier à Louis H. avec qui j'ai eu la chance de partager le même maître/directeur de thèse et la période de rédaction, avec aussi des expériences uniques au synchrotron... preuves d'ailleurs que c'est tout à fait possible de bien vivre ses expériences et de passer de très bons moments même quand les résultats ne sont pas au rendez-vous :) En parlant de synchrotron, merci au passage à James Ball et Thomas Connolley pour l'opportunité de faire de la 3D DRX et de la DCT à l'ESRF, ainsi que pour m'avoir proposé plusieurs scans de tomographie X à Diamond.

Pour en revenir au laboratoire, merci à Xavier, Sophie et Sylvain pour vos discussions sur le projet Aéroprint ; autant de personnes avec qui j'ai eu beaucoup de plaisir à partager pendant ce projet et dont j'ai aussi apprécié toutes les qualités scientifiques. Merci à tous les doctorants, post-doctorants, stagiaires, permanents pour les moments de partage et d'entraide, les parties de babyfoot ou de tennis, les 16h de vendredi, les team buildings, la période aux algécos qui

Cette thèse est accessible à l'adresse : https://theses.insa-lyon.fr/publication/2024ISAL0014/these.pdf
© [F. Steinhilber], [2024], INSA Lyon, tous droits réservés

n'était finalement pas si mal que ça... : merci Camille, Hélène notre super gestionnaire, Samuel, Adam, Julien, Théotime, Louis Lesage, Bassem, Mathilde, Quentin Saby, Laurabelle, Arnaud, Maël, Michel, Laura, Patrice, Stéphanie, Eric, Carole... et bien d'autres encore !

Merci également aux membres du GPM2 pour leur accueil et leur aide lors de mes quelques visites, je pense notamment à Charles et Mathis pour leur aide sur les essais de traction. Merci enfin à tous les autres acteurs de cette thèse : Victor, Charles et Christopher pour les échanges et les impressions d'échantillons, tous les autres collaborateurs du projet Aéroprint, les membres de mon jury de thèse pour s'être plongé dans mes travaux et pour les discussions qui en ont suivi, et finalement Dassault Aviation et la région AURA pour le financement de ces travaux.

Ces trois années de thèse n'auraient évidemment pas été aussi riches et vivantes sans la présence de toutes les personnes qui m'ont entouré au-delà du travail. Merci à ma famille pour leur soutien, ainsi que pour tout ce qu'ils m'ont apporté et qui m'a permis d'en arriver là aujourd'hui.

Merci à tous les amis de la Protection Civile : Stéphanie, Timon, Paul, Zachary, Lounès, Clotilde, Thibault, Dimitri, Marc, Grégoire, Christopher... la liste est encore longue ! Cette année et quelques avec vous aura été une expérience aussi intense qu'enrichissante, stimulante, faite de partages et de belles rencontres, de galères et d'entraide... le complément idéal pour redescendre les deux pieds sur terre dans les périodes d'intense réflexion, de code ou de rédaction :)

Un profond merci enfin à l'association UCM et toutes les personnes qu'elle m'a permis de rencontrer. Je n'aurais probablement pas été capable de commencer cette thèse sans toute l'aide, les compréhensions, le soutien et l'inspiration que vous m'avez apporté et qui continuent de m'animer aujourd'hui. Merci à tous les professeurs qui ont su m'accompagner avec bienveillance et profondeur : Anthony, Thibaut, Christiane, Alexis, Guillaume... Merci aussi pour les moments de partage avec tous les amis d'UCM en France, qui sont une profonde source de remise en question, d'inspiration, de joie et de soutien dans les moments de grand questionnement.

Un beau merci à tous 🙏 🍀 🌟

Cette thèse est accessible à l'adresse : https://theses.insa-lyon.fr/publication/2024ISAL0014/these.pdf
© [F. Steinhilber], [2024], INSA Lyon, tous droits réservés

Cette thèse est accessible à l'adresse : https://theses.insa-lyon.fr/publication/2024ISAL0014/these.pdf
© [F. Steinhilber], [2024], INSA Lyon, tous droits réservés

Summary

Manufacturing defects are known to significantly impact the fatigue properties of additively manufactured (AM) components. Notably, the large surface roughness, typical of AM processes, leads to increased stress concentrations that promote crack initiation, thereby reducing fatigue resistance.

Traditionally, surface roughness and related defects are evaluated using tools like white light interferometers. However, these instruments offer a limited, single-perspective and only partially three-dimensional analysis. Those limitations do not enable the thorough characterization of the complex surfaces and hidden defects typical in AM components.

This study describes a methodology for performing a 3D surface analysis using X-ray Computed Tomography (XCT) data. The method is illustrated on various samples, ranging from simple cylinders to more intricate architected structures. It turns out to be very efficient at detecting critical surface defects, such as notches hidden by partially melted powder particles.

The methodology is then applied to examine the effect of surface defects on the fatigue properties of Ti64 produced by Laser Powder Bed Fusion (L-PBF). This analysis includes both as-built surfaces and those subjected to post-treatments, specifically investigating the impact of Plasma electrolytic Polishing (PeP) and surface oxygen contamination (presence of an α-case layer) resulting from high-temperature heat treatment (860 °C).

Using XCT for 3D characterization, defects responsible for fatigue failure are identified, the latter being predominantly surface valleys. The method's ability to predict crack initiation locations is also evaluated, as well as its potential to estimate the fatigue resistance of a specimen before testing.

Cette thèse est accessible à l'adresse : https://theses.insa-lyon.fr/publication/2024ISAL0014/these.pdf
© [F. Steinhilber], [2024], INSA Lyon, tous droits réservés

Cette thèse est accessible à l'adresse : https://theses.insa-lyon.fr/publication/2024ISAL0014/these.pdf
© [F. Steinhilber], [2024], INSA Lyon, tous droits réservés

Résumé

Les défauts de fabrication sont connus pour avoir un impact significatif sur les propriétés de fatigue des composants élaborés par Fabrication Additive (FA). En particulier, l'importante rugosité de surface, typique des procédés de FA, génère des concentrations de contrainte locales qui favorisent l'amorçage de fissures, réduisant ainsi la résistance à la fatigue.

Traditionnellement, la rugosité de surface et les défauts associés sont caractérisés à l'aide d'outils tels que les interféromètres à lumière blanche. Toutefois, ces instruments offrent une analyse qui n'est que partiellement tridimensionnelle car limitée à une unique perspective. Ces limitations ne permettent pas une caractérisation approfondie des surfaces de composants élaborés par FA, qui peuvent avoir des géométries 3D complexes et des défauts de surface cachés derrière un importante rugosité.

Ce manuscrit décrit une méthodologie permettant d'effectuer une analyse de surface en 3D à partir d'une caractérisation par tomographie aux rayons X. La méthode est illustrée sur divers échantillons, allant de simples cylindres à des structures architecturées plus complexes. Elle s'avère efficace pour détecter les défauts de surface critiques, tels que les entailles cachées par des particules de poudre partiellement fondues.

La méthodologie est ensuite appliquée pour étudier l'impact des défauts de surface sur la tenue fatigue du Ti64 élaboré par fusion laser sur lit de poudre. Cette analyse porte à la fois sur les surfaces brutes de fabrication ou après différents post-traitements, en étudiant en particulier l'impact d'un polissage électrolytique plasma et de la contamination par l'oxygène de la surface (présence d'une couche d'α-case) résultant d'un traitement thermique à haute température (860 °C).

L'utilisation de la tomographie aux rayons X pour la caractérisation 3D des défauts a permis d'identifier ceux responsables de la rupture par fatigue, ces derniers étant principalement des vallées en surface. La capacité de la méthode à prédire le site d'amorçage des fissures est également évaluée, ainsi que son potentiel à estimer la résistance à la fatigue d'un spécimen avant essai.

Cette thèse est accessible à l'adresse : https://theses.insa-lyon.fr/publication/2024ISAL0014/these.pdf
© [F. Steinhilber], [2024], INSA Lyon, tous droits réservés

Cette thèse est accessible à l'adresse : https://theses.insa-lyon.fr/publication/2024ISAL0014/these.pdf
© [F. Steinhilber], [2024], INSA Lyon, tous droits réservés

Contents

Remerciements v

Summary ix

Résumé xi

Contents xiii

Introduction 1

1 Brief overview on defects harmfulness on L-PBF Ti64 fatigue properties 7
1.1 An introduction to fatigue . . . 8
1.2 Defects inherited from L-PBF: application to Ti64 . . . 11
1.2.1 A classification of defects based on their spatial distribution . . . 12
1.2.2 Surface defects . . . 13
1.2.3 Internal defects . . . 15
1.3 Impact of different defects on fatigue properties . . . 16
1.3.1 Identifying the defects at the origin of crack initiation . . . 16
1.3.2 A quantitative comparison of the impact of surface vs internal defects . . . 19
1.4 Modeling the impact of defects on fatigue properties . . . 23
1.4.1 A brief exploration of theory: K_t, K_f, K... which difference? . . . 23
1.4.2 Estimation of defects harmfulness in the case of L-PBF Ti64 . . . 27
1.5 Towards a 3D local characterization of AM surfaces . . . 34
Intermediate summary . . . 37

2 A methodology for the 3D characterization of surfaces using X-ray computed tomography: application to additively manufactured parts 39
2.1 Materials and XCT data acquisition . . . 40
2.2 3D surface characterization methodology . . . 41
2.2.1 Surface segmentation . . . 41
2.2.2 3D roughness calculation . . . 44
2.2.3 3D curvature calculation . . . 49
2.2.4 Quantification of the harmfulness of surface notches . . . 54
2.3 Application to parts with complex geometries . . . 56
2.3.1 Gyroid structure . . . 57
2.3.2 Octet-truss lattice structure . . . 59

Cette thèse est accessible à l'adresse : https://theses.insa-lyon.fr/publication/2024ISAL0014/these.pdf
© [F. Steinhilber], [2024], INSA Lyon, tous droits réservés

2.3.3 Impeller . . . 60
2.4 Application to the prediction of crack initiation sites in fatigue . . . 62
Intermediate summary . . . 70

3 Materials characterization **71**
3.1 Samples manufacturing . . . 71
3.1.1 Processing conditions . . . 71
3.1.2 Fatigue and tensile specimens . . . 73
3.2 Microstructure characterization . . . 76
3.2.1 Microstructure of the bulk material . . . 76
3.2.2 Microstructure near the surface . . . 78
3.3 Tensile properties . . . 82
3.4 Defects characterization using XCT . . . 84
3.4.1 Acquisition setup . . . 84
3.4.2 Porosity . . . 85
3.4.3 Surface defects . . . 88
Intermediate summary . . . 101

4 Fatigue properties and crack initiation mechanisms of as-built and post-treated specimens **103**
4.1 Fatigue properties and crack initiation mechanisms for as-built specimens . . . 104
4.1.1 Protocol for fatigue tests . . . 104
4.1.2 Results of fatigue tests . . . 104
4.1.3 Killer defects identification: the need for a 3D characterization . . . 111
4.2 Alpha-case formation and surface embrittlement induced by heat treatments . . . 120
4.2.1 Alpha-case formation . . . 120
4.2.2 Impact on tensile properties . . . 120
4.2.3 Impact on fatigue properties . . . 123
4.3 Improvement of fatigue properties by Plasma electrolytic Polishing (PeP) . . . 131
4.3.1 Principle of PeP surface treatment . . . 131
4.3.2 Conditions of PeP treatments applied to fatigue specimens . . . 133
4.3.3 Roughness of specimens polished by PeP . . . 138
4.3.4 Fatigue resistance improvement and change in crack initiation mechanism 146
Intermediate summary . . . 152

5 Quantitative analysis of surface defects harmfulness **153**
5.1 Surface defects segmentation . . . 154
5.1.1 Detailed methodology . . . 155
5.1.2 Segmentation of valleys and pit-like defects . . . 158
5.1.3 Segmentation of protrusions/peaks . . . 160
5.2 Relationships between fatigue resistance and parameters derived from the surface characterization using XCT . . . 160
5.2.1 Parameters selected to reflect surface defects harmfulness . . . 161
5.2.2 Correlation between the selected parameters and the fatigue lifetime . . . 163
5.3 Killer defect prediction . . . 168
5.3.1 Application to surface-treated specimens (PeP) . . . 169
5.3.2 Application to specimens with as-built surfaces . . . 178

Cette thèse est accessible à l'adresse : https://theses.insa-lyon.fr/publication/2024ISAL0014/these.pdf
© [F. Steinhilber], [2024], INSA Lyon, tous droits réservés

Intermediate summary 183

Conclusion and Perspectives **185**

A Comparison of different distance calculation methods **197**

B 3D Gaussian S-Filter using normalized convolution **203**

C Near-surface microstructure after PeP treatment **207**

References **211**

Cette thèse est accessible à l'adresse : https://theses.insa-lyon.fr/publication/2024ISAL0014/these.pdf
© [F. Steinhilber], [2024], INSA Lyon, tous droits réservés

Cette thèse est accessible à l'adresse : https://theses.insa-lyon.fr/publication/2024ISAL0014/these.pdf
© [F. Steinhilber], [2024], INSA Lyon, tous droits réservés

Introduction

Additive Manufacturing (AM) includes many processes allowing to manufacture components layer by layer from their Computer Aided Design (CAD). Among those, Laser Powder Bed Fusion (L-PBF) is one of the most common processes to produce metallic components [VAF 21].

AM of metallic components has recently received increasing interest. The aerospace field is one of the main drivers in this area and represented about 18.2% of the global additive manufacturing market in 2017 [NAJ 19]. Although its large-scale adoption requires further developments in numerous fields and long qualification and certification processes [SEI 17], several successful industrial applications have already been reported [THO 19, NAJ 19, Gen 18, Lie 17]. For instance, Boeing already started in 2017 using at least four additively manufactured titanium structural components for its 787 Dreamliner commercial aircraft [MEA 17]. Fig.1a-b show two other examples of additively manufactured aircraft components used by General Electric (GE) and Airbus.

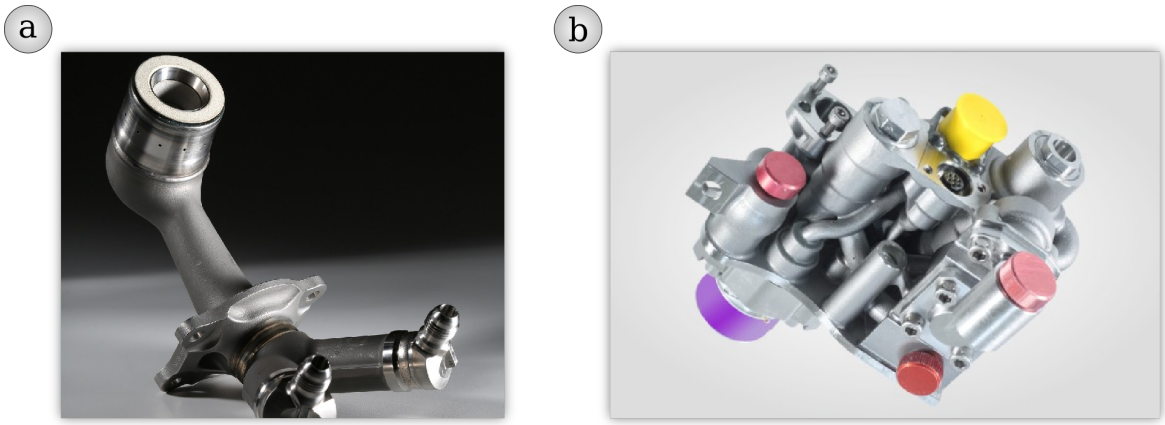

Figure 1 | Examples of industrial components manufactured by AM. (a) Fuel nozzle tip produced by GE for its LEAP engine [Gen 18]. GE had already produced such parts in more than 30 000 units in 2018. AM enabled the reduction of the weight of the part by 25% compared to its equivalent produced by conventional processes. Moreover, AM allowed the fabrication of this component in a single part, whereas its predecessor was made of about 20 parts welded together. (b) Additively manufactured valve block for a spoiler actuator made of titanium, tested in flight in an Airbus A380 airplane in 2017 [Lie 17]. The use of AM also enabled the reduction of the component weight as well as alleviating assembly steps.

Cette thèse est accessible à l'adresse : https://theses.insa-lyon.fr/publication/2024ISAL0014/these.pdf
© [F. Steinhilber], [2024], INSA Lyon, tous droits réservés

AM processes offer several advantages that explain their increasing popularity, even though not all industrial components can be advantageously replaced by an additively manufactured counterpart. Metallic AM is therefore often best suited for the manufacturing of high added-value complex components produced in small series [THO 19, ATZ 12]. In such cases, some of the advantages of AM processes are:

- A reduction of raw material usage, since AM parts are printed *near-net-shape* and require only limited machining operations.
- A reduction of the component weight, which is always a crucial issue in the aerospace industry (see the examples given in Fig.1a-b).
- The opportunity to simplify assemblies and avoid costly operations such as welding, which can also affect the durability of the material (Fig.1a).
- The possibility of having more efficient supply chains, e.g. by producing spare parts on demand rather than storing them over long periods.

However, some issues are still to be overcome to deploy metallic AM at a larger scale. Among those, AM components are still prone to different manufacturing defects such as pores or an important surface roughness [CAB 18] associated with various surface defects, see e.g. Fig.2a-b. Notch-like surface defects are known to strongly affect the mechanical resistance under cyclic loading (i.e. fatigue) [PER 19, PLE 20a]. Yet, the fatigue resistance is a key factor in many industrial applications. This is well illustrated in the review of [FIN 02], where 55% of the aircraft components failures were found to be caused by fatigue. One of the challenges of AM is therefore to better control these defects, understand their impact on fatigue properties, and if possible, eliminate them.

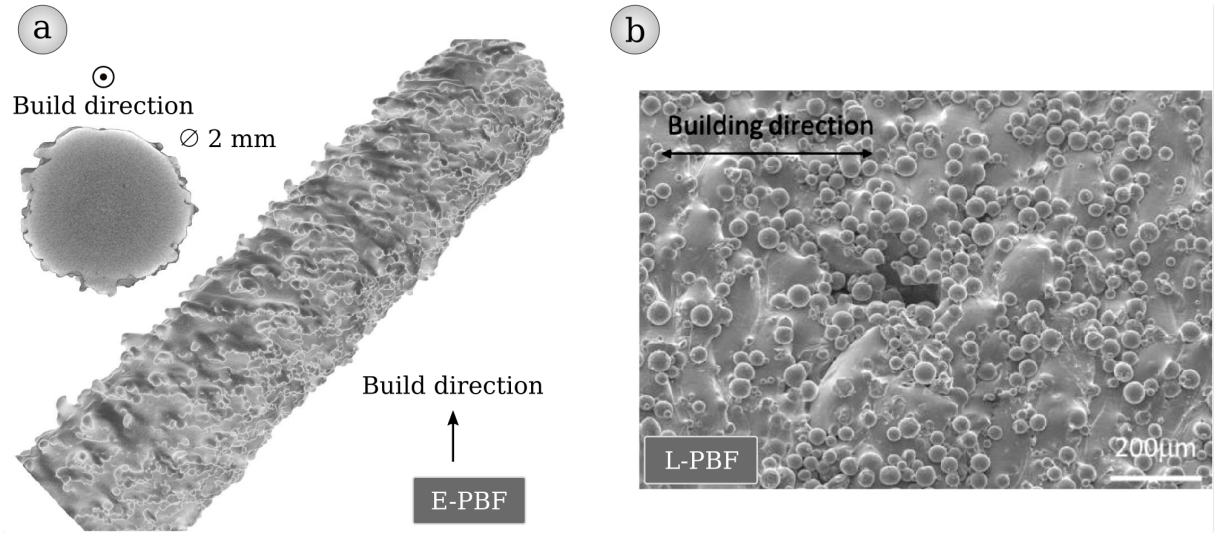

Figure 2 | Surfaces inherited from AM processes. (a) Surface of a Ti64 thin strut fabricated by Electron Powder Bed Fusion (E-PBF), adapted from [PER 19]. The surface is reconstructed from an X-ray Computed Tomography (XCT) scan. (b) The surface of a Ti64 sample manufactured by Laser Powder Bed Fusion (L-PBF), observed using Scanning Electron Microscopy (SEM) [NAK 19].

Cette thèse est accessible à l'adresse : https://theses.insa-lyon.fr/publication/2024ISAL0014/these.pdf
© [F. Steinhilber], [2024], INSA Lyon, tous droits réservés

The removal of surface defects by surface finishing methods is not a new topic and different solutions can be considered. However, these surface finishing methods were mostly designed for parts with simple shapes and/or limited surface roughness, typically inherited from machining. On the opposite, AM components often show both complex geometries and high surface roughness. Only a few surface finishing processes are possible in this case, and all have their own drawbacks or limitations. For instance, chemical polishing was proven to give interesting results [BAS 22, PER 20, BEZ 20], but requires the use of HF-based chemical solutions for Ti alloys [BAS 22], causing health and safety issues. All post-processing operations that may be required to remove and control defects from AM components can also represent an additional cost, reaching sometimes nearly half of the price of a component [THO 19]. Some of those surface finishing treatments are time-consuming, which may completely cancel the benefits of AM.

Post-processing operations should thus be avoided as much as possible. This means that it would be advantageous to use, whenever possible, components with their as-built surface to avoid expensive surface finishing operations. Doing so requires a good knowledge of the effect of surface defects on the mechanical properties, in particular fatigue.

One of the defects characterization techniques that has recently drawn an increasing interest is X-ray Computed Tomography (XCT) which shows several advantages. For example, it is the only Non-Destructive Technique (NDT) that is sensitive to defects regardless of their location, i.e. at the surface, in sub-subsurface or in the bulk material, see Fig.3a. Other techniques such as white light interferometry only allow for surface characterization, whereas eddy current or ultrasonic testing are sensitive to sub-surface defects only. XCT is also the most suitable technique to characterize the surface of components with complex geometries (e.g. internal channels), a key characteristic of AM components that often show complex geometries.

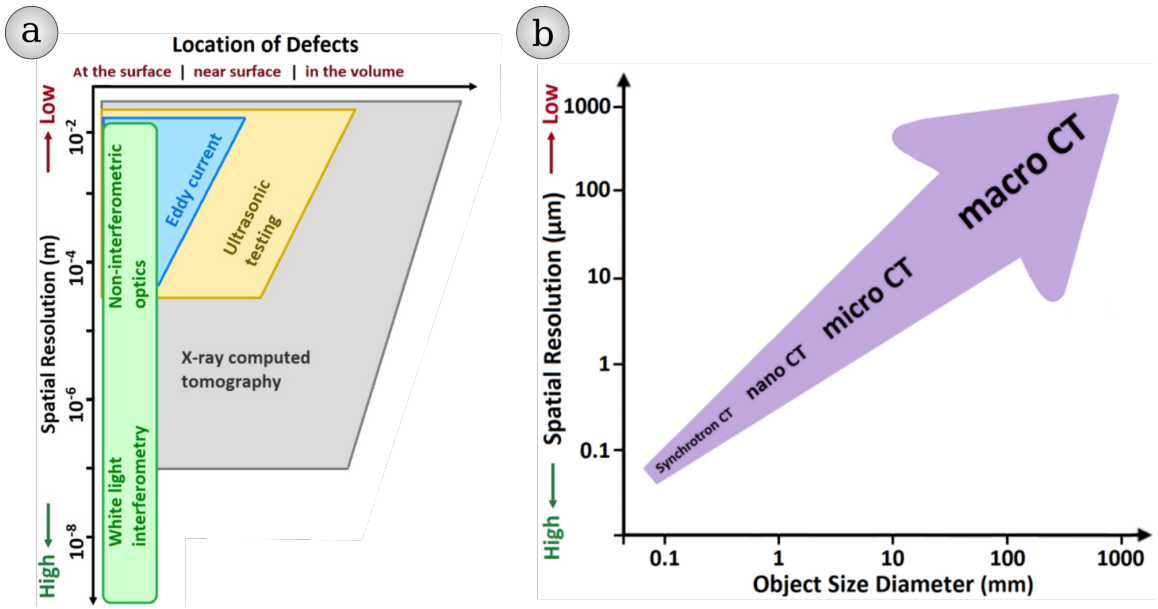

Figure 3 | (a) Comparison of some Non-Destructive Techniques (NDT), including XCT, in terms of achievable spatial resolution and ability to capture defects at different locations. From [VIL 19]. (b) Typical spatial resolutions achievable by X-ray Computed Tomography (CT in the figure) as a function of sample size. From [VIL 18a].

Cette thèse est accessible à l'adresse : https://theses.insa-lyon.fr/publication/2024ISAL0014/these.pdf
© [F. Steinhilber], [2024], INSA Lyon, tous droits réservés

Regarding spatial resolution, XCT provides generally significantly inferior resolutions than most advanced surface characterization techniques such as white light interferometry (Fig.3a). Nonetheless, achievable resolutions have been improved over the years and sub-micron resolutions can now be obtained, even with commercial XCT scanners [KAS 17], provided that the scanned object is small enough (Fig.3b). These recent advances make it an interesting option to gain a further understanding of defects in AM components. However, the use of XCT for the study of surface roughness is still limited, and further work is needed to take advantage of the opportunities offered by XCT, especially for additively manufactured parts.

The aim of this PhD work is to develop and apply XCT techniques to investigate the effect of surface integrity on the fatigue properties of additively manufactured components. This research is part of the AEROPRINT research project, financially supported by the Auvergne-Rhône-Alpes Region and Dassault Aviation (France). AEROPRINT's primary goal is to promote the industrial application of metallic AM in the aerospace sector. A pre-industrial demonstrator is developed in Dassault Aviation, with the possibility to produce titanium and aluminum parts by Laser Powder Bed Fusion (L-PBF). The project involves collaboration between various industrial and academic entities, including Dassault Aviation, AddUp, and the French Commissariat à l'Énergie Atomique et aux Énergies Alternatives (CEA).

These collaborations have enabled to cover a wide range of research topics, ranging from powder characterization and optimizing L-PBF process parameters to exploring different surface and heat treatments. This collaborative environment has also funded several PhD studies. In this regard, it is worth mentioning the one conducted by Quentin Gaillard [GAI 23a] that is complementary to the present PhD work and that primarily focuses on the influence of heat treatments on the static mechanical properties of the Ti64 alloy manufactured by L-PBF.

Cette thèse est accessible à l'adresse : https://theses.insa-lyon.fr/publication/2024ISAL0014/these.pdf
© [F. Steinhilber], [2024], INSA Lyon, tous droits réservés

This manuscript consists of 5 chapters that can be summarized as follows:

- **Chapter 1** offers a short review of the current knowledge on how manufacturing defects affect the fatigue properties of Ti64 alloy produced by L-PBF. It evaluates the extent of fatigue property degradation due to defects and identifies the most detrimental, which are typically surface defects in as-built samples. It also discusses some models from the literature that assess defect harmfulness using geometrical characterizations, e.g. from XCT.

  Chapter 2 describes in detail the 3D XCT characterization methodology used throughout this work to analyze surface defects. This method allows for the assessment of roughness and curvature on complex 3D surfaces typically observed in parts fabricated by additive manufacturing. A framework to quantify the impact of surface notch-like defects on fatigue properties is also proposed, thereby gauging the influence of the inherent rough surfaces from the L-PBF process.

  Chapter 3 introduces the Ti64 mechanical specimens fabricated by L-PBF examined in this study. The chapter covers defect characterization (including surface defects and porosity), microstructure, and tensile properties.

  Chapter 4 deals with the fatigue properties of L-PBF Ti64 samples after various post-treatments: heat treatments (stress-relief and at higher temperature), or a surface treatment (Plasma Electrolytic Polishing, denoted PeP). The objective is to quantify the impact of defects on fatigue properties and to identify the defect(s) responsible for failure through detailed 3D XCT characterizations, using the methodology developed in this work and detailed in Chapter 2.

  Chapter 5 explores the potential of XCT characterization of surface defects to estimate the fatigue resistance and predict the most critical defects that may lead to fatigue failure.

Finally, a conclusion summarizes the main findings of this work and outlines future research directions to build upon these results.

Cette thèse est accessible à l'adresse : https://theses.insa-lyon.fr/publication/2024ISAL0014/these.pdf
© [F. Steinhilber], [2024], INSA Lyon, tous droits réservés

Cette thèse est accessible à l'adresse : https://theses.insa-lyon.fr/publication/2024ISAL0014/these.pdf
© [F. Steinhilber], [2024], INSA Lyon, tous droits réservés

Chapter 1

Brief overview on defects harmfulness on L-PBF Ti64 fatigue properties

Contents

1.1 An introduction to fatigue 8
1.2 Defects inherited from L-PBF: application to Ti64 11
1.2.1 A classification of defects based on their spatial distribution 12
1.2.2 Surface defects 13
1.2.3 Internal defects 15
1.3 Impact of different defects on fatigue properties 16
1.3.1 Identifying the defects at the origin of crack initiation 16
1.3.2 A quantitative comparison of the impact of surface vs internal defects . . . 19
1.4 Modeling the impact of defects on fatigue properties 23
1.4.1 A brief exploration of theory: K_t, K_f, K... which difference? 23
1.4.2 Estimation of defects harmfulness in the case of L-PBF Ti64 27
1.5 Towards a 3D local characterization of AM surfaces 34
Intermediate summary 37

This chapter aims to provide the required insights to aid in comprehending the work conducted during this PhD. It primarily focuses on the core research topic — assessing how defects affect fatigue properties of Ti-6AL-4V (Ti64) alloy manufacturing by Laser Powder Bed Fusion (L-PBF).

Ample literature exists on this subject, providing valuable insights that guide research and highlight areas for improvement. Nonetheless, it seems also advisable to use previous studies with caution. Results obtained on L-PBF Ti64 exhibit variability — e.g. due to the large choice of machines and process parameters that have been used — and improvements in the L-PBF technology have occurred over the years. Consequently, conclusions from earlier studies might not directly apply today.

Cette thèse est accessible à l'adresse : https://theses.insa-lyon.fr/publication/2024ISAL0014/these.pdf
© [F. Steinhilber], [2024], INSA Lyon, tous droits réservés

Section 1.1 explains fatigue damage and the significant role of defects in fatigue properties. Section 1.2 outlines key defects in Ti64 manufactured by L-PBF. In Section 1.3, the impact of these defects on fatigue properties is discussed. Lastly, Section 1.4 presents methods proposed to estimate defect influence on fatigue properties, in particular in the case of materials manufactured by L-PBF. These methods may have various purposes, e.g. predicting defect impact on the fatigue limit (see Section 1.1 for a definition) or identifying the most critical defects within a population.

1.1 An introduction to fatigue

Fatigue corresponds to the damage of a material caused by repeated loading. One particularity of fatigue is that loading levels are often well below the yield strength of the considered material. Nevertheless, the repetitive nature of the loading still enables the initiation and propagation of cracks, finally causing irreversible damage and material failure. Fatigue is a key property in many industrial applications such as aeronautics. This emphasizes the need for better characterization and understanding of fatigue properties of materials, and the mechanisms involved.

Loading sequences experienced by industrial components in real cases can be very complex. To rationalize the study and facilitate interpretations, simple loading sequences and testing conditions are generally used. To keep this part short, we focus only on uni-axial fatigue tests, leaving aside torsion and bending fatigue, fretting fatigue, etc. In this case, a simple and widely used approach to characterize fatigue properties is to apply a cyclic — e.g. sinusoidal — loading to a specimen until failure. Repeating the same procedure for several specimens at different stress levels, it is possible to draw a so-called **S-N curve — or Wöhler curve — which is a plot of the applied stress as a function of the number of cycles to failure**, see Fig.1.1. The applied stress can be given in terms of maximum applied stress σ_{max} or stress amplitude $\sigma_a = \frac{\sigma_{max} - \sigma_{min}}{2}$, σ_{min} being the minimum applied stress.

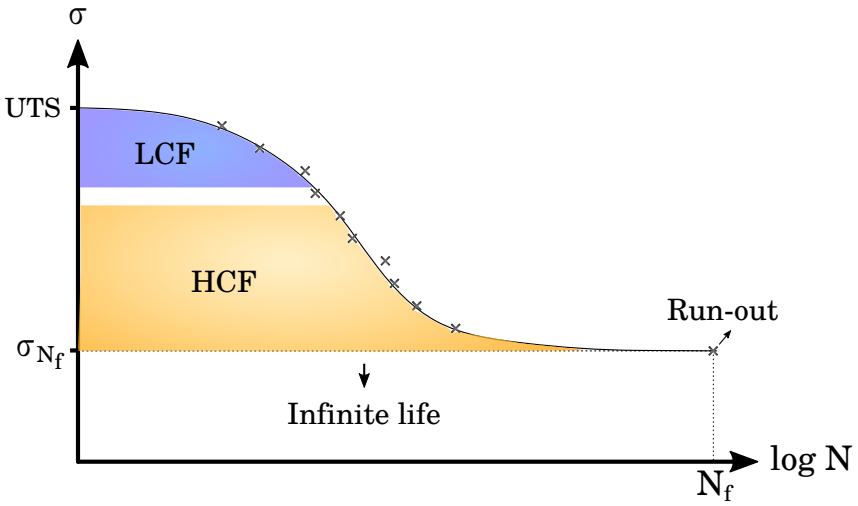

Figure 1.1 | Schematic of a typical Wöhler (or S-N) curve. Noteworthy stress levels — the tensile strength UTS and the fatigue limit — are indicated on the stress axis. The three main regions — LCF, HCF and infinite life — are delimited.

Cette thèse est accessible à l'adresse : https://theses.insa-lyon.fr/publication/2024ISAL0014/these.pdf
© [F. Steinhilber], [2024], INSA Lyon, tous droits réservés

Three main regions can be distinguished on a Wöhler curve:

1. The **Low Cycle Fatigue (LCF)** regime, where the applied stress is sufficient to cause macroscopic plastic deformation at every cycle. Resulting fatigue lives are usually lower than 10^4 cycles.
2. The **High Cycle Fatigue (HCF)** regime, where the applied stress is significantly lower than the yield strength of the material. Samples are loaded elastically at the macro-scale and the measured fatigue lives are generally greater than 10^5 cycles.
3. The **infinite life** regime, where the stress is lower than the *fatigue limit*. In this case, failure is considered to never occur. Strictly speaking, studies have actually shown that such a limit does not exist in general [BAT 99], meaning that no plateau is visible on the S-N curve. The concept of *fatigue strength* σ_N can therefore be used as a substitute. It corresponds to the highest stress level for which no failure is observed until a pre-defined number of cycles N — typically $2 \cdot 10^6$ or 10^7. Unbroken specimens are said to be *run-outs*.

Each Wöhler curve is measured under given conditions for the fatigue tests. These conditions can have a strong impact on the results. The main parameters describing a fatigue test and that have to be taken into account are the following:

- The stress ratio $R = \frac{\sigma_{min}}{\sigma_{max}}$
- The mean stress $\sigma_m = \frac{\sigma_{min}+\sigma_{max}}{2}$
- The frequency of applied loading f
- The environment: atmosphere, temperature, etc.
- The shape, size and surface roughness of fatigue specimens

Fig.1.2 summarizes the definition of $sigma_{min}$, σ_{max}, σ_a, σ_m and f.

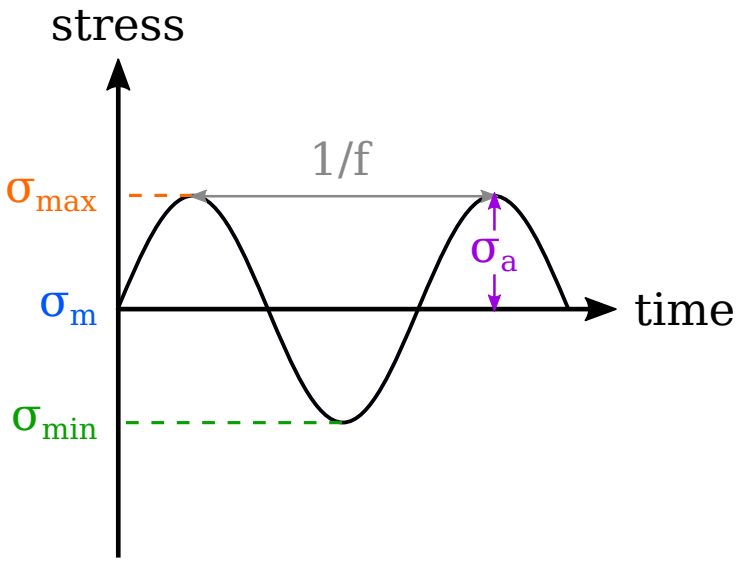

Figure 1.2 | Graphical definition of minimum and maximum and mean stresses during fatigue cycling σ_{min}, σ_{max}, and σ_m, of the stress amplitude σ_a and the frequency f.

Cette thèse est accessible à l'adresse : https://theses.insa-lyon.fr/publication/2024ISAL0014/these.pdf
© [F. Steinhilber], [2024], INSA Lyon, tous droits réservés

Characterizing a material by its Wöhler curve provides relevant information, e.g. to design industrial parts accordingly. However, to better understand the fatigue properties of a material, it is needed to go deeper and look at the micro-mechanisms causing fatigue failure.

Broadly speaking, **fatigue damage occurs in two main steps: crack initiation and crack propagation**, see Fig.1.3. At the end of these two steps occurs the final sudden failure of the material. Naturally, several cracks may coexist within a material and it is therefore possible for one to be in the initiation phase while another would already be in the propagation phase.

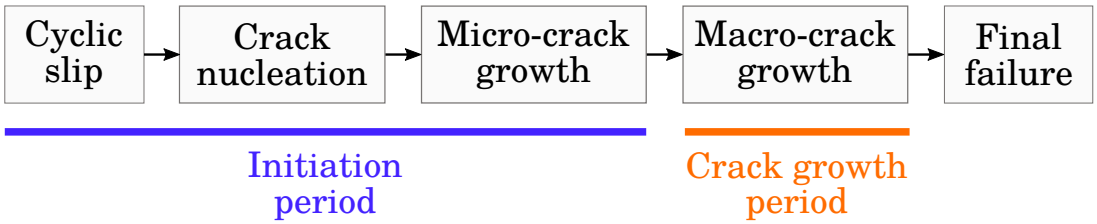

Figure 1.3 | Phases in fatigue life , adapted from [SCH 09, p.15].

The crack initiation period can be split into several steps. It begins with local **cyclic slip**, i.e. local plastic deformation at each loading cycle. The regions where cyclic slip preferentially occurs depend on the local stress field, which depends itself on the **defects** that act as stress concentrators. It is also influenced by the local microstructure since cyclic slip will be facilitated in grains with slip systems oriented unfavorably with respect to the loading direction [TUB 23, BOO 16, WU 23]. Cyclic slip eventually leads to the **nucleation** of a micro-crack, which will continue to grow under cyclic loading. At this step, crack growth is however still dependent on the environment of the initiation site — e.g. the local microstructure and stress field. Grain boundaries, or α/β interfaces in Ti alloys, can for instance act as barriers for micro-crack propagation. Depending on the local stress gradient, the crack may slow down at these obstacles or even stop definitely. For these reasons, **micro-crack growth** is still considered to be part of the initiation process. Only when crack growth becomes dependent on bulk properties alone, it can be considered a macro-crack.

Nonetheless, the limit between micro-crack and macro-crack propagation — or in other words, between crack initiation and growth — is highly dependent on the material studied. For instance, for a given material without any defect, the majority of the fatigue life may be spent to initiate the crack — see Fig.1.4. It might however be very different if defects such as inclusions, pores or surface scratches are present [ZER 19]. In the particular case of Additive manufacturing (AM), typical defects include pores, lacks of fusion or surface valleys — see next section for more details. Although they are different in nature, they will all in a similar manner act as stress concentration raisers and thus promote local plastic deformation. As a consequence, crack initiation may occur at the very beginning of cycling, bypassing a wide percentage of the fatigue life that was spent to initiate a crack. As a result, the fatigue strength will be drastically reduced. Thus, **defects can have a strong impact on fatigue strength by facilitating the crack initiation stage**.

Cette thèse est accessible à l'adresse : https://theses.insa-lyon.fr/publication/2024ISAL0014/these.pdf
© [F. Steinhilber], [2024], INSA Lyon, tous droits réservés

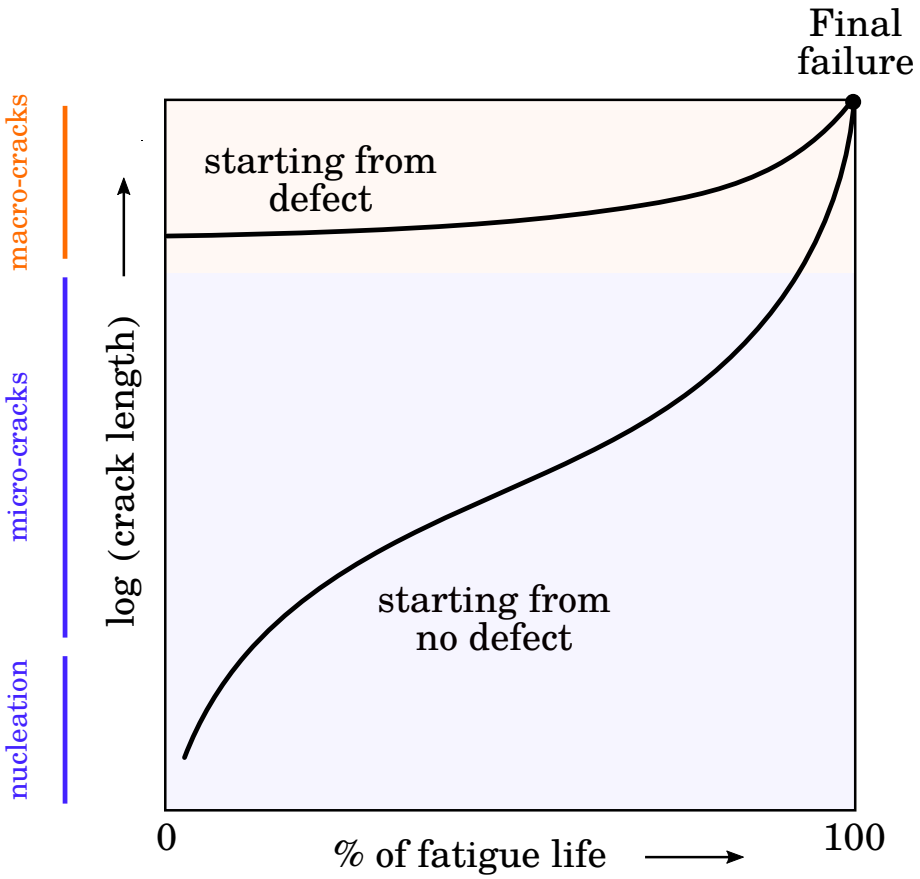

Figure 1.4 | Different scenarios of fatigue crack growth depending on whether crack initiation occurs at a defect or not. If a sufficiently large defect is present, almost all fatigue life corresponds to macro-crack propagation, while it is the inverse in the case where no defect is present. Adapted from [SCH 09, p.22].

1.2 Defects inherited from L-PBF: application to Ti64

A wide variety of defects can arise during additive manufacturing of metallic materials. Some of them are harmless regarding fatigue properties, while others are known to be of major concern. These defects range from dimensional deviation to cracks, pores and lacks of fusion to surface valleys and unmelted powder particles [SAN 21]. The scope of this review is limited to the main ones found in Ti64 manufactured by Laser Powder Bed Fusion (L-PBF). Furthermore, it focuses on defects inherent in the L-PBF process, albeit optimized. Therefore, it does not consider those that can be attributed to misuse of the process or an accidental event during manufacturing.

Cette thèse est accessible à l'adresse : https://theses.insa-lyon.fr/publication/2024ISAL0014/these.pdf
© [F. Steinhilber], [2024], INSA Lyon, tous droits réservés

1.2.1 A classification of defects based on their spatial distribution

Surface defects vs. internal defects

A first method to classify defects is to distinguish surface defects from internal ones. The two are very different regarding their location and shape, the means to characterize them, the post-treatments to remove them or their impact on mechanical properties.

Sub-surface defects vs internal defects

Among the internal defects, we can also distinguish *sub-surface defects*, present in the outermost layer of the material, from *internal defects*, located outside this area. They are similar in terms of morphology and physical origin, but **higher concentrations of pores are often observed in the sub-surface region** [BER 17]. This inhomogeneity can arise due to an excess of energy density near the surface which can lead to the formation of keyhole pores — see Section 1.2.3 for details about keyhole pores. This excess energy can for example come from a bad process parameters adjustment for the contour scan, an extra laser pass that is added at the contour of the printed part, among others to improve surface roughness.

Thus, Fig.1.5 adapted from [KAR 23] shows that a reduction of laser scanning speed (and therefore an increase in energy density) for the contour scan results in an increase in sub-surface pore density. In a more subtle way, sub-surface pores can come from the deceleration and acceleration of the laser beam at turning points (at the end of laser tracks). Those tend to increase the time spent by the laser at those specific locations and therefore the local energy density [MAR 19, AND 19a, MAN 16]. Strategies exist to alter process parameters at turning points to compensate for this effect [MAR 19, MAN 16].

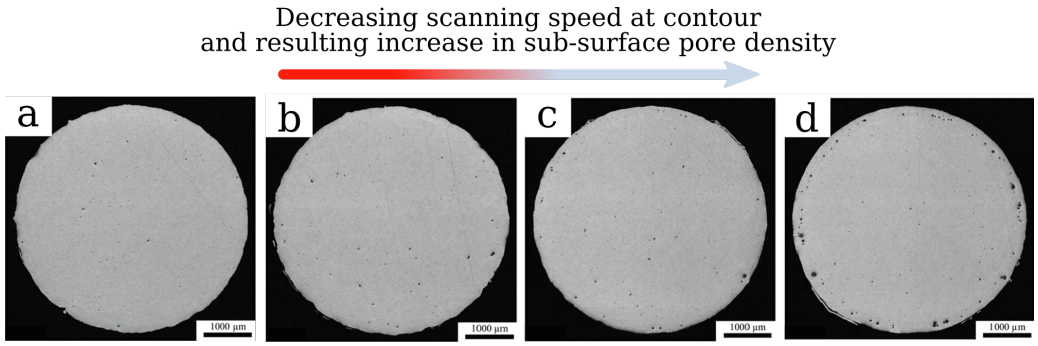

Figure 1.5 | Increase in sub-surface pore density with a decrease in laser scanning speed in the contour scan. The figure is adapted from [KAR 23]. Samples are fabricated by L-PBF using pre-alloyed A20X aluminum powder.

Sub-surface defects are also of particular interest regarding their impact on mechanical properties. Indeed, **the same defect will be much more harmful if it is at a sufficiently close distance from the surface than if it is in the core**, as is discussed in Section 1.3.

Finally, sub-surface defects have the advantage of being the only internal defect that can be detected by some Non-Destructive Testing (NDT) methods such as Eddy Current, or eliminated by some surface treatments such as machining or chemical polishing. However, regarding this last point, surface treatments involving material removal may also transform these defects into surface defects, making them even more harmful [PER 20].

Cette thèse est accessible à l'adresse : https://theses.insa-lyon.fr/publication/2024ISAL0014/these.pdf
© [F. Steinhilber], [2024], INSA Lyon, tous droits réservés

1.2.2 Surface defects

Surface defects in the case of L-PBF samples include:

- **Partially melted powders** stuck to the surface. Even if they contribute to surface roughness, they do not have a significant impact on mechanical properties [KAN 18]. However, they may still cause other issues such as the detachment of powder grains in hydraulic tubes [ZHA 21]. They are found to be most present in down-skin regions, while it is much less the case in up-skin regions [PYK 13, CAB 18]. Fig.1.6 shows partially melted powders on the surface of an L-PBF sample characterized by SEM.
- **Spatters**, which are particles ejected from the melt pool during manufacturing [LI 22, ZHA 17, AHM 20, LAD 16, PAU 23, GUN 18]. When not evacuated by the airflow set up in the build chamber, spatters contaminate the next powder layer. Since their size is sometimes much larger than powder particles used for manufacturing, the laser may be unable to completely melt them. This mechanism can lead to the presence of large particles associated with lack of fusion defects at the sample surface as well as in the bulk material [PES 20, LI 22, WAN 22]. Fig.1.7a-c show examples of fatigue failure caused by the presence of spatters at the specimen surface.
- **Dross**, which is characterized by the presence of large protuberances most often in down-skin regions. Down-skin regions refer here to the ones that are facing the build plate (and therefore the powder bed), in opposition to up-skin regions which face away from the build plate. Dross formation is a consequence of the low thermal conductivity of the powder bed, which causes heat accumulation in overhangs and thus an excessive melting of powders [CHA 22, FEN 21, LIN 23, DEP 18, VIA 22, CAL 14]. Furthermore, the melt pool tends to sink into the powder bed in down-skin regions, which results in large protuberances. Fig.1.8 gives an example of a sample fabricated by Electron Laser Powder Bed Fusion (E-PBF), where dross formation can occur similarly to L-PBF.
- **Valleys**, which will be called equivalently **notches**. Valleys can have multiple origins. In up-skin and vertical regions, they can arise due to the superposition of fused powder layers – see Fig.1.6 for an example. The resulting surface often looks like a stack of plates or a staircase, which is why this effect is sometimes called *plate-pile like* or *staircase* effect [PYK 13, ZHA 19, PER 19]. Similarly, dross formation induces the presence of valleys in down-skin regions. Regardless of their origin, these **valleys generate significant stress concentrations that are detrimental to mechanical performances, especially in fatigue** [PER 19, KAN 18, CHA 15].

Cette thèse est accessible à l'adresse : https://theses.insa-lyon.fr/publication/2024ISAL0014/these.pdf
© [F. Steinhilber], [2024], INSA Lyon, tous droits réservés

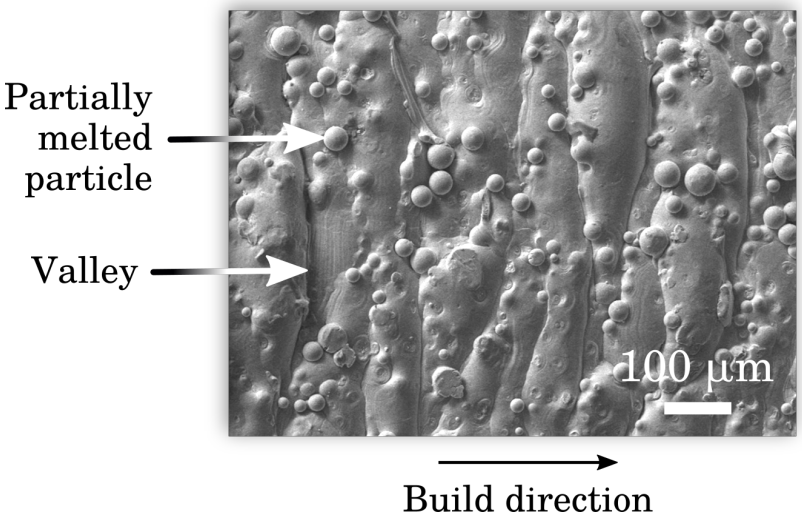

Figure 1.6 | SEM observation of an L-PBF as-built surface highlighting partially melted powders and valleys. Adapted from [BEN 17].

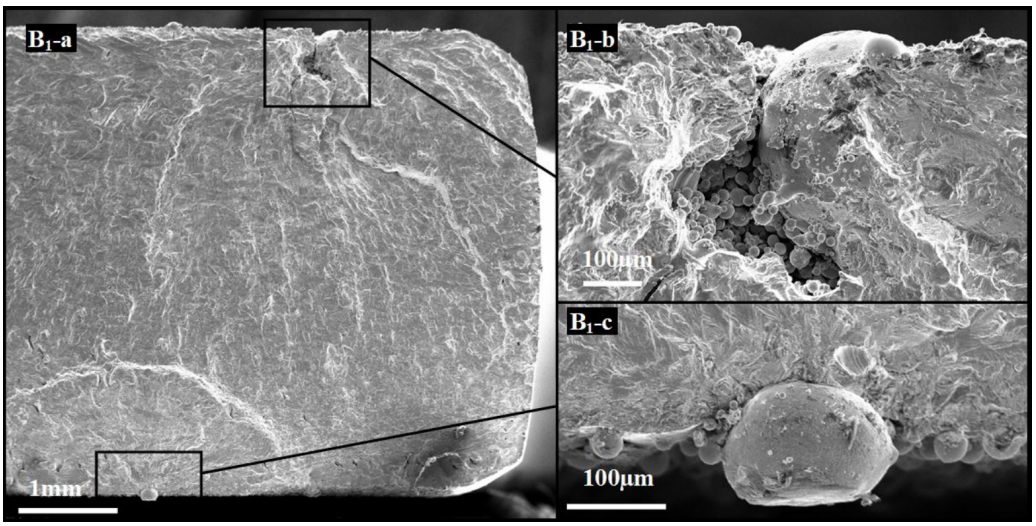

Figure 1.7 | Fatigue failure from two surface spatters in IN625 manufactured by L-PBF [PES 20, Fig.3.28]. It can be seen that the spatter at the origin of the largest crack caused the formation of a lack of fusion.

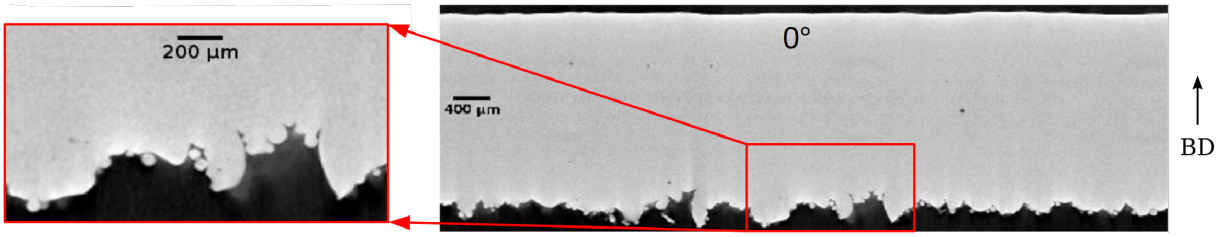

Figure 1.8 | XCT slice showing an example of dross formation in the down-skin region of a 2 mm cylinder fabricated by Electron Powder Bed Fusion, adapted from [PER 19].

Cette thèse est accessible à l'adresse : https://theses.insa-lyon.fr/publication/2024ISAL0014/these.pdf
© [F. Steinhilber], [2024], INSA Lyon, tous droits réservés

1.2.3 Internal defects

The main internal defects in L-PBF Ti64 are pores. Several types can be distinguished according to their size, morphology and physical origin, leading to the following categories:

- **Lacks of fusion (LOF)** which can form when the energy density provided by the laser source is insufficient to completely melt the powder [GUN 18, p.45]. This is for instance the case when the hatch spacing (distance between adjacent tracks) is too large [ABO 14], resulting in bad overlapping between adjacent laser tracks. Lacks of fusion may also occur because of irregularities in the powder bed, spatters or exceptionally large powder particles [DEP 18, WAN 22, PAL 18].
  Lacks of fusion often present complex and elongated geometries — see Fig.1.9) — with the major axis orthogonal to the build direction. Furthermore, they are usually larger than other types of porosity [HU 20a]. They can also be identified by the presence of unmelted powder particles, as can be seen in Fig.1.9.
- **Keyhole porosity**, formed on the contrary in cases where the energy density is too high [BAY 19]. They are generally smaller than lack of fusion defects (∼60 µm according to [VAY 20]), their morphology is often spherical [LIU 20] as in Fig.1.10a but can sometimes be more elongated and angular as illustrated in Fig.1.10b.
- **Pores originating from powders**. During powder atomization, some gas can be trapped inside the solidified powder particles [BIA 11]. Those gas pores may remain even after L-PBF, resulting in some additional porosity. They are generally of small size (∼5 µm in [VAY 20]) and have a very spherical morphology. Their quantity can be greatly reduced by using a technique such as plasma atomization to manufacture the powders.

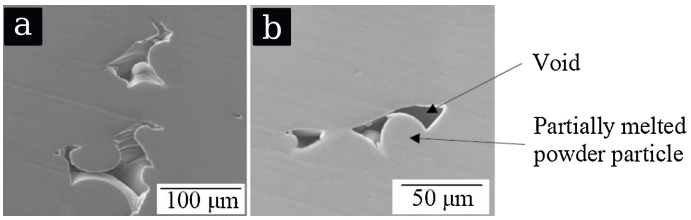

Figure 1.9 | Lacks of fusion in L-PBF Ti64 observed using SEM by [PAL 18]

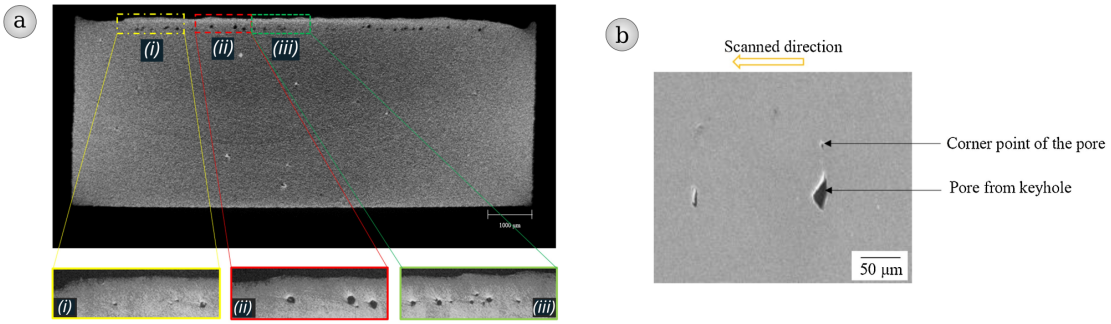

Figure 1.10 | Keyhole porosity observation in L-PBF Ti64. (a) XCT slice showing keyhole porosity, from [BAY 19]. Keyhole pores are visible all along the last laser track, at the top of the image. (b) SEM image of a non-spherical keyhole pore, from [PAL 18].

Cette thèse est accessible à l'adresse : https://theses.insa-lyon.fr/publication/2024ISAL0014/these.pdf
© [F. Steinhilber], [2024], INSA Lyon, tous droits réservés

1.3 Impact of different defects on fatigue properties

The defects described above have unequal impacts on fatigue properties. Some of them are critical, while others can be considered to be harmless. This section presents the ranking of the most harmful defects, suggested by various results from the literature. It also described several attempts that were made to quantify their impact on fatigue properties.

A first approach to finding the most harmful defects is to identify the ones that cause crack initiation on fractured surfaces. The more frequently a defect is found to initiate a crack, the more harmful it is considered to be. This analysis is addressed in Section 1.3.1.

It is also possible to study the relative influences of different defects by comparing the mechanical properties of samples including a controlled defect population. For example, additive manufacturing was employed to generate deterministic defects [LES 22]. More simply, it is also possible to compare as-built samples — i.e. without any post-treatment — to others subjected to Hot Isostatic Pressing (HIP) and/or machining and polishing. In this way, the impact of surface and internal defects can be studied relatively independently to determine which ones are the most harmful. This analysis is detailed in Section 1.3.2.

1.3.1 Identifying the defects at the origin of crack initiation

1.3.1.1 Prevalence of surface notches

For an as-built surface, crack initiation occurs most often at a surface notch [KAS 15, CHA 18, CAR 19, YU 19] as shown in Fig.1.11. In the study of [CHA 18], a surface defect is for example found to be at the origin of failure in 10 cases out of 13 for both L-PBF and E-PBF Ti64 samples with an as-built surface. For [CAR 19, KAH 17, MIL 22], it is even the case for 100% of the observed initiation sites.

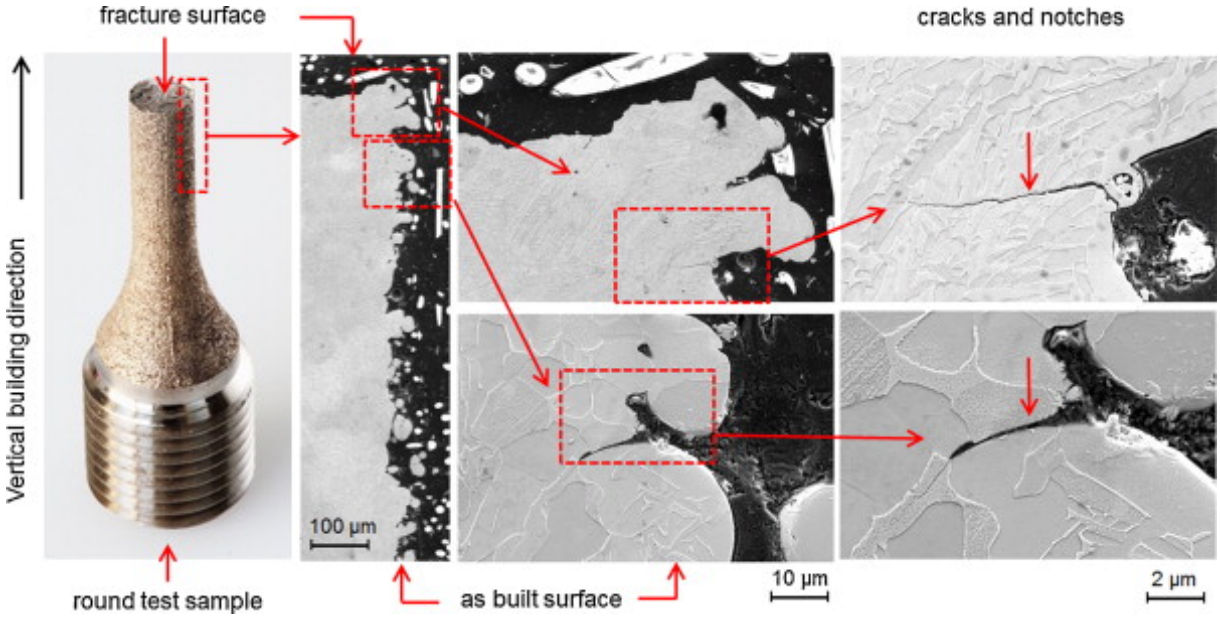

Figure 1.11 | Fatigue crack initiation at surface notches in L-PBF Ti64 [KAS 15]

.

Cette thèse est accessible à l'adresse : https://theses.insa-lyon.fr/publication/2024ISAL0014/these.pdf
© [F. Steinhilber], [2024], INSA Lyon, tous droits réservés

Several reasons can explain this prevalence of crack initiation at surface defects. The results of FEM calculations given in Fig.1.12 show for example that a surface pore generates a higher stress concentration than a pore located in the bulk material. In the y-axis of the graph, σ is the applied stress whereas σ_{zz}^{max} is the maximum stress component in the direction of applied stress. Therefore, the ratio σ_{zz}^{max}/σ quantifies the stress concentration induced by the pore. In the x-axis, r is the pore radius whereas d is the distance of the pore center to the surface. As shown on the small schematics, the ratio $r/(r+d)$ tends to 0 for a pore deeply embedded in the bulk material and equals 0.5 when the pore is in direct contact with the surface. Above 0.5, it is an open pore, i.e. a spherical notch. From this graph, it can be seen that a spherical notch of radius r (i.e. $r/(r+d) = 1$) causes the same stress concentration as a spherical pore of diameter $2r$ in the core material (in the case $r/(r+d) \to 0$). In other words, a spherical surface hole causes the same stress concentration as an internal spherical hole of twice its size.

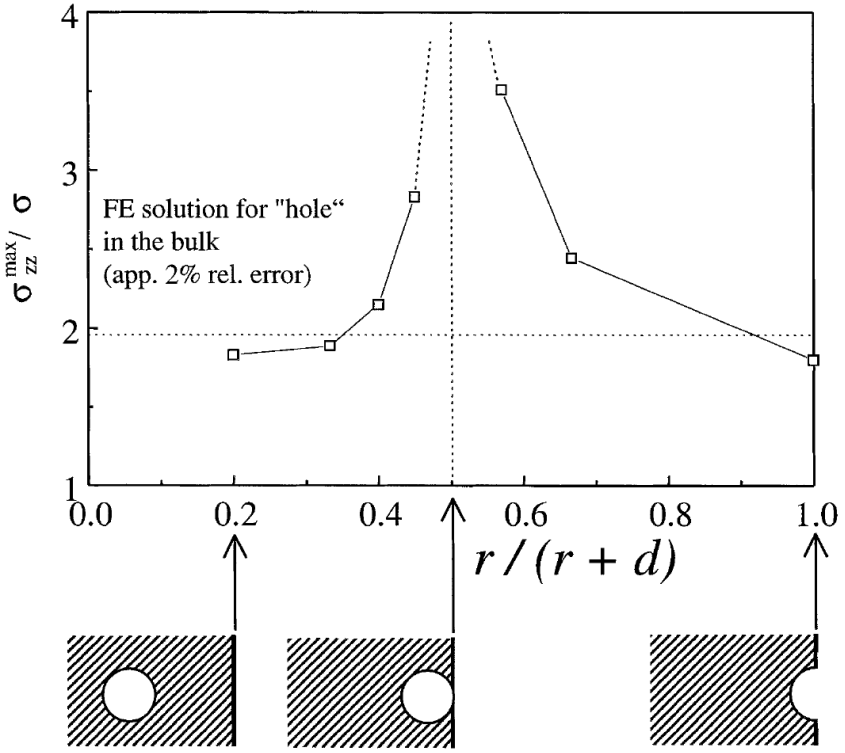

Figure 1.12 | Evolution of stress concentration induced by a spherical pore in function of its distance to the surface. The figure is drawn from [BOR 02] who obtained these results using FEM. σ is the applied stress whereas σ_{zz}^{max} is the maximum stress component in the direction of applied stress. r is the radius of the pore, whereas d is the distance of the center of the pore to the surface. Therefore, the pore touches the surface for $r/(r+d) = 0.5$.

Another particularity of surface defects is that they are exposed to the external environment. Conversely, internal defects are in contact with vacuum or inert gas. It has been shown that the presence of air can have a deleterious effect on the fatigue life of the Ti64 alloy and in particular on the threshold stress intensity factor K_{th}, which is the minimum stress intensity factor required to induce a significant crack growth [XU 21, JUN 21, IRV 74].

Cette thèse est accessible à l'adresse : https://theses.insa-lyon.fr/publication/2024ISAL0014/these.pdf
© [F. Steinhilber], [2024], INSA Lyon, tous droits réservés

1.3.1.2 Importance of proximity to the surface

Crack initiation on an internal defect can sometimes be seen, even on samples with an as-built surface [LIU 14]. This was for example observed in 3 cases out of 13 in the study of [CHA 18] on the fatigue of L-PBF and E-PBF Ti64.

In such cases, the defect is often located in the sub-surface region [LIU 14, AND 19b]. As an example, [TAM 17] observed in Ti64 manufactured by E-PBF that for 10 out of 11 cases where initiation was found to occur from a pore, the pore was located in the sub-surface region. Like surface defects, **sub-surface defects are therefore particularly harmful.** The reasons are also similar. FEM calculations introduced previously in Fig.1.12 show that the stress concentration induced by an internal defect increases when its distance to the surface decreases. Such a stress concentration promotes crack initiation and can provoke the rapid failure of the ligament that separates the pore from the surface. This creates a large defect at the surface, which will be particularly harmful for the reasons invoked in the previous paragraph.

1.3.1.3 Comparing internal defects: lack of fusion defects vs spherical pores

When a specimen is machined, surface defects – which are the most harmful – are removed. Consequently, the remaining internal defects become the most critical ones and are often found to be the cause of fatigue failure [KAS 15, Fig.15c]. This effect is more pronounced for samples with polished surfaces since in the case of machined surfaces, grooves are still present at the surface and can promote crack initiation [YU 19].

Among all internal defects, lacks of fusion are generally identified as the most critical ones [GON 15, PLE 20c, SAN 20, LAR 18]. This is due to their elongated shape and larger size. For example, [CHA 18] observed in the case of machined L-PBF Ti64 specimens 25 initiations on lack of fusion defects against 12 on smaller internal defects such as spherical pores. The effect is even more pronounced when specimens are printed with their axis parallel to the build direction, since lacks of fusion are in this case perpendicular to the loading direction.

Similarly, by comparing the mechanical behavior of L-PBF Ti64 manufactured with different process parameters (excessive vs insufficient energy input), [GON 15] concluded that keyhole pores – that are small and spherical – do not significantly impact mechanical properties even for volume fractions of the order of 1%. On the opposite, lacks of fusion generated by an insufficient energy input – that are larger and elongated – already lead to a substantial decrease of mechanical properties for volume fractions of 1%. This effect is visible for both tensile and fatigue properties.

According to the study of [AND 19b] dedicated to the fatigue properties of 316L stainless steel fabricated by L-PBF, the first-order factor remains the proximity of the defect to the surface. The defect responsible for the failure, located in the sub-surface region, had thus in several cases a size much smaller (up to 3.6 times) than that of the largest defect observed in the core of the sample.

To summarize, it is finally possible to give a first qualitative classification of the types of defects by order of increasing harmfulness in fatigue for Ti64:

$$\textbf{Surface notches} > \left| \begin{array}{ccc} \textbf{Lacks of fusion} & > & \textbf{Spherical pores} \\ \textbf{Sub-surface} & > & \textbf{Core} \end{array} \right.$$

Cette thèse est accessible à l'adresse : https://theses.insa-lyon.fr/publication/2024ISAL0014/these.pdf
© [F. Steinhilber], [2024], INSA Lyon, tous droits réservés

1.3.2 A quantitative comparison of the impact of surface vs internal defects

To estimate the relative influence of internal and surface defects more quantitatively, the impact of the following different post-treatments can be compared:

- No Hot Isostatic Pressing (HIP) or surface modification (denoted as-built here)
- HIP only (no modification of surface defects while internal ones are healed)
- Machining/polishing (suppression of surface defects while internal ones are still present)
- Machining/Polishing + HIP (suppression of both internal and surface defects)

Since machining or polishing enables the removal of surface defects and HIP allows the removal of internal ones, the combination of these conditions enables decorrelating the influence of these two families of defects.

Of course, the conclusions must be nuanced for several reasons:

- Machining/polishing without HIP will bring defects that were previously located in the sub-surface directly at the surface. Even if surface notches present in as-built surfaces are removed, new surface defects can therefore be created [CHI 21, CAR 19].
- Machining leaves residual stresses at the surface that can have a strong influence on the mechanical behavior. Typically, if compressive stresses are generated, they will inhibit crack initiation at the surface.
- HIP treatments — carried out at very high temperatures (∼900 °C) — will cause significant modifications in the microstructure such as broadening of α-laths, which may influence fatigue properties.
- Not all pores are necessarily closed after HIP [PLE 20b, LI 19] and it has therefore been observed in some cases that crack initiation occurs on a partially closed pore [CHA 17].

Nonetheless, many studies report the influence of defects on fatigue properties by comparing the above conditions and most of them show good agreement with each other. Among others, the work of [MAS 18] is representative of most of the published results. The fatigue performance of the as-built, HIP, machined, and HIP+machined conditions was compared in rotary bending fatigue tests. Comparing these different conditions, [MAS 18] arrived at the following ranking in terms of performance:

AB surface w/o HIP $<$ **AB surface with HIP** $\ll$ **Polishing w/o HIP** $\ll$ **Polishing with HIP**

where *AB* is an abbreviation for *as-built*.

Cette thèse est accessible à l'adresse : https://theses.insa-lyon.fr/publication/2024ISAL0014/these.pdf
© [F. Steinhilber], [2024], INSA Lyon, tous droits réservés

Fig.1.13 shows the Wöhler curves obtained by [MAS 18] in more detail.

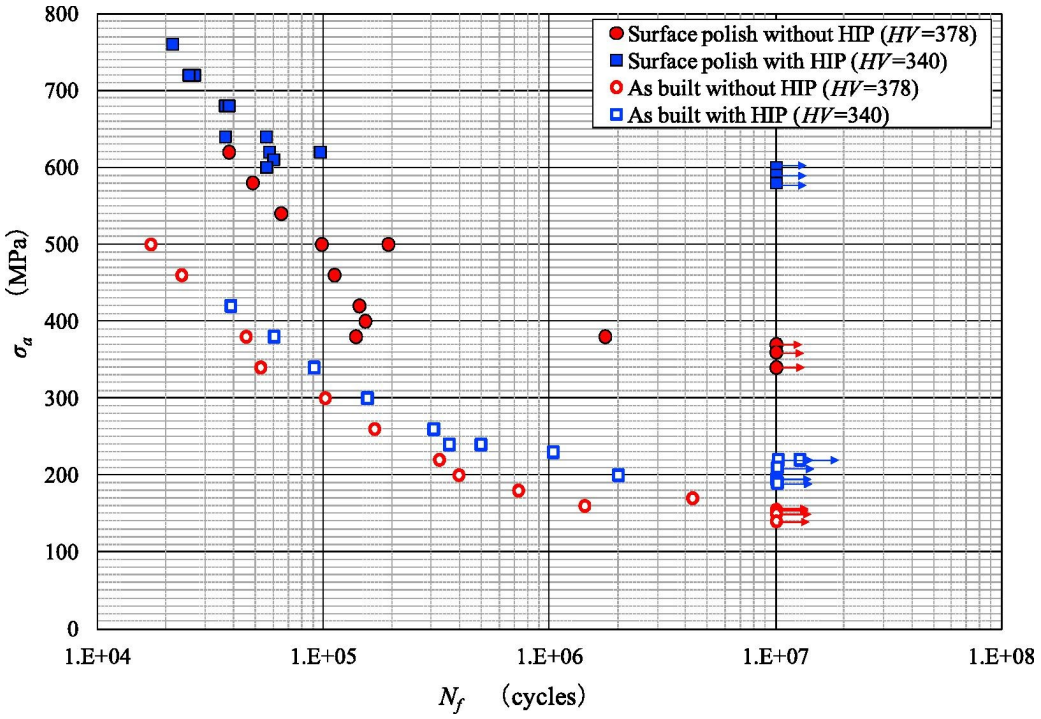

Figure 1.13 | Wöhler curves obtained with or without polishing and HIP of L-PBF Ti64 [MAS 18] (60Hz rotational bending tests on vertically built specimens)

Before comparing the fatigue performances of the different conditions, we can already notice in Fig.1.13 that the differences in fatigue performance between conditions are more pronounced for longer fatigue lives. It is in this zone that crack initiation represents the most important fraction of fatigue life (compared to the crack propagation regime); the influence of defects therefore tends to be exacerbated.

The Wöhler curves also generally show more scattering on machined or polished specimens than on as-built surface specimens. This is slightly noticeable in Fig.1.13, but the effect can be even more pronounced — see for example [WYC 13]. This difference in behavior can be attributed to the fact that in the as-built condition, there is a very large statistical representation of surface defects in each specimen. Conversely, on machined or polished specimens, the critical defect density is lower and therefore there may be statistically more variation in fatigue life from one specimen to another.

We can see that **the beneficial effect of HIP is limited on specimens with an as-built surface**: the fatigue strength at 10^7 cycles σ_{10^7} is 155 MPa with an as-built surface without HIP and 195 to 220 MPa in the as-built + HIP condition — which represents an improvement of 25-42%. Once again, we see **the most deleterious effect of the surface defects** present for an as-built surface in comparison with the effect of the internal defects suppressed by HIP. This effect can be partly attributed to the fact that tests are performed in rotational bending, thus favoring crack initiation at the surface. However, the same tendency can be found in several other studies with tests not carried out by rotary bending (see e.g. references given in Tab.1.1): greater harmfulness of surface defects is observed.

Cette thèse est accessible à l'adresse : https://theses.insa-lyon.fr/publication/2024ISAL0014/these.pdf
© [F. Steinhilber], [2024], INSA Lyon, tous droits réservés

Compared with the application of HIP without any surface modification, polishing without HIP allows a much more significant increase of σ_{10^7} from 155 MPa to 370 MPa (139% improvement) because the surface defects have been removed. Finally, **the application of a HIP treatment together with surface polishing yields the best results**. The first-order defects once the polishing is done are indeed the pores and their elimination by HIP makes it possible to obtain a fatigue strength of 610 MPa — i.e. an improvement of 294% compared to polishing without HIP. For comparison with Ti64 obtained by conventional processes, [VAY 19] measured on rolled Ti64 a fatigue limit of 676 MPa at $R = -1$, and [KAH 17] measured a fatigue strength at 5×10^6 cycles of 800 MPa at $R = 0.1$ for forged Ti64.

The same trends are found by many authors, whether for fatigue tests at $R = -1$ [CHA 18, VAY 19, KAS 15] or $R = 0.1$ [WYC 13, GRE 17, KAH 17, BAG 17]. [PER 18] also came to the same conclusions on E-PBF Ti64.

[EDW 14] on the other hand finds little influence of polishing (see Fig.1.14a), contrary to what is generally observed in the literature. In this particular case, the poor performance in the polished state (200 MPa at 10^6 cycles) could be explained by the high porosity observed — see Fig.1.14b-c. Under such conditions, the influence of porosity could eventually become non-negligible compared to that of the surface state. It is also possible that polishing has brought these pores to the surface, making them even more harmful.

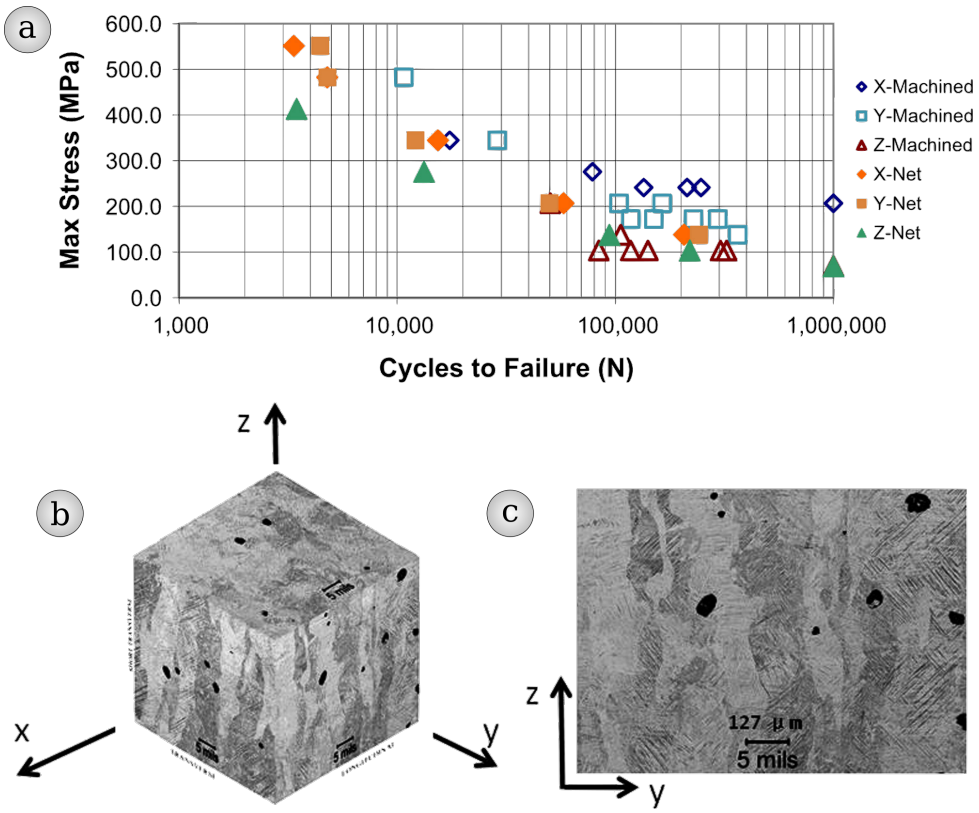

Figure 1.14 | (a) Wöhler curves obtained for varying surface states ("Net" = as-built) and build directions by [EDW 14] ($R = -0.2$). (b) and (c) Optical microscope characterization of the corresponding material, showing a high pore density [EDW 14].

Cette thèse est accessible à l'adresse : https://theses.insa-lyon.fr/publication/2024ISAL0014/these.pdf
© [F. Steinhilber], [2024], INSA Lyon, tous droits réservés

To conclude this section, Tab.1.1 gathers estimations of the fatigue limit of L-PBF Ti64 found in several studies from the literature. In most cases, the fatigue limit is estimated by the fatigue strength at 10^7 cycles.

Study	Surface state	Build direction	Heat treatment	R	σ_f estimate (MPa)
[VAY 19]	as-built	Z	750 °C 1h Ar + HIP	-1	223
	Machined	Z	750 °C 1h Ar + HIP	-1	513
[KAS 15]	as-built	Z	HIP + 700 °C 1h	-1	~ 200
	Machined	Z	HIP + 700 °C 1h	-1	~ 350
[LEU 13]	Machined	Z	HIP	-1	620
[MAS 18]	as-built	Z	SR	-1	155
	as-built	Z	SR + HIP	-1	195-220
	Polished	Z	SR	-1	370
	Polished	Z	SR + HIP	-1	610
[GON 15]	Polished	Z	None	0.1	350
[GRE 17]	as-built	Z	710 °C 2h (vac.)	0.1	200
	as-built	Z	HIP	0.1	170
	Machined	Z	710 °C 2h (vac.)	0.1	470
[BAG 17]	as-built	Z	540 °C 4h (vac.) + HIP	0.1	300
	Machined	Z	540 °C 4h (vac.) + HIP	0.1	775
[KAH 17]	as-built	Z	650 °C 3h (Ar)	0.1	300
	as-built	Z	650 °C 3h (Ar) + HIP	0.1	300
	Polished	Z	650 °C 3h (Ar) + HIP	0.1	500-600
[REK 15]	as-built	XZ	800 °C 2h	0.1	230
[RA 13]	Machined	-	None	0.1	550
[WYC 13]	as-built	45°	650 °C 3h (vac.)	0.1	210
	Polished	45°	650 °C 3h (vac.)	0.1	510

Table 1.1 | Fatigue limit σ_f estimations for L-PBF Ti64 in several studies , for varying stress ratios R, surfaces states, heat treatments (SR = Stress Relieving) and orientations (Z $\perp$ build plate). Most of the time, the fatigue limit is estimated by the fatigue strength at 10^7 cycles.

Cette thèse est accessible à l'adresse : https://theses.insa-lyon.fr/publication/2024ISAL0014/these.pdf
© [F. Steinhilber], [2024], INSA Lyon, tous droits réservés

1.4 Modeling the impact of defects on fatigue properties

Many studies have focused on modeling the impact of defects on fatigue properties. Their aim is often, for a given population of defects, to estimate the resulting fatigue life [ROM 18, PEG 19, XU 21]. When trying to understand more deeply the mechanisms at the origin of the influence of defects, it can also be a goal in itself to find a model that quantifies the relative harmfulness of the different defects [TAM 17, PLE 20a]. Such a model can help to understand which parameters are the most relevant to defects harmfulness – e.g. its size, proximity to the surface, etc. It therefore provides information about which types of defects have to be most avoided. In the best case scenario, one can even hope to predict before a fatigue test the *killer defect* – i.e. the one which will cause failure. Such a prediction tends to be complex and attempts made so far often shown limited success.

Several physical quantities are used in the literature when trying to quantify defects' harmfulness. Common ones are the **stress concentration factor** K_t, the **fatigue notch factor** K_f and the **stress intensity factor** K. These parameters describe different physical phenomena. It is thus interesting to understand the physical meaning behind the choice of one or another to quantify defects' harmfulness.

1.4.1 A brief exploration of theory: K_t, K_f, K... which difference?

Fig.1.15 completes Fig.1.3 by adding the physical quantity which is theoretically relevant to predict the material behavior at each step of the overall fatigue life according to [SCH 09]. One can see that according to this author, the relevant parameter for crack initiation is the stress concentration K_t.

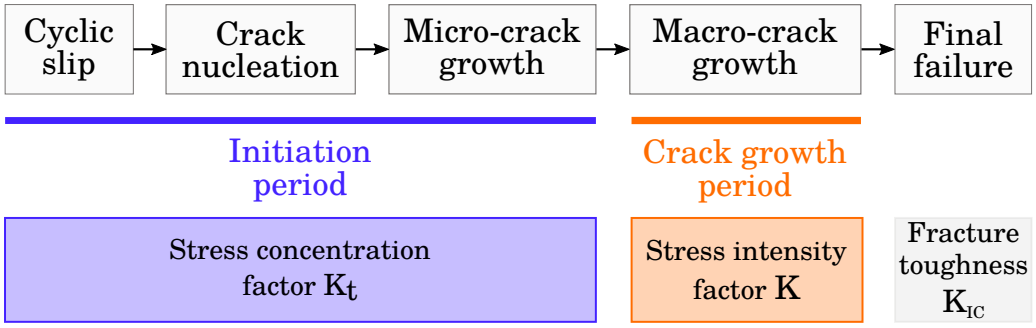

Figure 1.15 | Different stages in fatigue life and dedicated physical quantities. Adapted from [SCH 09, p.15].

1.4.1.1 The stress concentration factor K_t

The stress concentration factor K_t is employed to quantify stress increases at specific points within a component due to variations in geometry. Specifically, it represents the ratio of the maximum stress σ_{peak} experienced by the material to the nominal stress $\sigma_{nominal}$ that the material would encounter without stress concentration. It is worth noting that K_t does not encompass stress increments resulting from a reduction in cross-sectional area within a component. The definition of K_t according to [SCH 09] is presented in Fig.1.16 and Eq.1.1.

Cette thèse est accessible à l'adresse : https://theses.insa-lyon.fr/publication/2024ISAL0014/these.pdf
© [F. Steinhilber], [2024], INSA Lyon, tous droits réservés

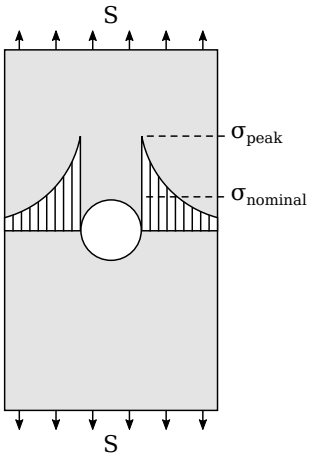

Figure 1.16 | Stress concentration induced by a central hole in a plate , adapted from [SCH 09, Fig.3.1].

$$K_t = \frac{\sigma_{peak}}{\sigma_{nominal}} \tag{1.1}$$

Elevated stress concentration triggers unusually high localized stresses. This, in turn, can activate cyclic slip and potentially lead to crack initiation. Hence, K_t can be regarded as a useful parameter for assessing crack initiation. **From this perspective, the influence of defects can be quantified by considering their role as stress and strain enhancers.**

For simple geometries, analytical formulas expressing K_t as a function of geometrical parameters can be found in the literature. For instance, [ING 13] showed that the stress concentration generated by an elliptical notch in a semi-infinite panel is given by Eq.1.2 — see Fig.1.17 for an illustrative scheme.

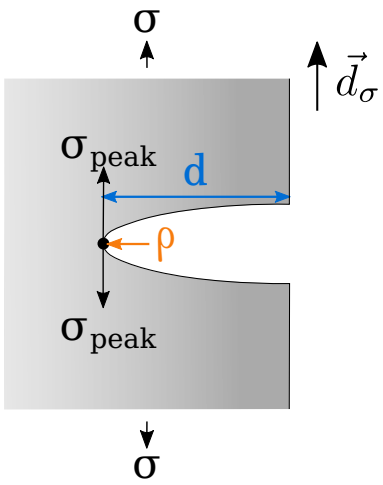

Figure 1.17 | Stress concentration induced by an elliptical notch in a semi-infinite panel submitted to a stress σ in the direction $\vec{d}_\sigma$ perpendicular to the ellipse major axis. d and ρ are respectively the depth of the notch and the radius of curvature at its root.

$$K_t = 1 + 2\sqrt{\frac{d}{\rho}} \tag{1.2}$$

where d is the depth of an elliptical notch in a semi-infinite panel, ρ is the radius of curvature and K_t is the stress concentration at its root.

Cette thèse est accessible à l'adresse : https://theses.insa-lyon.fr/publication/2024ISAL0014/these.pdf
© [F. Steinhilber], [2024], INSA Lyon, tous droits réservés

1.4.1.2 K_f and the Theory of Critical Distance (TCD)

However, it has long been known that **the difference in fatigue strength between a smooth (without any notch) and a notched specimen is generally not well predicted by the simple use of** K_t. This led to the definition of the fatigue notch factor K_f, which is simply the ratio between the fatigue strengths of smooth and notched specimens [WEI 95] – see Eq.1.3.

$$K_f \overset{\text{def}}{=} \frac{\text{Fatigue strength of smooth specimen}}{\text{Fatigue strength of notched specimen}} \tag{1.3}$$

Various expressions have then been proposed to describe the $K_f - K_t$ relation. The most common and easiest one is probably the one in Eq.1.4. It considers that the difference between K_f and K_t is given by a material constant, the *notch-sensitivity factor* q [MAJ 10].

$$q \overset{\text{def}}{=} \frac{K_f - 1}{K_t - 1} \tag{1.4}$$

However, such an expression does not explain the physics behind K_f: it somehow hides the question behind another parameter, q. Moreover, K_f actually depends not only on the material but also on other parameters such as the stress gradient –i.e. how fast the tensile stress decreases in the material near the defect –which, unlike K_t, depends on the notch size.

Again, many expressions have been proposed to refine the $K_f - K_t$ relation so that it can account for these effects. One can for example cite the work of [PET 59] which considers the stress that has to be compared to the fatigue limit (of smooth specimens) is not the one at the notch root, but the one at a certain distance beneath the surface. Using some approximations, he arrives at Eq.1.5.

$$K_f = 1 + \frac{K_t - 1}{1 + {}^{\alpha}/_{\rho}} \tag{1.5}$$

where ρ is the radius of curvature at the notch root and α a material constant.

Works in this field gradually led to the definition of a broader theory, the Theory of Critical Distances (TCD) [TAY 08]. The main idea is simple: **to induce crack initiation, a stress raiser has to increase stress not only at a surface hot spot but also over some critical distance/volume beneath the surface**. A possible justification for this is that for a crack to initiate, it needs to overcome microstructural barriers such as grain boundaries or interfaces with other phases during the early stages of crack propagation (i.e. small crack propagation). If the stress fades away too fast from the stress raiser, the remaining stress may not be high enough to overcome these obstacles [Val 00].

Several methods are proposed in the TCD to calculate this stress. The simpler is the point method, which goes back to the idea of Peterson [PET 59]. It consists of taking the stress at a given distance $L/2$ from the hot spot generated by the stress raiser. It is also possible to calculate an average stress by integrating stress along a line, over an area or a volume. The characteristic distance L is a material constant and can be calculated from the threshold stress intensity factor K_{th} and the fatigue strength of a smooth specimen σ_0 using Eq.1.6.

$$L = \frac{1}{\pi}\left(\frac{K_{th}}{\sigma_0}\right)^2 \tag{1.6}$$

Cette thèse est accessible à l'adresse : https://theses.insa-lyon.fr/publication/2024ISAL0014/these.pdf
© [F. Steinhilber], [2024], INSA Lyon, tous droits réservés

where K_{th} is the threshold stress intensity factor and σ_0 is the fatigue strength of a smooth specimen. Note that these two parameters should to be measured using conditions representative of the loading experienced by the studied sample (stress ratio R for instance). This expression of the L parameter is discussed in more detail in [TAY 08].

The TCD has proven to yield satisfying results in many applications, including on engineering components and for various fatigue loading. Among others, [GIL 22] studied the ability of TCD to predict the impact of surface notches of as-built AM surfaces on fatigue properties. However, **this method requires to know the precise stress distribution inside the material**. Although FEM is now widely used and can provide such data, its use can be prohibited by high computation times in cases of large and complex geometries. This is typically the case for as-built surfaces obtained with additively manufactured components. In such cases, calculations are done mostly on 2D profiles or small surfaces to have reasonable calculation times [BAR 21, VAY 19, HAM 20], which is a strong limitation.

1.4.1.3 The stress intensity factor K

The stress intensity factor (SIF, or K) is a parameter that describes the stress state at a crack tip. It is therefore a parameter related to the propagation of an already existing crack: high stress intensity factors will induce a fast crack propagation. The relation between SIF and crack propagation rate can be modeled using laws such as the one proposed by [PAR 61].

Although the stress intensity factor SIF is a parameter related to propagation and not crack initiation, **it is very often used to model the harmfulness of defects. In other words, the defects are assimilated to cracks of equivalent size**. This can be justified by the fact that for a sufficiently large defect, the crack initiation step can be reduced to a very short time, the majority of fatigue life being spent on long crack propagation (which is governed by the SIF at the crack tip). This effect was depicted in Fig.1.4.

Moreover, as soon as a crack initiates from a given defect, the resulting stress intensity factor is close to the one of a crack whose length is the sum of the defect and the crack one. Even though this is an approximation and the SIF will be over-estimated at the beginning of propagation, when the size of the crack emanating from the defect gets larger, its SIF becomes equivalent to the SIF of a crack of similar size but with no defect. This effect is shown in the case of a circular hole in a finite plate in Fig.1.18.

In other words, if the defect is large enough, it may be suitable to consider the defect to be a crack from the beginning, and therefore to define an associated SIF that will reflect the severity of the defect. This approach has been widely used in many applications in the literature. **The equivalent SIF is commonly calculated using the Murakami parameter, which is the square root of the projected area of the defect in the loading direction** [MUR 83]. This parameter is then often used to estimate the fatigue limit σ_ω of a specimen containing a defect using Eq.1.7 [MAS 18, YIN 23].

$$\sigma_\omega = \frac{C \cdot (HV + 120)}{\sqrt{area}^{1/6}} \tag{1.7}$$

where σ_ω is in MPa, HV is the Vickers hardness in kgf/mm^2, and $\sqrt{area}$ is the highest Murakami parameter measured for the defects contained in the specimen, in µm. The constant C is equal to 1.43 for a surface defect and 1.56 for an internal one.

Cette thèse est accessible à l'adresse : https://theses.insa-lyon.fr/publication/2024ISAL0014/these.pdf
© [F. Steinhilber], [2024], INSA Lyon, tous droits réservés

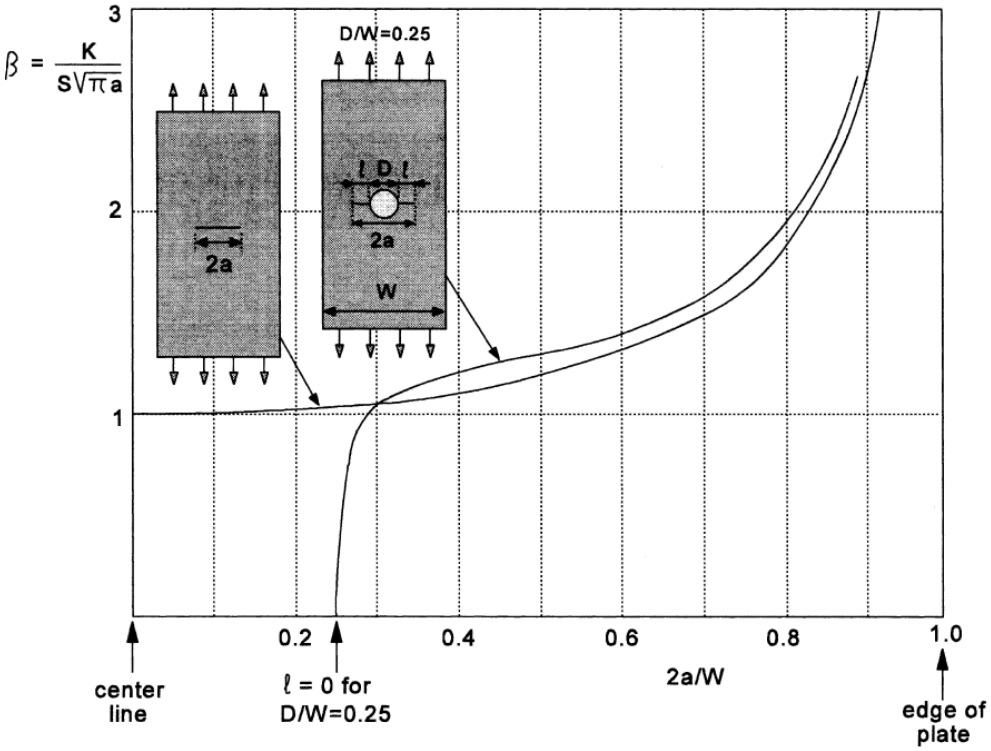

Figure 1.18 | Comparison of the stress intensity factor of a central crack and of a hole with two edge cracks. Taken from [SCH 09, Fig.5.8]. As the cracks propagate (i.e. as $^{2a}/_{W}$ increases), the stress intensity factor in the case of the two edge cracks initiated on the hole rapidly reaches the same value as the one of the central crack.

1.4.2 Estimation of defects harmfulness in the case of L-PBF Ti64

1.4.2.1 The Murakami parameter $\sqrt{area}$

The impact of defects on the fatigue properties is **very often quantified using the Murakami parameter**, which is the square root of the area of the defect projection along the loading direction. It is usually noted $\sqrt{area}$. [MUR 02] has shown that there is a good correlation between this parameter and the SIF of a crack. In cases where it seems reasonable to assimilate the defect to a crack, the $\sqrt{area}$ parameter seems therefore a good option to estimate its harmfulness.

Thus, the Murakami parameter has been used in several materials to predict the impact of various defects on the fatigue limit: inclusions in steels [MUR 02], but also artificial surface defects in conventionally processed Ti64 [MAT 03]. Since then, many studies questioned its validity on additively manufactured materials [PER 20, MAS 18, ROM 17, BAR 23, BER 17, TAM 17].

Although the simple definition of the Murakami parameter as the square root of the projected area is straightforward in the case of isolated core defects, some adaptations are needed for particular cases. It is for instance the case to take into account the proximity of a defect to the surface, the proximity of two neighboring defects or even the irregular morphology of defects.

Cette thèse est accessible à l'adresse : https://theses.insa-lyon.fr/publication/2024ISAL0014/these.pdf
© [F. Steinhilber], [2024], INSA Lyon, tous droits réservés

Fig.1.19a-e introduce the definition of this effective parameter $\sqrt{area}_{eff}$ used by [MAS 18].

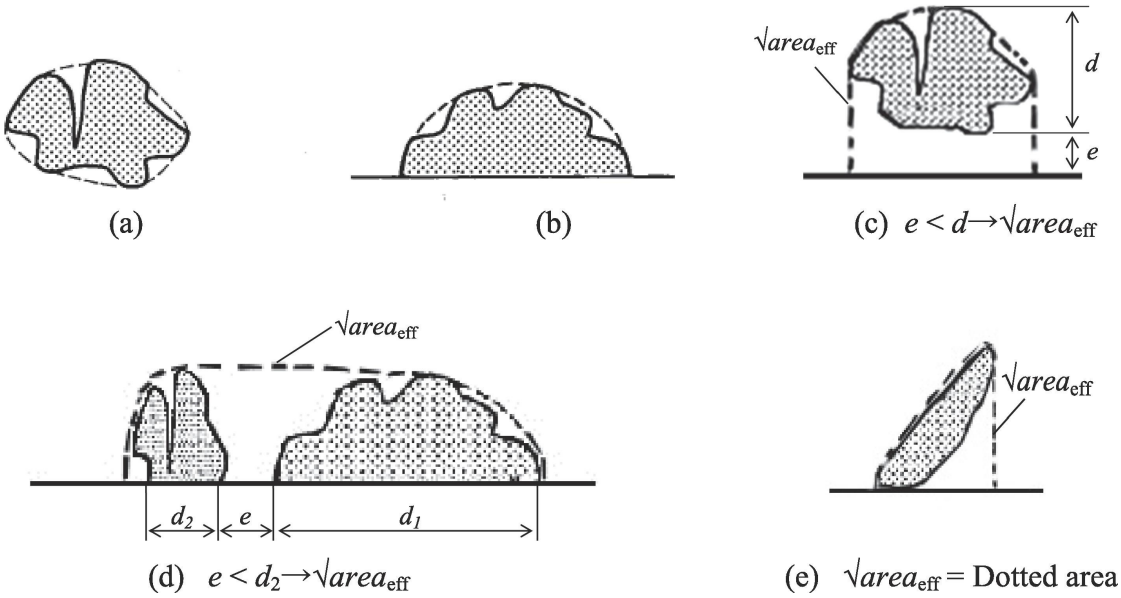

Figure 1.19 | Definition of the effective Murakami parameter $\sqrt{area}_{eff}$ in different configurations [MAS 18]. The figures correspond to the projection of the defects in the plane perpendicular to the stress. (a) Internal non-spherical defect. (b) Surface defect. (c) Sub-surface defect. (d) Interaction between two adjacent defects. (e) Inclined defect in contact with the surface

.

It can be noticed that this parameter allows – at least partially – to take into account the greater harmfulness of internal defects located near the surface. Indeed, it can be seen that the whole ligament connecting such a defect to the surface is considered mechanically inefficient and part of the defect. This effect is taken into account when the distance of the defect to the surface is smaller than its size. This is consistent with Fig.1.12 which showed that the stress concentration induced by a spherical pore is higher when its distance to the surface is smaller than its radius.

The Murakami parameter is often measured post-mortem on a fracture surface. The defect responsible for failure can then be identified and its projected area measured (by SEM for example). Typical $\sqrt{area}$ values of (internal and surface) defects responsible for failure in materials manufactured by L-PBF are given thereafter. They give an order of magnitude of the size of the defects that can cause failure, even if the studies in question concern machined or polished specimens:

- [HU 20b] found values between 30 µm and 72 µm on 21 machined Ti64 specimens, with an average of 61 µm.
- [MAS 18] measured values between 25 µm and 138 µm on 12 polished Ti64 specimens, with an average of 49 µm.
- [AND 19b] found values between 42 µm and 109 µm on 10 polished 316L specimens, with an average value of 69 µm (only the specimens manufactured with the best process parameters are considered).

Cette thèse est accessible à l'adresse : https://theses.insa-lyon.fr/publication/2024ISAL0014/these.pdf
© [F. Steinhilber], [2024], INSA Lyon, tous droits réservés

Fig.1.20 shows the estimations of fatigue life for polished L-PBF and E-PBF Ti64 specimens using the Murakami parameter [MAS 18]. We observe a rather good estimation of the fatigue limit by the model in the case of L-PBF specimens. All the failed specimens were cycled at a stress higher than the predicted fatigue limit σ_ω (taking into account the presence of defects), while several specimens cycled at the fatigue limit did not break after 10^7 cycles. On the other hand, the model is not working well for the E-PBF specimens, since several specimens broke under the predicted fatigue limit.

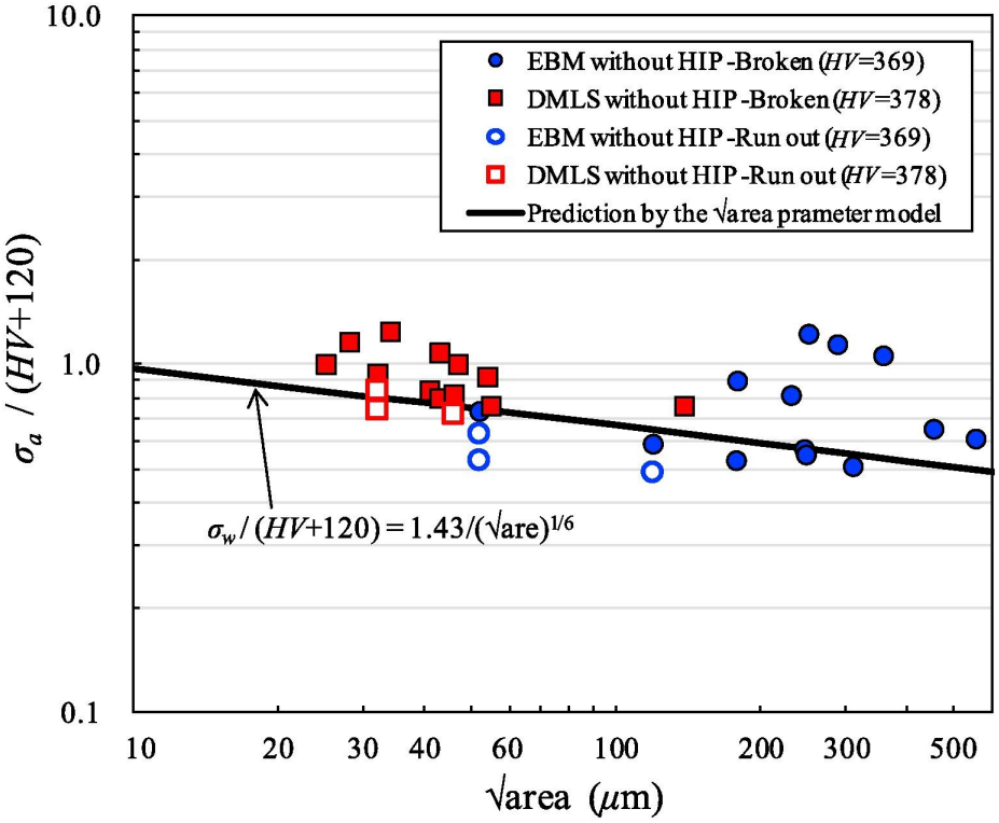

Figure 1.20 | Fatigue limit σ_w prediction for L-PBF and E-PBF polished specimens using the Murakami parameter and Eq.1.7 [MAS 18]. The fatigue limit prediction from the model corresponds to the black line, whereas experimental data is in red and blue. Note that in this figure, the ordinate does not correspond directly to the stress amplitude during the σ_a test but to the amplitude normalized by the factor (HV+120) found in the σ_ω formula. The acronym DMLS (Direct Metal Laser Sintering) refers here to L-PBF process and EBM (Electron Beam Melting) refers to EBM.

In addition to estimating the impact of defects on the fatigue limit, it can be interesting to evaluate their impact on fatigue life reduction in the finite life domain. Several studies have for example evaluated the possibility of predicting the killer defect by characterizing the defect population. [PER 20] proposed a prediction using the Murakami parameter $\sqrt{area}$. For this purpose, E-PBF Ti64 chemically polished specimens were scanned using XCT before testing and the defects with the largest $\sqrt{area}$ were identified. Fatigue tests in uni-axial tension (R=0.1) were then performed and the defects responsible for failure were identified.

Cette thèse est accessible à l'adresse : https://theses.insa-lyon.fr/publication/2024ISAL0014/these.pdf
© [F. Steinhilber], [2024], INSA Lyon, tous droits réservés

It can be found in Fig.1.21 that for the 13 tested specimens, **the defect responsible for the failure was systematically among the most critical defects identified using the parameter $\sqrt{area}$**. However, Fig.1.21 also shows that **the killer defect is rarely the one predicted by the model**, which shows its limits. [AND 19a, Fig.III-38 p.160] followed the same methodology on L-PBF 316L and came to similar conclusions.

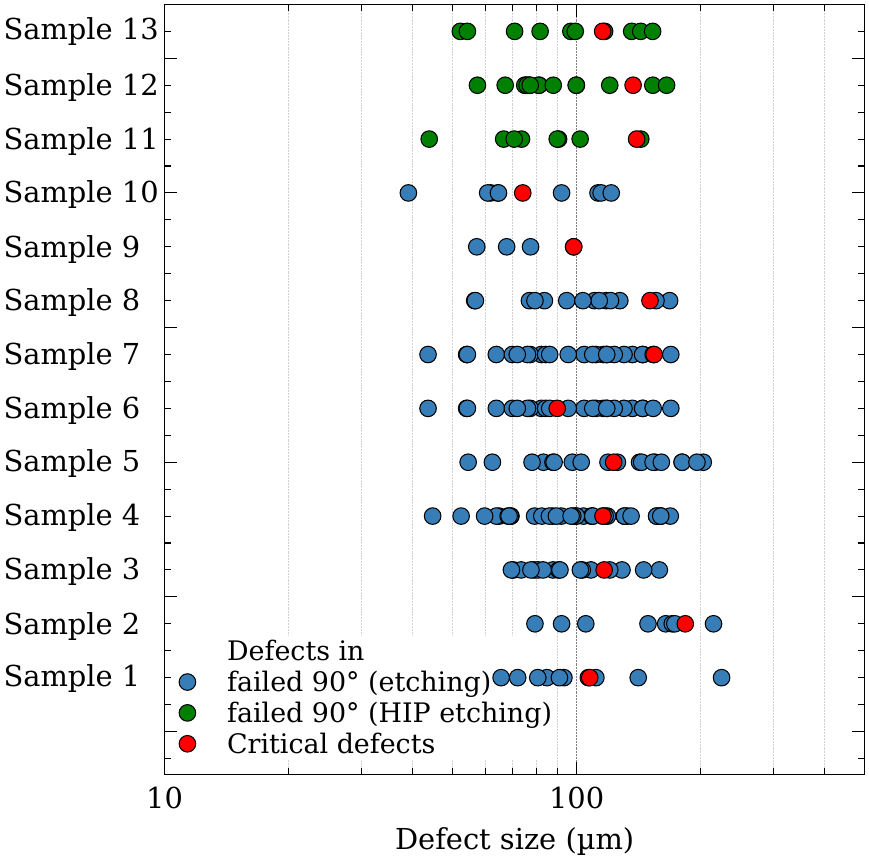

Figure 1.21 | Attempts to predict the killer defect in E-PBF chemically polished Ti64 fatigue specimens ($R = 0.1$) using the $\sqrt{area}$ parameter [PER 20]. For each specimen, the main defects detected using XCT are ranked according to their size – i.e. the $\sqrt{area}$ parameter. The killer defects identified after fatigue testing are highlighted in red. Ten specimens have undergone only chemical etching (in blue) while three did also undergo HIP treatment (in green).

Another important limit of this approach is that **it is limited to specimens whose defects can be clearly delineated** as shown in Fig.1.19a-e, as is the case for internal or surface pores. In the case of L-PBF Ti64, it means that it can only be used for machined or polished specimens. Indeed, as discussed in Section 1.3.1, these are the only cases where most of the cracks will initiate on pores. Conversely, for specimens with an as-built surface, the defects at the origin of failure are most often notch-like defects. These have more complex shapes and are difficult or even impossible to delineate since they tend to be interconnected with each other (see Fig.1.22a-b for an example of interconnected valleys). **Other methods may therefore have to be used to characterize the mechanical severity of valley-type defects.**

Cette thèse est accessible à l'adresse : https://theses.insa-lyon.fr/publication/2024ISAL0014/these.pdf
© [F. Steinhilber], [2024], INSA Lyon, tous droits réservés

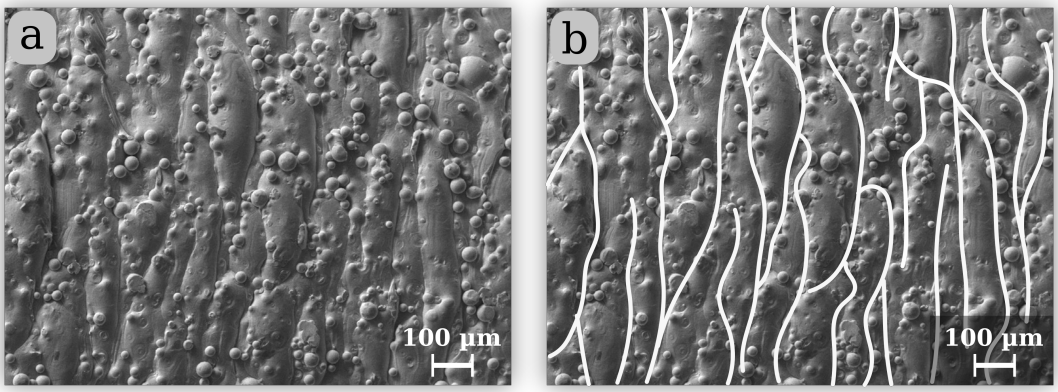

Figure 1.22 | Highlight of complex surface valleys geometry on a vertical as-built surface of a Ti64 sample manufactured by L-PBF, adapted from [BEN 17]. (a) SEM-SE observation of the surface. (b) Delineation of valleys in white.

The study of [NAK 19] also suggests that the $\sqrt{area}$ parameter as defined in Fig.1.19a-e is not suited to characterize specimens with as-built surfaces. In this work, the fatigue limits of L-PBF and E-PBF Ti64 specimens with as-built surfaces have been estimated. They were found to be of 155 MPa and 140 MPa respectively (for non-HIPed specimens). According to the observed fractured specimens in [NAK 19], failure occurs at the surface for as-built surfaces. Furthermore, no obvious and clearly delineated defects could be found on the SEM fracture surface. Eq.1.7 has then been used to estimate the $\sqrt{area}$ parameter of the hypothetical defect leading to the experimentally measured fatigue limit. The obtained values are 16 505 µm and 9635 µm respectively, which was very far from reality.

To overcome this issue, the authors used semi-analytical formulas to estimate an equivalent $\sqrt{area}$ (denoted $\sqrt{area}_R$) parameter based on roughness parameters measurement — see Eq.1.8 and Eq.1.9. These formulas were proposed by [MUR 02] for surfaces with periodical notches of given depth and separated by a given distance. To use these formulas in the case of as-built surfaces, [NAK 19] proposed to replace the notch depth and the notch-to-notch distance by R_a and R_{Sm} roughness parameters respectively. By doing so, they could find more consistent $\sqrt{area}_R$ values (264 µm and 203 µm for E-PBF and L-PBF specimens respectively). Such approaches, based on roughness parameter measurements, are detailed in the next section.

$$\frac{\sqrt{area}_R}{R_{Sm}} = 2.97\left(\frac{S_z}{R_{Sm}}\right) - 3.51\left(\frac{S_z}{R_{Sm}}\right)^2 - 9.51\left(\frac{S_z}{R_{Sm}}\right)^3, \text{ for } \frac{S_z}{R_{Sm}} \leqslant 0.195 \tag{1.8}$$

$$\frac{\sqrt{area}_R}{R_{Sm}} \approx 0.38, \text{ for } \frac{S_z}{R_{Sm}} \geqslant 0.195 \tag{1.9}$$

where S_z is the maximum surface height [Int 21] and R_{Sm} the mean width of profile elements.

To conclude, the $\sqrt{area}$ parameter (with its initial definition) yields interesting results — even if still perfectible in several cases — to account for the severity of internal or surface pores which can be clearly delineated. However, samples with as-built surfaces require other solutions.

Cette thèse est accessible à l'adresse : https://theses.insa-lyon.fr/publication/2024ISAL0014/these.pdf
© [F. Steinhilber], [2024], INSA Lyon, tous droits réservés

1.4.2.2 Estimation of surface defects impact on fatigue by roughness measurements

Since surface defects are of primary importance in the case of as-built L-PBF Ti64 specimens, many studies have been published on the relation between surface state and fatigue properties. Most often, the surface state is characterized using standard roughness parameters, whose definition can be found in standards such as [Int 21]. In many cases, the only parameter used is the arithmetic average roughness (R_a in 2D and S_a for areal measurements).

For instance, [MIA 21] tried to correlate the fatigue limit of E-PBF Ti64 specimens from several studies with R_a, using a simple curve fitting. Even though a reasonable fit is found, such relations tend to be valid only in particular cases and do not provide tools that can be used in a broader context (different materials, manufacturing processes, build directions, etc.). Furthermore, only a few studies are compared in [MIA 21], which makes the fit questionable.

In general, the R_a parameter is therefore not considered to be a good candidate to correlate with fatigue performance [ZAB 18, GOC 19], especially for as-built surfaces of AM materials which often show much more complex geometries than more usual machined surfaces. This is understandable since R_a only reflects the average surface state, while fatigue properties are rather determined by the few most critical defects present in the material.

Several studies — concerning both AM and conventional machined materials — conclude therefore that **a parameter such as the maximum valley depth (R_v/S_v) is better suited** [TAY 91, GOC 19]. However, even in the case of [GOC 19] who found a correlation between S_v and fatigue life, it can be seen that **a lot of scatter remains** — see Fig.1.23a-d.

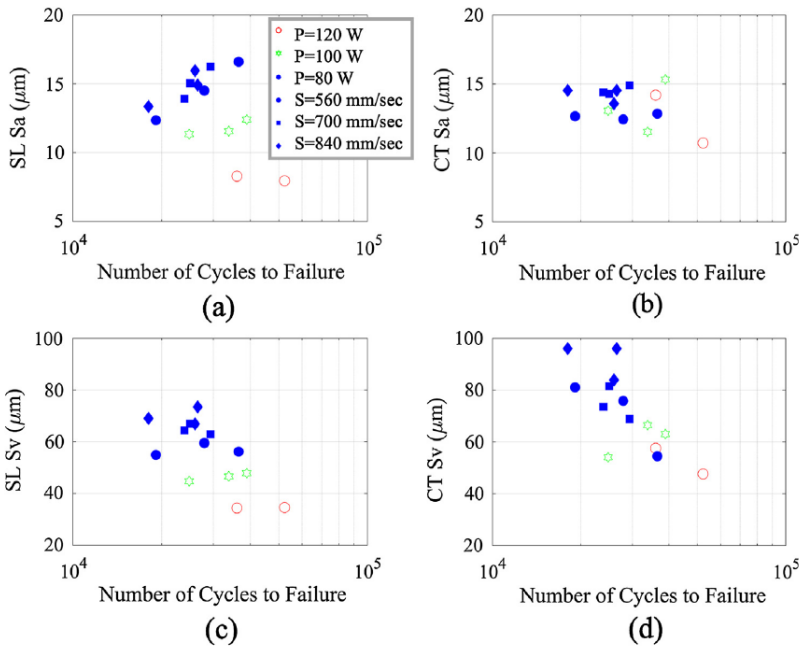

Figure 1.23 | Correlation between roughness parameters S_a/S_v and fatigue life of L-PBF IN718 specimens, taken from [GOC 19]. Fatigue tests were carried out at R=0.1 and σ_{max} = 900 MPa with a frequency of 5 Hz. (a) S_a measured by Structured Light scanning (SL) (b) S_a measured by XCT (c) S_v measured using by SL) (d) S_v measured by XCT.

Cette thèse est accessible à l'adresse : https://theses.insa-lyon.fr/publication/2024ISAL0014/these.pdf
© [F. Steinhilber], [2024], INSA Lyon, tous droits réservés

To go a step further, **several models have been proposed to combine several roughness parameters to get a better prediction of the fatigue properties** [LE 21, ARO 99, ARO 02, BHA 23, PEG 19]. As mentioned previously, [MUR 02] proposed for example a semi-analytical formula to calculate an equivalent $\sqrt{area}$ parameter associated with surface roughness. For its part, [ARO 99] proposed to compute an effective stress concentration $\overline{K_t}$ using Eq.1.10. Note that this equation is derived from Eq.1.2 shown previously. The fatigue notch factor K_f can then be computed as discussed in Section 1.4.1. Using this methodology, [PEG 19] and [LEE 20] obtained reasonable S-N curve predictions for L-PBF Ti64 and 304L stainless steel specimens. However, more studies are needed to estimate the relevance of such an approach.

$$\overline{K_t} = 1 + n\left(\frac{R_a}{\overline{\rho}}\right)\left(\frac{R_y}{Rz}\right) \tag{1.10}$$

where R_a, R_y and R_z are the arithmetic average roughness, peak-to-valley height and 10-point roughness respectively. $\overline{\rho}$ is the average radius determined from the dominant profile valleys. $n = 2$ for uniform tension and $n = 1$ for shear loads.

[POM 20] used similarly an estimation of K_f using roughness and curvature measurements, but in a more local approach. The objective was to try predicting, on top of the fatigue limit, the area of crack initiation. To achieve this result, the surface of the specimen is first segmented into 1 mm squares. For each of them, K_f is calculated from the maximum depth of the valley in this zone and the radius of curvature at the bottom of the notch, determined using Focus Variation microscopy (FV). Fig.1.24 shows that with this methodology, the area of crack initiation — marked by a red cross) — could be effectively identified.



Figure 1.24 | $K_{f,s}$ **map computed using focus variation microscopy on a cast aluminum bending fatigue specimen [POM 20].** The crack initiation site is highlighted by the red cross and is found to occur in the area of maximum $K_{f,s}$.

Such an approach seems promising in the particular case of as-built AM surfaces but has been deployed in a limited number of studies. To go further, it would also be interesting to make an even more local characterization. Indeed, the segmentation in Fig.1.24 of the surface using 1 mm squares is somehow arbitrary and one can suppose that a different segmentation could have led to different results. Furthermore, the defect causing failure is not precisely identified in this case.

Cette thèse est accessible à l'adresse : https://theses.insa-lyon.fr/publication/2024ISAL0014/these.pdf
© [F. Steinhilber], [2024], INSA Lyon, tous droits réservés

1.5 Towards a 3D local characterization of AM surfaces

The previous sections discussed how to use roughness measurements to quantify surface defects' severity. However, it is also worth noting that the way the roughness is measured can be of primary importance. This is especially true for as-built surfaces inherited from L-PBF, and more generally from AM processes. Indeed, since AM allows greater design freedom, additively manufactured parts often show **more complex shapes** than those obtained with conventional processes. Architected structures are a typical example [FOR 16, SOR 21]. In such cases, standard contact-based roughness instruments or optical systems provide incomplete information due to limited access to the surface. Additionally, at the micro-scale, surfaces inherited from AM exhibit a large variety of surface defects such as notches, protrusions or unmelted powders [SAN 21, PER 19, CHA 22]. The interaction between all those defects can make the analysis even more challenging. For instance, **overhanging surface features or unmelted powder particles can hide underlying notches**, as depicted in Fig.1.25. This complexity highlights **the need for both instruments and analysis tools that can accurately characterize complex 3D structures and surface features**[1].

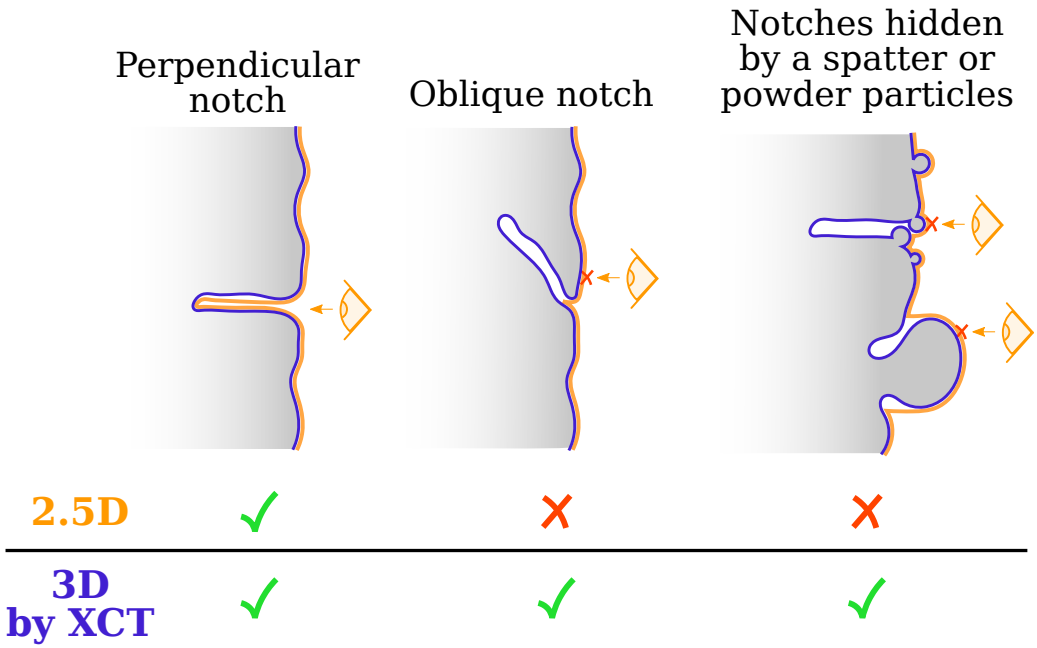

Figure 1.25 | Schematic showing the interest of characterizing AM as-built surfaces in 3D using XCT. Several examples are shown, corresponding to different surface defects. The orange lines show surfaces as seen by a 2.5D characterization tool which probes the surface from a single point of view and without the ability to look through matter. The blue lines correspond to the true surfaces, i.e. the one which would ideally be obtained through XCT using a high resolution, with no noise nor artifacts. In two of the three examples shown, the 2.5D surface characterization fails to account for notches because they are hidden by other surface features.

[1] Note that the term *surface feature* is used here because it is very common in the field of surface characterization and has more general meaning than *surface defects*. Surface features can thus refer to specific elements of the surface that are to be characterized because they may be beneficial for a given application, whereas surface defects refer only to features considered as undesirable.

Cette thèse est accessible à l'adresse : https://theses.insa-lyon.fr/publication/2024ISAL0014/these.pdf
© [F. Steinhilber], [2024], INSA Lyon, tous droits réservés

While many studies report 3D roughness analyses, stricto sensu most of them are not fully 3D measurements. These approaches have limitations in terms of sample geometry and surface features they can characterize. These limitations can originate from the instruments used for raw surface acquisition, such as interferometers or confocal microscopes. The data representation used for subsequent analysis can also lead to information loss. To clarify this, key concepts will be introduced hereafter to differentiate existing approaches for 3D surface characterization and their actual capability to characterize complex 3D structures and surface features.

Surface characterization often involves optical instruments like white light interferometry or confocal microscopy [MIN 14, HAM 20, FOX 18, TOW 16, ALI 20]. These instruments use *unidirectional* light sources, characterizing the surface from a single perspective. Consequently, **surface topography is projected onto a single plane** – the one perpendicular to the light source. This yields height maps with a single z-coordinate value for each (x,y) point on a regular grid. As the third (z-axis) dimension is only partially used, this data representation can be referred to as *2.5D* [HAI 13, THO 18]. Accordingly, instruments like interferometers or confocal microscopes will be termed 2.5D instruments hereafter.

2.5D characterization is feasible for surfaces with simple geometries like planes or cylinders. For complex surfaces, irregularities often prevent the measurement tool from accessing certain areas. This is obvious in AM parts with sophisticated geometries. Even when aiming at characterizing flat and accessible regions, limitations persist if the surface topography includes hidden features. This effect is depicted in Fig.1.25. Orange lines in Fig.1.25 show that a 2.5D surface characterization manages to describe a notch only if the latter is perpendicular to the surface. **It fails if the notch is oblique or hidden by partially melted powders and/or spatters.**

In order to overcome such limitations, developments have recently been made in the field of *free-form metrology* [JIA 20a, ABD 13], which aims at characterizing surfaces of complex and arbitrary shapes. Raw surface acquisition can now be achieved through instruments like structured light scanners [WAN 21, SHA 21] or commercial X-ray tomographs [LOU 19b, ZAN 19, FOX 18, THO 18]. These tools offer *omnidirectional* characterization, thereby facilitating the characterization of complex surfaces. To fully harness this omnidirectional capability, alternative data representations are required. The 2.5D representation limits each (x,y) point to only one z-coordinate, imposing a substantial constraint. To mitigate this, free-form metrology adopts surfaces represented as meshes or point clouds composed of three-dimensional points (x,y,z). Multiple points with identical x and y coordinates can thus exist.

While the free-form surface representation is versatile, it requires **novel analysis techniques different from 2.5D methodologies**, e.g. for surface filtering. Although some studies have employed free-form representations [LOU 19b, GRA 23, ABD 13, MCB 20], this approach is rarely used. Even when surfaces are captured using methods like XCT, **they are often reduced to a 2.5D height map** for subsequent analysis [FOX 18, THO 18, PAG 18, KER 12, LIF 21]. This trend stems from the fact that surface analysis operations, such as filtering of roughness parameters measurement, can be much more complicated when using a complete 3D representation instead of a simpler 2.5D one [JIA 20a].

Thus, some technical issues still need to be overcome to obtain more robust results. Even though the existing solutions may be sufficient, they are often sophisticated and therefore not necessarily user-friendly. They require advanced computer programming skills to be implemented and important computational resources. Further work is thus needed to address these challenges and promote the broader adoption of free-form metrology.

Cette thèse est accessible à l'adresse : https://theses.insa-lyon.fr/publication/2024ISAL0014/these.pdf
© [F. Steinhilber], [2024], INSA Lyon, tous droits réservés

Another distinction can be made between instruments that are able to look through matter (e.g. XCT) and those that are not (e.g. structured light scanning). Although 3D light scanning enables the characterization of complex geometries, it will be limited for parts with inaccessible areas (e.g. lattice structures or internal channels) or too complex/small surface features. On the contrary, the ability of XCT to look through matter and have access to internal features enables – at least in theory – the characterization of any shape and account for any hidden surface features. Hence, as depicted by blue lines in Fig.1.25, XCT succeeds in properly accounting for complex 3D surface features such as notches hidden by unmelted powder, provided that the spatial resolution is sufficiently high. **This makes XCT an interesting option for the characterization of surface defects inherited from AM processes such as L-PBF.**

Tab.1.2 summarizes the different factors that can influence the capability of the various instruments to properly characterize surfaces with intricate 3D macroscopic shapes and/or hidden microscopic surface features.

	2.5D instruments (e.g. interferometers)	**Structured light scanning**	**XCT**
Source directionality	Unidirectional	Omnidirectional	Omnidirectional
Data representation	2.5D	3D possible	3D possible
Ability to look through matter	No	No	Yes
Possible to characterize complex 3D components	No	Yes	Yes
Possible to account for hidden micro-features	No	No	Yes

Table 1.2 Factors influencing the ability of different instruments to properly characterize surface with complex macroscopic shapes and hidden surface micro-features (e.g. notches hidden by unmelted powder particles).

Cette thèse est accessible à l'adresse : https://theses.insa-lyon.fr/publication/2024ISAL0014/these.pdf
© [F. Steinhilber], [2024], INSA Lyon, tous droits réservés

Intermediate summary

Defects act as stress concentration sites, facilitating crack initiation and consequently influencing fatigue resistance. In Ti64 manufactured by Laser Powder Bed Fusion (L-PBF), defects can manifest as internal anomalies (e.g., pores) or surface irregularities (e.g., valleys). Recent research has revealed that surface defects exert a more pronounced impact on fatigue resistance than internal ones, particularly for specimens with as-built surfaces. Notably, the presence of surface defects can lead to a substantial reduction in fatigue resistance. For example, the fatigue limit σ_f is typically 2 to 2.5 times higher for machined or polished specimens (where surface defects have been eliminated) compared to as-built specimens with surface defects – see Tab.1.1. This underscores the significance of developing surface treatments suitable for Additive Layer Manufacturing (AM) that can eliminate these defects.

Traditional methods employed to gauge the impact of defects on fatigue properties (e.g., the $\sqrt{area}$ parameter) may not be well-suited for accounting for surface defects in as-built samples. This is because surface defects in these cases often exhibit intricate and challenging-to-define morphologies such as interconnected valleys. Alternative strategies have been suggested, involving the coupling of surface roughness and curvature measurements to account for the mechanical severity of as-built surfaces. While these approaches show promise, further investigation is required to validate their efficacy.

In the context of surface characterizations, it seems relevant to question whether conventional tools and ensuing analysis workflows are equipped to address defects that have the most critical implications for fatigue properties. Traditional surface characterization primarily takes place in 2D or 2.5D, which may not adequately capture hidden features commonly found in as-built surface features (e.g. notches concealed by unmelted powder particles). Recent advancements in X-ray Computed Tomography (XCT) and free-form metrology (which pertains to 3D surface characterization) offer promising perspectives in this regard. However, such approaches are still relatively uncommon, and solutions for analyzing free-form surfaces are often intricate and relatively unknown. Further investigation is thus necessary to assess the applicability of such tools and enhance their accessibility.

Cette thèse est accessible à l'adresse : https://theses.insa-lyon.fr/publication/2024ISAL0014/these.pdf
© [F. Steinhilber], [2024], INSA Lyon, tous droits réservés

Cette thèse est accessible à l'adresse : https://theses.insa-lyon.fr/publication/2024ISAL0014/these.pdf
© [F. Steinhilber], [2024], INSA Lyon, tous droits réservés

Chapter 2

A methodology for the 3D characterization of surfaces using X-ray computed tomography: application to additively manufactured parts

Contents

2.1 Materials and XCT data acquisition 40
2.2 3D surface characterization methodology 41
2.2.1 Surface segmentation 41
2.2.2 3D roughness calculation 44
2.2.3 3D curvature calculation 49
2.2.4 Quantification of the harmfulness of surface notches 54
2.3 Application to parts with complex geometries 56
2.3.1 Gyroid structure 57
2.3.2 Octet-truss lattice structure 59
2.3.3 Impeller 60
2.4 Application to the prediction of crack initiation sites in fatigue 62
Intermediate summary 70

This chapter introduces **a workflow for 3D surface characterization using XCT**, measuring both **roughness** and **curvature**. By combining these two measurements, we propose **a parameter representative of the severity of surface features with respect to mechanical properties**. This parameter is subsequently applied to the prediction of crack initiation sites on chemically polished Ti64 samples produced by Electron beam Powder Bed Fusion (E-PBF) and subsequently polished. Note that such a methodology could be applied to a large variety of other applications not related to mechanics, e.g. to study the impact of surface roughness on the osseointegration of biomedical implants [DIA 22, ALL 11].

Cette thèse est accessible à l'adresse : https://theses.insa-lyon.fr/publication/2024ISAL0014/these.pdf
© [F. Steinhilber], [2024], INSA Lyon, tous droits réservés

The aim of Chapter 2 is also to demonstrate the benefit of characterizing surfaces inherited from AM as free-form surfaces, taking into account hidden micro-features and opening new avenues to characterize components showing intricate macroscopic shapes. Hence, several application cases are shown with samples of complex shapes, such as architected structures.

2.1 Materials and XCT data acquisition

Different samples were used to demonstrate the application of the developed workflow. Most of them were manufactured by **Electron Powder Bed Fusion (E-PBF)** using an ARCAM A1 machine and **Ti64** powders. To characterize their as-built surface, no surface treatment was applied. Powder grain size distribution ranged from 60 µm to 100 µm and the layer thickness was set to 50 µm. More details about the processing conditions can be found in [PER 19]. To characterize their surface, samples were scanned using laboratory XCT.

A **2 mm vertically built cylinder** was first used as a simple example. It was scanned using a cone beam phoenix | x-ray V | tome | x laboratory tomograph with a voltage of 90 kV, a current of 240 µA, an exposure time of 333 ms and 720 projections. No physical filter was used during scan acquisition. Reconstruction was performed using a standard filtered back projection algorithm (phoenix datos x software). The voxel size used was 2.5 µm, but volumes were downscaled by a factor 2 before further analysis[1]. The resulting voxel size is 5 µm.

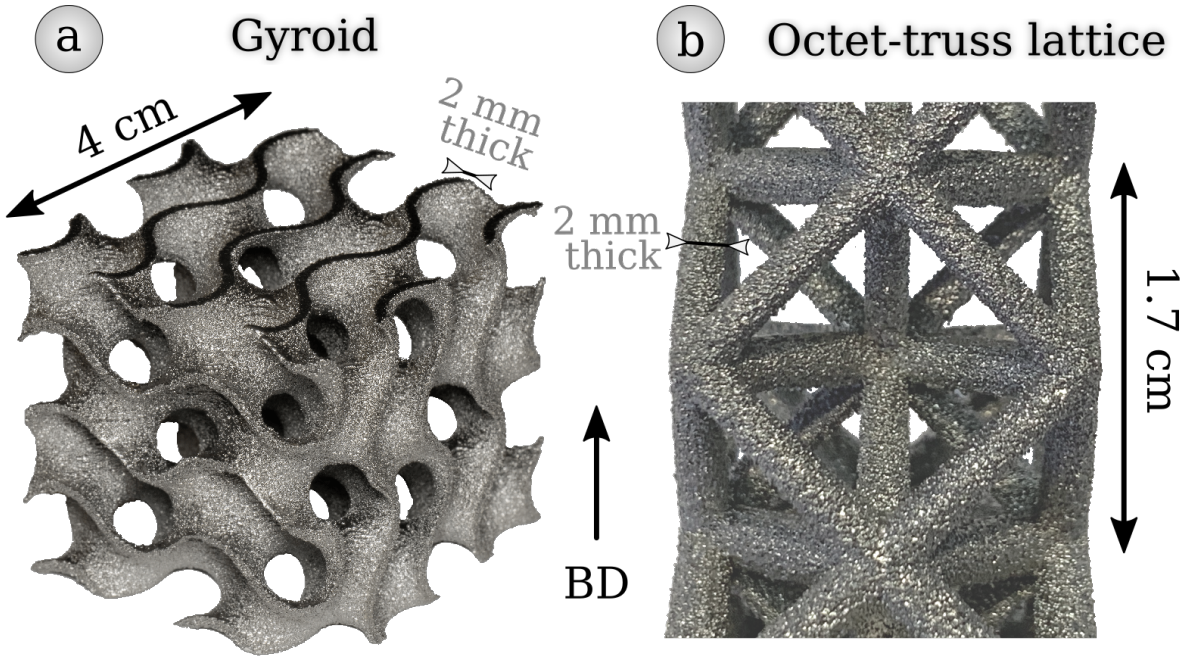

Figure 2.1 | Ti64 architected structures fabricated by E-PBF. (a) Gyroid structure. (b) Octet-truss lattice structure.

Two Ti64 architected structures were also characterized: a **gyroid structure** [SCH 70, YAN 19, SOR 21] and an **octet-truss lattice structure**, see Fig.2.1a-b. Surfaces were kept as-built in both cases.

[1]The data were retrieved from the work of [PER 18], who performed this downscaling to reduce data size.

Cette thèse est accessible à l'adresse : https://theses.insa-lyon.fr/publication/2024ISAL0014/these.pdf
© [F. Steinhilber], [2024], INSA Lyon, tous droits réservés

XCT scans were made with an RX Solutions laboratory tomograph using a Cu filter to mitigate beam hardening artifacts. The main acquisition parameters are summarized in Tab.2.1. Two scans were acquired at different resolutions for the gyroid structure. For all architected structures, reconstructions were done using an implementation of the FDK algorithm [FEL 84].

Sample	Gyroid	Gyroid	Octet truss
Voxel size (µm)	5	10	10
V (kV)	230	230	230
I (µA)	35	70	58
Cu Filter (mm)	1.4	1	1
Number of projections	3616	3616	2240
Exposure time (ms)	2000	333	500

Table 2.1 | Acquisition parameters for XCT scans performed using the RX Solutions laboratory tomograph.

Finally, a Ti64 impeller manufactured by L-PBF was scanned at the BM18 beamline at ESRF synchrotron[2], using a voxel size of 18.5 µm.

All XCT scans were converted to 8-bit after reconstruction to reduce data size. After conversion, volumes size were 158 Mo, 4.6 Go, 5.1 Go and 8.9 Go for the cylinder, the gyroid (10 µm scan), the octet-truss lattice and the impeller respectively.

2.2 3D surface characterization methodology

2.2.1 Surface segmentation

The first step of surface characterization is the segmentation, i.e. the extraction of the surface from XCT scans. Since it can be affected by noise, a **noise-reducing filter** is applied to the reconstructed volume before further calculations. An edge-preserving filter is used to preserve a detailed description of the surface [JAI 16]. A median filter is used because it provides satisfying results while keeping computing time reasonable for large volumes.

After filtering, the sample is **segmented from the volume through thresholding**. Here, thresholding aims at separating the two main peaks of the grayscale histogram, which will be referred to as dark (voids) and bright (sample) peaks – see Fig.2.2. Several methods can be used to automatically determine an optimal threshold. One of the most popular is Otsu's method [OTS 79, VAN 22]. The latter assumes that all voxels are separated into two classes based on their gray level while minimizing the inter-class variance. It yields in most cases consistent and robust results.

[2]The data could be obtained thanks to the help of Dr. Wolfgang Kitsche (design and sizing; testing; Institute of Space propulsion), Katia Artzt, Tarik Merzouk, Ahmet Turak, Jan Haubrich, Guillermo Requena (LPBF building, materials characterization, machine operation etc., Institute of Materials Research).

Cette thèse est accessible à l'adresse : https://theses.insa-lyon.fr/publication/2024ISAL0014/these.pdf
© [F. Steinhilber], [2024], INSA Lyon, tous droits réservés

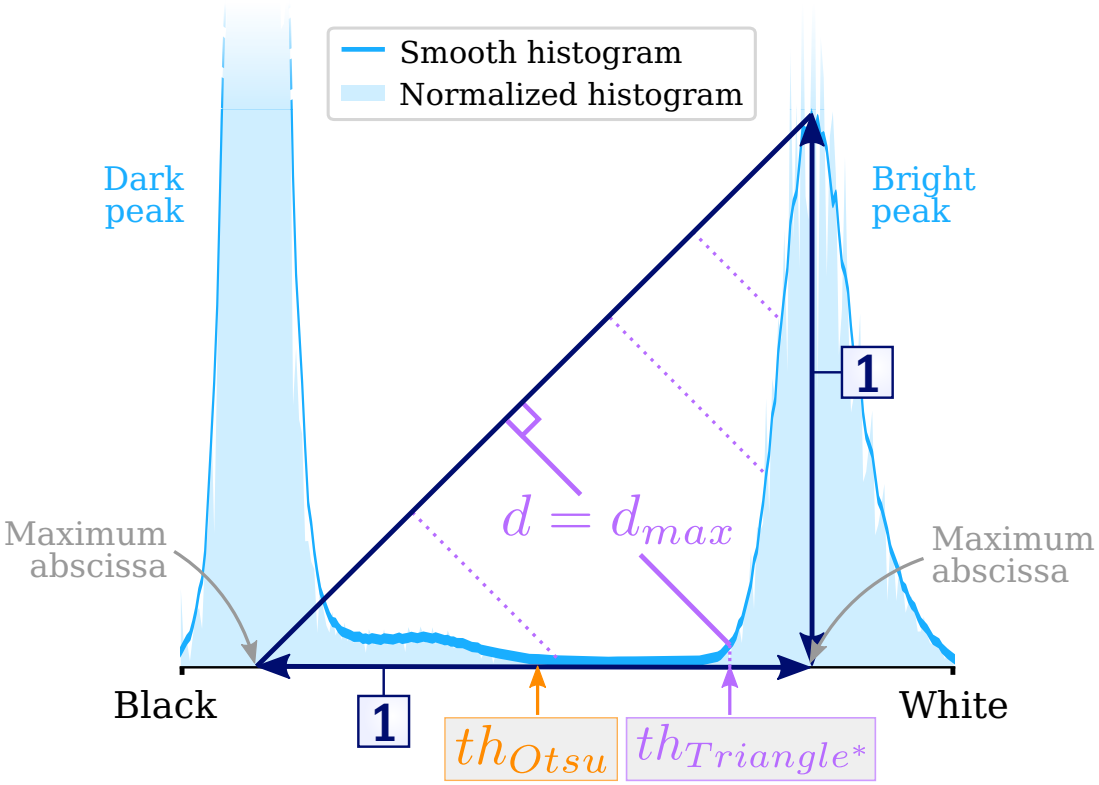

Figure 2.2 | Definition of the TTBH, illustrated based on the E-PBF cylinder normalized grayscale histogram.

However, it may not always be the best choice if one is looking for some specific surface features such as surface defects that will be prone to initiate failure during mechanical loading. In this specific case, partially melted particles are unlikely to be of much interest. They can even hide more severe surface defects such as notches. Contrariwise, deep and sharp notches are very often the most critical defects and are therefore of great interest. However, the sharpest ones are often difficult to segment from XCT data, because the corresponding voxels show intermediate grayscale values. This leads Otsu's method to consider many of them as foreground voxels, erasing notches from the surface although they are the most interesting defects when questions related to crack initiation and failure must be tackled.

This effect can be seen in Fig.2.3a and Fig.2.3b. Fig.2.3a shows an XCT radial slice of a 2 mm as-built E-PBF cylinder, where two deep notches can be seen. Fig.2.3b shows in orange the pixels considered as foreground using Otsu's threshold for segmentation. It can be seen that **both notches are not properly accounted for when using Otsu's threshold**, although they are clearly visible on the grayscale image in Fig.2.3a.

A threshold corresponding to a higher grayscale value than Otsu's one will be certainly more adapted to capture such severe surface defects. Indeed, both partially melted particles and sharp notches typically show intermediate grayscale values because they are at the interface between matter and air. Thus, selecting a threshold that stands at the end of the plateau — just at the left border of the histogram's bright peak — will enable to discard some parts of unmelted powder particles while better capturing sharp notches.

Cette thèse est accessible à l'adresse : https://theses.insa-lyon.fr/publication/2024ISAL0014/these.pdf
© [F. Steinhilber], [2024], INSA Lyon, tous droits réservés

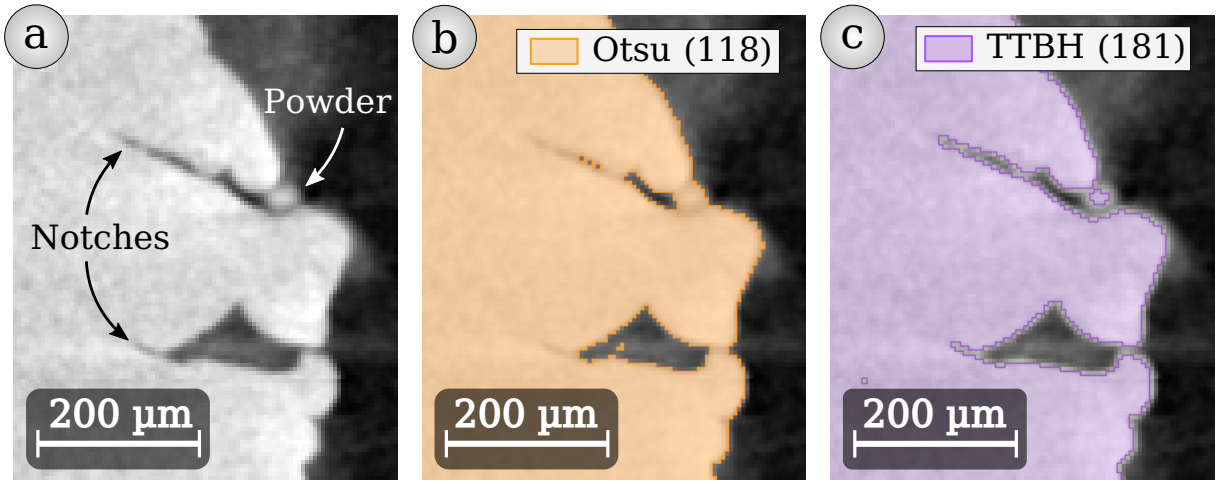

Figure 2.3 | (a) XCT 8-bit radial slice showing two sharp notches and a powder particle (voxel = 5 µm). (b) Otsu's threshold application (orange area) (c) TTBH application (purple area).

The thresholding method proposed is inspired by the triangle threshold introduced by [ZAC 77]. It is thereafter referred to as the *Triangle Threshold for Bimodal Histograms (TTBH)*. Its principle is described schematically in Fig.2.2, and ImageJ/Python implementations have been made available on an online repository [STE 23].

First, if the histogram is too noisy, it may be useful to smooth it. In the present work, a moving average of size 10 is applied. Second, the histogram is normalized so that both the bright peak maximum and the distance between the two histogram peaks are equal to 1. Finally, the desired threshold is simply the gray value which maximizes the distance d as defined in Fig.2.2. As required, the obtained threshold is located just at the left edge of the bright peak. Fig.2.3b-c show that **the two sharp notches are better captured using the TTBH** than by Otsu's method. The powder grain is cropped, which can be both an advantage and a drawback, depending on which surface features one aims to characterize.

It may be worth mentioning that this thresholding method is particularly sensitive to noise and artifacts (e.g. beam hardening). This can be at least partially compensated by the use of the proper noise-reducing filter beforehand. It may also be relevant in some cases to make a compromise between the TTBH and Otsu's threshold. A simple and convenient way to do that can be to calculate both and take an intermediate value.

Following segmentation, the volume undergoes a cleaning process to remove all internal pores or tiny objects caused by measurement noise. This cleaned binary volume is subsequently referred to as the *sample mask*, illustrated in Fig.2.4b. In our case, the sample surface is defined as the *surface mask* depicted in Fig.2.4c. It is the binary mask whose foreground is composed of all surface voxels. These surface voxels are the foreground voxels of the sample mask which have at least one background voxel as a first neighbor. A connectivity of 1 is used to determine neighbors.

Cette thèse est accessible à l'adresse : https://theses.insa-lyon.fr/publication/2024ISAL0014/these.pdf
© [F. Steinhilber], [2024], INSA Lyon, tous droits réservés

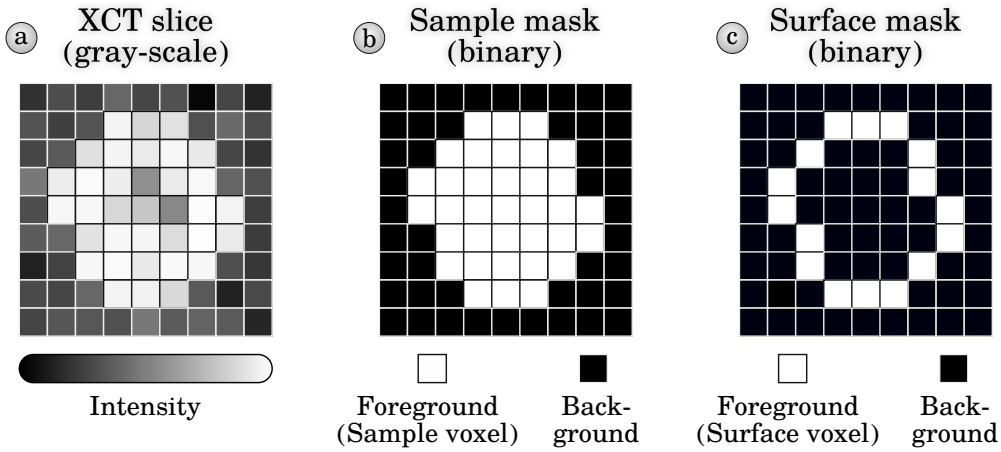

Figure 2.4 | (a) Schematic example of a grayscale XCT slice. (b) Corresponding sample mask. (c) Corresponding surface mask.

2.2.2 3D roughness calculation

The topography of a surface is often divided into 4 components, each one corresponding as a first approximation to a range of spatial frequencies: the object's form, the waviness, the roughness, and the micro-roughness [POM 19, Int 12]. Most commonly, only the roughness component is considered significant for characterizing surface micro-features such as notches or unmelted powder particles. The form and waviness typically represent geometric deviations, while micro-roughness is often viewed as measurement noise. The objective is therefore to discriminate roughness from these other components to achieve a complete surface characterization.

In the case of a conventional 2.5D surface characterization, the shape of the characterized surface is necessarily simple (plane, cylinder...). Form removal, which consists of subtracting the component geometry, can thus be done rather easily using least-squares optimization. Filters are then used to discriminate roughness from waviness (L-filter) and micro-roughness (S-filter). In both cases, the Gaussian filter is the default option [Int 12].

However, 2.5D characterization is only possible for parts with simple geometry, as discussed in Section . To take full advantage of XCT, a 3D surface representation must be used — e.g. a mesh or a point cloud made of points with arbitrary (x,y,z) coordinates. In this case, the roughness characterization workflow can be more challenging. In particular, the form removal step is complex when no analytical expression is adapted. For 3D printed parts, a first approach consists of using as a reference the CAD file or a nominal geometry derived from analytical formulas [**?**, PAG 18]. This is sometimes done to measure geometrical deviations between the manufactured part and its CAD model [SAV 07, JIA 10, VIL 18b]. However, this requires the CAD file or an analytical model to be available, and the geometrical deviations to be small enough to get an accurate measurement.

If the CAD file cannot be used, it is possible to smooth the raw surface and use the result as a reference. In this case, **the roughness is defined as the distance between the surface and a smoothed version of it**. Many studies already addressed this topic, see the work of [JIA 20a] for an extensive review. In such studies, surfaces are generally meshed and may be smoothed using morphological filters [LOU 13b, LOU 19b], diffusion-based filters [JIA 11], anisotropic diffusion-based filters [TAS 02], or wavelet decomposition [JIA 20b].

Cette thèse est accessible à l'adresse : https://theses.insa-lyon.fr/publication/2024ISAL0014/these.pdf
© [F. Steinhilber], [2024], INSA Lyon, tous droits réservés

The methodology presented here follows the same principle of surface smoothing and distance measurement. It can thus be applied to complex geometries without any need for prior knowledge. However, unlike most common processing workflows, in our case, the surface is not extracted as a mesh for calculations. Instead, **all calculations are done on the digital volume** obtained by XCT. One of the advantages is that it can be implemented in standard open-source image analysis software such as ImageJ. The overall image analysis workflow is schematically illustrated in Fig.2.5. An example of the application of such a workflow using ImageJ has also been made available in an online repository [STE 23].

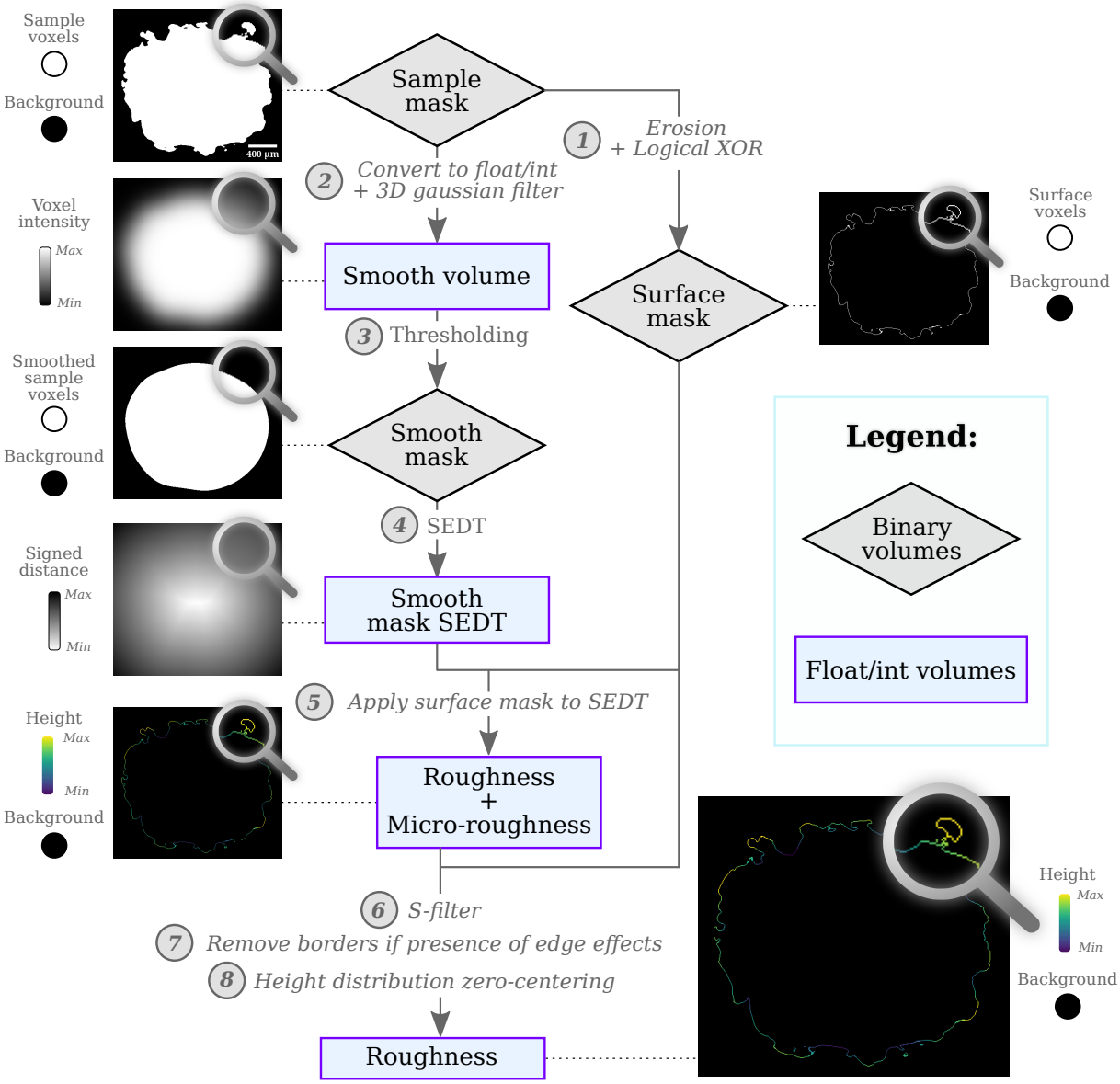

Figure 2.5 | Workflow proposed for the 3D roughness computation. The sample mask and surface mask are defined in Fig.2.4b-c. The images shown correspond to transverse cross-sections of a 2 mm E-PBF Ti64 cylinder at different steps of the calculation.

Cette thèse est accessible à l'adresse : https://theses.insa-lyon.fr/publication/2024ISAL0014/these.pdf
© [F. Steinhilber], [2024], INSA Lyon, tous droits réservés

The proposed workflow only uses as input data the sample mask, whose computation is detailed in Section 2.2.1.

The **first step** is the **computation of the surface mask** – also defined in Section 2.2.1. The latter will be used at the end of the workflow to extract data from volumes only at the voxels of interest – i.e. the surface voxels. The surface mask can be obtained by applying an erosion to the sample mask and then computing the logical XOR operation between the sample mask and the result of the erosion.

The **second step** of the workflow is the **smoothing** step. It is done here by converting the sample mask to float or integer values and applying a 3D Gaussian filter[3]. The chosen degree of smoothing will determine the limit between roughness on the one hand and waviness/form on the other hand. It is quantified by the *cut-off wavelength* λ_c [Int 15], which is the wavelength considered to discriminate form and waviness from roughness. From an image processing point of view, a Gaussian filter is more often adjusted using the standard deviation σ, which can be easily derived from the cut-off wavelength following Eq.2.1.

$$\sigma = \sqrt{\frac{\ln 2}{2}} \cdot \frac{\lambda_c}{\pi} \approx 0.187 \cdot \lambda_c \tag{2.1}$$

where σ and λ_c are the standard deviation and the cut-off wavelength of the Gaussian filter respectively.

ISO standards provide rules to appropriately set the value of the parameter λ_c [Int 12]. Although they are meant for 2D filters applied to height maps, they are used by extension in the developed workflow to adjust the 3D Gaussian filter. Ideally, the choice should be made by observing the surface and identifying the features that need to be characterized as roughness. It is then advised to set λ_c to be five times the size of the largest feature of interest, choosing among a list of predetermined values (0.25 mm, 0.8 mm, 2.5 mm, etc.) [Int 12]. This choice is somehow arbitrary, especially for surfaces obtained by AM with complex topologies. This can explain the large variations of values used in the literature on AM materials [LOU 19a]. [GRA 23] used for example a cut-off wavelength of 0.25 mm while [VET 14] used several values up to 2 mm.

In the **third step** of the workflow, **the smoothed volume obtained after filtering is segmented by thresholding**. This results in a smoothed version of the sample mask denoted hereafter as the smooth mask. The latter is then used as a reference for roughness calculation. The most straightforward choice for the threshold value is the mean value between the values corresponding to background and foreground voxels (e.g. 127.5, if the background is 0 and foreground voxels are 255). However, this leads in general to some volume shrinkage, especially for large λ_c values. To avoid this problem, the threshold value is instead determined automatically so that the smooth mask volume equals the volume of the original mask.

The **fourth step** aims at **computing the distance between the sample surface and its smoothed version**. For this purpose, the Signed Euclidean Distance Transform (SEDT) is computed from the smooth mask[4]. This results in a float volume where the value at each

[3] An alternative solution, not developed here, would be to perform smoothing by applying a 3D morphological filter [LOU 13a, JIA 20a] on the sample mask.

[4] Several methods can be used for the distance computation. The SEDT is given as an example here because it is a very common operation that can be easily found on software such as ImageJ. However, it may lead to some bias in the measured roughness for a smooth surface scanned with a large voxel size. Other methods may in such cases lead to more accurate results. This topic is discussed in Appendix A.

Cette thèse est accessible à l'adresse : https://theses.insa-lyon.fr/publication/2024ISAL0014/these.pdf
© [F. Steinhilber], [2024], INSA Lyon, tous droits réservés

foreground voxel is the distance to the nearest background voxel, and contrariwise for the values at the background voxels. The distances are signed, e.g. positive for background voxels and negative for foreground voxels.

At the **fifth step**, the surface mask is applied to the smooth mask SEDT. This results in a sparse volume where most of the voxels have the same background value (e.g. 0), except the surface voxels which hold the distances to the smooth mask, i.e. the sought roughness values.

The **sixth step** consists in applying an **S-filter**. This aims at removing the highest frequencies, in other words, the micro-roughness. The standard filter used for this purpose is again a Gaussian filter [Int 12]. The cut-off wavelength used for this filter is commonly denoted λ_S. A procedure to calculate the S-filter using 3D Gaussian filters only based on normalized convolution [KNU 93] is described in B. This filtering step becomes particularly relevant if the voxel size set for XCT scans is not small enough to properly describe the surface topography. When the voxel size approaches the dimensions of surface features, the surface tends to be oversimplified and discretized, yielding a staircase appearance. Such oversimplification can result in sharp fluctuations in the roughness measurement. Using the S-filter helps to moderate such abrupt changes.

The **seventh step** addresses **edge effects** that arise due to Gaussian filtering [Int 16]. When computing the filtered value for a particular voxel using the Gaussian kernel, surrounding voxels are taken into account. However, for those voxels near the XCT scan boundary, the convolution radius might extend past this boundary. For these voxels, the XCT scan has to be extrapolated, for instance using an arbitrary constant value. The most common choice is zero. This value aligns well with our needs since 0 represents the background value that is assumed to envelop the sample. However, this method can result in biased values for surface voxels too close to the scan boundary. For example, in the context of a cylinder scan, the topmost and bottommost surface voxels may contain such biased values.

Various solutions have been suggested to address this challenge for 2D or 2.5D roughness measurements [JAN 12]. **The most straightforward solution is to discard roughness values for points located too close to the edges**, typically within a distance of the cut-off value or half of it. In the described workflow, the approach adopted involves cropping the upper and lower borders by a width of $\frac{\lambda_c}{2}$ wherever necessary. However, if this method results in discarding too much data, other strategies, based on extrapolation or the use of normalized convolution [KNU 93], can be employed in the Gaussian filtering step. This would allow the user to address edge effects without the need to truncate volumes later on.

Lastly, the **eighth step** ensures that the **height distribution is zero-centered**, meaning the average height is zero. This condition is intuitive and is assumed when computing certain roughness parameters like S_{sk} and S_{ku}. To achieve this, the average height is subtracted from the height of each surface voxel.

An example of roughness calculated on a 2 mm diameter cylinder fabricated by E-PBF is shown in Fig.2.6. The initial sample's surface and the smooth reference surface are displayed, as well as the derived roughness. Note that points closer than $\frac{\lambda_c}{2}$ to the upper and lower boundaries were discarded at the end of the computation. The triangle threshold for bimodal histograms presented in Section 2.2.1 was used for surface segmentation and a cut-off wavelength λ_c of 0.8 mm has been chosen for roughness calculation. Regarding the S-filter cut-off λ_s, a value of three times the voxel size (0.015 mm) was used.

Cette thèse est accessible à l'adresse : https://theses.insa-lyon.fr/publication/2024ISAL0014/these.pdf
© [F. Steinhilber], [2024], INSA Lyon, tous droits réservés

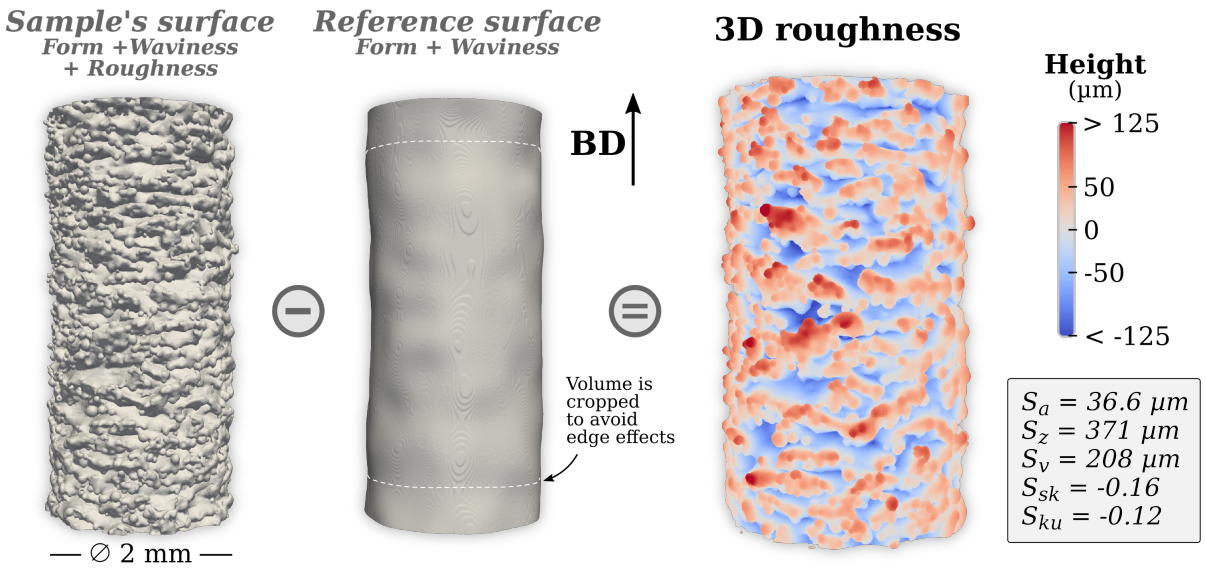

Figure 2.6 | Surface roughness measurements, as described in Fig.2.5, applied to a 2 mm diameter as-built E-PBF cylinder. Computations were made from an XCT scan with a voxel size of 5 µm. Cut-off values were set to $\lambda_c = 0.8$ mm and $\lambda_S = 0.015$ mm = 3 voxel size. To avoid edge effects, points closer to the boundaries than $\frac{\lambda_c}{2}$ were discarded.

The most conventional roughness parameters can be computed easily from the obtained 3D roughness measurement. Formulas that have been used to compute roughness parameters in this chapter and subsequent ones are given in Eq.2.2.

$$S_a = \frac{1}{n} \sum_{\text{surface voxels}} |h| \tag{2.2a}$$

$$S_q = \sqrt{\frac{1}{n} \sum_{\text{surface voxels}} h^2} \tag{2.2b}$$

$$S_z = \left(\max_{\text{surface voxels}} h \right) - \left(\min_{\text{surface voxels}} h \right) \tag{2.2c}$$

$$S_v = - \min_{\text{surface voxels}} h \tag{2.2d}$$

$$S_{sk} = \frac{m_3}{m_2^{3/2}} \tag{2.2e}$$

$$S_{ku} = \frac{m_4}{m_2^2} - 3 \tag{2.2f}$$

where

$$m_i = \frac{1}{n} \sum_{\text{surface voxels}} (h - \bar{h})^i \tag{2.2g}$$

is the biased i^{th} central moment, n is the number of surface voxels, h is the height of a given surface voxel and $\bar{h}$ is the mean height over all surface voxels.

Cette thèse est accessible à l'adresse : https://theses.insa-lyon.fr/publication/2024ISAL0014/these.pdf
© [F. Steinhilber], [2024], INSA Lyon, tous droits réservés

S_a, S_q, S_z, and S_v parameters have intuitive definitions. However, additional explanation may be required to understand the concepts behind S_{sk}, S_{ku}.

The skewness parameter (S_{sk}) reflects the asymmetry of the height distribution. When S_{sk} is positive, the distribution leans towards positive height values, indicating that the surface is primarily composed of peaks. Conversely, when S_{sk} is negative, the distribution leans towards negative height values, suggesting that the surface is dominated by valleys. The kurtosis parameter (S_{ku}) signifies the sharpness of the height distribution. A high S_{ku} value characterizes a distribution with elongated tails and which is sharp near its mean value. This can imply the presence of sharp peaks or valleys on the surface.

All these definitions are mostly identical to the ones provided in ISO standards for 2.5D roughness measurements [Int 21]. However, it is worth noting that using the same formula with 2.5D or 3D will not necessarily lead to the same value for all parameters (even when ignoring the ability of 3D measurements to capture features invisible to 2.5 measurements). Subtle differences may arise, as discussed in [JIA 20a].

As far as computational performance is concerned, the use of 3D operations makes **the presented roughness calculation methodology demanding in terms of Random Access Memory (RAM)**. This can be a limitation for large volumes, which can be overcome to a certain extent by dividing the volume and performing computations in several steps. **Processing time is nonetheless reasonably low** since efficient implementations exist for the operations used. As an example, the computation for the 158 Mo XCT scan of the cylinder in Fig.2.6 took around 1 min on a conventional laptop with 8 CPU cores and using the ImageJ macro provided in [STE 23].

A Python implementation is also available in [STE 23], with some improvements to limit RAM usage and significantly increase computation speed. It also proposes an alternative algorithm for the distance calculation step (4th step), based on a so-called Nearest Neighbor Search (NNS). The NNS-based method is not readily available in ImageJ but has the advantage of requiring much less RAM than the SEDT-based method. Furthermore, it provides more accurate results when the surface to characterize is very smooth, typically when the S_a roughness parameter yields a value close to the voxel size. For this reason, roughness computations are carried out using the NNS method from Chapter 3 onwards, although they are carried out using the SEDT method for the whole of Chapter 2. For the interested reader, a more detailed presentation of the NNS-based method and a comparison of the measurement errors obtained by SEDT and NNS methods for different surface states are provided in Appendix A.

2.2.3 3D curvature calculation

The curvature κ is a measure of how a curve (in 2D) or a surface (in 3D) bends at a particular point. For a curve, it corresponds to the inverse of the radius ρ of the osculating circle at this given point, as schematically shown in Fig.2.7a.

Curvature is a more complex concept for surfaces and several definitions exist. The closest 3D equivalent of the curvature in 2D would be the *directional curvature*, which measures how much the surface bends along a particular direction. When the surface bends outward, the directional curvature is positive; conversely, it is negative. This requires a prior definition of which side of the surface is considered to be the outside. Although directional curvature can be calculated in an infinite number of directions, two are of particular interest. These are the direction of *minimum curvature* $\vec{d}_{min}$ and the one of *maximum curvature* $\vec{d}_{max}$ (the sign being

Cette thèse est accessible à l'adresse : https://theses.insa-lyon.fr/publication/2024ISAL0014/these.pdf
© [F. Steinhilber], [2024], INSA Lyon, tous droits réservés

considered), also known as *principal directions*. The corresponding curvatures are called the principal curvatures κ_{min} and κ_{max}.

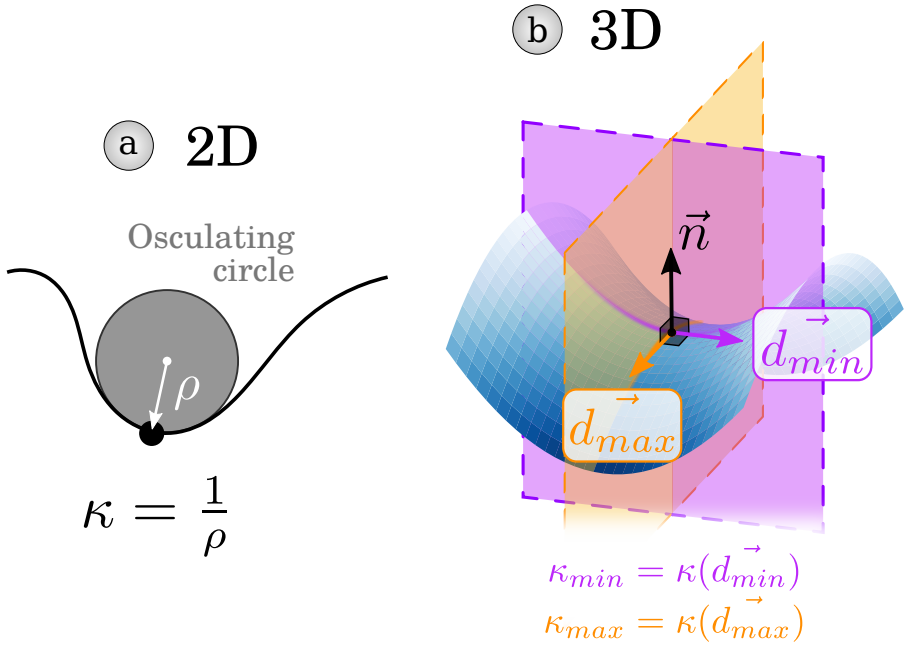

Figure 2.7 | (a) Definition of the curvature κ and the radius of curvature ρ for a curve in 2D. (b) Schematic representation of a saddle-like surface. The normal $\vec{n}$ and the principal directions are indicated at the saddle point. In this particular case, $\kappa_{min} < 0$ and $\kappa_{max} > 0$.

Fig.2.7b shows an example of a saddle-type surface, where $\vec{d}_{min}$ and $\vec{d}_{max}$ are respectively displayed in purple and orange.

Knowing principal directions and curvatures, the directional curvature in any direction can be derived using Eq.2.3 [TAU 95].

$$\begin{aligned} \kappa(\vec{v}) &= \begin{pmatrix} v_n \\ v_{min} \\ v_{max} \end{pmatrix}^{\top} \cdot \begin{pmatrix} 0 & 0 & 0 \\ 0 & \kappa_{min} & 0 \\ 0 & 0 & \kappa_{max} \end{pmatrix} \cdot \begin{pmatrix} v_n \\ v_{min} \\ v_{max} \end{pmatrix} \\ &= v_{min}^2 \cdot \kappa_{min} + v_{max}^2 \cdot \kappa_{max} \end{aligned} \tag{2.3}$$

where $\kappa(\vec{v})$ is the directional curvature in the direction $\vec{v}$, $\vec{v} = v_n \cdot \vec{n} + v_{min} \cdot \vec{d}_{min} + v_{max} \cdot \vec{d}_{max}$ is an arbitrary vector and $\vec{n} = \vec{d}_{min} \times \vec{d}_{max}$ is the surface normal.

Finally, two other common curvatures are often used: the *mean curvature* κ_{mean} and the *Gaussian curvature* κ_{gauss} (see definitions in Eq.2.4 and Eq.2.5):

$$\kappa_{mean} = \frac{\kappa_{min} + \kappa_{max}}{2} \tag{2.4}$$

$$\kappa_{gauss} = \kappa_{min} \cdot \kappa_{max} \tag{2.5}$$

Cette thèse est accessible à l'adresse : https://theses.insa-lyon.fr/publication/2024ISAL0014/these.pdf
© [F. Steinhilber], [2024], INSA Lyon, tous droits réservés

Although exact curvatures may be derived for parametric surfaces defined by analytical formulas, **only estimations are possible for digital surfaces** such as the one obtained by XCT. Several techniques can be used for this purpose. Point clouds can for example be approximated locally by a quadratic surface, which enables to derive curvature estimates from the obtained analytical formula [CAZ 05].

For surfaces defined as the boundary of a collection of voxels in 3D, integral invariants-based estimators have demonstrated their interests both in terms of accuracy and efficiency [LAC 17]. The principle is to move a spherical convolution kernel of radius r_{curv} along the surface – see Fig.2.8 for an example in 2D. Its intersection with the volume enables the estimation of some differential geometrical quantities.

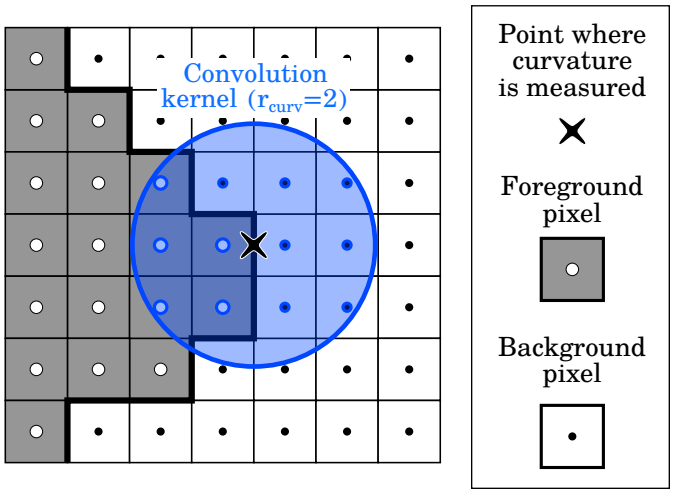

Figure 2.8 | Principle of integral invariant based curvature measurement from a digital shape. The example is given in 2D for clarity, but the principle remains the same for volumes. Here, the intersection area between the convolution kernel and the object is measured by counting the number of pixels whose center falls into the kernel of radius r_{curv}.

For example, κ_{mean} is directly related to the volume of the intersection between the convolution kernel and the object. Hence, an estimation of κ_{mean} at a given boundary point can be computed using Eq.2.6 [COE 14].

$$\kappa_{mean}\left(r_{curv}\right) = \frac{16}{3 \cdot r_{curv}} \cdot \left(\frac{1}{2} - \frac{V_{inter}\left(r_{curv}\right)}{\frac{4}{3} \cdot \pi \cdot r_{curv}^3}\right) \tag{2.6}$$

where r_{curv} is the radius of the spherical convolution kernel and $V_{inter}(r_{curv})$ is the portion of the convolution kernel's volume that resides inside the surface's boundary. By computing the covariance matrix of the intersection instead of its volume, it is possible to design estimators for the complete curvature tensor and thus estimate likewise principal curvatures and directions [LAC 17].

Since **computations are made on volumes**, this offers the opportunity to perform computations using software such as ImageJ. Using Eq.2.6, κ_{mean} can for instance be computed using a linear convolution. Since an optimized implementation of this method is already available in the open-source C++ library DGtal, it has been used in the present work [DGt 22].

Cette thèse est accessible à l'adresse : https://theses.insa-lyon.fr/publication/2024ISAL0014/these.pdf
© [F. Steinhilber], [2024], INSA Lyon, tous droits réservés

The only parameter needed to perform the calculation is the radius of **the convolution kernel r_{curv}, which is the scale at which the curvature is computed**. Although this parameter is of great importance and has a quite intuitive meaning, it can be hard to properly set in practice. A first constraint that limits the possible values for r_{curv} is the resolution of the XCT scan, since a minimum of a few voxels are necessary to limit noise in the measured curvature. If one aims to minimize the noise while keeping the curvature measurement at a fine scale, it was found useful to apply a denoising filter after curvature computation. For this purpose, we used the same Gaussian filter that was used for the S-filter in Section 2.2.2.

The choice of the convolution radius can also be driven by physical considerations and depends on the scale of the surface features of interest. This is the case in the example shown in Section 2.2.2, where curvature at a large scale can be used to detect biased roughness measurements near sharp geometrical features. Section 2.4 also discusses the relevance of curvature measured at different scales to predict crack initiation sites in fatigue applications.

The various definitions of curvatures introduced previously are complementary because they carry different information, see e.g. Fig.2.9a-e. Depending on the objective, one definition can be more relevant than others. Mean curvature is for example a relevant parameter concerning surface tension and wetting issues [BLU 19]. Triply Periodic Minimal Surfaces (TPMS) such as gyroids, which can be manufactured using AM processes [YUA 19, TIL 23, POL 22, KHR 21], are also characterized by a zero mean curvature. Such structures were for example found to achieve interesting energy absorption properties [ZHA 18]. Gaussian curvature provides complementary information. For instance, a surface characterized by a zero Gaussian curvature is a developable surface (e.g. a cylinder). In the present work, curvature is computed to characterize surface notches and distinguish them from other surface features. The maximum and Gaussian curvatures do not seem to be suited for this purpose, as they will have the same value (zero) both on a perfectly flat surface without any notch and at the root of a linear notch in a plane.

The choice between the other curvatures being less straightforward, Fig.2.9a-e are helpful to guide our final choice. Fig.2.9b displays an artificial object showing ideal notches with different geometries. Each of those notches represents a configuration that can be found locally on a real surface, see Fig.2.9a. Notches A are cups, i.e. areas where $\kappa_{min} < 0$ and $\kappa_{max} < 0$. Notch B exhibits a saddle-like geometry, with principal curvatures of opposite signs. Notches C are linear ones in a plane, i.e. $\kappa_{min} < 0$ and $\kappa_{max} = 0$. Two orientations are shown to demonstrate that it is possible to discriminate different notches based on their orientation.

Three curvatures are computed on this artificial object, namely κ_{min}, κ_{mean} and κ_{σ}. $\kappa_{\sigma} = \kappa\left(\vec{d_{\sigma}}\right)$ is the directional curvature along the direction $\vec{d_{\sigma}}$ (vertical in this case). The comparison of the three curvatures in Fig.2.9c-e makes it possible to identify which one highlights best the different notches.

The first one is **the minimum curvature κ_{min}, which successfully captures all notches**. Furthermore, all have the same κ_{min} value. The second curvature is κ_{mean}. Cups (type A) have the lowest κ_{mean} value whereas linear notches (C) show intermediate values. This difference is not necessarily desirable, since cups are not expected to reduce the mechanical properties more than linear notches. Even worse, κ_{mean} tends to 0 for the saddle-like notch (B). Although this notch was chosen as an example for the sake of clarity and seems far from a real case, there are many regions of the surface where $\kappa_{min} < 0$ and $\kappa_{max} < 0$. Thus, κ_{mean} seems less relevant than κ_{min} to detect notches in general because it is somehow biased by the κ_{max} contribution.

Cette thèse est accessible à l'adresse : https://theses.insa-lyon.fr/publication/2024ISAL0014/these.pdf
© [F. Steinhilber], [2024], INSA Lyon, tous droits réservés

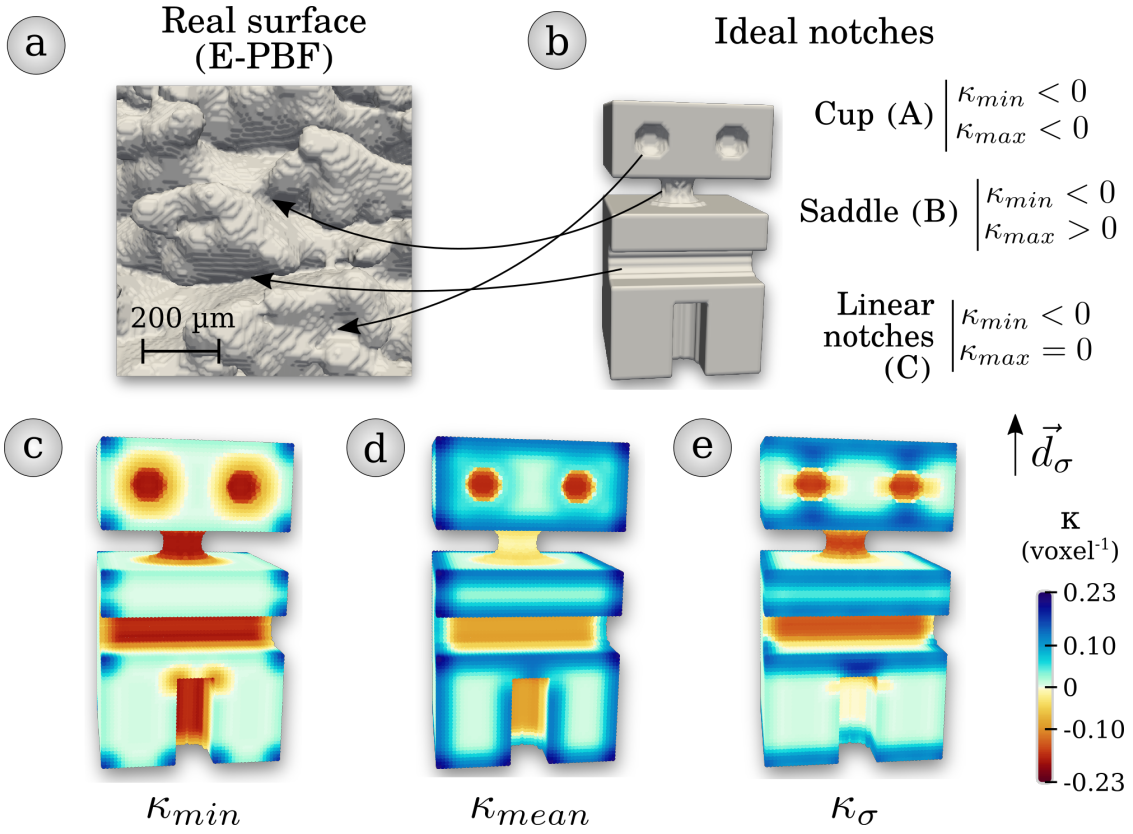

Figure 2.9 | Guide for the choice of relevant curvatures for the characterization of notches. (a) Notches visible on a surface mesh extracted from an XCT scan of an as-built surface inherited from E-PBF. (b) Artificial object used as model, with different types of notches. Each notch present in the artificial object shows a configuration that can be found on a real surface. (c) κ_{min}, (d) κ_{mean}, and (e) κ_σ measurements on the artificial object. κ_σ is here computed assuming that $\vec{d}_\sigma$ is vertical. Notch roots have by definition a radius of curvature of 5 voxels (i.e. $\kappa = 0.2$).

Finally, the third curvature is the directional one, κ_σ. As illustrated in Fig.2.9e, all notches are well identified except the one parallel to $\vec{d}_\sigma$. High κ_σ values are also more concentrated at notches roots in comparison with κ_{min}. **κ_σ can thus be considered the most appropriate choice when one aims at characterizing surface features with a specific orientation with respect to a loading direction.**

Based on these considerations, both κ_{min} and κ_σ were thus computed on the same cylindrical sample used in Section 2.2.2, see Fig.2.10a-b. Since the sample is a fatigue specimen meant to be loaded along its axis, κ_σ was computed along this direction. A radius of 30 µm (= 6 voxel size) was chosen here for the convolution kernel. An additional filter was used similarly to what has been done for roughness, using λ_S = 0.025 mm = 5 voxel size. These choices were made to provide a sufficiently detailed curvature measurement without being too much affected by noise. Fig.2.10a shows that κ_{min} underlines the presence of notches, which correspond to the lowest values. κ_σ greatly attenuates the vertical notches, which can be seen when comparing enlarged views in Fig.2.10a and Fig.2.10b.

Cette thèse est accessible à l'adresse : https://theses.insa-lyon.fr/publication/2024ISAL0014/these.pdf
© [F. Steinhilber], [2024], INSA Lyon, tous droits réservés

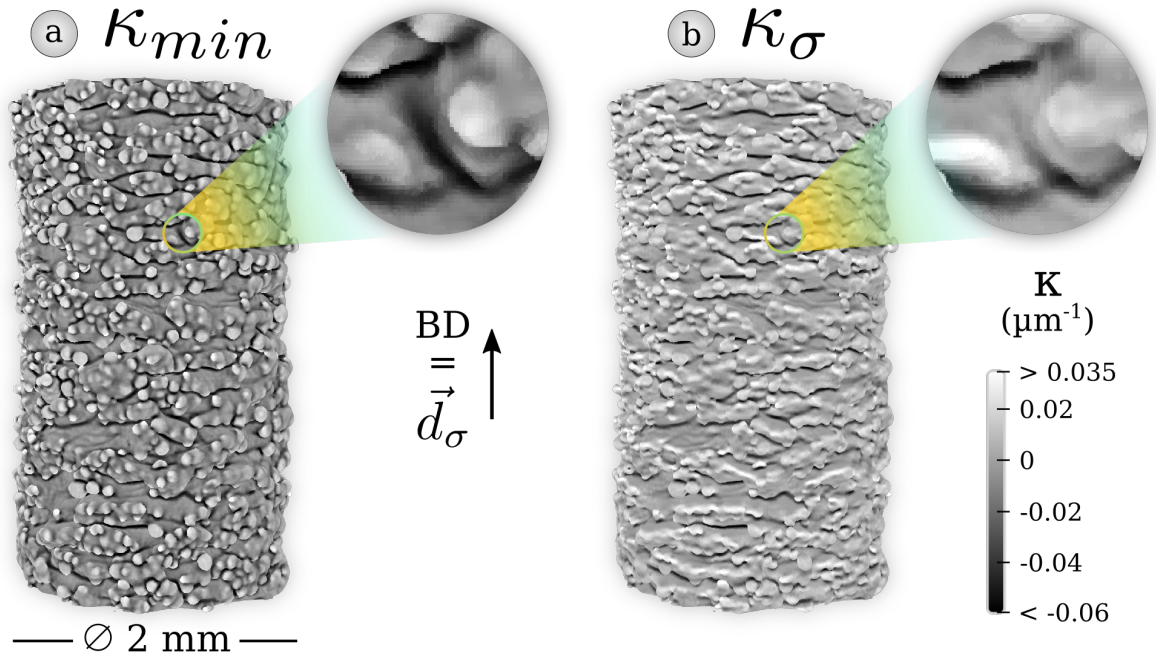

Figure 2.10 | (a) κ_{min} and (b) κ_σ measurements on an as-built cylindrical sample fabricated by E-PBF. Computations were made from an XCT scan with a voxel size of 5 µm, using $r_{curv} = 30\,\mu m = 6$ voxel size and $\lambda_S = 0.025\,mm = 5$ voxel size. The magnifying windows provide an enlarged view on a notch parallel to $\vec{d}_\sigma$. It shows that κ_σ manages to ignore it, whereas notches perpendicular to the loading direction are kept.

2.2.4 Quantification of the harmfulness of surface notches

The objective here is to combine both roughness and curvature to derive a parameter accounting for the mechanical severity of surface features. For surfaces derived from AM, the surface features that are expected to have the most significant impact on mechanical properties are notches [KAN 18, PER 19, PLE 20b]. To account for this notch effect, the simple analytical formula given in Eq.2.7 is used. It gives the stress concentration factor at the root of an elliptical notch in a semi-infinite panel, in the absence of plastic deformation [ING 13]. The two parameters required to estimate the stress concentration factor K_t are the notch depth d and the radius of curvature at its root ρ (see Fig.2.11).

$$K_t = 1 + 2\sqrt{\frac{d}{\rho}} \tag{2.7}$$

In the previous sections, d is estimated by the local height, which corresponds to roughness, while ρ was defined by the inverse of the curvature κ_σ. Some approximations still have to be made to apply Eq.2.7 using those parameters.

First, it is important to emphasize that both the roughness and curvature, as calculated in Section 2.2.2 and 2.2.3, are estimates. Therefore, their values may depend on the method

Cette thèse est accessible à l'adresse : https://theses.insa-lyon.fr/publication/2024ISAL0014/these.pdf
© [F. Steinhilber], [2024], INSA Lyon, tous droits réservés

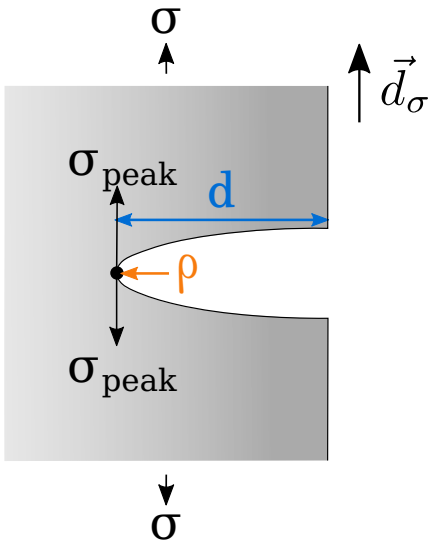

Figure 2.11 | Elliptical notch in a semi-infinite panel, submitted to a tensile stress σ in the direction $\tilde{d}_\sigma$ perpendicular to the ellipse major axis. d and ρ are respectively the depth of the notch and the radius of curvature at its root. This notch generates a stress concentration given by Eq.2.7, which means that the local stress at its root σ_{peak} is higher than the nominal stress in the section.

and parameters used for their measurement. The curvature values, for instance, are notably influenced by changes in the convolution radius r_{curv} and in the voxel size. While there are theoretical proofs, such as the one presented by [COE 14], showing that integral invariant-based calculations approach exact curvature values as voxel size reduces, the resolution required to observe this might be very high. Keeping this in mind, one should treat these estimated values as semi-quantitative ones, that can for instance be used for ranking the severity of notches.

Another approximation to consider is that Eq.2.7 is valid at the notch tip, which might be hard to detect automatically. As a result, the formula has been generalized and applied to every point on the surface where both $\kappa_\sigma < 0$ and $d < 0$. This means it is used across the entire notches, not just at their root. While Eq.2.7 might not be applicable for numerous points, the highest values will still be found at the notch roots where the depth is maximal and the curvature is minimal. Therefore, the values derived are still relevant, especially when identifying areas with the highest stress concentration. In other words, **it provides a semi-quantitative parameter that reflects the mechanical severity of surface notches**. Finally, an approximate value of K_t, called K_t^*, can be computed at the sample surface using Eq.2.8.

$$K_t^* = 1 + 2\sqrt{height \cdot \kappa_\sigma} \text{ where } height < 0,\ \kappa_\sigma < 0 \tag{2.8}$$

where K_t^* **is the estimated local stress concentration**, $height$ is the local surface height obtained from roughness measurements and κ_σ is the directional curvature along the loading direction.

Fig.2.12a-b show an example of a K_t^* map computed from the same cylindrical sample used in the previous sections. Roughness and curvature (κ_{sigma}) values used for computations are the ones presented in Section 2.2.2 and 2.2.3.

Cette thèse est accessible à l'adresse : https://theses.insa-lyon.fr/publication/2024ISAL0014/these.pdf
© [F. Steinhilber], [2024], INSA Lyon, tous droits réservés

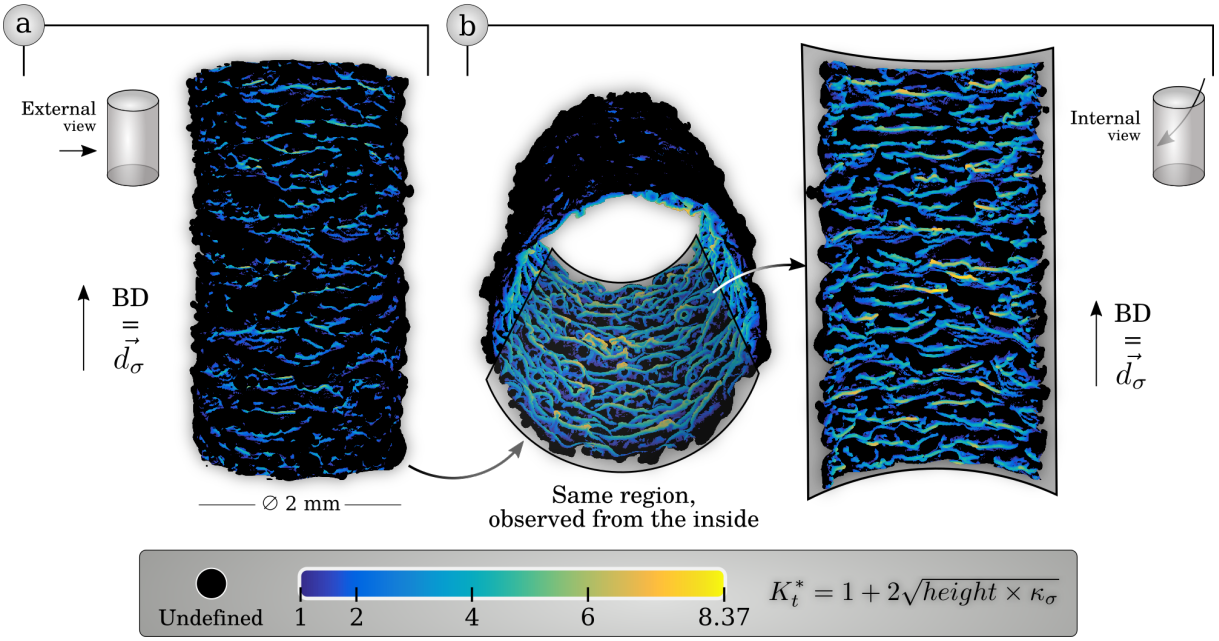

Figure 2.12 | K_t^* maps of a 2 mm diameter cylindrical sample fabricated by E-PBF. The K_t^* formula is given in Eq.2.8 and makes use of the roughness and curvature measured in the previous sections. The curvature κ_σ is computed in the direction of the cylinder axis, which also corresponds to the build direction. The points where K_t^* is not defined — because $d \geqslant 0$ or $height \geqslant 0$ — are by default colored in black. The parameters used for computations are $\lambda_c = 0.8\,\text{mm}$ | $\lambda_S = 0.015\,\text{mm}$ for roughness, and $r_{curv} = 50\,\mu\text{m}$ | $\lambda_S = 0.025\,\text{mm}$ for curvature. (a) Surface as seen from the exterior of the sample. (b) Surface as seen from the interior of the sample. The internal point of view is obtained from the surface extracted from the XCT scan.

Different views of the surface can be provided. The first one in Fig.2.12a is the usual *external view*, which corresponds to what can be seen using a conventional 2.5D surface characterization. The area shown is the same as in Fig.2.6 and Fig.2.10a-b. The two other views shown in Fig.2.12b, are *internal views* which can be generated after extracting the surface from the XCT scan. They offer a unique way to identify deep and sharp notches that would very often be hidden using conventional characterization methods, see the comparison between Fig.2.12a and Fig.2.12b. Once again, this illustrates the interest in characterizing the surface as a 3D free-form one obtained by XCT.

2.3 Application to parts with complex geometries

In order to test the ability of the methodology developed in this work to characterize complex geometries, three examples were studied: a gyroid structure and an octet-truss lattice structure manufactured by E-PBF, as well as an impeller manufactured by L-PBF. All would be impossible to characterize thoroughly using conventional 2.5D characterization tools and methodologies.

Cette thèse est accessible à l'adresse : https://theses.insa-lyon.fr/publication/2024ISAL0014/these.pdf
© [F. Steinhilber], [2024], INSA Lyon, tous droits réservés

2.3.1 Gyroid structure

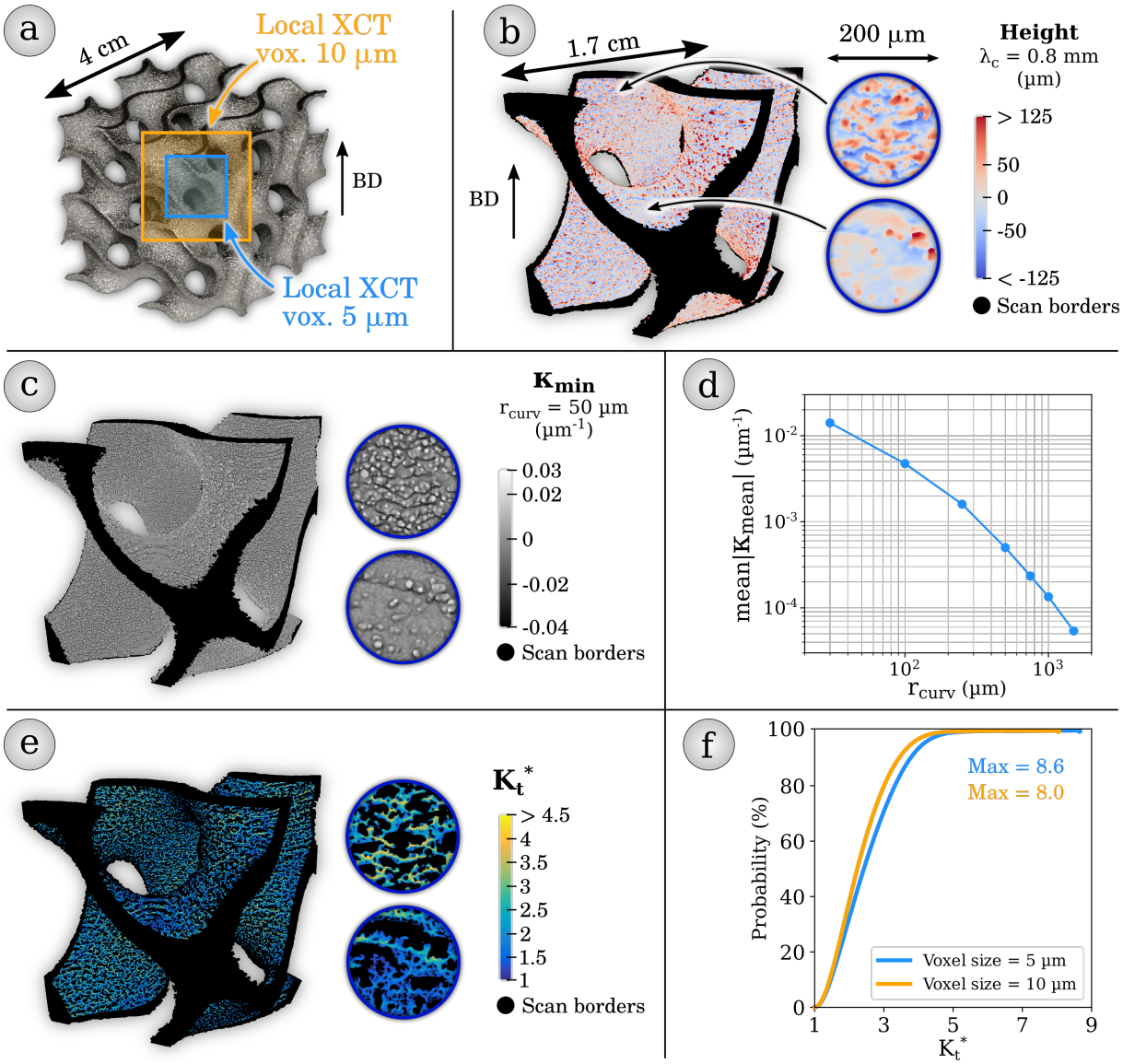

Figure 2.13 | 3D characterization of an E-PBF Ti64 gyroid. The 3D roughness maps shown were obtained from the XCT scan made with a 10 µm voxel size. (a) Picture of the gyroid sample. (b) 3D roughness map with magnifying windows showing a down-skin and an up-skin region (λ_c = 0.8 mm and λ_S = 0.05 mm). c) 3D minimum curvature map with magnifying windows showing a down-skin and an up-skin region (r_{curv} = 50 µm and λ_S = 0.05 mm). ()d) Cumulative distribution function of K_t^* for both voxel sizes. The same area was used for the comparison of both scans.

Fig.2.13a shows a picture of the gyroid. Two local tomography scans [STO 08] were acquired at the center of the structure. Large artifacts were observed on the XCT scans, which made the use of the presented threshold for bimodal histograms inappropriate. Otsu's threshold was found to be more efficient in this case. To examine the influence of voxel size on roughness, curvature,

Cette thèse est accessible à l'adresse : https://theses.insa-lyon.fr/publication/2024ISAL0014/these.pdf
© [F. Steinhilber], [2024], INSA Lyon, tous droits réservés

and K_t^* measurements, two distinct voxel sizes were employed: 5 µm and 10 µm. In either case, roughness and curvature calculations were done using $\lambda_c = 0.8\,\text{mm}$ and $r_{curv} = 50\,\mu\text{m}$.

Fig.2.13b shows the measured roughness 3D map obtained from the lowest resolution scan. Two magnifying windows are also displayed to illustrate a down-skin and an up-skin region. One can notice, quantitatively, the higher roughness in the down-skin area. The roughness parameters measured for both voxel sizes are summarized in Tab.2.2. The average roughness S_a is slightly lower for the lower-resolution scan, which is consistent since a lower resolution tends to smooth the surface.

The higher maximum height S_z and maximum valley depth S_v are respectively 52 µm and 45 µm higher for the higher resolution scan, compared with the lower resolution one. Since the difference is roughly the same for S_z and S_v, it can be concluded in the present case that **sharp and deep notches are slightly better captured using a smaller voxel size**. The improvement is less significant for surface features that have positive height values such as unmelted powder particles.

The skewness S_{sk} (= asymmetry) and kurtosis S_{ku} (= sharpness) values are also consistent with this conclusion. The increase of S_{ku} with a higher resolution means that the surface height distribution contains more extreme values. The decrease in S_{sk} may also be related to the fact that notches are better taken into account. Thus, both S_{ku} and S_{sk} suggest that using a smaller voxel size allows for a better capture of notches, in particular the deepest ones.

Voxel sizes, S_a, S_v and S_z in µm

Voxel size	S_a	S_v	S_z	S_{sk}	S_{ku}
5	37.3	420	812	0.42	3.6
10	36.6	375	760	0.55	3.1

Table 2.2 Roughness parameters measured from the gyroid XCT scans with two voxel sizes using $\lambda_c = 0.8\,\text{mm}$ and $\lambda_S = 0.05\,\text{mm}$. To ensure consistency between the values measured for the two voxel sizes, the parameters were evaluated using only the roughness values present on the surface available in both scans.

Fig.2.13c shows the 3D κ_{min} map on the same surface as Fig.2.13b. Fig.2.13d illustrates how curvature evolves with respect to the convolution radius r_{curv}. The mean curvature is used here since it is known that it should equal zero for an ideal gyroid, i.e. with no roughness. The average value across the entire surface is represented by the average of absolute values $mean|\kappa_{mean}|$, analogous to the role $S_a = mean|height|$ plays in roughness metrics. As observed in Fig.2.13d, $mean|\kappa_{mean}|$ tends to zero with increasing r_{curv} values. This is because a larger r_{curv} measures curvature at a larger scale, corresponding more to the gyroid shape (with zero mean curvature) than microscopic surface features, which have pronounced curvatures.

Finally, Fig.2.13e-f show the K_t^* measurements derived from roughness and curvature. Note that since the gyroid could be mechanically loaded in any direction, the minimum curvature is used instead of κ_σ to compute K_t^*. Fig.2.13e shows the 3D K_t^* map obtained from the scan performed with a 10 µm voxel size. Meanwhile, the cumulative distribution functions of the K_t^* parameter for both voxel sizes are given in Fig.2.13f. The obtained K_t^* values are slightly higher for the 5 µm voxel size scan. This can, once again, be attributed to the better ability at high resolution to properly capture sharp and deep notches.

Cette thèse est accessible à l'adresse : https://theses.insa-lyon.fr/publication/2024ISAL0014/these.pdf
© [F. Steinhilber], [2024], INSA Lyon, tous droits réservés

However, for both roughness and K_t^* measurements, the benefits from decreasing the voxel size by a factor of 2 appear rather limited. The values obtained from the two voxel sizes turn out to be in good agreement. Considering that a voxel size reduction by a factor of 2 results in an eightfold increase in volume size and limits the analysis of larger objects, **the benefits might not justify the trade-offs in this case**.

2.3.2 Octet-truss lattice structure

While the gyroid shows the ability to characterize a complex 3D structure, it is a favorable example regarding the roughness measurement because it does not have sharp features like corners where roughness measurements will tend to be biased. To account for this effect, the second example chosen is an octet-truss lattice structure which, contrary to the gyroid case presents sharp features. Fig.2.14a shows the κ_{min} 3D map of the octet-truss. Here again, one has a good perception of the volume and surface topography details when the curvature is used for the 3D rendering.

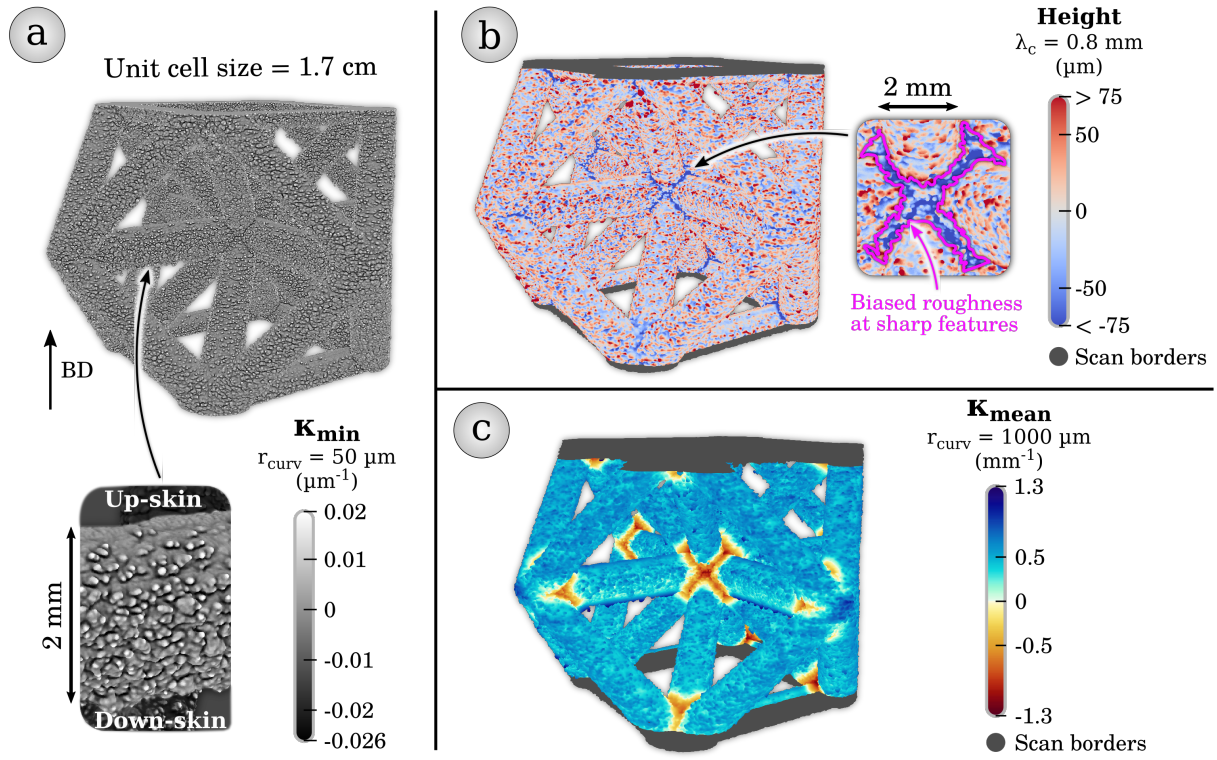

Figure 2.14 | 3D characterization of an E-PBF Ti64 octet-truss lattice structure. (a) 3D minimum curvature map ($r_{curv} = 50\,\mu m$ and $\lambda_S = 0.05\,mm$). (b) 3D roughness map ($\lambda_c = 0.8\,mm$ and $\lambda_S = 0.05\,mm$) with magnifying windows showing the region near the lattice node where roughness measurements are biased. (c) 3D mean curvature map computed at large scale ($r_{curv} = 1000\,\mu m$ and $\lambda_S = 0.05\,mm$). Nodes, where roughness measurements are biased, can be identified thanks to their low mean curvature. The region highlighted in purple in b corresponds to the one with a mean curvature lower than $-0.4\,mm^{-1}$.

Cette thèse est accessible à l'adresse : https://theses.insa-lyon.fr/publication/2024ISAL0014/these.pdf
© [F. Steinhilber], [2024], INSA Lyon, tous droits réservés

Fig.2.14b shows the 3D roughness map using a cut-off wavelength $\lambda_c = 0.8\,\text{mm}$. It can be seen that **roughness is successfully measured everywhere on the octet-truss lattice, except at nodes** where points' height is significantly lower than it should be (see the regions delineated in purple). This shows the limit of the Gaussian filter to derive the reference surface and roughness measurements near sharp features.

It is possible to get around this issue by discarding the roughness values in those regions. This can be done manually or with the help of a mean curvature computation. In the case of the octet-truss lattice structure, the mean curvature was measured using the integral invariant approach described in Section 2.2.3 and a large convolution radius of 1 mm, see Fig.2.14c. It can be seen that nodes are characterized by a very low mean curvature at this scale. For example, the regions delimited in purple in Fig.2.14b were obtained by thresholding the mean curvature using a manually chosen value of $-0.4\,\text{mm}^{-1}$.

The limitation of this method is that it does not enable the estimation of roughness at sharp features. Those may, however, be areas of particular interest. For example, it is the case if the aim is to quantify the impact of surface roughness on mechanical properties. Indeed, sharp features will have a stress concentration effect that will add to that due to the presence of surface notches. Even though this problem is complex and has no ideal solution, **more advanced smoothing methods such as anisotropic diffusion of normals [TAS 02] may be relevant in such cases** as a replacement for the conventional Gaussian filter. They are indeed used to smooth surfaces while keeping sharp features of the objects form. This could lead to less biased roughness values at sharp features.

Concerning the K_t^* values obtained for complex structures, it is worth noting that the computed values estimate only the stress concentration generated by the surface topography at a micro-scale. For a more complete characterization, one may want to add the contribution of the macroscopic geometry. The latter may be computed using Finite Element Modeling (FEM) on the ideal part geometry. The same calculations could also be used to estimate locally the direction of maximum principal stress. These directions could then be used to compute the curvature instead of using a single direction for the whole part.

2.3.3 Impeller

Finally, the methodology has been applied to an impeller manufactured by L-PBF to show a *real-case* example. To keep a reasonably low voxel size (18.5 µm), only about one-half of the impeller has been scanned. Fig.2.15a-b and Fig.2.16a-b show the 3D characterization of the component from two points of view. Roughness was computed using $\lambda_c = 0.25\,\text{mm}$ and $\lambda_S = 0.09\,\text{mm}$. The relatively low λ_c value allows for minimizing the occurrence of biased roughness values at sharp features such as corners. The curvature is measured using $r_{curv} = 100\,\mu\text{m}$, this value being larger than in the previous cases because of the larger voxel size.

Fig.2.15a-b show well the complex internal structure of the component. Magnifying windows make it possible to see that even with a 18.5 µm voxel size, the as-built surface roughness can still be distinguished.

Fig.2.16a-b show the outside of the impeller. First, it is worth mentioning that although most of the surface seems to appear in red in Fig.2.16a, this is only a matter of point of view. Indeed, the small square window showing an internal view shows that valleys (in blue) are for the most part hidden in the external view.

Cette thèse est accessible à l'adresse : https://theses.insa-lyon.fr/publication/2024ISAL0014/these.pdf
© [F. Steinhilber], [2024], INSA Lyon, tous droits réservés

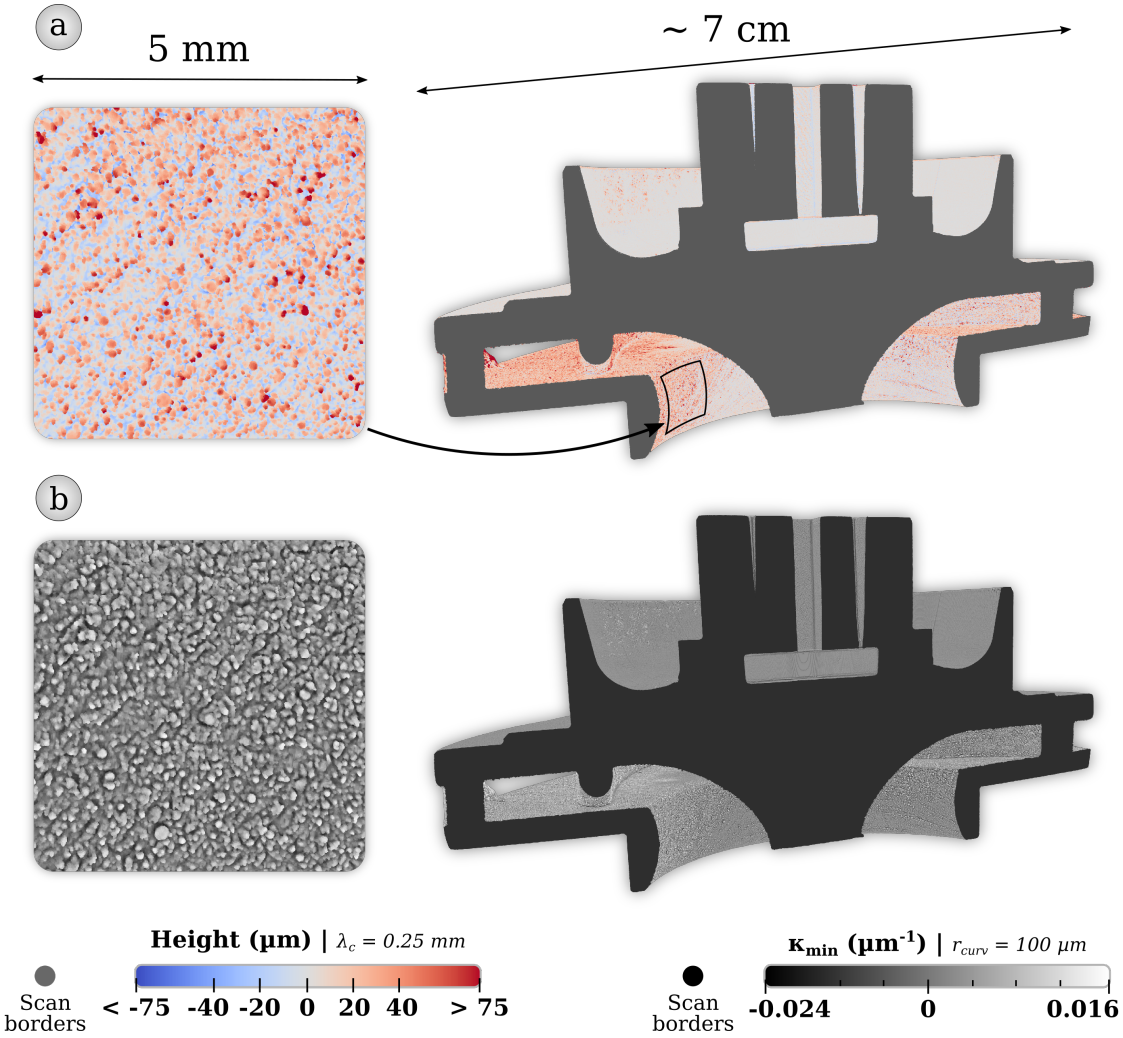

Figure 2.15 | 3D characterization of a half Ti64 impeller manufactured by L-PBF (view of the section plan). The XCT scan was obtained at the BM18 beamline at ESRF synchrotron with a voxel size of 18.5 µm. (a) 3D roughness map (λ_c = 0.25 mm and λ_S = 0.09 mm). (b) 3D minimum curvature map (r_{curv} = 100 µm, without subsequent denoising filter).

The magnifying windows show some specific features such as regularly spaced marks, characteristic of surfaces that were machined after printing. A piece of scrap is also visible on the left part of the window and may have been generated during the machining step. Because this scrap is very thin, it leads to very high roughness values (~450 µm). This shows the difficulty that can arise when characterizing large real-case components: **some unexpected features may always lead to abnormal values**, requiring a cleaning step to be conducted after calculations.

Cette thèse est accessible à l'adresse : https://theses.insa-lyon.fr/publication/2024ISAL0014/these.pdf
© [F. Steinhilber], [2024], INSA Lyon, tous droits réservés

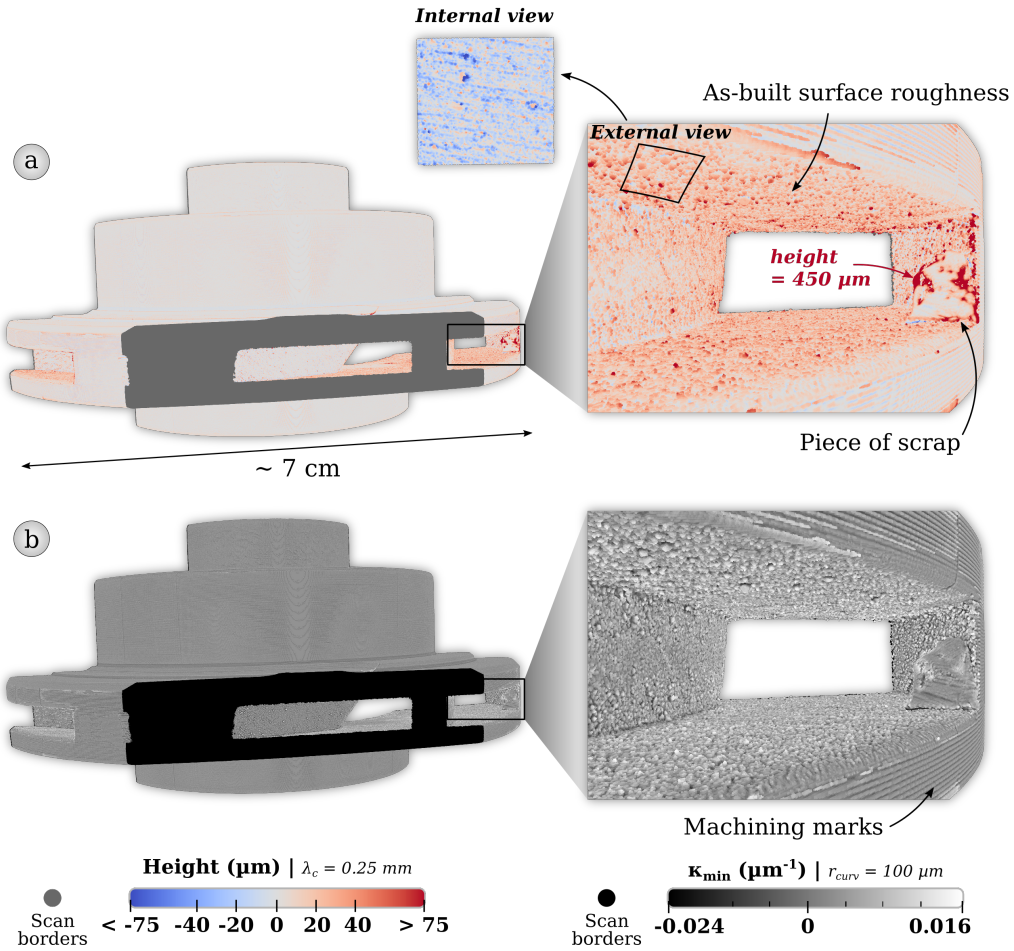

Figure 2.16 | 3D characterization of a half Ti64 impeller manufactured by L-PBF (view from the outside). The XCT scan was obtained at the BM18 beamline at ESRF synchrotron with a voxel size of 18.5 µm. (a) 3D roughness map (λ_c = 0.25 mm and λ_S = 0.09 mm). (b) 3D minimum curvature map (r_{curv} = 100 µm, without subsequent denoising filter).

2.4 Application to the prediction of crack initiation sites in fatigue

The methodology we developed was assessed for its ability to predict crack initiation sites during fatigue testing. Several studies attempted such predictions [PER 20, AND 19a, PLE 20b, TAM 17]. In many cases, the Murakami parameter $\sqrt{area}$ is employed to quantify the defects' harmfulness. However, its applicability to complex surfaces, like those from AM processes, is limited. Instead, characterizations based on local roughness and curvature measurements may offer a more versatile approach for these surfaces.

The method proposed, initially designed for complex surfaces, was first tested on a simpler scenario to predict crack initiation sites. Specifically, we looked at cases where defects leading to failure were easily delineated, allowing for $\sqrt{area}$ measurements. **This facilitated a compari-**

Cette thèse est accessible à l'adresse : https://theses.insa-lyon.fr/publication/2024ISAL0014/these.pdf
© [F. Steinhilber], [2024], INSA Lyon, tous droits réservés

son between our proposed method and the conventional $\sqrt{area}$ parameter, evaluating which approach yielded better, comparable, or less conclusive results.

As a reference, we used the results from [PER 20] who employed the $\sqrt{area}$ parameter, and applied our method using the same XCT data to measure roughness, curvature, and K_t^*.

The method from [PER 20] is summarized below. For more details, the reader is redirected to the original publication. The samples used are 2 mm diameter E-PBF cylindrical fatigue specimens which were chemically etched. Only a few surface defects remain after etching, which generally enables their unambiguous delineation. Still, the $\sqrt{area}$ measurement had to be done manually for each defect, which is a time-consuming process. Therefore, for each specimen, the $\sqrt{area}$ measurement was done only on a pre-defined set of defects whose depth was below a certain threshold. These critical defects were chosen based on depth estimates from 2.5D roughness measurements using XCT scans. Note that a 2.5D approach is not necessarily a strong limitation in such a case since the surfaces obtained after etching show much less re-entrant features than more complex as-built surfaces.

After the etched sample was characterized by XCT, they were tested in fatigue (R=0.1). The fracture surfaces were observed using SEM to identify the initiation site on each specimen, see Fig.2.18a. An XCT scan of the fracture surface was also acquired. It was possible to identify the same initiation site that was found based on SEM observations, see Fig.2.18b. Finally, by comparing the XCT scans before and after fatigue testing, the killer defect that led to failure was identified and compared to all others.

In the present study, roughness, curvature, and K_t^* measurements were computed instead of the $\sqrt{area}$ parameter. Samples' surfaces were segmented using the triangle threshold for bimodal histograms presented in Section 2.2.1. Roughness and curvature were studied individually (even if K_t^* is theoretically more relevant) to evaluate their ability to capture the most critical defects. To study the influence of the cut-off wavelength λ_c and the convolution radius for curvature measurements r_{curv} on the quality of the prediction, a parametric study was conducted using $\lambda_c \in \{0.25, 0.8, 2.5, 8\}$ mm and $r_{curv} \in \{30, 50, 75, 100, 125, 150, 200\}$ µm. Both roughness and curvature values were subsequently filtered using a cut-off $\lambda = 0.025$ mm. For the sake of clarity, only the most relevant results are discussed.

Several *scores* can be used to gauge the efficacy of a given metric (like $\sqrt{area}$ or K_t^*) in predicting crack initiation sites. Two complementary approaches are used in this work.

The first method consisted of **ranking defects based on their predicted harmfulness**. Thus, if the actual killer defect was given a rank of 1, it means that it was successfully identified. On the contrary, a rank of 10 means that 9 defects were considered to be more harmful than the actual killer defect. To determine this rank in our case, the surface voxels belonging to the killer defect were first identified manually. Afterwards, the most critical value (in terms of height, curvature or K_t^*) of the killer defect was computed. For height and curvature, it corresponds to the lowest one, whereas for K_t^* it corresponds to the highest one. Then, the surface was thresholded using this value, so that only surface voxels considered to be more critical than the killer defect were kept. The number of remaining voxel aggregates was then counted to determine the ***rank*** of the killer defect (e.g. one remaining aggregate corresponds to a rank of 2). This clustering step can be done using algorithms such as labeling − available in ImageJ − or DBSCAN [EST 96]. Here, the DBSCAN algorithm was used with a neighbor distance of 10 voxels (= 50 µm) and no threshold on the number of points needed to form a cluster (which means that no point is considered as noise).

Cette thèse est accessible à l'adresse : https://theses.insa-lyon.fr/publication/2024ISAL0014/these.pdf
© [F. Steinhilber], [2024], INSA Lyon, tous droits réservés

Our secondary approach for evaluating crack initiation site predictions involved **comparing the metric value of the killer defect against its most severe counterpart on the entire surface**. Specifically, we calculated the ratio between these values, which will be referred hereafter as the ***percentage*** score. This complements the ranking approach. For instance, one can consider a killer defect ranked at 20 using the K_t^* parameter. While this rank might suggest K_t^* is not ideally suited for pinpointing the crack initiation site, the K_t^* value at the killer defect might still be 4.5, with the peak value across all defects being 5. In this scenario, the killer defect's severity is 90% of the maximum, implying that other factors like microstructure might account for the 10% gap. Consequently, the prediction may not be as off as the rank suggests. In this case, it could mean that the parameter gave a good quantification of the impact of surface topography on crack initiation, but that many defects actually have similar harmfulness. In such a case, other factors than surface topography such as microstructure should probably be taken into account and could explain why a certain defect caused crack initiation rather than another.

Still, **this percentage score should always be interpreted with caution**. The first reason is that several defects may seem to have comparable harmfulness because of an insufficient resolution of XCT scans. Indeed, with an insufficient resolution, the sharpest notches' roots will tend to be smoothed. As a consequence, curvature measurements will tend to saturate to a certain threshold, and notches depth may also be sometimes underestimated. As a consequence, all the most severe notches may lead to similar roughness, curvature and K_t^* values, although this does not reflect the reality. This effect of XCT scan resolution was discussed to some extent in Section 2.3.1. A second reason is that $\sqrt{area}$, curvature, roughness and K_t^* estimate different physical quantities. Therefore, direct percentage comparisons between these metrics can be misleading. An example of this is that it may seem just as relevant to consider the stress intensity factor associated with the $\sqrt{area}$ parameter rather than this parameter itself, using Eq.2.9. This amounts to assimilating the defect with a crack of the same $\sqrt{area}$ [MUR 02, p.16-21]. Due to the square root presence in Eq.2.9, the percentages are substantially altered, despite evaluating the same defects. As such, when analyzing percentage values, especially across different physical properties, it is paramount to proceed with caution and compare them alongside ranks.

$$K_{Imax} \approx 0.65 \cdot \sigma \cdot \sqrt{\pi\sqrt{area}} \tag{2.9}$$

where K_{Imax} is the maximum stress intensity factor along the front of the crack that would emanate from the surface defect considered and σ is the uniform tensile load applied, in our case, along the vertical $\vec{d_\sigma}$ direction).

Tab.2.3 and Tab.2.4 showcase respectively ranks and percentages scores from ten samples, corresponding to samples 1-10 in [PER 20]. Note that in the second column giving the rank obtained from the $\sqrt{area}$ parameter, the second number corresponds to the number of defects that were pre-sectioned by [PER 20] for the manual measurement. Colors give information about the quality of the prediction: a green cell indicates a good prediction and the color tends to red as the quality of the prediction decreases.

From what has been said up to now, the most natural parameter in our study would be K_t^* ($\lambda_c = 0.8\,\text{mm} \mid r_{curv} = 30\,\mu\text{m}$). The choice of λ_c is dictated by the estimated size of the relevant surface features (see Section 2.2.2) and r_{curv} is chosen as small as enabled by the scan resolution. Although for most samples the killer defect has a rank inferior to 10, none is

Cette thèse est accessible à l'adresse : https://theses.insa-lyon.fr/publication/2024ISAL0014/these.pdf
© [F. Steinhilber], [2024], INSA Lyon, tous droits réservés

Ranks

Sample	$\sqrt{area}$ [PER 20]	κ_σ $r_{curv} = 30\,\mu m$	height $\lambda_c = 0.8\,mm$	K_t^* $\lambda_c = 0.8\,mm$ $r_{curv} = 30\,\mu m$	κ_σ $r_{curv} = 100\,\mu m$	K_t^* $\lambda_c = 0.8\,mm$ $r_{curv} = 100\,\mu m$	K_t^* $\lambda_c = 8\,mm$ $r_{curv} = 100\,\mu m$
1	4/10	83	55	44	28	32	1
2	2/7	3	2	3	3	3	2
3	5/18	2	24	20	2	15	19
4	9/34	46	6	7	15	4	1
5	11/19	2	12	8	2	11	17
6	15/23	11	10	4	3	7	16
7	2/15	50	5	9	4	6	3
8	3/16	13	4	9	1	4	15
9	1/4	1	2	2	1	1	2
10	5/10	36	5	6	35	7	7
Median	4/16	12	5	7	3	6	5

Table 2.3 | Killer defect ranks for $\sqrt{area}$, local height, κ_σ, and K_t^* parameters measured at different scales. Ranks are computed for samples 1 to 10 from the study of [PER 20]. The median ranks over all samples are also computed for each parameter. The second number in the $\sqrt{area}$ column corresponds to the number of defects that were pre-sectioned by [PER 20] for the manual $\sqrt{area}$ measurement.

Percentages

Sample	$\sqrt{area}$ [PER 20]	κ_σ $r_{curv} = 100\,\mu m$	K_t^* $\lambda_c = 0.8\,mm$ $r_{curv} = 100\,\mu m$
1	48	84	71
2	86	97	89
3	74	100	82
4	78	94	92
5	61	98	89
6	53	89	91
7	85	94	89
8	97	100	97
9	100	100	100
10	61	66	83
Median	76	96	89

Table 2.4 | Killer defect predictions percentage scores for $\sqrt{area}$, κ_σ, and K_t^* parameters. Scores are computed for samples 1 to 10 from the study of [PER 20]. The median percentages over all samples are also computed for each parameter.

Cette thèse est accessible à l'adresse : https://theses.insa-lyon.fr/publication/2024ISAL0014/these.pdf
© [F. Steinhilber], [2024], INSA Lyon, tous droits réservés

successfully identified and two are clearly mis-estimated. The obtained median rank over all samples is 7, which is not as good as the one achieved using the $\sqrt{area}$ parameter (4). Besides, K_t^* measured with these parameters is hardly more relevant than roughness alone, and both show in the end similar results. As for κ_σ ($r_{curv} = 30\,\mu m$), although it shows good results for 4 samples (rank inferior to 3), it is irrelevant for other samples.

It may not be particularly surprising that κ_σ ($r_{curv} = 30\,\mu m$) alone leads to poor predictions since it lacks information at a larger scale, which is given by roughness. However, the fact it does not bring significant improvement when combined with roughness could also be due to a **lack of resolution**. Indeed, with a 5 µm voxel size, notch roots tend to be overly discretized and therefore smoothed. It may thus be difficult to obtain relevant curvature measurements at such a small scale. Another interpretation is that **curvature at a small scale may not be the most relevant parameter** when trying to predict fatigue crack initiation. This is in a sense one of the assumptions made when using the $\sqrt{area}$ parameter since it already assimilates the defect as a crack and therefore does not consider the curvature at its root.

However, **when measured at a larger scale, it is observed that curvature provides interesting predictions**. Fig.2.17 presents the evolution of the median values and standard deviations of ranks obtained for all samples for a given r_{curv}. A good prediction capability is characterized on this graph by a small median rank and a small standard deviation as well. An optimum can be seen around 100-125 µm. For $r_{curv} = 100\,\mu m$ in particular, the obtained median rank is 3. As can be seen in Tab.2.3, only three killer defects got a rank higher than 4 — namely for samples 1, 4 and 10.

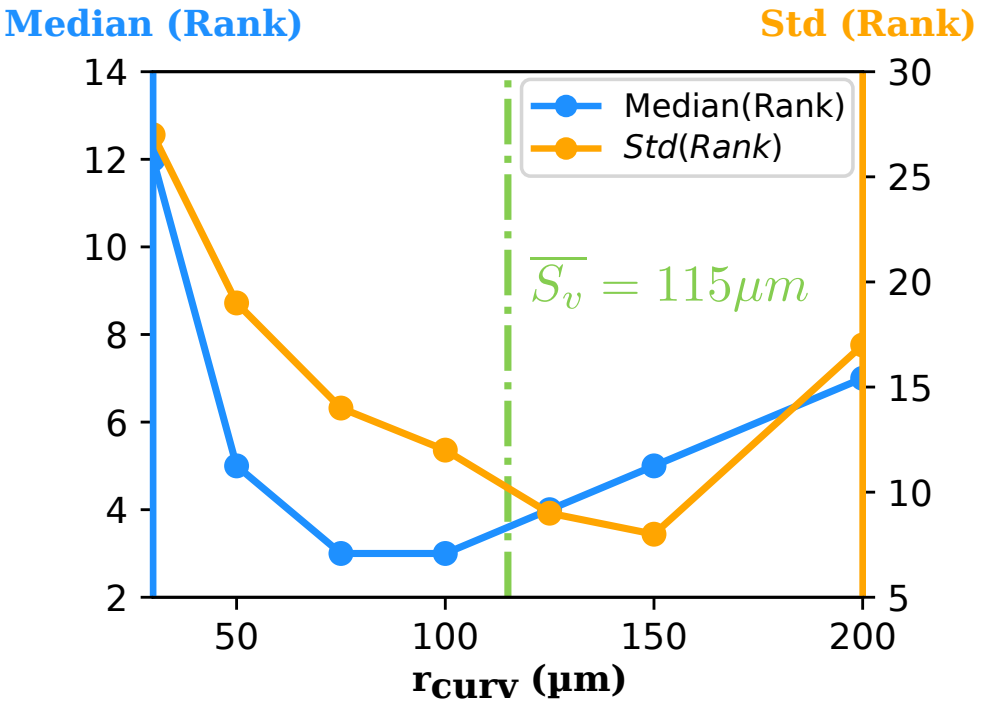

Figure 2.17 | Quality of initiation sites prediction by κ_σ, depending on the r_{curv} used for curvature computation. The quality of predictions is quantified through the median and the standard deviation of ranks obtained over all samples. The green vertical line corresponds to the mean of maximum depths S_v measured for all samples with $\lambda = 0.8\,mm$.

Cette thèse est accessible à l'adresse : https://theses.insa-lyon.fr/publication/2024ISAL0014/these.pdf
© [F. Steinhilber], [2024], INSA Lyon, tous droits réservés

In those cases, however, predictions are very far from experimental results. Fig.2.18d-f and Fig.2.18g-j show some roughness, curvature and K_t^* maps for one best-case scenario (Sample 8) and one worst-case scenario (Sample 1) respectively.

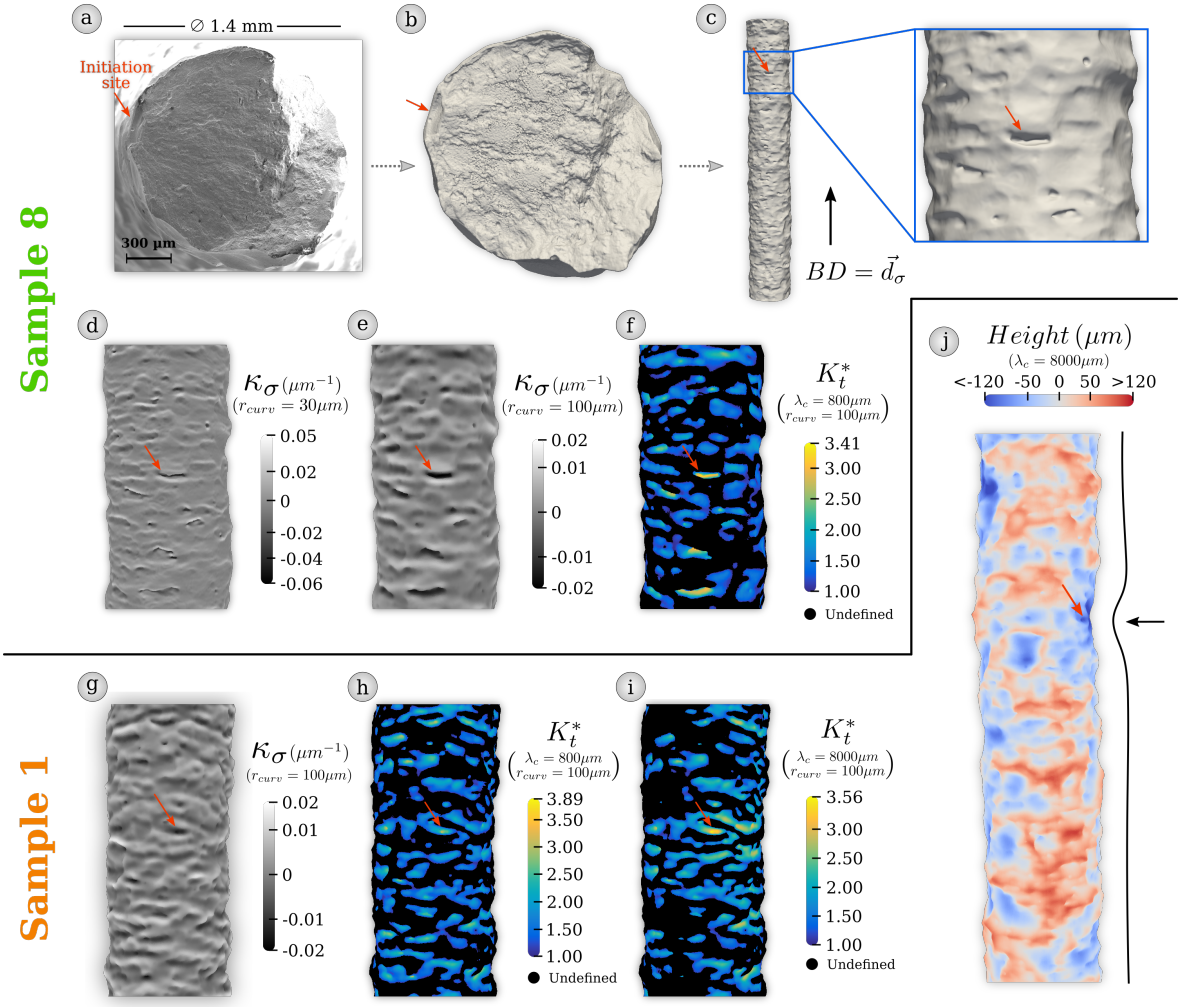

Figure 2.18 | Some illustrations of the samples used for the killer defect prediction study. Samples and XCT volumes used are the same as in [PER 20] (E-PBF Ti64 chemically etched cylinders). (a) Fracture surface of sample 8, observed by SEM-SE. (b) Fracture surface of sample 8, extracted from XCT volume. (c) Surface of sample 8 before fatigue testing, where the killer defect is highlighted with a red arrow. (d-f) Curvatures and K_t^* maps computed for sample 8. (g-j) Curvature, K_t^* and roughness maps computed for sample 1.

One can also notice that the percentage score for $r_{curv} = 100\,\mu m$ is very high for most samples, with a median percentage of 96%. In other words, it is observed that in most cases, crack initiation occurs on a surface feature whose curvature κ_σ ($r_{curv} = 100\,\mu m$) is close to the minimum (maximum in absolute value) reached on the whole surface. This highlights the relevance of κ_σ ($r_{curv} = 100\,\mu m$) parameter, but as discussed above, it could also suggest that most severe notches root tend to be smoothed, leading to similar value for many of them.

Cette thèse est accessible à l'adresse : https://theses.insa-lyon.fr/publication/2024ISAL0014/these.pdf
© [F. Steinhilber], [2024], INSA Lyon, tous droits réservés

The given results raise the question of why curvature provides much better results for $r_{curv} = 100\,\mu m$ than for $r_{curv} = 30\,\mu m$. A possible explanation is that in this case, curvature is not measured at the scale of notches roots anymore but rather at the scale of the entire defects themselves. Therefore, it can better take into account the severity of the whole defect, by taking into account its sharpness at a large scale but also its size — a contribution that is normally provided by the depth measurement in Eq.2.7. Thus Fig.2.19b shows that by using a radius r_{curv} of the order of magnitude of the depth of the deepest notch, it is possible to efficiently make the distinction between a deep notch and a shallow notch using curvature measurements. On the contrary, Fig.2.19a shows that using a small radius provides more local information and thus will not be able to make the difference between two notches of different depth but with the same curvature at their roots. On this topic, it is interesting to note that the average maximum valley depth S_v measured over all samples (using $\lambda = 0.8\,mm$) is $115\,\mu m$. As can be seen in Fig.2.17, this corresponds well to the optimal r_{curv}, which is consistent with the proposed interpretation. This also suggests that **S_v could be a first guess to set r_{curv} parameter appropriately**, although more tests on more diverse surface states would be required to confirm this hypothesis.

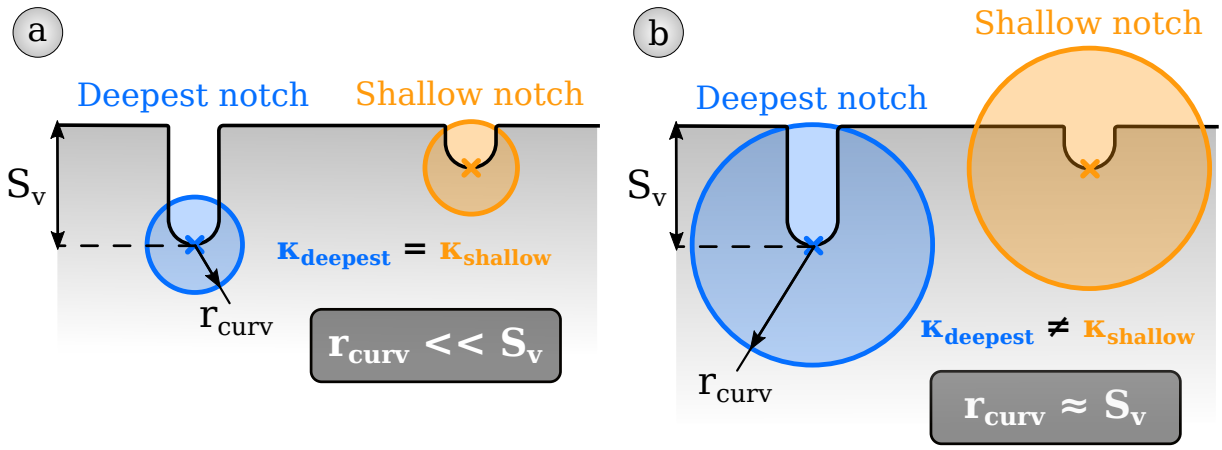

Figure 2.19 | Schematic example showing curvature measurements on two notches with identical curvatures at their root but different depth. One of the notches is the deepest notch on the whole surface (i.e. its depth equals to S_v roughness parameter) while the other is a rather shallow notch. The curvature measurement is done using (a) a small convolution radius r_{curv} taking into account notches roots only, (b) a large r_{curv} of the order of magnitude of S_v. A comparison between (a) and (b) shows that computing curvature with the largest radius enables the differentiation of both notches, thus taking into account the notch depth. On the contrary, a more local curvature measurement using a small radius will not enable to distinguish the two notches.

Since $r_{curv} = 100\,\mu m$ brings better results than $r_{curv} = 30\,\mu m$ — when curvature is considered alone, it seems interesting to see if the predictions obtained with K_t^* are also better when computing curvature at this scale. Tab.2.3 shows that it is not really the case, the results obtained being similar to what was obtained with $r_{curv} = 30\,\mu m$. It can still be noted that for two of the three "worst-case scenarios" (Samples 1, 4 and 10), the prediction is largely improved by the the addition of roughness. This may come from the fact that in this case, roughness still better takes into account the topology at a larger scale than curvature, thus providing relevant complementary information in some cases. Furthermore, it is interesting to

Cette thèse est accessible à l'adresse : https://theses.insa-lyon.fr/publication/2024ISAL0014/these.pdf
© [F. Steinhilber], [2024], INSA Lyon, tous droits réservés

note that in most cases, the percentage score reached using K_t^* ($\lambda = 0.8\,\text{mm} \mid r_{curv} = 100\,\mu\text{m}$) seems rather good, with a median value of 89%. Therefore, the incapacity of the method to accurately identify crack initiation sites may be linked to other factors (such as microstructure) or insufficient XCT scan resolution. The percentage scores for $\sqrt{area}$ are given for information, but as discussed previously, it seems difficult to draw any conclusion by comparing them with percentages obtained from K_t^* or curvature measurements.

It is interesting to note that for Sample 1, Tab.2.3 shows that predictions are particularly poor both for κ_σ ($r_{curv} = 100\,\mu\text{m}$) and K_t^* ($\lambda_c = 0.8\,\text{mm}$; $r_{curv} = 100\,\mu\text{m}$). By inspecting the surface of this sample, it can be seen that the sample geometry significantly deviates from a cylinder at the crack initiation site location, where a blunt notch can be seen. This can be seen in Fig.2.18j. The roughness measurement in the same figure, made with a large cut-off wavelength of 8 mm, reveals that computing roughness at such a large scale enables one to take into account such a large defect. Therefore, computing K_t^* ($\lambda_c = 0.8\,\text{mm}$; $r_{curv} = 100\,\mu\text{m}$) enables to successfully predict the crack initiation site.

However, in other cases such as for Sample 8, the smaller defect size makes it more relevant to look at a smaller scale. This suggests **it may be relevant to perform a multi-scale analysis** of the surface. This is naturally done when the is measured manually, which is coherent with the fact that sample 1 initiation site is the fourth most critical defect according to the manual $\sqrt{area}$ measurement. To do it in a more automated way, roughness and curvature could be computed at different scales by adjusting λ_c and r_{curv} parameters. The way those measurements may be used together is not straightforward. However such a multi-scale approach is not new and several works have already been conducted on similar topic [JIA 20a, BAR 19, GO 16, LEV 15]. Thus, it would be interesting to explore these approaches to take the proposed analysis a step further.

Cette thèse est accessible à l'adresse : https://theses.insa-lyon.fr/publication/2024ISAL0014/these.pdf
© [F. Steinhilber], [2024], INSA Lyon, tous droits réservés

Intermediate summary

This chapter presented a methodology for the 3D characterization of surface topography using XCT data, focusing on measuring both roughness and 3D curvature. While this methodology has broader applications, we emphasized its usefulness on samples produced by additive manufacturing and dedicated to mechanical applications.

Key findings can be summarized as follows:

- The proposed methodology could effectively account for hidden surface features on surfaces inherited from E-PBF. For example, the 3D method can identify notches that traditional 2.5D techniques would miss.
- The method effectively captures roughness and curvature in complex geometries such as architected structures. While the results are encouraging, certain geometric features, like sharp edges, present challenges in roughness assessments. In such instances, more sophisticated metrological tools might offer deeper insights.
- We have tailored the methodology to make it accessible, even for those unfamiliar with advanced data analysis tools and programming. For example, we deliberately used standard image analysis techniques, such as 3D Gaussian filtering, to extract roughness from the raw surface. This approach can be applied using popular software like ImageJ. With the Gaussian filter being a standard operation for the analysis of 2D and 2.5D roughness, guidelines from ISO standards can be adapted for the presented 3D workflow.
- Several tools have been introduced to leverage this 3D characterization in understanding the mechanical implications of surface notches. For instance, it was found that the standard Otsu's thresholding missed some of the sharpest notches. We proposed an alternative, the triangle threshold for bimodal histogram, which yielded better results in this case. Additionally, 3D curvature measurements enable the derivation of curvature in the direction of principal stress, κ_σ, underscoring the mechanical consequences of notches aligned perpendicular to the loading direction. Finally, we also proposed a model that integrates roughness and curvature data to compute a parameter, K_t^*, that reflects the stress concentration induced by surface notches.
- Employing roughness, curvature, and K_t^* metrics, we sought to predict crack initiation during fatigue. These predictions paralleled the findings by [PER 20], which studied the fatigue behavior of chemically etched E-PBF cylinders. Only a few defects remained after etching, which made it possible to quantify their harmfulness using the conventional $\sqrt{area}$ metric. Broadly speaking, our crack initiation site predictions were comparable to the ones found using the $\sqrt{area}$ parameter. Notably, among roughness, κ_σ, and K_t^*, κ_σ demonstrated superior predictive ability. For instance, using κ_σ ($r_{curv} = 100\,\mu m$), the actual crack initiation site was among the 3 most severe defects identified for 6 samples over 10. In a more general case, the proposed methodology offers new opportunities, being adaptable to surfaces with advanced topological complexity, a challenge for the $\sqrt{area}$ metric. Furthermore, improved results could be achieved by characterizing the surface at multiple scales, modifiable through parameters like the cut-off wavelength λ_c and the convolution radius r_{curv}, used for roughness and curvature measurements.

Cette thèse est accessible à l'adresse : https://theses.insa-lyon.fr/publication/2024ISAL0014/these.pdf
© [F. Steinhilber], [2024], INSA Lyon, tous droits réservés

Chapter 3

Materials characterization

Contents

3.1 Samples manufacturing 71
3.1.1 Processing conditions 71
3.1.2 Fatigue and tensile specimens 73
3.2 Microstructure characterization 76
3.2.1 Microstructure of the bulk material 76
3.2.2 Microstructure near the surface 78
3.3 Tensile properties 82
3.4 Defects characterization using XCT 84
3.4.1 Acquisition setup 84
3.4.2 Porosity 85
3.4.3 Surface defects 88
Intermediate summary 101

In Chapter 2, various materials were discussed through multiple case studies. However, the next chapters of this manuscript will focus on a single material, namely Ti64 manufactured by L-PBF. The upcoming sections will concentrate on some of its main characteristics, namely its manufacturing process, microstructure, tensile properties, and defects.

It is worth noting that the manufacturing conditions for the samples match those used in Quentin Gaillard's work [GAI 23a]. Gaillard's research mainly investigated microstructural and static properties after different heat treatments. To gain a comprehensive understanding of these aspects, readers are therefore encouraged to refer to Gaillard's work, which serves as a valuable resource for this chapter.

3.1 Samples manufacturing

3.1.1 Processing conditions

The samples studied hereafter were manufactured by Laser Powder Bed Fusion (L-PBF) using a FormUp 350 AddUp machine of the first generation. The production was carried out by the French company Dassault Aviation at Argonay (Savoie, France). The machine used was

Cette thèse est accessible à l'adresse : https://theses.insa-lyon.fr/publication/2024ISAL0014/these.pdf
© [F. Steinhilber], [2024], INSA Lyon, tous droits réservés

equipped with two YAG 500 W lasers, operating at a wavelength of 1070 nm. Each laser was responsible for one-half of the build plate.

The samples were made from Ti-6Al-4V Grade 5 powder produced by TEKNA through plasma atomization. The results of particle size characterization by sieving are presented in Tab.3.1. In addition, it is worth noting that 1% in mass of powder particles were found to have a size larger than 25 µm.

D_{10}	D_{50}	D_{90}
8 µm	14 µm	20 µm

Table 3.1 | Powder particle size characterization, performed by sieving.

The chemical composition of the powder can be found in Tab.3.2. It is worth highlighting that only fresh powder was employed. This decision was made to minimize variations in oxygen contamination, defect formation and mechanical properties, as these can arise from the recycling of powder [MAH 22].

Ti	Al	V	Fe	O	C	N	H
Base	6.22	3.87	0.18	0.14	0.009	0.02	0.004

Table 3.2 | Powder chemical composition (in mass %).

The powder bed was deposited using a roll. Although it enables obtaining a compact powder bed, it requires some caution for the manufacturing of thin elements, as freshly printed thin layers might be swept away by the roll. Thus, the printing of vertical specimens (presented thereafter) required the use of *"sarcophagus-like"* support structures that consolidated the powder bed and prevented specimens from bending towards the rolling direction. See Fig.3.4 and Fig.3.5 for examples of such support structures.

Within the build chamber, a controlled atmosphere was maintained, with a laminar flow of argon (Ar). The build plate did not undergo any pre-heating during the printing process.

Other processing parameters such as the laser power and scanning speed cannot be given for confidentiality reasons. However, the scanning strategy is illustrated schematically in Fig.3.1, as it is of primary importance to understand subsequent descriptions of microstructural features and defects.

Each layer underwent scanning in two stages. First, the bulk material was melted using a cross-hatching approach with a 90° angle between each layer. Subsequently, two contour scans were implemented. The first contour scan is positioned on the outermost part of the sample.

Following the manufacturing process, the build plates were subjected to **cleaning** within an ultrasonic bath containing water. This step is required to eliminate loose powder particles. The build plates (plate + samples) were not sandblasted, primarily to prevent changes in surface roughness and to avoid obscuring surface defects like valleys.

A **stress-relief heat treatment** of 2 h at 720 °C was then applied. XRD measurements done by Quentin Gaillard [GAI 23a] showed that for the material considered, this heat treatment achieves a complete relaxation of residual stresses. Here, the heat treatment was applied on the entire build plate to prevent potential deformations that might arise if samples were detached before undergoing stress relief.

Cette thèse est accessible à l'adresse : https://theses.insa-lyon.fr/publication/2024ISAL0014/these.pdf
© [F. Steinhilber], [2024], INSA Lyon, tous droits réservés

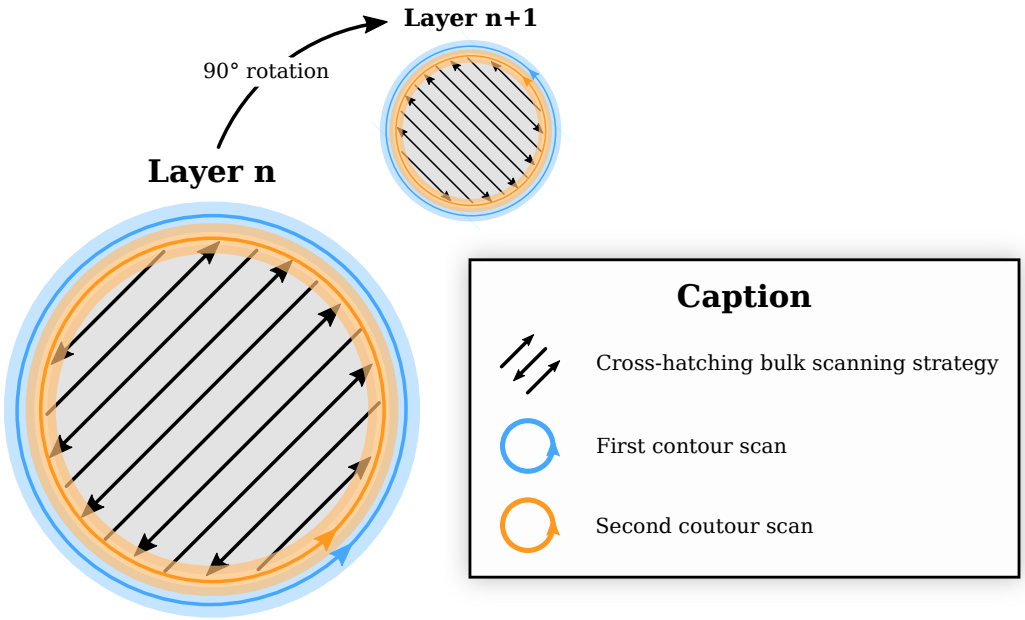

Figure 3.1 | **Scanning strategy adopted for sample manufacturing.** Bulk material is first melted using a cross-hatching strategy, followed by two contour scans. A 90° rotation is done between each layer.

Subsequently, **specimens were detached from the build plate**, and the support structures were manually removed. A final ultrasonic bath was used to **clean** the samples, removing residual powder particles trapped between the specimens and support structures. At this stage, the samples were prepared for subsequent characterization.

3.1.2 Fatigue and tensile specimens

The samples used in the present PhD work were either flat tensile or cylindrical fatigue specimens. Their geometry is given in Fig.3.2 and Fig.3.3 respectively.

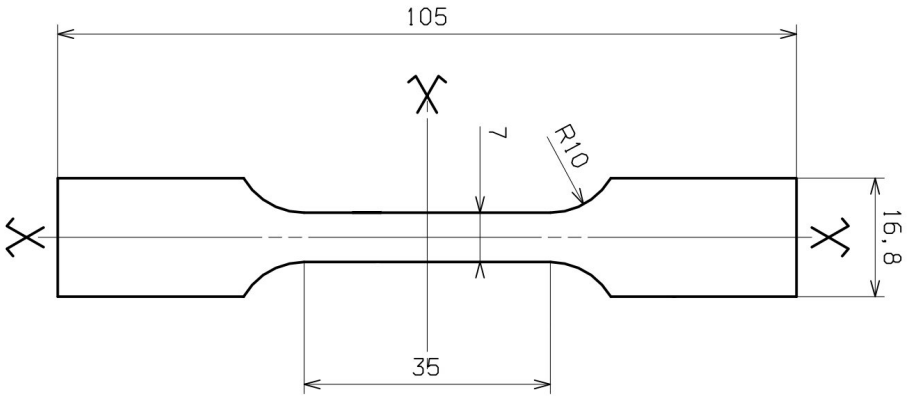

Figure 3.2 | Drawing of the flat tensile specimens. The dimensions are given in mm. The specimen width equals 3.00 ± 0.02mm.

Cette thèse est accessible à l'adresse : https://theses.insa-lyon.fr/publication/2024ISAL0014/these.pdf
© [F. Steinhilber], [2024], INSA Lyon, tous droits réservés

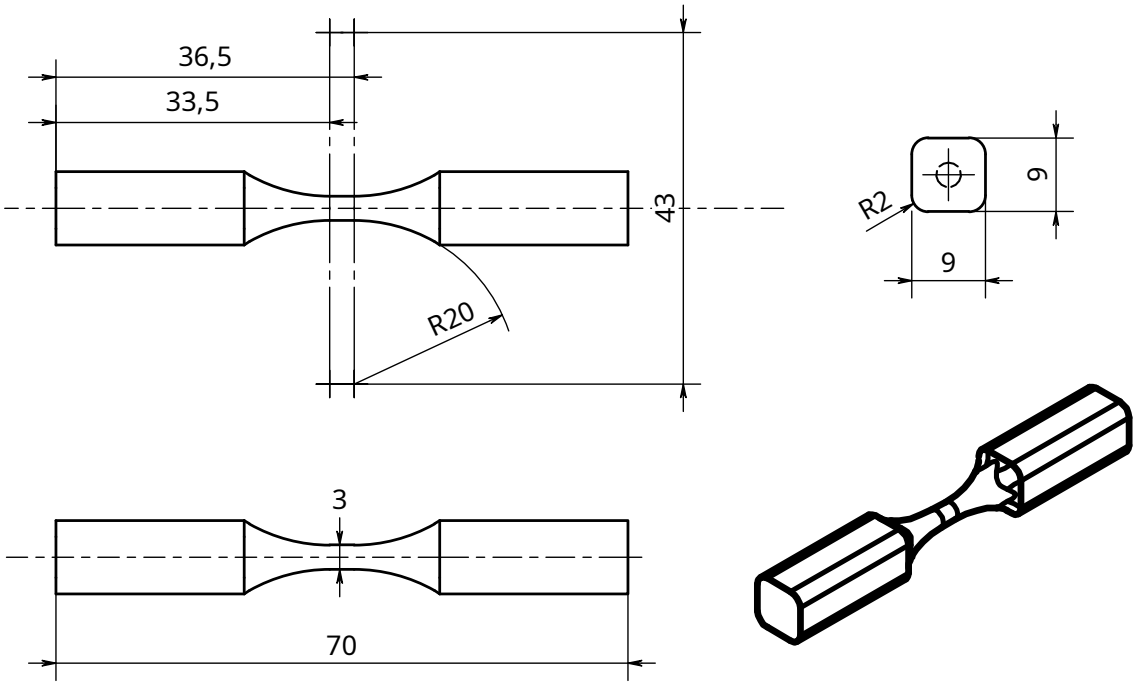

Figure 3.3 | Geometry of the cylindrical fatigue specimens. Dimensions are given in mm.

Tensile specimens were printed in three orientations: **vertical** ((along the Z-axis), at a **45°** angle with respect to the build direction, and **horizontal** (XZ). Pictures of the printed samples with their support structures can be seen in Fig.3.4. The vertical specimens employed "*sarcophagus-like*" support structures, while more standard supports were used for the 45° specimens. Although not visible in Fig.3.4, the only points of contact between the supports and specimens are located on the specimen heads. The middle portion of the support structures approaches the specimen without direct contact. Additionally, small pillars were used as supports within the gauge length of the XZ specimens. However, after being manually removed, these pillars left noticeable surface irregularities that are expected to adversely impact the mechanical properties, please refer to Section 3.3 for further details.

For the **fatigue specimens**, two build orientations were investigated: **vertical (Z) and 45°**. Images of both types of specimens are shown in Fig.3.5. Similar support structures as those used for the tensile specimens were employed. The primary distinction is that the 45° specimens are not fully supported within the gauge length. Similar to the tensile specimens, the only points of contact between these supports and the specimens are located on the specimen heads.

Cette thèse est accessible à l'adresse : https://theses.insa-lyon.fr/publication/2024ISAL0014/these.pdf
© [F. Steinhilber], [2024], INSA Lyon, tous droits réservés

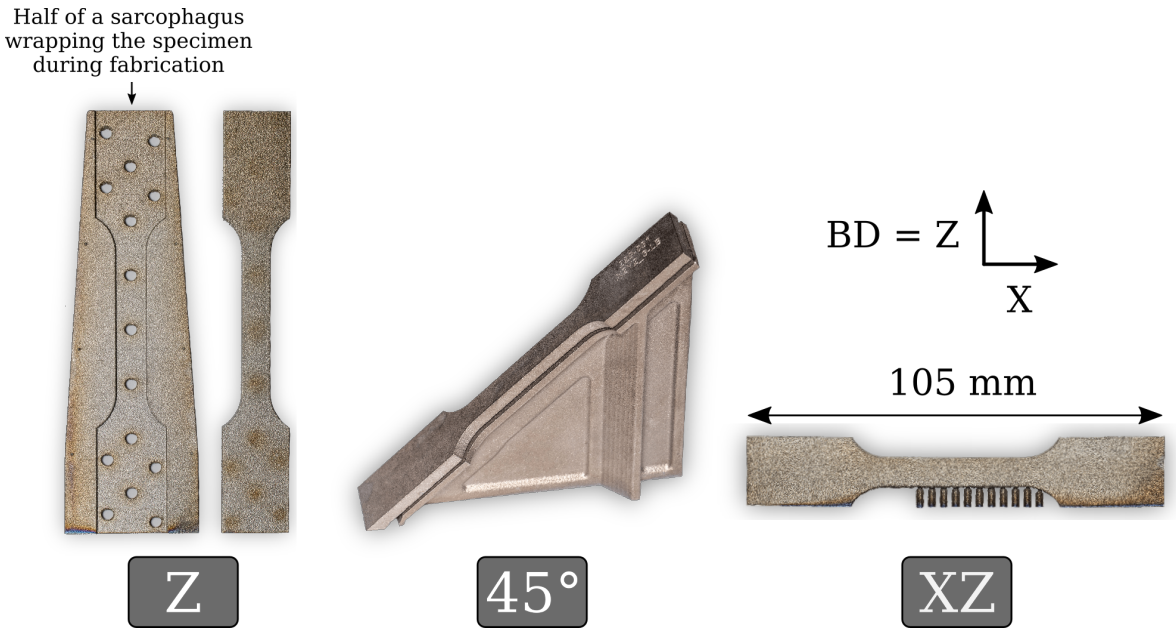

Figure 3.4 | Pictures of printed tensile specimens and their support structures. Specimens were printed in the (a) vertical (Z), (b) 45° and (c) horizontal (XZ) directions. Pictures courtesy of Quentin Gaillard.

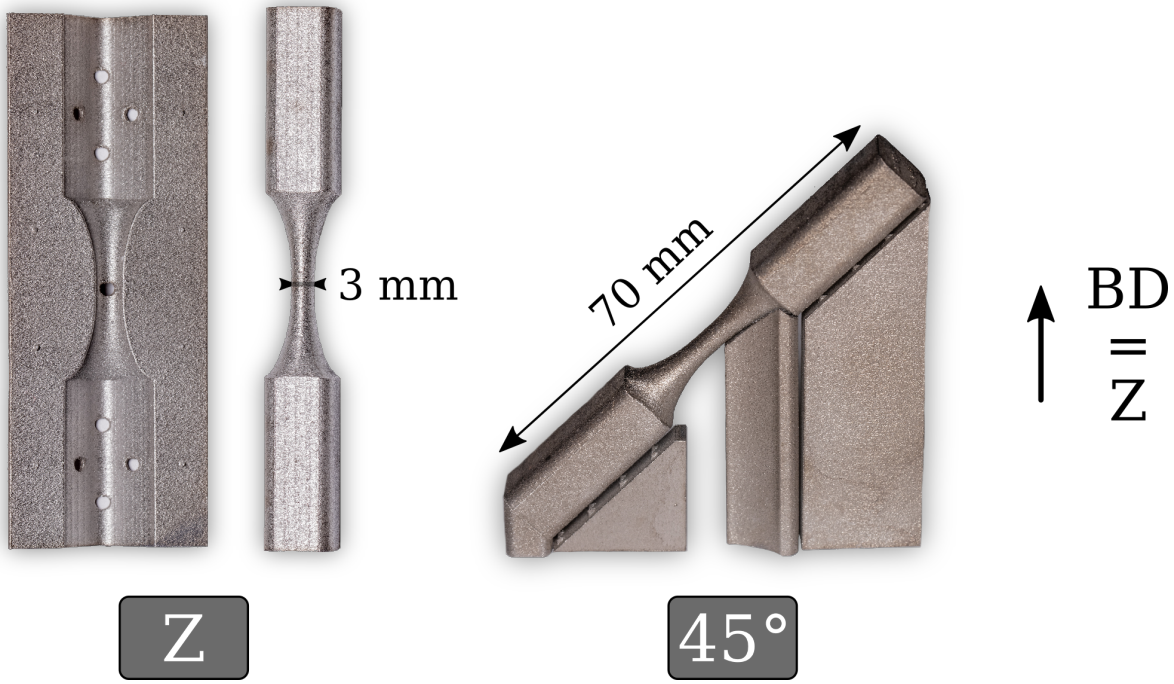

Figure 3.5 | Pictures of printed fatigue specimens and their support structures. Specimens were printed in the (a) vertical (Z) and (b) 45° directions. Pictures courtesy of Quentin Gaillard.

Cette thèse est accessible à l'adresse : https://theses.insa-lyon.fr/publication/2024ISAL0014/these.pdf
© [F. Steinhilber], [2024], INSA Lyon, tous droits réservés

3.2 Microstructure characterization

All microstructure characterizations presented in this section are directly drawn from Quentin Gaillard's work [GAI 23a, GAI 23b]. They have been summarized to extract the most relevant conclusions that contribute to the interpretation of the results in this manuscript. However, for a more comprehensive understanding of this subject, readers are advised to refer to [GAI 23a, GAI 23b], which provides a detailed and well-illustrated study. It is worth reiterating that the manufacturing conditions employed in his study align with those used in the current work. Notably, despite 15 mm × 15 mm × 15 mm cubes being used in Gaillard's study for microstructure characterization, the resulting microstructure mirrors that of the fatigue specimens employed in this study.

Microstructure analysis involved the use of EBSD (Electron Back Scattered Diffraction) maps, revealing the crystallographic orientation of grains. All these maps were generated using the build direction (Z) as the reference.

The showcased maps can be classified into two types. The first type pertains to the α phase orientation map, depicting the actual microstructure of the material following printing and the subsequent stress-relief heat treatment. The second map represents the reconstructed prior β_0 phase orientation map, illustrating the state of the β phase immediately after solidification and before the subsequent martensite transformation — i.e. during the L-PBF process. Here, it is reconstructed by using the α phase orientation map, following the procedure described in [GAI 23a].

3.2.1 Microstructure of the bulk material

Fig.3.6a-f and Fig.3.7a-f illustrate EBSD maps depicting the bulk microstructure in a vertical (Z) plane and a horizontal (XY) plane, respectively. In particular, Fig. 3.6a and Fig.3.7a display α phase orientation maps, while Fig. 3.6d and Fig.3.7d showcase prior β_0 phase orientation maps.

In Fig.3.6d, it is noticeable that immediately after solidification, **the prior β_0 phase shows a columnar structure growing along the build direction**, which is characteristic of additively manufactured materials. The XY map in Fig.3.7d exhibits a distinct *chessboard pattern*, resulting from the cross-hatching scanning strategy employed for printing and the 90° rotation between each layer.

The inverted pole figures, depicted in Fig.3.6e-f and Fig.3.7e-f, reveal that the prior β_0 phase is strongly textured. Specifically, the prior β_0 grains were oriented with the (001) plane parallel to Z, and both the (100) and (010) planes were aligned with the laser scanning directions.

Following rapid cooling, the prior β_0 phase undergoes martensite transformation. Columnar β_0 grains transform into fine α' (martensite) laths. Subsequent stress-relief (2 h at 720 °C) initiates the martensite decomposition $\alpha' \rightarrow \alpha + \beta$. [GAI 23a] estimated, using Differential Scanning Calorimetry (DSC), that this transformation can start at temperatures as low as 470 °C, well below the heat treatment temperature. The resulting microstructure consists of **a mixture of entangled α laths** along with **a minor fraction of β phase** ($2.2 \pm 0.3\%$ according to [GAI 23b]). It is actually challenging to definitively ascertain whether the laths consist exclusively of α phase or if some α' remains. However, since this matter is not central to the primary focus here, the subsequent analysis will proceed with the assumption that the martensite decomposition is completed and only the α phase is present.

Cette thèse est accessible à l'adresse : https://theses.insa-lyon.fr/publication/2024ISAL0014/these.pdf
© [F. Steinhilber], [2024], INSA Lyon, tous droits réservés

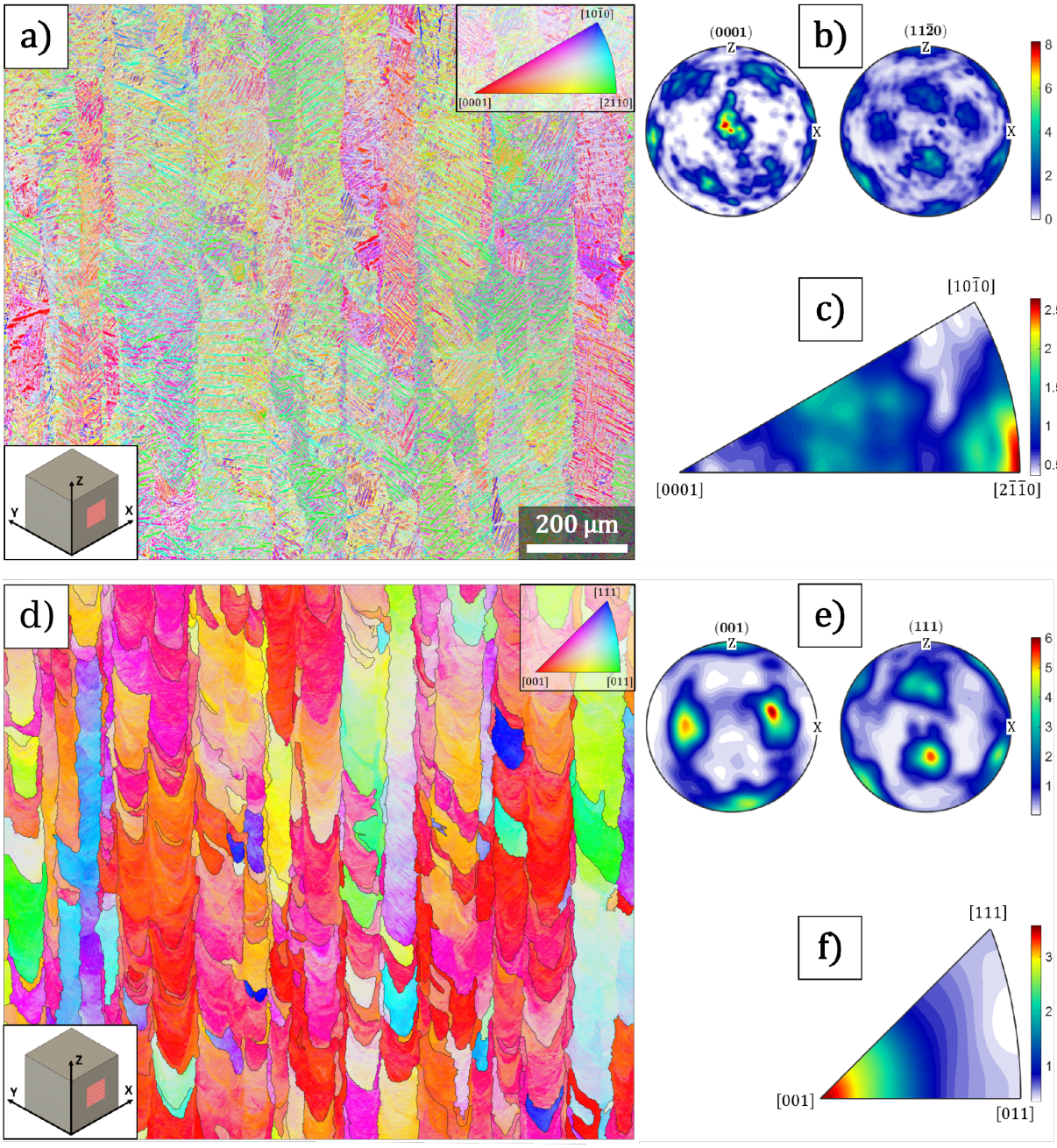

Figure 3.6 | EBSD analysis of the bulk material in a vertical plane (i.e. parallel to the build direction Z), adapted from [GAI 23a]. Crystallographic orientation maps of (a) α and (d) prior β_0 phases. Pole figures of (b) α and (e) prior β_0 phases. Inverse pole figures of (c) α and (f) prior β_0 phases. The build direction Z is taken as a reference. The maps are 1.25 mm × 1.1 mm wide and are collected with a step size of 0.6 µm.

Cette thèse est accessible à l'adresse : https://theses.insa-lyon.fr/publication/2024ISAL0014/these.pdf
© [F. Steinhilber], [2024], INSA Lyon, tous droits réservés

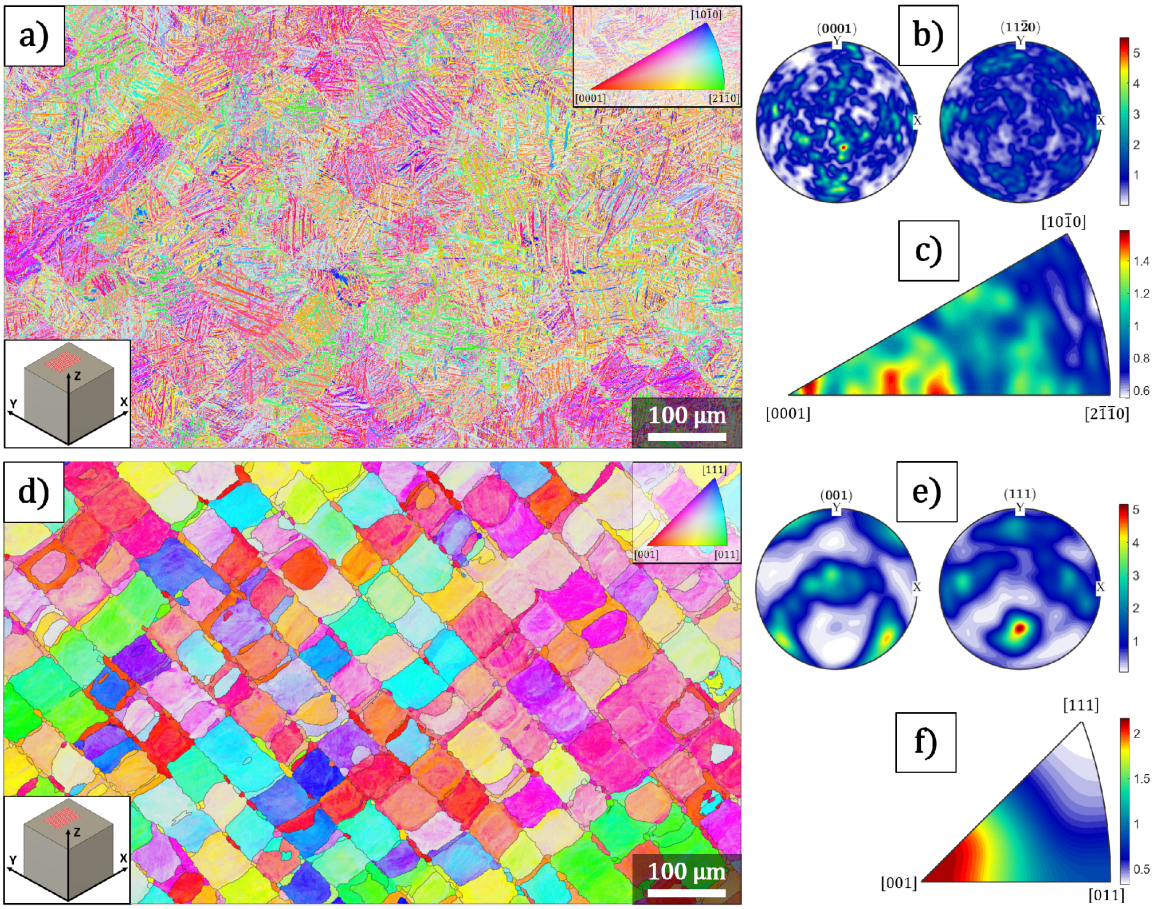

Figure 3.7 | EBSD analysis of the bulk material in a horizontal plane (i.e. perpendicular to the build direction Z), adapted from [GAI 23a]. Crystallographic orientation maps of (a) α and (d) prior β_0 phases. Pole figures of (b) α and (e) prior β_0 phases. Inverse pole figures of (c) α and (f) prior β_0 phases. The build direction Z is taken as a reference. The maps are 1 mm × 0.6 mm wide and are collected with a step size of 0.6 µm.

Fig.3.6a and Fig.3.7a provide insight into the morphology and crystallographic orientation of α laths. Due to crystallographic constraints dictated by the Burger orientation relationships, these laths can have only 12 orientations relative to a given prior β_0 grain orientation. This leads to **a less pronounced texture** compared to the prior β_0 phase. EBSD data indicate an average thickness of α-laths of 0.5 µm, correlating with **a relatively high hardness of 394 ± 4 $HV_{1\,kg}$**.

3.2.2 Microstructure near the surface

Noticeable differences exist between the microstructure within the bulk material and that near the surface. Fig.3.8a-c provide a clearer representation of three distinct regions. The bulk material is found at approximately 600 to 800 µm beneath the surface. The second region, referred to as the sample *border*, spans from about 150 µm below the surface. Lastly, the third region termed the sample *contour*, encompasses a depth of around 150 µm, approximately corresponding to the two laser contour scans conducted during printing.

Cette thèse est accessible à l'adresse : https://theses.insa-lyon.fr/publication/2024ISAL0014/these.pdf
© [F. Steinhilber], [2024], INSA Lyon, tous droits réservés

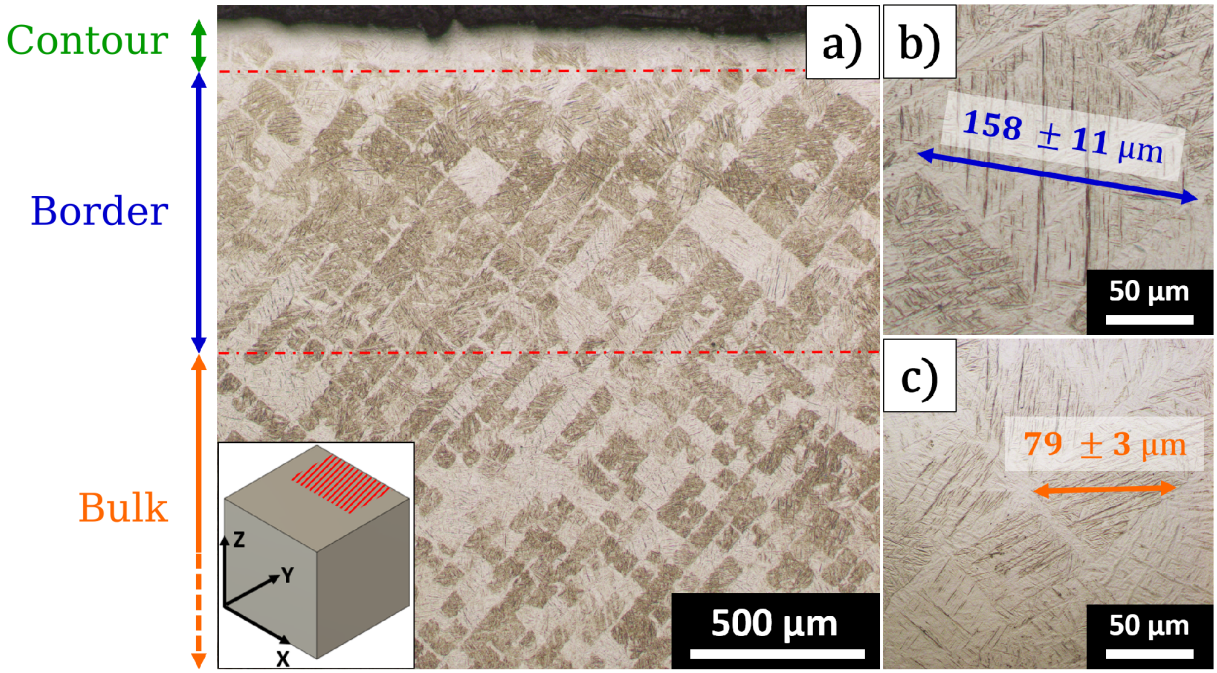

Figure 3.8 | Optical microscope observation of the microstructure in a horizontal plane (perpendicular to build direction), adapted from [GAI 23a]. (a) Large view revealing the presence of three regions (bulk, border and contour). Zoomed view in (b) border area and (c) bulk area.

Given that the microstructure of the bulk material has been previously discussed, the subsequent focus will be solely on the distinctive features of the border and contour zones. In this context, EBSD maps were generated near the surface within vertical (Z) and horizontal (XY) planes — refer to Fig.3.9a-j and Fig.3.10a-j respectively. Similar to the bulk microstructure, these maps characterize both α and prior β_0 phases.

The **border** region (spanning from 150 µm to 600 to 800 µm beneath the surface) exhibits a microstructure similar to that of the bulk material. Nevertheless, **the prior β_0 grains in this zone appear to be twice the size** of those in the bulk material — see Fig.3.8b-c and Fig.3.10f. An explanation has been proposed by [GAI 23a] to rationalize this phenomenon. It hypothesizes that at the beginning of a laser track, the preceding adjacent laser track might not have had sufficient time to fully solidify near the surface. Consequently, in such instances, β_0 grains might solidify from a melt pool twice the usual size, accounting for the observation of larger β_0 grains.

The **contour** area shows **a notably distinct microstructure**. In the immediate subsurface region (approximately within 0 to 50 µm), small prior β_0 grains are apparent, elongated in a direction close to Z. The slight deviation from the perfect alignment along the vertical axis can be attributed to local variations in thermal gradients near the surface. Beyond 50 µm, prior β_0 grains exhibit elongation both towards Z and perpendicular to the surface.

Across all these regions and regardless of the prior β_0 grain morphology and texture, the microstructure following printing and heat treatment consists of fine α laths, with minor texturing.

Cette thèse est accessible à l'adresse : https://theses.insa-lyon.fr/publication/2024ISAL0014/these.pdf
© [F. Steinhilber], [2024], INSA Lyon, tous droits réservés

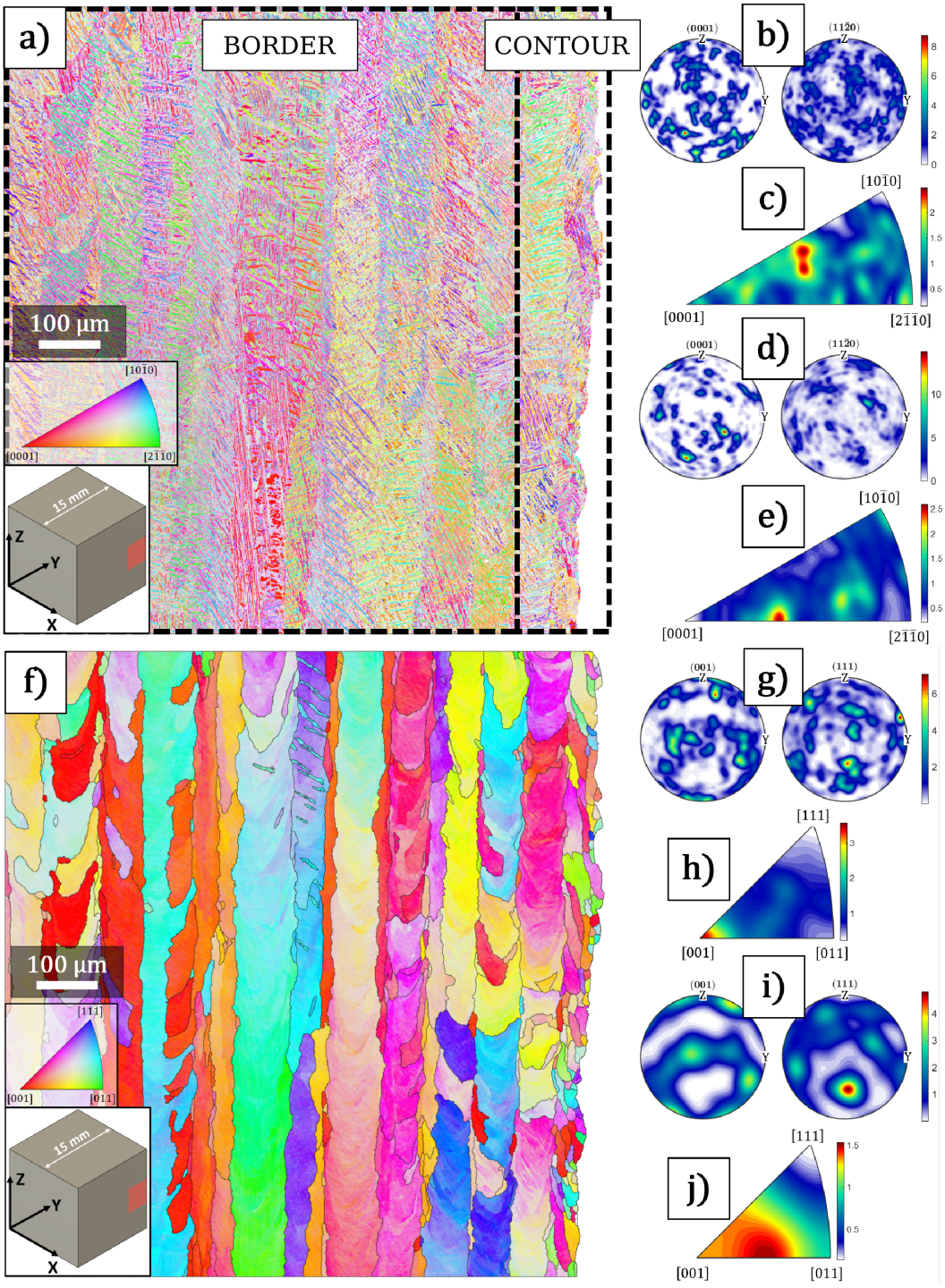

Figure 3.9 | EBSD analysis of the microstructure near the surface in a vertical plane (i.e. parallel to the build direction Z), adapted from [GAI 23a]. Crystallographic orientation maps of (a) α and (f) prior β_0 phases. Pole figures of (b) α and (g) prior β_0 phases in the border area. Inverse pole figures of (c) α and (h) prior β_0 phases in the border area. Pole figures of (d) α and (i) prior β_0 phases in the contour area. Inverse pole figures of (e) α and (j) prior β_0 phases in the contour area. The build direction Z is taken as a reference. The maps are 1 mm × 1 mm wide and are collected with a step size of 0.5 µm.

Cette thèse est accessible à l'adresse : https://theses.insa-lyon.fr/publication/2024ISAL0014/these.pdf
© [F. Steinhilber], [2024], INSA Lyon, tous droits réservés

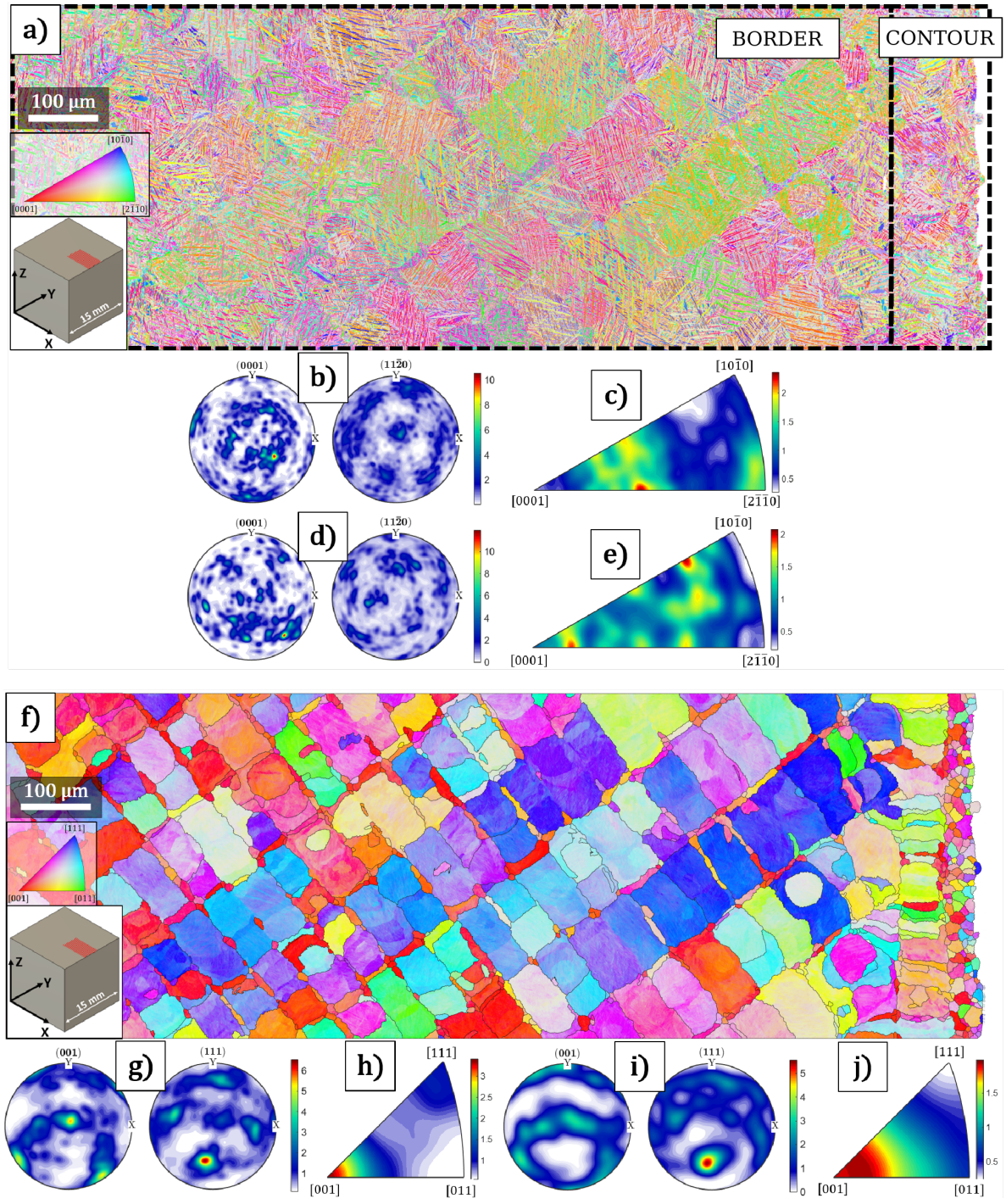

Figure 3.10 | EBSD analysis of the microstructure near the surface in a horizontal plane (i.e. perpendicular to the build direction Z), adapted from [GAI 23a]. Crystallographic orientation maps of (a) α and (f) prior β_0 phases. Pole figures of (b) α and (g) prior β_0 phases in the border area. Inverse pole figures of (c) α and (h) prior β_0 phases in the border area. Pole figures of (d) α and (i) prior β_0 phases in the contour area. Inverse pole figures of (e) α and (j) prior β_0 phases in the contour area. The build direction Z is taken as a reference. The maps are 1.45 mm × 0.5 mm wide and are collected with a step size of 0.4 µm.

Cette thèse est accessible à l'adresse : https://theses.insa-lyon.fr/publication/2024ISAL0014/these.pdf
© [F. Steinhilber], [2024], INSA Lyon, tous droits réservés

3.3 Tensile properties

Tensile tests were conducted at room temperature using an MTS 250 machine with a 100 kN load cell. The displacement rate was set to 0.525 mm/min. A GOM ARAMIS 6M Digital Image Correlation (DIC) system was employed to measure strain.

The investigation involved two Z, three 45°, and three XZ specimens. For stress calculations, the sections were assessed using XCT – refer to Section 3.4 for detailed XCT data acquisition information. In this context, all specimens were scanned over a length of 2.3 mm, with a voxel size of 6.5 µm. The mean of all XCT scan sections along the 2.3 mm distance was then computed for each specimen and employed for stress computation.

Tensile curves are depicted in Fig.3.11. The mechanical properties were extracted from the tensile response, including the Yield Stress (YS) measured at a plastic deformation of 0.02%, the Ultimate Tensile Strength (UTS), and the elongation to failure (ϵ_f).

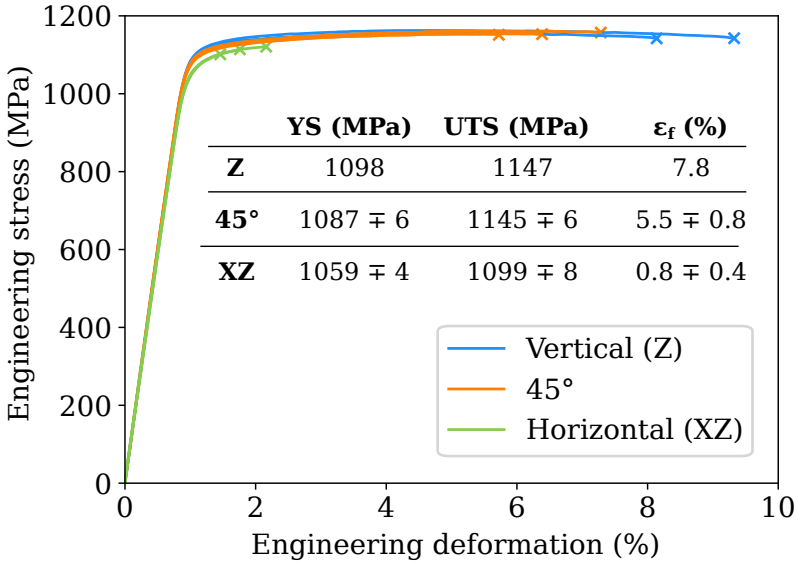

Figure 3.11 | Tensile curves measured for the three build directions. Values for YS, UTS and ϵ_f are presented in the form (mean ± std). Standard deviation is not measured for Z specimens, since two values are not enough to get a meaningful estimation.

The measured YS and UTS values exhibit strong reproducibility and consistency with results from the literature [NGU 22, GRE 17, KAS 15, BEN 18, VAN 12, CAI 15]. The slightly lower strength of the horizontal (XZ) specimens can likely be attributed to the significant protuberances that remain after support structure removal. These defects substantially increase the XCT-measured section of the specimen, though they are not expected to contribute to the strength of the material.

In contrast to tensile strength, elongation to failure demonstrates substantial variation, depending on the build orientation. Specifically, **XZ specimens display very little deformation before failure** ($\bar{\epsilon_f}$ = 0.8%). Once again, this could partially stem from support structures within the gauge length, which leave pronounced surface defects. However, findings from [GAI 22] suggest that an additional factor contributes to this lack of ductility. This study reveals that even for tensile specimens with the bottom surface (affected by support structures)

Cette thèse est accessible à l'adresse : https://theses.insa-lyon.fr/publication/2024ISAL0014/these.pdf
© [F. Steinhilber], [2024], INSA Lyon, tous droits réservés

machined, an unusually low elongation to failure is observed. Notably, the tensile specimens used in [GAI 22] share the same manufacturing conditions as the samples in this study, except for the machining step.

Microstructure might be responsible for this phenomenon. Indeed, Fig.3.12b reveals a linear pattern on the fracture surface of XZ specimens, which is absent for the Z specimen in Fig.3.12a. These lines are interpreted as indications of delamination at the interface between prior β_0 columnar grains. In the case of XZ specimens, these columnar grains are oriented perpendicularly to the loading direction.

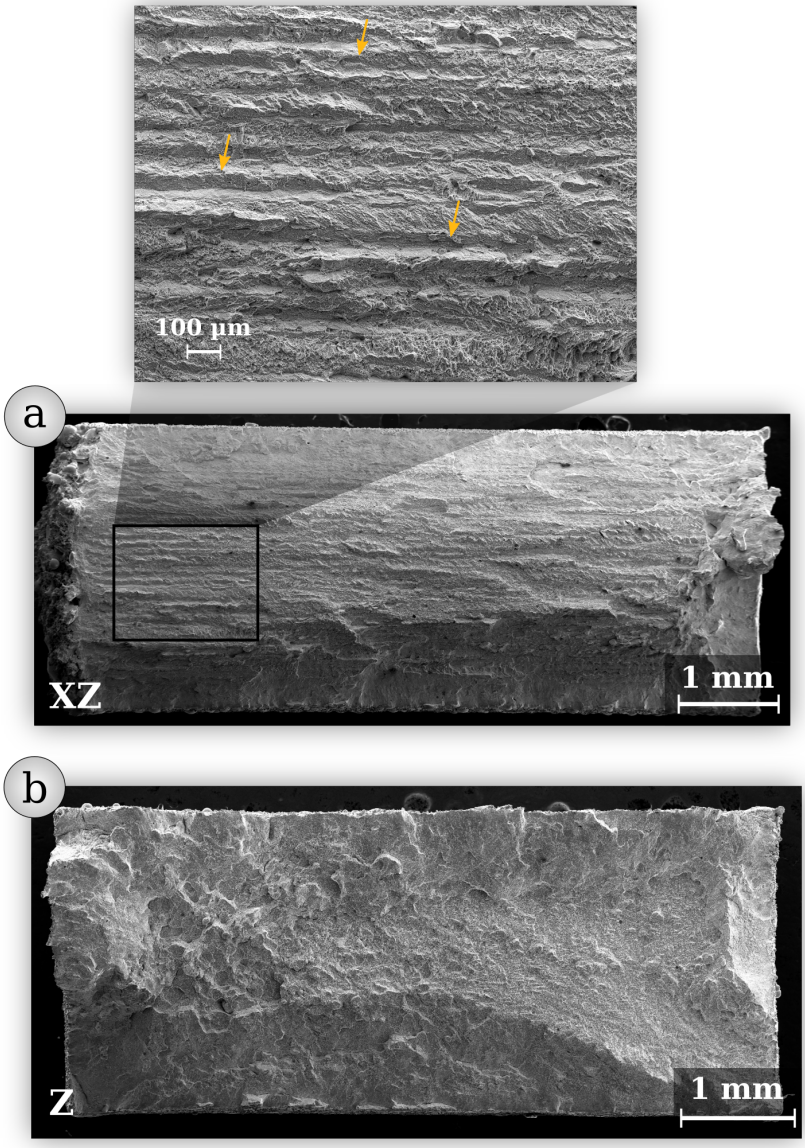

Figure 3.12 | SEM-SE observations of tensile fracture surfaces for (a) an XZ and (b) a Z specimen. On the XZ specimen, delamination can be seen at the interface of prior β_0 grain boundaries, leaving linear patterns on the fracture surface (see orange arrows).

Cette thèse est accessible à l'adresse : https://theses.insa-lyon.fr/publication/2024ISAL0014/these.pdf
© [F. Steinhilber], [2024], INSA Lyon, tous droits réservés

For more comprehensive insights into the tensile properties, readers are encouraged to refer to the work of [GAI 23a], who characterized material manufactured under identical conditions as in this study. Additionally, this work provides further details about the impact of microstructure and its evolution under various heat treatments.

3.4 Defects characterization using XCT

3.4.1 Acquisition setup

XCT was extensively employed to scan a relatively large portion of the gauge length of both tensile and fatigue specimens, primarily to assess their defects. The scanning procedure used a cone beam phoenix | x-ray V | tome | x-laboratory tomograph, operating at a voltage of 140 kV and a current of 80 µA, while acquiring 1200 projections. To counteract beam hardening artifacts, a 0.1 mm Cu filter was introduced during the acquisition. Following the acquisition, radiographs underwent a 3×3 median denoising filter. Reconstruction was subsequently performed using a standard filtered back projection algorithm facilitated by the proprietary software phoenix datos|x. A numerical filter was additionally employed during reconstruction to further mitigate the remaining beam hardening artifacts.

For each specimen, three scans were conducted along its longitudinal axis. The number of scans was chosen primarily to ensure that for fatigue specimens, failure always occurs in an area that was characterized by XCT. Details regarding the voxel size used, the resulting characterized length (taking into account the 3 scans), and the number of specimens scanned are summarized in Tab.3.3, for both tensile and fatigue specimens.

	Tensile specimens	**Fatigue specimens**
Number of scanned specimens	Z: 2 - 45°: 3 - XZ: 3	Z: 29 - 45°: 27
Voxel size (µm)	6.5	3
Characterized length (mm)	23	11

Table 3.3 | Number of specimens scanned by XCT, voxel size and characterized length for tensile and fatigue specimens.

Following reconstruction, the scans were converted into 8-bit unsigned volumes and merged using an automated Python script developed in-house. To reduce noise, a $2 \times 2 \times 2$ median filter was subsequently applied to the resulting volume. This volume was then directly employed for defect characterization, as detailed in the next sections.

As discussed in Chapter 1, defects can be classified into two primary groups: internal defects (primarily pores) and surface defects. Due to their distinct shapes, origins, and methods to characterize them, the two categories are examined separately in dedicated sub-sections. The focus of this characterization, in both cases, is confined to the L-PBF Ti64 fatigue specimens. The analysis was made using 29 Z specimens and 27 45° specimens.

Cette thèse est accessible à l'adresse : https://theses.insa-lyon.fr/publication/2024ISAL0014/these.pdf
© [F. Steinhilber], [2024], INSA Lyon, tous droits réservés

3.4.2 Porosity

To perform a quantitative characterization of porosity, pores need first to be segmented from XCT volumes. Here, like often, this step is done by thresholding. Since conventional automatic threshold calculation methods were found to miss too many pores, a higher threshold value has been used. Specifically, an intermediate value between conventional Otsu's threshold and the triangle threshold for bimodal histograms (as introduced in Chapter 2) was chosen. The limit was set at 70%, meaning that the chosen threshold equals the sum of 70% of the triangle threshold for bimodal histograms and 30% of Otsu's threshold.

Despite applying a median filter to XCT scans before thresholding, residual noise remained, leading to segmentation errors where some voxels were mistakenly identified as porosity. To address this, all pores with an equivalent diameter (defined by Eq.3.1) smaller than 12 µm (= 4 voxels) were considered noise and subsequently removed.

Following this procedure, the resulting **porosity is below 0.002%** for all samples analyzed. **This remarkably low value** confirms that the process parameters were efficiently optimized to achieve a nearly fully dense material.

To further enhance the characterization, pores were evaluated in terms of equivalent diameter, sphericity, and distance from the surface. The equivalent diameter D_{eq} is defined as the diameter of the sphere having the same volume as the pore (see Eq.3.1).

$$D_{eq} = \sqrt[3]{\frac{6 \cdot V}{\pi}} \tag{3.1}$$

where V is the volume of the pore. It is calculated using the marching cubes algorithm [LOR 87].

Sphericity S offers insights into pore morphology, representing the ratio of the area of a sphere with the same volume as the pore to the actual surface area of the pore (cf. Eq.3.2). A value of 1 denotes a perfect sphere, while lower values indicate irregularly shaped pores. Fig.3.13 illustrates pores with varying sphericity values.

$$S = \frac{\pi^{1/3} (6V)^{2/3}}{A} \tag{3.2}$$

where V and A are respectively the volume and the surface area of the pore. The marching cubes algorithm was used to measure both. This is an important computational detail because using the number of voxels to measure volume, as is often done, can lead to noticeable errors for small pores. In this study, for example, it resulted in many pores having a sphericity greater than one, which is theoretically impossible.

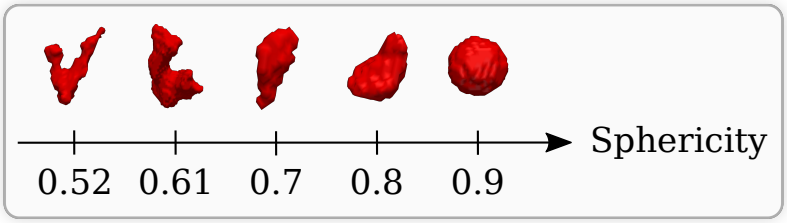

Figure 3.13 | Scale showing the evolution of pore morphology with increasing sphericity. Pores surfaces were extracted using the marching cubes algorithm.

Cette thèse est accessible à l'adresse : https://theses.insa-lyon.fr/publication/2024ISAL0014/these.pdf
© [F. Steinhilber], [2024], INSA Lyon, tous droits réservés

Fig.3.14b-d display distributions for equivalent diameter, sphericity, and distance from the surface. These distributions make easier quantitative comparisons between the two specimen build orientations (Z and 45°), as well as variations between specimens of the same orientation.

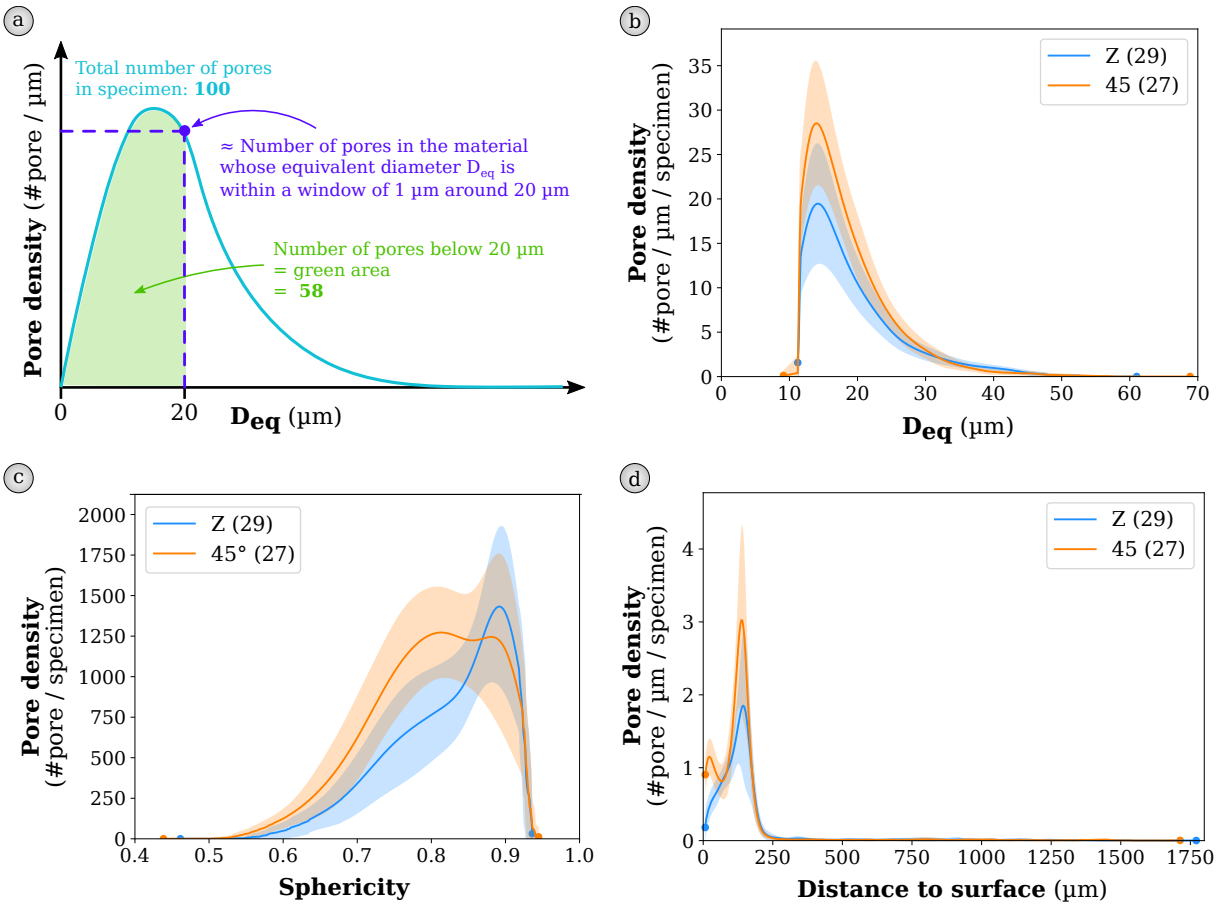

Figure 3.14 | Distributions of pores equivalent diameter D_{eq}, sphericity and distance to surface. (a) Schematic example of pore distribution. Distributions are here computed so that their integral equals the number of pores in the specimen. (b) D_{eq}, (c) Sphericity and (d) Distance to surface distributions. For each graph, lines correspond to mean distributions obtained for all samples while shaded areas represent an interval of one standard deviation from mean lines. Mean distributions are computed separately for vertically built (Z) and 45° specimens. The number of characterized specimens for each build orientation is specified in the graph legend.

To accomplish this, normalized probability distributions were first computed individually for each specimen through kernel density estimation (KDE) using a Gaussian kernel. The bandwidth was determined following Silverman's rule of thumb [SIL 98, p.45]. To mitigate edge effects, the obtained distributions were cropped based on the minimum and maximum values found in the data. Following cropping, they were normalized to ensure an integral of 1.

Cette thèse est accessible à l'adresse : https://theses.insa-lyon.fr/publication/2024ISAL0014/these.pdf
© [F. Steinhilber], [2024], INSA Lyon, tous droits réservés

The probability distributions for each specimen were then multiplied by the number of detected pores in that specimen. That way, the resulting distributions can provide insights into the number of pores rather than probabilities. For instance, as shown in Fig.3.14a, the area under the distribution between 0 µm and 20 µm indicates the number of pores in the sample with an equivalent diameter less than 20 µm. This approach enables differentiation between samples exhibiting similar pore size probability distributions but varying pore densities.

As these distributions were calculated across numerous specimens, they were averaged to yield a single mean distribution for each parameter (D_{eq}, S, and distance from the surface). To account for specimen variations, shaded areas around the distribution curves represent one standard deviation from the mean curve.

Fig.3.14b demonstrates that for both build orientations, **all pores exhibit equivalent diameters smaller than 70 µm**. The majority are notably smaller – 81% and 88% being less than 30 µm for the Z and 45° specimens, respectively. This graph also indicates that more pores are measured in 45° specimens, with an average increase of 29%.

In addition to their relatively compact size, **pores tend to have high sphericity values**, as illustrated in Fig.3.14c. This tendency is more pronounced for Z specimens. Combining size and sphericity data suggests that most pores are of the keyhole type, as opposed to lack of fusion defects. Lack-of-fusion defects typically possess larger dimensions and irregular shapes, resulting in lower sphericity values.

Fig.3.14d offers insightful information about pore distribution within specimens. **The majority is concentrated in a subsurface layer**, with 62% and 71% being situated within 200 µm from the surface for Z and 45° specimens, respectively. The main peak in both Z and 45° distributions indicates that pores tend to form at a specific depth from the surface, approximately 140 µm. This aligns with the overlap region between contour laser tracks and bulk material. One hypothesis to explain this could be that inappropriate laser contour scanning parameters or overlap adjustment might be responsible for these pores. Excessive overlap could for instance lead to locally high energy density, encouraging keyhole instabilities and pore formation. It is worth noting that even considering this over-concentration of sub-surface porosity, the specimens still show a high density ($> 99.9\%$).

An additional peak, close to 0 µm, is observed in the 45° distribution in Fig.3.14d. This corresponds to pores detected in the down-skin region, just beneath the surface. XCT scan resolution does not allow precise identification of whether these are actual internal pores. Most are likely open pores or, more specifically, roots of thin surface valleys not accurately captured during volume segmentation. Manual inspection of XCT scans supports this assumption for the majority of these pores, although resolution is insufficient for some of them. Some may be internal pores resulting from the closure of surface valleys. Notably, these pores tend to exhibit an elongated morphology, which partly explains the higher number of pores with intermediate sphericity values in the 45° specimens (see Fig.3.14c).

To summarize, the vast majority of pores found in 45° specimens are similar to those observed in Z specimens in terms of size, shape, and location: most are small (< 30 µm) and roughly spherical pores located at the interface between contour and bulk laser scanning strategies (≈ 140 µm deep).

Cette thèse est accessible à l'adresse : https://theses.insa-lyon.fr/publication/2024ISAL0014/these.pdf
© [F. Steinhilber], [2024], INSA Lyon, tous droits réservés

3.4.3 Surface defects

The characterization of surface defects presents greater complexity compared to internal defects, particularly for as-built surfaces. In many cases, defects are not isolated and well-defined objects. Instead, they often involve a combination of various irregularities on the surface, forming for instance interconnected valleys. Nonetheless, certain typical surface features can still be identified. To enable more quantitative comparisons, the surface roughness is then assessed using standard roughness parameters.

3.4.3.1 Types of surface defects

Fig.3.15 and Fig.3.16 show the main surface defects identified on Z and 45° specimens. For both types of specimens, it includes:

- Unmelted powder particles
- Spatters
- Large protrusions on vertical surfaces
- Dross in down-skin regions (see Section 1.2.2 for dross definition)
- Valleys (also referred to as notches)

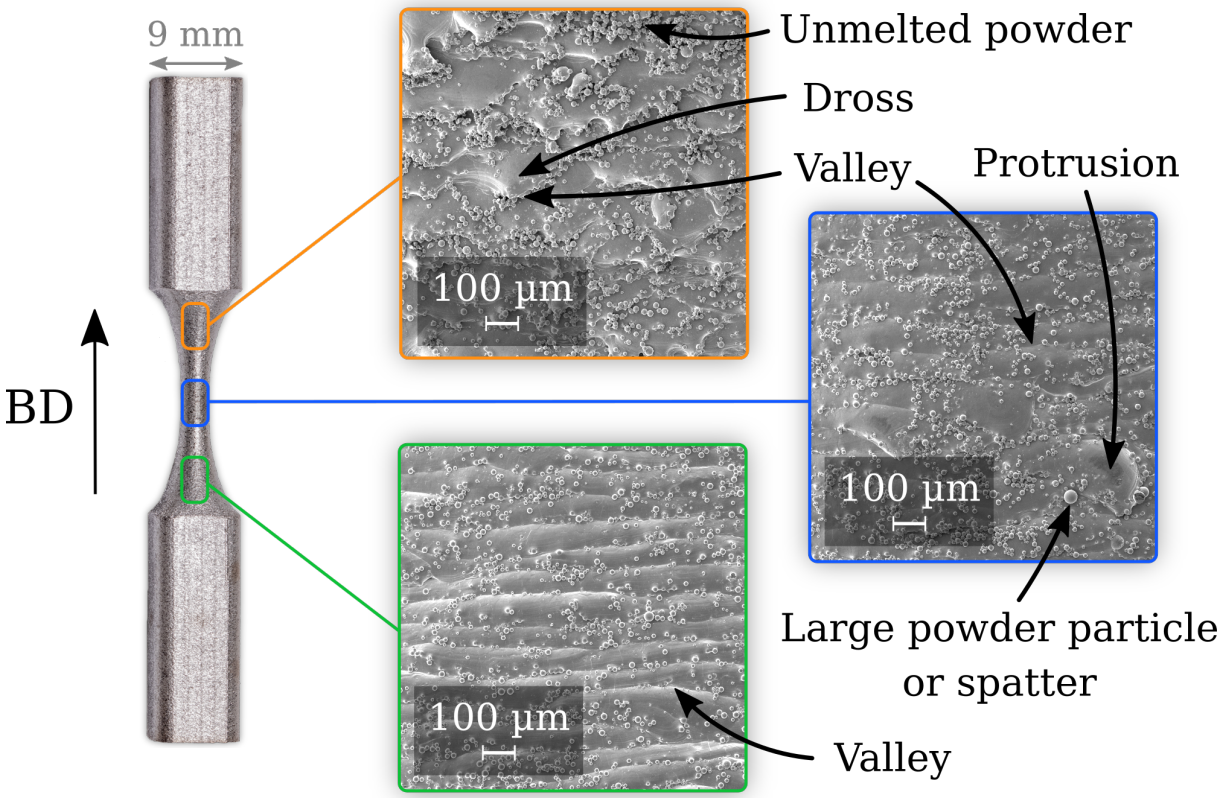

Figure 3.15 | Examples of surface defects on a Z specimen. Enlarged views show SEM-SE images of different areas along the specimen.

Cette thèse est accessible à l'adresse : https://theses.insa-lyon.fr/publication/2024ISAL0014/these.pdf
© [F. Steinhilber], [2024], INSA Lyon, tous droits réservés

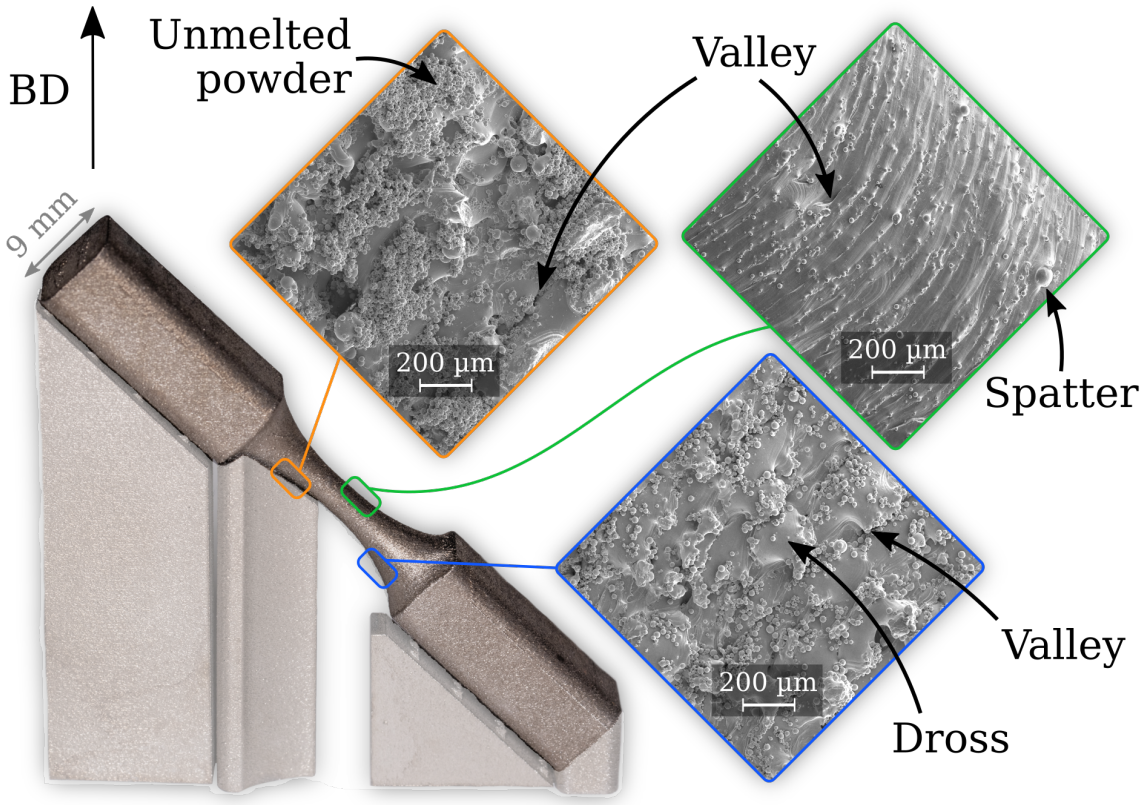

Figure 3.16 | Examples of surface defects on a 45° specimen. Enlarged views show SEM-SE images of different areas along the specimen. Support structures used during manufacturing are shown using a different color.

Unmelted powder particles

Unmelted powder particles can be identified in various regions, with down-skin areas showing the most prevalence, even after post-manufacturing cleaning steps.

While unmelted powders are not expected to affect the mechanical properties, they can raise concerns about health and safety, as well as lead to other functional issues like fluid contamination in hydraulic systems. They can also make the observation of more important surface features difficult.

Efforts were made to further clean specimens after the removal of support structures, and see if US bath cleaning is suited for this purpose. To do so, one Z and one 45° specimen were subjected to XCT scanning at three stages:

1. Directly after support structures removal.
2. After 10 min ultra-sonic (US) cleaning in ethanol.
3. After an additional manual cleaning with a plastic brush and ethanol.

Cette thèse est accessible à l'adresse : https://theses.insa-lyon.fr/publication/2024ISAL0014/these.pdf
© [F. Steinhilber], [2024], INSA Lyon, tous droits réservés

The evolution of the surface condition is depicted in Fig.3.17a-c and Fig.3.18a-c. These images represent the curvature (κ_{min}) in a 3D representation, derived from XCT scans at each stage. The κ_{min} representation helps in detecting powder particles, which exhibit a high positive value (displayed in white). Images from each step were taken from the same area to facilitate comparison, and Otsu's threshold was used to enhance the visibility of powder particles during segmentation.

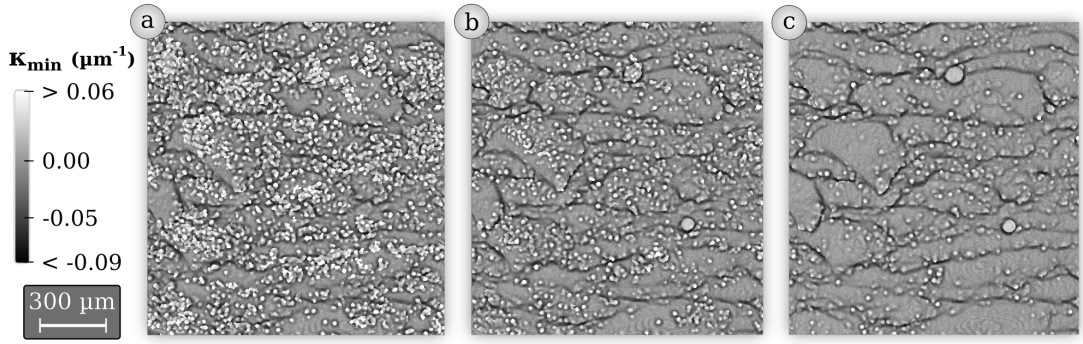

	a	b	c
S_a (µm)	10.5	10.1	9.5
S_v (µm)	61	62	59
S_z (µm)	165	161	137
	t_0 = after support structure removal	t_0 + 10 min **US bath**	t_0 + 10 min US bath + **brush cleaning** + 5 min US bath

Figure 3.17 | Surface of a Z specimen before and after several cleaning steps. The same region is shown in three images, and roughness measurements were made using the surface extracted from the whole XCT scan. Images are curvature 3D representations obtained from XCT scans. The surface is segmented using Otsu's threshold to better visualize powder particles. Curvature and roughness were computed using the following parameters: $\lambda_c = 0.8\,\text{mm}$, $r_{curv} = 20\,\mu\text{m}$ and no S-filter.

The results indicate that US cleaning enables the removal of a large part of powder particles. However, **a significant quantity of powder remains** and can partially be removed by cleaning with a plastic brush. This means that (for the experimental conditions investigated) even after US cleaning, a substantial number of powder particles remain, although they are not firmly attached to the surface. This can be a concern, as mentioned earlier.

From a research standpoint, this highlights the great importance of thorough surface cleaning. As depicted in Fig.3.18a-c, the valleys remain often concealed and hidden by particles before cleaning. Given that the primary importance of comprehensive surface cleaning (including brush-based methods) was realized only during the mid-phase of this PhD research, some of the characterized specimens underwent US cleaning alone, while others also underwent manual cleaning using a plastic brush. This can potentially contribute to dispersion in roughness measurements, which show some variations depending on the cleaning step — see Fig.3.17a-c and Fig.3.18a-c.

Cette thèse est accessible à l'adresse : https://theses.insa-lyon.fr/publication/2024ISAL0014/these.pdf
© [F. Steinhilber], [2024], INSA Lyon, tous droits réservés

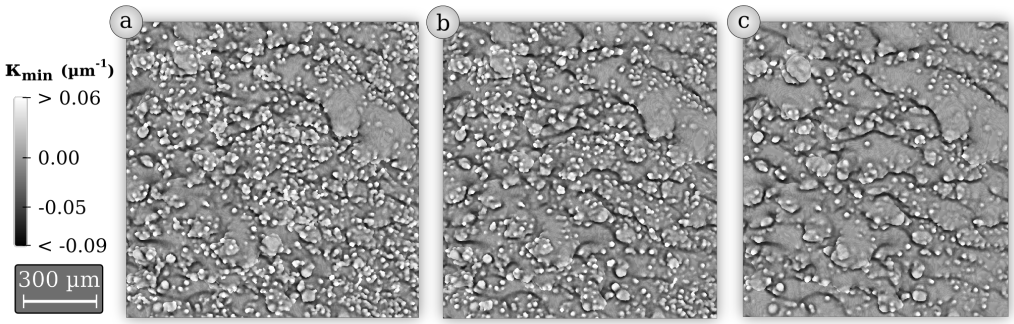

	a	b	c
S_a (µm)	18.4	18.7	17.4
S_v (µm)	95	104	99
S_z (µm)	254	265	219
	t_0 = after support structure removal	t_0 + 10 min **US bath**	t_0 + 10 min US bath + **brush cleaning** + 5 min US bath

Figure 3.18 | Down-skin surface of a 45° specimen before and after several cleaning steps. The exact same region is shown in three images. Images are curvature 3D representations obtained from XCT scans. The surface is segmented using Otsu's threshold to better visualize powder particles. Curvature and roughness were computed using the following parameters: $\lambda_c = 0.8\,\text{mm}$, $r_{curv} = 20\,\mu\text{m}$ and no S-filter.

Spatters

Large particles can occasionally be observed (see e.g. Fig.3.16). Here, "large" refers to sizes that significantly exceed the expected maximum powder particle size of 25 µm. Although no in-depth study has been carried out concerning their origin, they are considered to be most likely spatters. For the sake of simplicity, they will therefore be referred to as such hereafter. However, some may also originate from the initial powder itself.

Large protrusions

Large protrusions are frequently observed, particularly on vertical walls. In these areas, they exhibit a distinctive morphology that is not commonly reported in the literature. Fig.3.19 illustrates some of these protrusions on a 3D representation of a Z specimen obtained via XCT. The representation combines roughness and curvature data to make visualization easier. Notably, protrusions are identified by their height, depicted in red in Fig.3.19.

These protrusions are generally quite large (around 300 to 400 µm wide) and have a curved water-drop shape. Furthermore, their spatial distribution appears non-random, although it can vary significantly between specimens. For instance, Fig.3.19 shows that several protrusions are vertically aligned. They also tend to be denser on one side of the specimen, while the other side presents a more conventional plate-pile appearance. The most plausible explanation is that these protrusions correspond to the initiation or termination points of the laser tracks, where variations in energy density or melt-pool dynamics could contribute to the formation of such defects.

Cette thèse est accessible à l'adresse : https://theses.insa-lyon.fr/publication/2024ISAL0014/these.pdf
© [F. Steinhilber], [2024], INSA Lyon, tous droits réservés

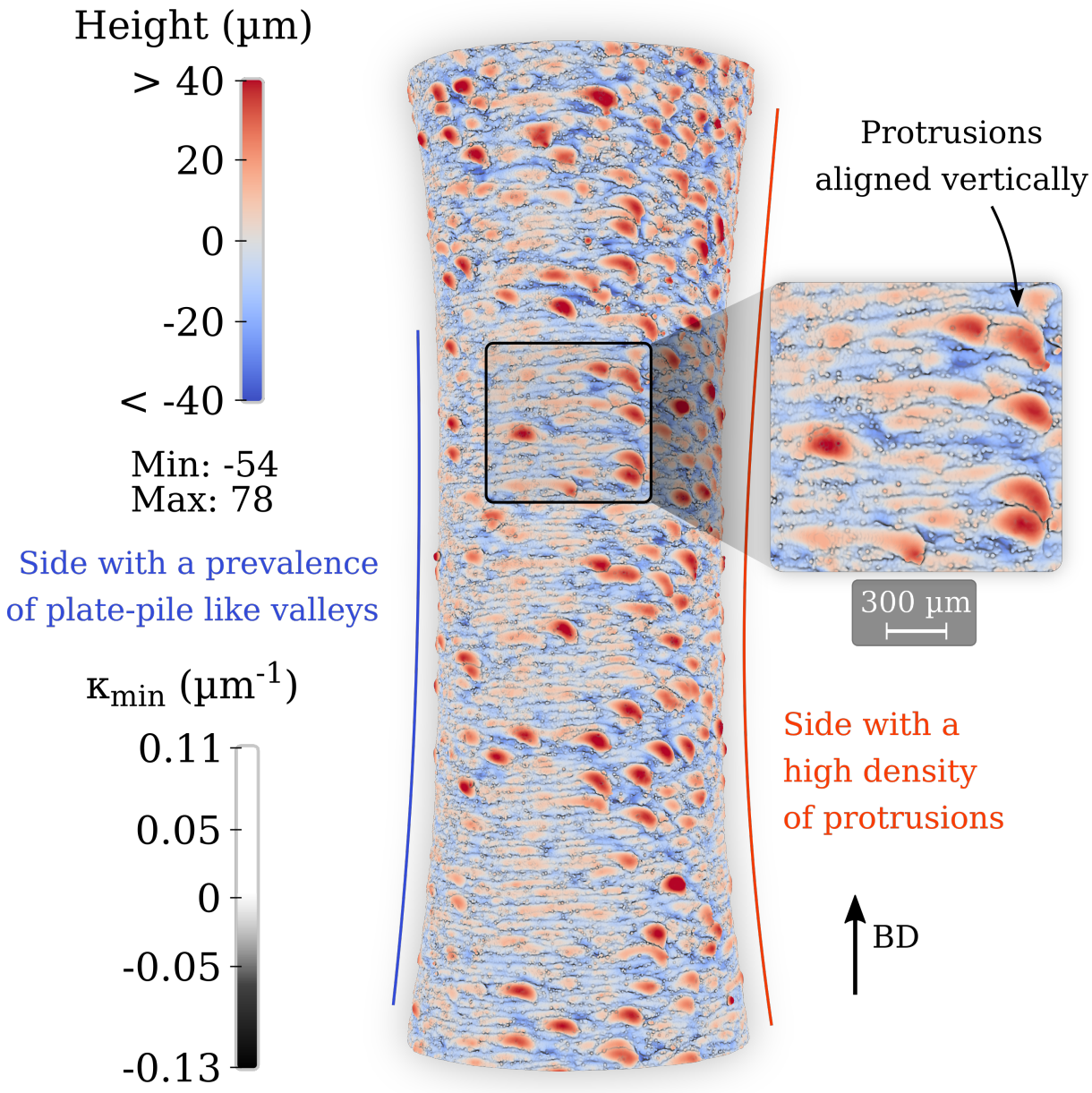

Figure 3.19 | 3D representation of a Z specimen. Height and curvature are superimposed for better visualization, the curvature being shown with some transparency. Height and curvature are measured using $\lambda_c = 0.8\,\text{mm}$, $r_{curv} = 12\,\mu\text{m} = 4 \times$ voxel size and $\lambda_S = 9\,\mu\text{m} = 3 \times$ voxel size. Surface segmentation from the XCT scan was done using Otsu's threshold.

Dross

Dross is widely visible in down-skin regions — refer to Section 1.2.2 for dross definition. This leads to the presence of significant protrusions and valleys in between, see Fig.3.20. The protrusions vary in shape and size, but are frequently observed to be a few hundred µm wide.

Cette thèse est accessible à l'adresse : https://theses.insa-lyon.fr/publication/2024ISAL0014/these.pdf
© [F. Steinhilber], [2024], INSA Lyon, tous droits réservés

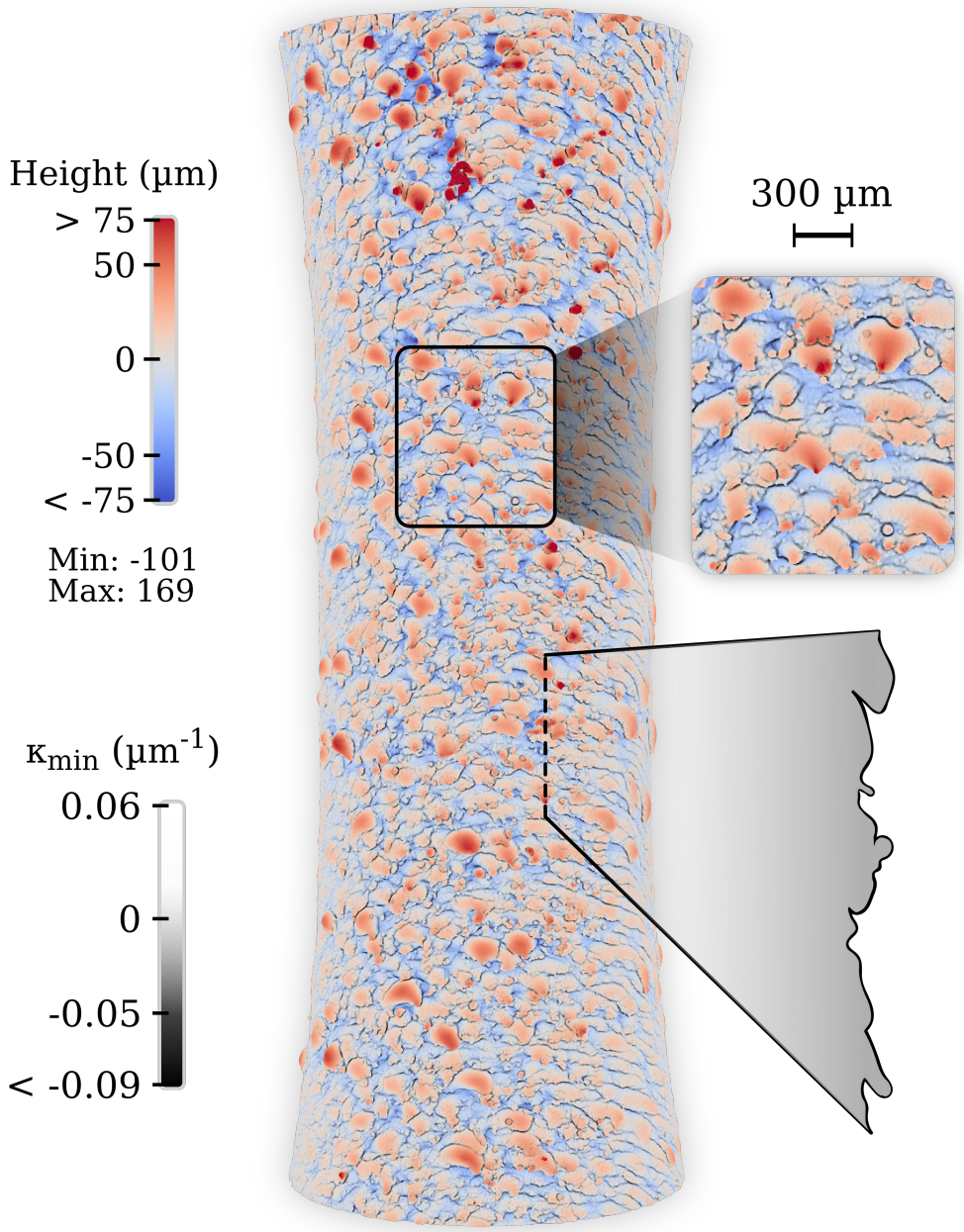

Figure 3.20 | Down-skin surface of a 45° specimen. Height and curvature measurements are superimposed for better visualization, the curvature being shown with some transparency. Height and curvature were measured using $\lambda_c = 0.8\,\text{mm}$ and $r_{curv} = 20\,\mu\text{m}$. No S-filter was used. The TTBH was used to better reveal dross and the resulting valleys.

Valleys

Valleys can be seen everywhere on the surface but with different morphologies depending on their location.

Cette thèse est accessible à l'adresse : https://theses.insa-lyon.fr/publication/2024ISAL0014/these.pdf
© [F. Steinhilber], [2024], INSA Lyon, tous droits réservés

In up-skin and vertically built areas, valleys primarily stem from the plate-pile effect. In this case, they tend to be relatively evenly spaced and aligned perpendicular to the build direction. However, the spacing between valleys does not precisely correspond to the layer height as one might anticipate. For instance, their spacing is found equal to 75 µm in the green window in Fig.3.15, which is almost twice the layer height (40 µm). Additionally, these valleys are often elongated yet shallow.

Conversely, valleys in down-skin regions are related to dross formation. They are often deeper than plate-pile-like valleys in vertical areas and more irregular. Since dross formation occurs parallel to the build direction, resulting valleys tend to be oriented at 45° with respect to the surface (see Fig.3.21). Furthermore, large quantities of unmelted powders attached to the surface and filling valleys often obscure them. This complexity can make their characterization using conventional surface assessment tools like tactile probes or interferometers more difficult. Even XCT scans may struggle to accurately detect valleys due to the presence of powder particles that obstruct their visibility. These issues are illustrated in Fig.3.21.

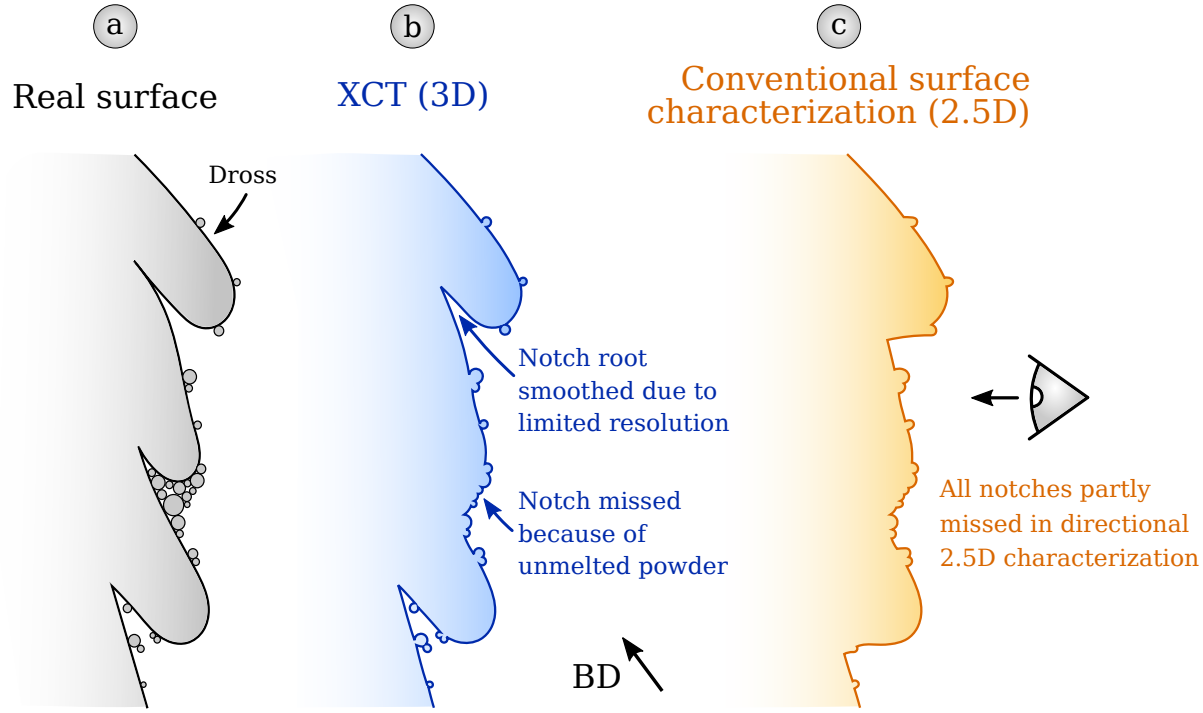

Figure 3.21 | Schematic representation of the down-skin region of a 45° specimen, showing dross formation and resulting valleys oriented at 45°. (a) Real surface, (b) Surface as it could be seen by XCT, and (c) Surface as seen by a conventional (2D or 2.5D directional) surface characterization tool such as interferometry. Since valleys are inclined, a 2.5D characterization will miss a large part of them. XCT provides better results, although unmelted powder particles can also obscure notches.

Cette thèse est accessible à l'adresse : https://theses.insa-lyon.fr/publication/2024ISAL0014/these.pdf
© [F. Steinhilber], [2024], INSA Lyon, tous droits réservés

To prevent unmelted powder particles from hiding notches, the use of the Triangle Threshold for Bimodal Histograms (TTBH, defined in Chapter 2) to segment specimens' surface was found to be very effective.

In Fig.3.22a, the conventional use of Otsu's threshold results in powder particles masking significant portions of the surface. Conversely, Fig.3.22b demonstrates that the triangle threshold for bimodal histograms substantially reduces this effect, uncovering other surface features like dross and resulting valleys. This thresholding approach yields outcomes similar to those of specimen cleaning using both ultrasonic bath treatment and brushing, as depicted in Fig.3.22c. The triangle threshold for bimodal histograms even surpasses physical cleaning in its efficiency in removing powder particles. Consequently, this threshold will be extensively employed throughout this work, including for surface roughness quantification.

Cette thèse est accessible à l'adresse : https://theses.insa-lyon.fr/publication/2024ISAL0014/these.pdf
© [F. Steinhilber], [2024], INSA Lyon, tous droits réservés

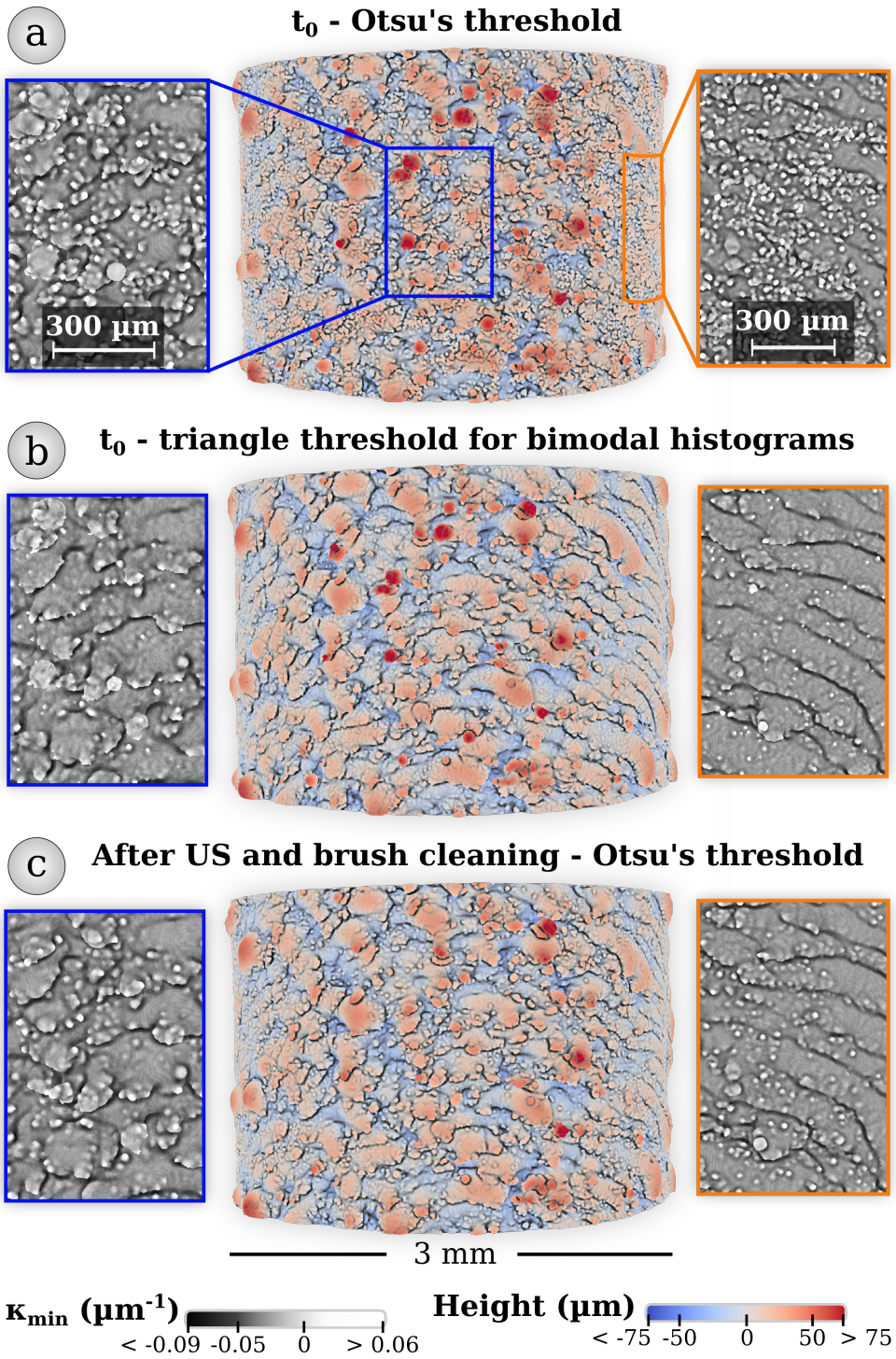

Figure 3.22 | Comparison of the efficiency of sample cleaning and the use of the TTBH to eliminate powder particles from XCT scans. (a) Surface obtained before any cleaning (step t_0 in 3.18) using Otsu's threshold, (b) Surface obtained before any cleaning using TTBH and (c) Surface obtained after both US and brush cleaning, obtained using Otsu's threshold. Roughness and curvature were computed using $\lambda_c = 0.8\,\text{mm}$, $r_{curv} = 20\,\mu\text{m}$ and no S-filter. Roughness and κ_{min} are superimposed in central pictures by displaying κ_{min} with some transparency. Pictures on the side represent κ_{min} only.

Cette thèse est accessible à l'adresse : https://theses.insa-lyon.fr/publication/2024ISAL0014/these.pdf
© [F. Steinhilber], [2024], INSA Lyon, tous droits réservés

3.4.3.2 Quantitative surface roughness

To provide a more quantitative description of the surface states of the specimens, several roughness parameters were computed. The roughness data employed for this analysis was obtained from XCT scans. The calculated parameters encompass the arithmetical mean height (S_a), root mean square height (S_q), maximum height (S_z), maximum valley depth (S_v), height distribution skewness (S_{sk}) and kurtosis (S_{ku}). The mathematical definitions and practical implementations used to compute these parameters are detailed in Chapter 2.

Similar to the porosity characterization, roughness parameters are measured for 29 Z specimens and 27 45° specimens. Since the surface states significantly differ between the up-skin and down-skin regions of the 45° specimens, the parameters are computed separately for these areas. The definitions for up-skin and down-skin regions used in the calculations are depicted in Fig.3.23. In the case of Z specimens, the whole surface was used. The calculation region has a length of 9 mm along the specimen axis, accounting for a portion of the specimen's fillet radius.

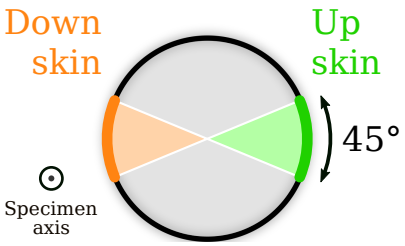

Figure 3.23 | **Definition of up-skin and down-skin regions** used for roughness parameters calculation on 45° specimens.

Results were summarized in the form of violin plots, which are enhanced versions of box plots. The way those plots can be read is detailed in Fig.3.24.

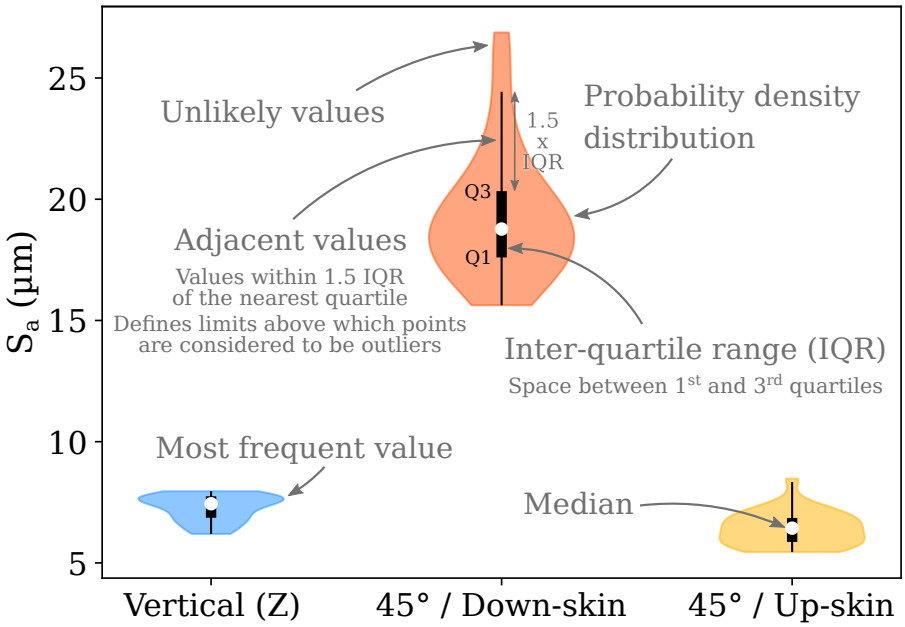

Figure 3.24 | Presentation of violin plots for roughness parameters.

Cette thèse est accessible à l'adresse : https://theses.insa-lyon.fr/publication/2024ISAL0014/these.pdf
© [F. Steinhilber], [2024], INSA Lyon, tous droits réservés

Given the size of the observed surface features, a cut-off wavelength of 0.8 mm was estimated to be the best compromise for roughness computation. However, it is worth noting that other values may be relevant and lead to significant differences in roughness parameter values. As an example, Fig.3.25a-b show violin plots for S_a parameter using two cut-off wavelengths: 0.25 mm and 0.8 mm.

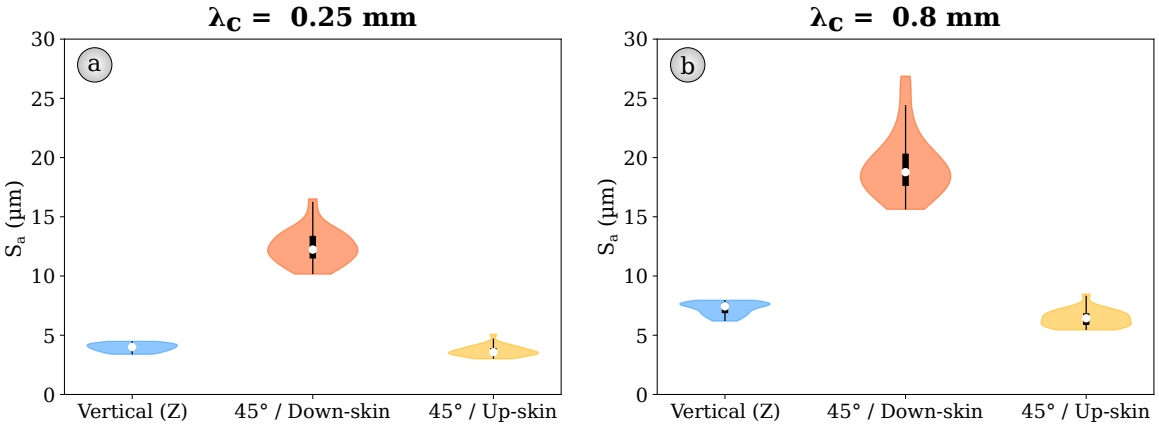

Figure 3.25 | Violin plots for S_a parameter computed for (a) $\lambda_c = 0.25$ mm and (b) 0.8 mm. In both cases, an S-filter was applied using $\lambda_S = 0.03$ mm = 10 voxel size.

Although tendencies between build orientations and down-skin/up-skin areas are the same for both cut-off wavelengths, absolute values are significantly different. For instance, the median S_a value in down-skin area of 45° specimens is around 12.2 µm for $\lambda_c = 0.25$ mm whereas it is only about 18.8 µm for $\lambda_c = 0.8$ mm. One should therefore always be careful when comparing roughness parameter values computed with different workflows, in particular, different cut-off wavelengths. In the present case, all characterizations done hereafter use the same cut-off wavelength to overcome this issue. In all cases, an S-filter is also applied after roughness computation, using a cut-off $\lambda_S = 0.03$ mm.

Violin plots for S_a, S_q, S_z, S_v, S_{sk} and S_{ku} parameters are shown in Fig.3.26a-f. Mean values for these parameters are summarized in Tab.3.4.

	Vertical	**45° Down-skin**	**45° Up-skin**
S_a **(µm)**	7.3 ± 0.5	19.3 ± 2.6	6.4 ± 0.7
S_q **(µm)**	10.3 ± 0.7	26.1 ± 3.7	8.6 ± 1.0
S_z **(µm)**	150 ± 25	269 ± 51	120 ± 21
S_v **(µm)**	64 ± 15	117 ± 30	59 ± 17
S_{sk}	1.0 ± 0.3	0.8 ± 0.2	0.2 ± 0.5
S_{ku}	4.2 ± 1.6	2.5 ± 1.0	3.6 ± 3.0

Table 3.4 | Roughness parameters, computed for Z specimens (29 sp.) as well as down-skin and up-skin regions of 45° specimens (27 sp.). Roughness was computed from XCT data using the 3D characterization workflow introduced in Chapter 2. The cut-off values for filters were set to $\lambda_c = 0.8$ mm and $\lambda_S = 0.03$ mm. Values presented in the format (mean ± std).

Cette thèse est accessible à l'adresse : https://theses.insa-lyon.fr/publication/2024ISAL0014/these.pdf
© [F. Steinhilber], [2024], INSA Lyon, tous droits réservés

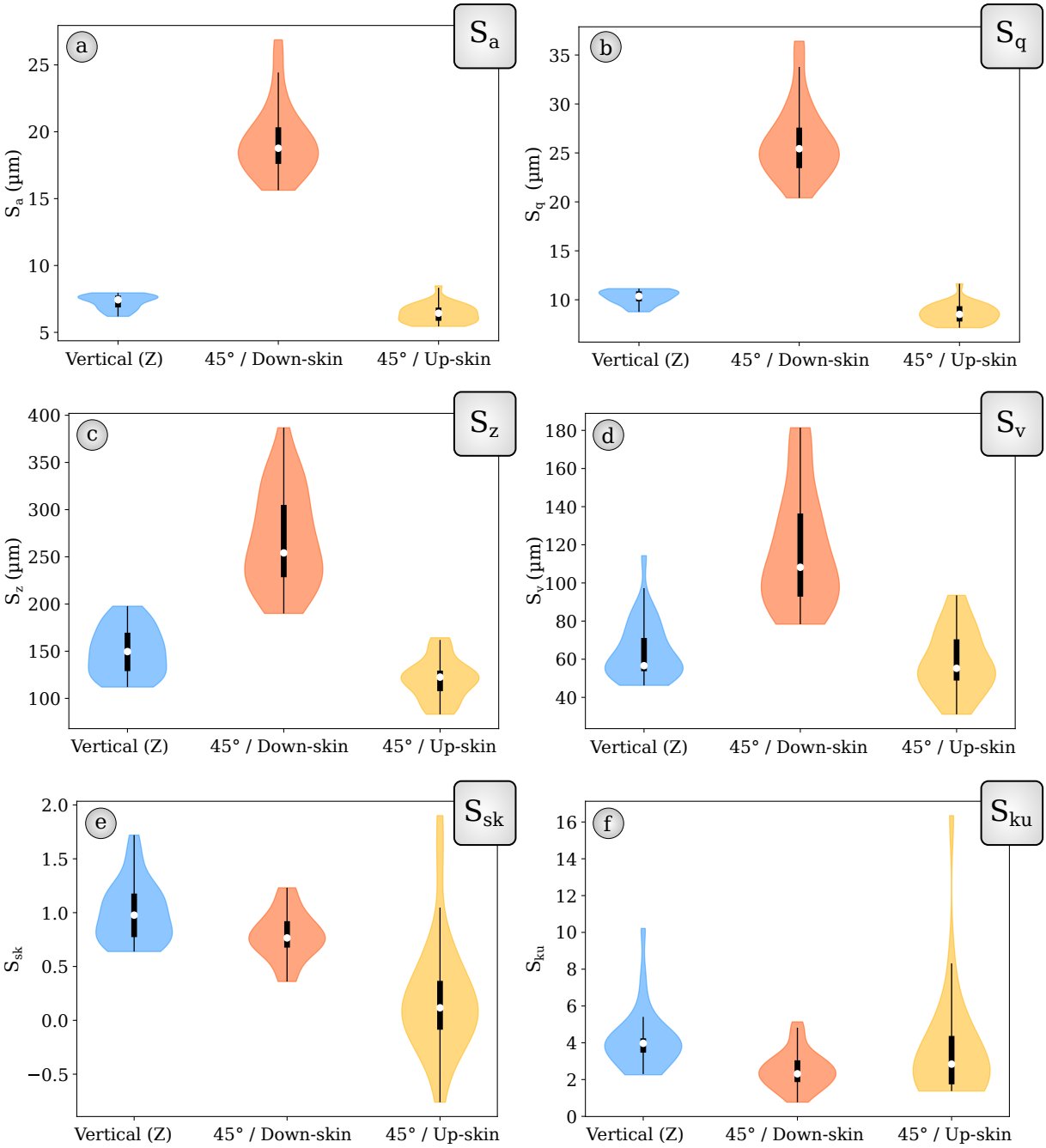

Figure 3.26 | Violin plots for roughness parameters (a) S_a, (b) S_q, (c) S_z, (d) S_v (e) S_{sk} and (f) S_{ku}. Roughness is computed using $\lambda_c = 0.8\,\text{mm}$ and $\lambda_S = 0.03\,\text{mm}$. Violin plots were computed using 29 Z and 27 45° specimens.

Cette thèse est accessible à l'adresse : https://theses.insa-lyon.fr/publication/2024ISAL0014/these.pdf
© [F. Steinhilber], [2024], INSA Lyon, tous droits réservés

Fig.3.25a and Fig.3.26a show that, on average, down-skin surfaces of 45° specimens are significantly rougher compared to up-skin and vertical surfaces. Vertical specimens are also slightly rougher than up-skin areas of 45° specimens. All these observations are consistent with qualitative observations made on SEM images in Fig.3.15 and Fig.3.16.

Similar conclusions can be drawn from S_z and S_v parameters in Fig.3.26b-c, even though discrepancies between different conditions are smaller. This could be explained by the fact that even though vertical surfaces and up-skin regions are much smoother on average, they may still contain some relatively large defects. This could also explain why S_{ku} can reach higher values for those two conditions — see Fig.3.26f. However, these observations may also come from the fact that the area characterized is eight times smaller for up-skin and down-skin regions of 45° specimens than for Z specimens.

Regarding the skewness measurements presented in Fig.3.26e, most surfaces tend to be peak-dominated ($S_{sk} > 0$). However, some of the 45° specimens display negative skewness in up-skin regions. This positive skewness is attributed to the occurrence of protrusions in vertical regions and to dross in down-skin areas. In contrast, up-skin regions usually lack such protrusions but often feature plate-like valleys. This might account for the instances of negative skewness. Yet, spatters appear sometimes in these areas, possibly explaining the exceptionally high skewness (and kurtosis) observed in a few specimens.

Cette thèse est accessible à l'adresse : https://theses.insa-lyon.fr/publication/2024ISAL0014/these.pdf
© [F. Steinhilber], [2024], INSA Lyon, tous droits réservés

Intermediate summary

Ti64 samples were manufactured by L-PBF and submitted to a stress-relief at 720 °C for 2 h to completely alleviate residual stresses. The surfaces were maintained in their as-built state to study surface defects. To investigate the influence of build orientation, fatigue specimens were produced in two orientations (Z and 45°), while tensile specimens were prepared in three orientations (vertical (Z), 45°, and horizontal (XZ)).

The material exhibited a microstructure and tensile properties consistent with the existing literature. The microstructure consisted of fine α laths (averaging around 0.5 µm thickness) along with a minor fraction of β phase ($2.2 \pm 0.3\%$). Prior β_0 grains were reconstructed from EBSD data and showed a typical columnar morphology with the growth direction parallel to the build direction. They showed a significantly different morphology near the surface, which can probably be explained by differences in local energy density and thermal gradients during printing. Everywhere, though, the final microstructure is primarily composed of α laths and exhibits only little texturing. For more detailed information regarding the material microstructure, readers are encouraged to refer to [GAI 23a] and [GAI 23b].

Compared to conventional wrought Ti64 [NGU 22], the tensile strength was relatively high ($\bar{YS} = 1098$ MPa for Z specimens), but the elongation to failure was rather limited ($\bar{\epsilon_f} = 7.8\%$ for Z specimens). This can be attributed partly to the aforementioned fine microstructure. XZ specimens displayed notably low ductility ($\bar{\epsilon_f} = 0.8\%$), possibly due to the presence of significant defects left after support removal. Additionally, prior β_0 grain boundaries, aligned perpendicular to the loading direction for these specimens, seemed to serve as weak points contributing to premature failure.

XCT-based characterization revealed very low porosity ($< 0.002\%$) with predominantly near-spherical and small-sized pores (over 80% smaller than 30 µm). However, the majority of these pores were located beneath the surface (≈ 140 µm deep), likely originating from contour scans.

Surface roughness was also evaluated via XCT, utilizing the 3D characterization approach introduced in Chapter 2. The surface roughness was found to be relatively low in comparison to literature values, particularly for up-skin and vertical regions. For instance, the mean S_a value across all Z specimens was 7.3 µm. In contrast, down-skin regions exhibited higher roughness with a mean S_a of 19.3 µm. Among the observed surface defects with the potential to influence fatigue properties, valleys were prominent. These valleys originated from the plate-pile effect in up-skin and vertical surfaces, and from dross formation in down-skin regions. These valleys could exhibit intricate morphologies with re-entrant features, frequently concealed by unmelted powder particles. Conventional 2.5D surface characterization tools may encounter limitations in properly assessing such surfaces, making XCT a suitable solution for this purpose.

Cette thèse est accessible à l'adresse : https://theses.insa-lyon.fr/publication/2024ISAL0014/these.pdf
© [F. Steinhilber], [2024], INSA Lyon, tous droits réservés

Cette thèse est accessible à l'adresse : https://theses.insa-lyon.fr/publication/2024ISAL0014/these.pdf
© [F. Steinhilber], [2024], INSA Lyon, tous droits réservés

Chapter 4

Fatigue properties and crack initiation mechanisms of as-built and post-treated specimens

Contents

4.1 Fatigue properties and crack initiation mechanisms for as-built specimens 104
4.1.1 Protocol for fatigue tests . . . 104
4.1.2 Results of fatigue tests . . . 104
4.1.3 Killer defects identification: the need for a 3D characterization . . . 111
4.2 Alpha-case formation and surface embrittlement induced by heat treatments . . . 120
4.2.1 Alpha-case formation . . . 120
4.2.2 Impact on tensile properties . . . 120
4.2.3 Impact on fatigue properties . . . 123
4.3 Improvement of fatigue properties by Plasma electrolytic Polishing (PeP) 131
4.3.1 Principle of PeP surface treatment . . . 131
4.3.2 Conditions of PeP treatments applied to fatigue specimens . . . 133
4.3.3 Roughness of specimens polished by PeP . . . 138
4.3.4 Fatigue resistance improvement and change in crack initiation mechanism . 146
Intermediate summary . . . 152

Cette thèse est accessible à l'adresse : https://theses.insa-lyon.fr/publication/2024ISAL0014/these.pdf
© [F. Steinhilber], [2024], INSA Lyon, tous droits réservés

4.1 Fatigue properties and crack initiation mechanisms for as-built specimens

4.1.1 Protocol for fatigue tests

Fatigue tests were performed under laboratory conditions (room temperature and pressure) using servo-hydraulic machines equipped with 100 kN load cells. These tests were carried out at constant stress amplitude using a sinusoidal waveform and at a frequency f of 10 Hz. The stress ratio was set at $R = 0.1$. Tests that exhibited no failure after 10^7 cycles were stopped and categorized as *run-outs*.

Specimens were first tested with their as-built surfaces. A stress-relief heat treatment of 2 h at 720 °C was applied to these specimens, ensuring they were free of residual stresses. In this condition, 22 Z and 18 45° specimens underwent testing. Among these, 10 Z and 10 45° specimens were XCT scanned both before and after failure for in-depth analysis.

The stress levels were calculated based on a theoretical section of $S = \pi\frac{(3\,\mathrm{mm})^2}{4} \approx 7.07\,\mathrm{mm}^2$. Yet, minor geometrical deviations from the CAD definition meant that the effective specimen gauge diameter was slightly reduced. Thus, the mean section of the gauge area for all XCT scanned specimens was determined, and the average and standard deviation were calculated for each build orientation. The obtained values are $6.91 \pm 0.07\,\mathrm{mm}^2$ for Z specimens and $6.99 \pm 0.32\,\mathrm{mm}^2$ for 45° specimens. They were used for correcting stress levels in Wöhler curves. However, for the sake of simplicity, the same rounded theoretical stress levels − i.e. those obtained using the theoretical section − will be used in the discussions for both Z and 45° specimens.

In addition to as-built specimens, four machined and manually polished (M&P) vertical specimens were tested as a reference. These specimens were initially machined from rectangular bars through turning and then manually polished with SiC P1200 paper. Thus, they were free of both the as-built surface roughness and the high concentration of subsurface pores highlighted in Section 3.4.2. Following their preparation, a supplementary stress-relief heat treatment of 2 h at 660 °C was performed. This ensured the elimination of any residual stresses potentially arising from machining and polishing while keeping the microstructure almost unchanged.

4.1.2 Results of fatigue tests

The Wöhler curves obtained for the different conditions are shown in Fig.4.1. These curves will be analyzed in light of fracture surface observations and previous defect characterizations.

Wöhler curves indicate that **fatigue strengths of as-built specimens are consistent with those found in the literature**. See Tab.1.1 presented in the state of the art for a comparison. For both Z and 45° specimens, the fatigue strength at 10^7 cycles is estimated to be around 250 MPa.

Cette thèse est accessible à l'adresse : https://theses.insa-lyon.fr/publication/2024ISAL0014/these.pdf
© [F. Steinhilber], [2024], INSA Lyon, tous droits réservés

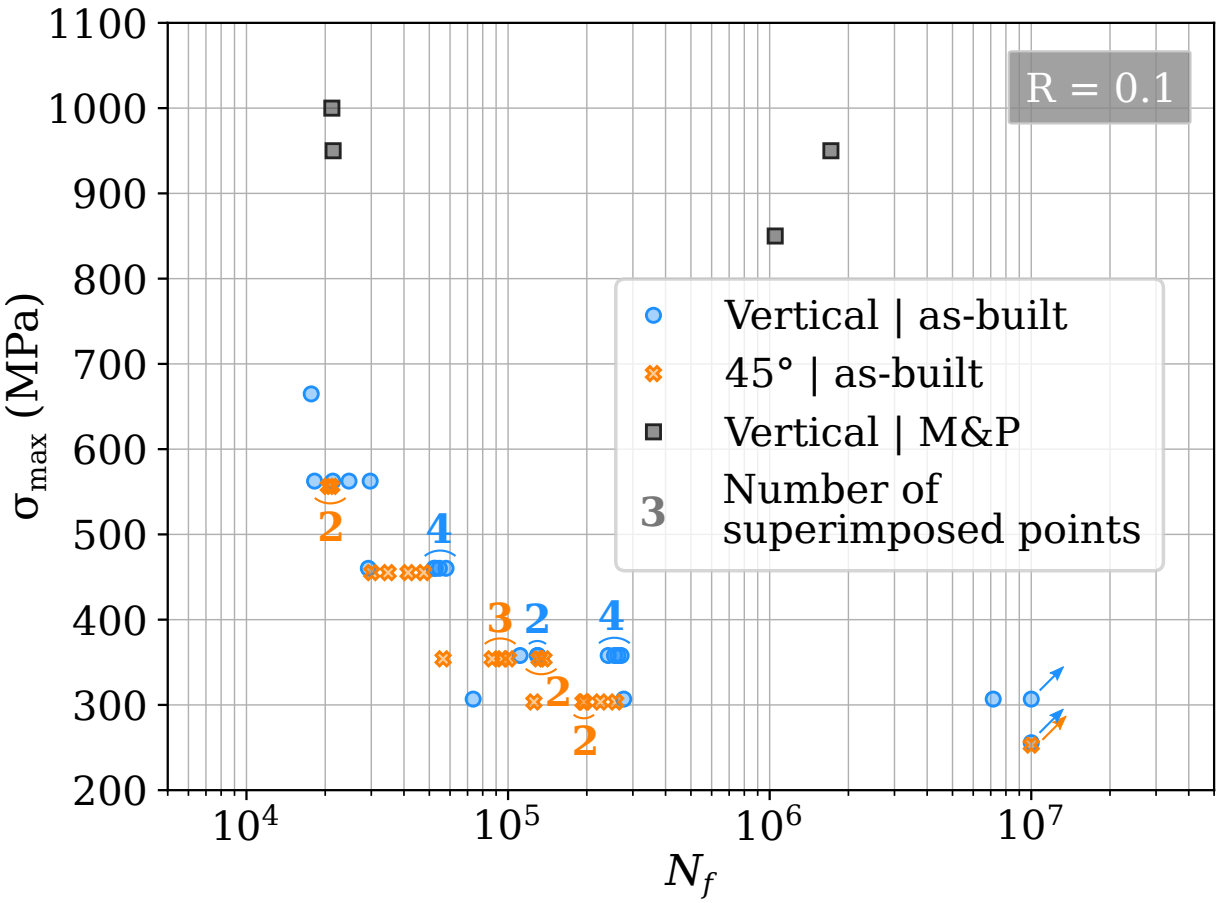

Figure 4.1 | **Wöhler curves of as-built specimens.** M&P specimens are also represented as a reference. They were submitted to a stress-relief treatment (2 h at 660 °C) after machining and polishing. Fatigue tests are performed at $R = 0.1$.

Fig.4.2a-b show fracture surfaces for as-built Z and 45° specimens. The relatively flat region in the upper parts of Fig.4.2a-b show unambiguously that in both cases, cracks initiated from the surface. More generally, it has been observed that **crack initiation always occurred at the surface for as-built specimens**. It is worth noting that no single defect can be identified in Fig.4.2a-b, and that crack initiation seems to have occurred in vast zones. This does not necessarily mean that multiple cracks initiated at different locations since this usually leads to the formation of more ridges than what can be seen in Fig.4.2a-b. The mechanism behind this particular fracture surface morphology is discussed in Section 4.1.3.2.

Fig.4.1 shows that **M&P specimens exhibit significantly higher fatigue strength than as-built specimens**. Despite the low number of tested specimens, fatigue strength at 10^6 cycles of M&P specimens can be estimated at about 850 MPa. By looking at M&P fracture surfaces in Fig.4.3a-b, this huge difference can be explained by a change in the crack initiation mechanism. Indeed, all crack initiations occurred on an internal pore in the case of M&P specimens. The pore was deep inside the material (< 290 µm below the surface) in 3 cases over 4, whereas it was directly beneath the surface in one case. Fig.4.2a-b show two surface crack initiations on as-built specimens and Fig.4.3a-b show two crack initiations on bulk pores of different sizes in polished ones.

Cette thèse est accessible à l'adresse : https://theses.insa-lyon.fr/publication/2024ISAL0014/these.pdf
© [F. Steinhilber], [2024], INSA Lyon, tous droits réservés

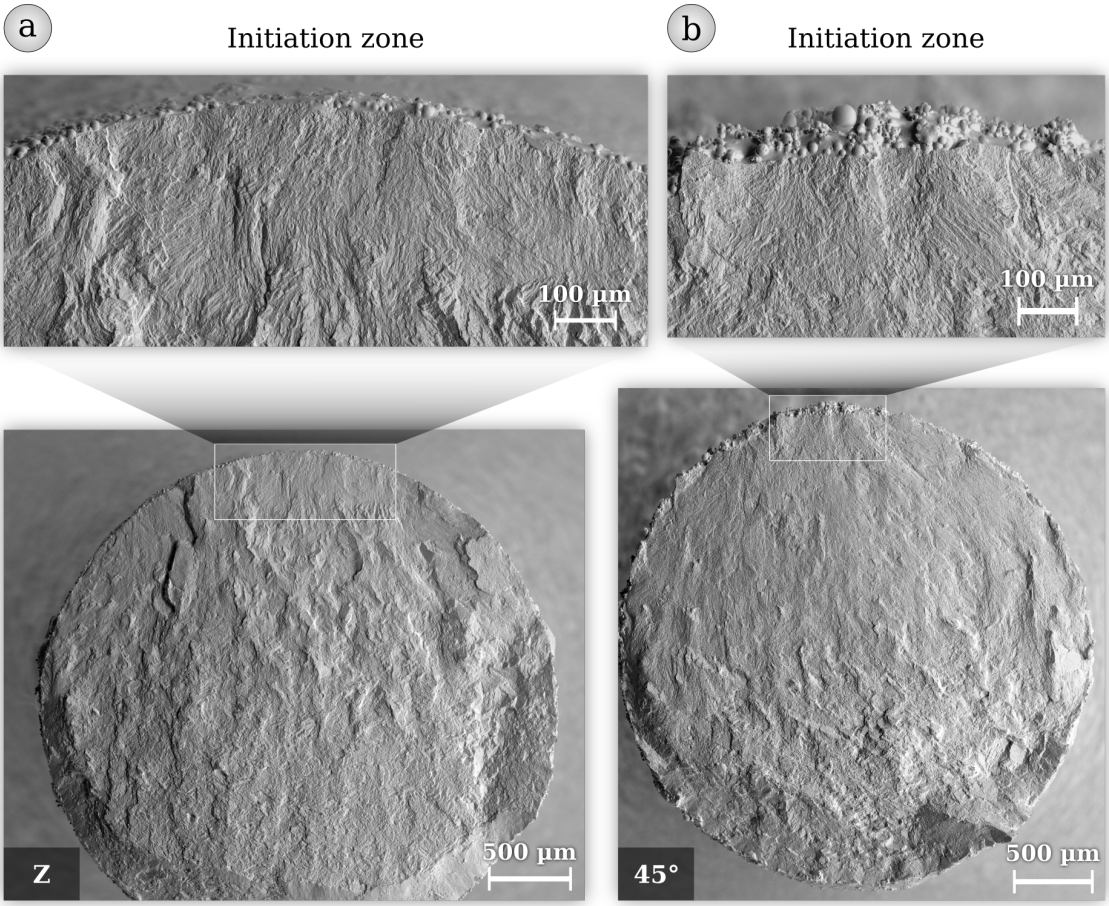

Figure 4.2 | SEM-BSE topographical mode observations showing crack initiation at as-built specimens surface. (a) Fracture surface of a Z specimen tested at 300 MPa and that failed after 73 547 cycles cycles. (b) Fracture surface of a 45° specimen tested at 300 MPa and that failed after 193 381 cycles.

These results confirm that in our case and as it was reported several times in the literature, **surface defects of as-built samples are much more critical than internal pores**. Only when surface defects are removed by machining/polishing, do pores become potential crack initiation sites. Note that for as-built specimens, the high density of sub-surface pores described in Section 3.4.2 seem to have negligible impact on the fatigue resistance compared to surface defects.

Concerning the M&P specimens, it is also interesting to note that their fatigue strength seems to be in the upper range of what can be found in the literature for L-PBF Ti64 (see again Tab.1.1 in the state of the art for details). This can be primarily attributed to the good bulk material integrity, which, as shown in Section 3.4.2, contains only a few pores of limited size and rather high sphericity. This can be confirmed by the fracture surfaces in Fig.4.3a-b of both polished specimens that were tested at 950 MPa. In those two cases, crack initiation was caused by small rounded pores. This is especially true in Fig.4.3b, where the killer defect is a perfectly spherical pore of only 11 µm.

Cette thèse est accessible à l'adresse : https://theses.insa-lyon.fr/publication/2024ISAL0014/these.pdf
© [F. Steinhilber], [2024], INSA Lyon, tous droits réservés

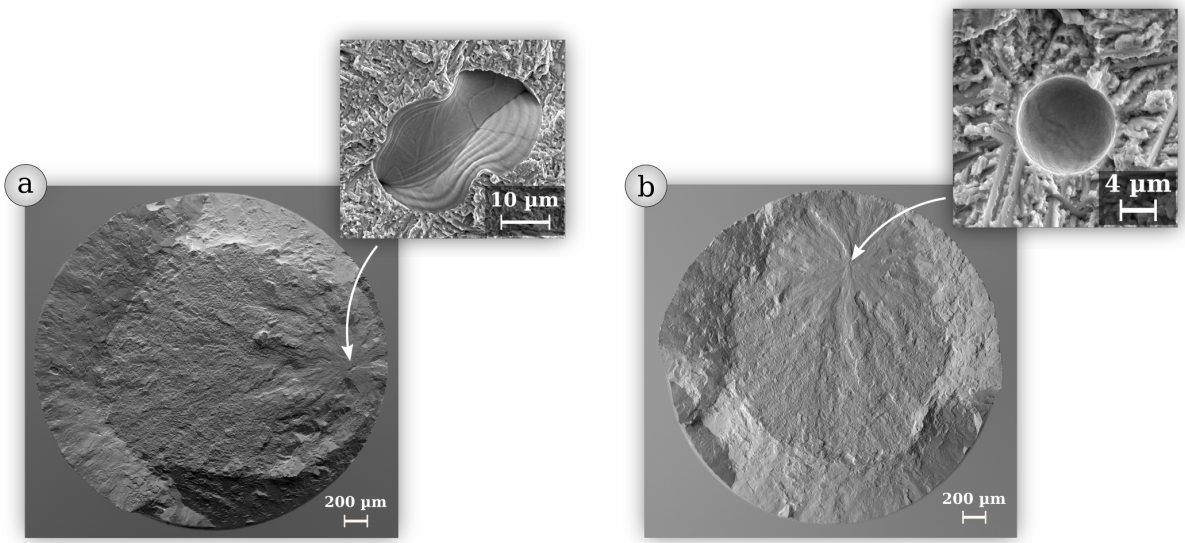

N_f = 24 441 (950 MPa) N_f = 1 714 472 (950 MPa)

Figure 4.3 | SEM observations of two polished specimens fracture surfaces showing crack initiation at small rounded pores. Large views are obtained in BSE topographical mode, whereas higher resolution images are obtained in SE mode.

The good properties of polished specimens still need to be qualified because of the reduced number of specimens and the large scatter observed. The two specimens tested at 950 MPa reach for instance very different fatigue lives: one breaks at 21 441 cycles while the other lasts almost 100 times longer (1 714 472 cycles). This can be attributed to significant differences between the defect populations of both specimens. Thus, the equivalent diameter can be estimated to be 52 µm in Fig.4.3a, much larger than the 11 µm found in Fig.4.3b. Furthermore, the pore in Fig.4.3a is much less spherical than the one in Fig.4.3b. A Hot Isostatic Pressing treatment (HIP) could in this case be relevant to remove porosity and therefore achieve more reproducible fatigue properties.

However, a HIP treatment would significantly affect the microstructure. This could have adverse effects, since the fine microstructure obtained after low-temperature heat treatment (2 h at 720 °C) could also contribute to the good observed properties. However, it seems difficult to draw a conclusion on this question since contradictory studies exist to explain which microstructure should be the most efficient regarding fatigue properties [POL 14]. The lamellar microstructure obtained with L-PBF could be rather advantageous regarding crack propagation, as cracks could tend to deviate from their trajectory during propagation to follow α-laths interfaces [GAL 17]. All these bifurcations imply that more energy is needed to propagate cracks. This hypothesis is coherent with the high density of micro-cracks found in the propagation zone of the fracture surface and which most likely follow α-laths interfaces, see e.g. Fig.4.4. Some studies even state that finer α-laths will result in better fatigue strength [LIU 19, LIU 17]. As a reminder, the α-laths width in the present study is particularly small ($\approx$ 0.5 µm, see [GAI 23b]). However, other studies suggest conversely that better fatigue strengths can be reached with coarser laths [GAL 17, WAN 23] and further work would thus be needed to clarify the matter.

Cette thèse est accessible à l'adresse : https://theses.insa-lyon.fr/publication/2024ISAL0014/these.pdf
© [F. Steinhilber], [2024], INSA Lyon, tous droits réservés

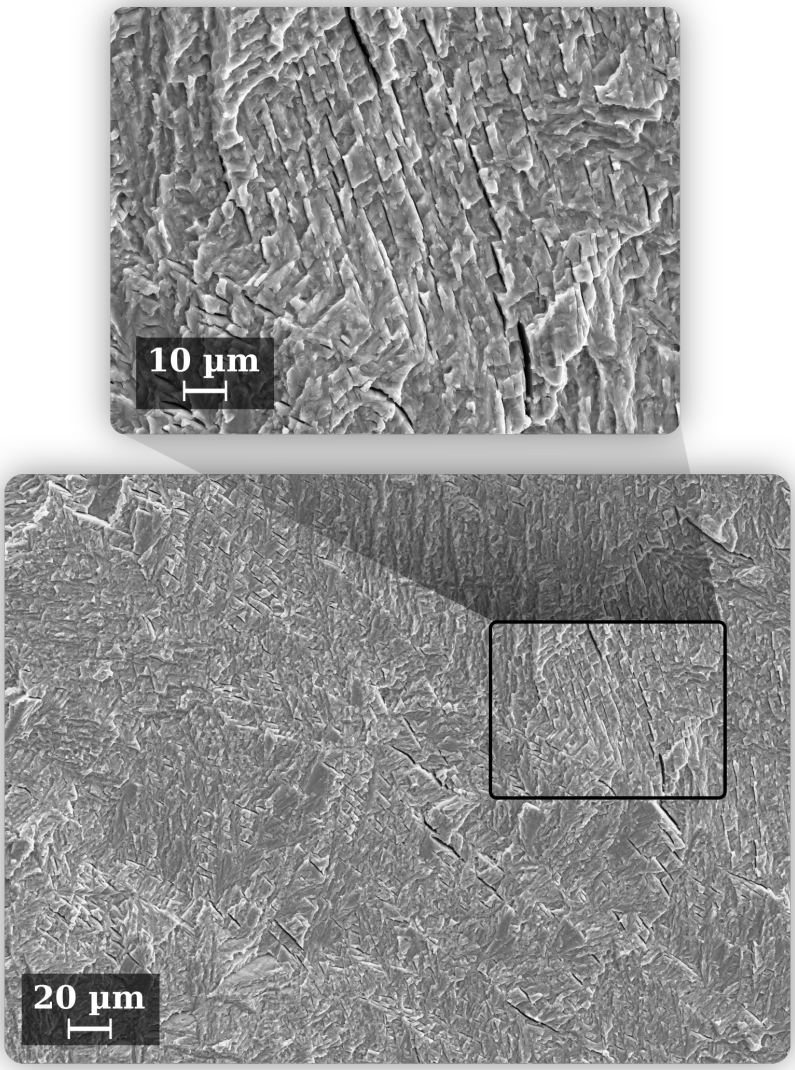

Figure 4.4 | Crack bifurcations visible on the propagation zone of a fracture surface. The specimen is a vertical one, tested at 350 MPa and which failed after 241 406 cycles. Observations are made using an SEM in SE mode.

Regarding 45° specimens, it is interesting to note that **all crack initiations occurred in the down-skin region**, as has already been found in the literature [PEG 18]. Again, this is coherent with roughness measurements in Section 3.4.3.2 showing that the down-skin region is much rougher than the up-skin one. This probably explains why, as can be noticed in Fig.4.1, the fatigue life of the 45° specimens is on average slightly lower than that of the Z specimens, especially at lower stresses. For instance, at 350 MPa, median cycles to failure for Z and 45° specimens are 255 152 cycles and 97 800 cycles, respectively. Nevertheless, the distinction between Z and 45° orientations is minimal compared to the larger difference between as-built and M&P specimens.

Cette thèse est accessible à l'adresse : https://theses.insa-lyon.fr/publication/2024ISAL0014/these.pdf
© [F. Steinhilber], [2024], INSA Lyon, tous droits réservés

Looking in more detail into the position of initiation sites in 45° specimens, it can be noticed that failure occurred most frequently in the lower section, closer to the build plate during fabrication (see Fig.4.5a). This observation is not reflected in Z specimens. Fig.4.5b highlights this trend, plotting the initiation sites position along the specimen axis in 10 Z and 10 45° specimens. A position of 0 means that the initiation site is located in the middle of the gauge length.

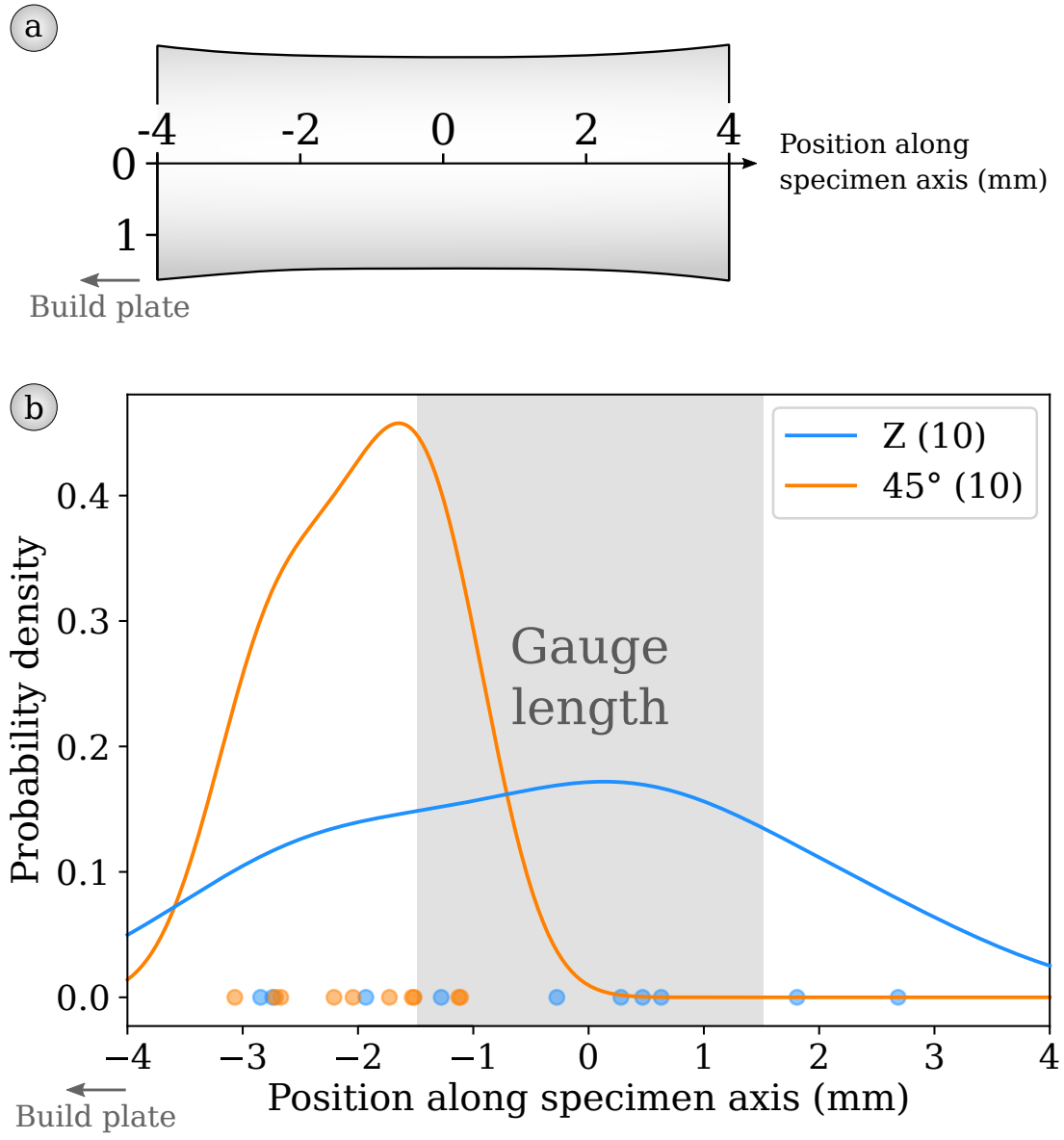

Figure 4.5 | Initiation sites positions along specimen axis for Z and 45° specimens. Each point corresponds to a specimen. 10 Z and 10 45° were used for this study. For each specimen, the initiation site has been identified on the corresponding XCT scan following the methodology described in Section 4.1.3. The position of the initiation site was then estimated. A position of 0 means that the initiation site is located in the middle of the gauge length. Probability density curves were computed by kernel density estimation.

Cette thèse est accessible à l'adresse : https://theses.insa-lyon.fr/publication/2024ISAL0014/these.pdf
© [F. Steinhilber], [2024], INSA Lyon, tous droits réservés

Calculations were done to determine if the preferential crack initiation in lower sections of 45° can be explained by roughness inhomogeneity. More precisely, roughness parameter profiles were computed along the specimens' axis. To do so, for a given specimen and for 50 evenly spaced positions along its axis, points within a 1 mm high transverse segment were selected (see Fig.4.6a). Then, S_a and S_v roughness parameters were calculated using the local height measurements performed at these points from XCT data using a cutoff $\lambda_c = 0.8\,\text{mm}$.

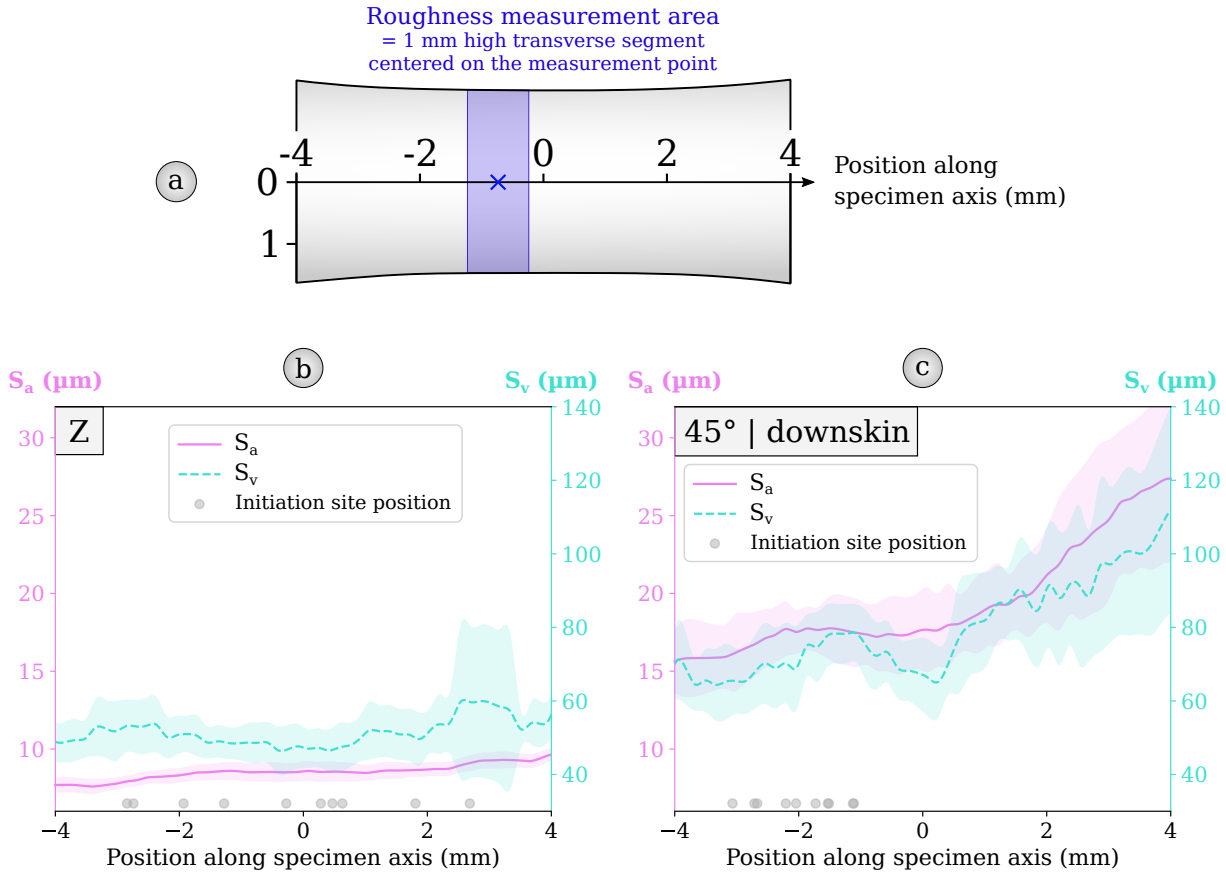

Figure 4.6 | Roughness profiles along specimens' axis. (a) Scheme showing the area used to measure roughness parameters at each position along a specimen axis. (b) S_a and S_v profiles for Z specimens. (b) S_a and S_v profiles for down-skin regions of 45° specimens. In (b) and (c), gray points indicate the position of initiation sites. Roughness parameters were measured using only specimens where the initiation site has been identified (10 Z and 10 45° specimens). Curves represent the average roughness profile (among specimens of the same build orientation) whereas shaded areas correspond to a distance of one standard deviation from the average curves.

Refer to Fig.4.6b for roughness parameters profile visuals for Z specimens, and Fig.4.6c for those of 45° specimens. Due to the consistent failure in the down-skin region of 45° specimens, only points from this region were used in roughness computations. For a clearer definition of this down-skin region, see Fig.3.23.

As can be seen in Fig.4.6b, S_a and S_v roughness parameters show only little variations along the specimen axis of Z specimens. This is consistent with the uniform distribution of initiation sites marked by gray spots.

Cette thèse est accessible à l'adresse : https://theses.insa-lyon.fr/publication/2024ISAL0014/these.pdf
© [F. Steinhilber], [2024], INSA Lyon, tous droits réservés

Conversely, Fig.4.6c reveals an upward trend in both S_a and S_v values along the axis in the down-skin region of 45° specimens. This is probably due to the fact that because of the presence of the fillet radius, the upper part of 45° specimens is nearly horizontal during manufacturing. Conversely, lower parts are near vertical, which leads to smoother surfaces.

Surprisingly, **initiation sites predominantly cluster in lower parts of 45° specimens, i.e. where S_a and S_v values are lowest**. This tends to indicate that surface roughness might not be the sole determinant of initiation site position. Another influencing factor might for instance be the presence of support structures under the upper sections of 45° specimens during manufacturing (see Fig.3.5 for an image of support structures). Lower parts of the specimens where failure occurs did not require the use of support structures and were therefore built directly on the powder bed. Such factors might lead to a slightly different microstructure (due to differences in thermal history) or minor geometric shifts (due to residual stresses), potentially influencing fatigue crack initiation.

In any case, these results indicate that **roughness parameters (or at least the simple S_a and S_v parameters) are not necessarily reliable indicators for the fatigue performance of L-PBF as-built specimens**.

4.1.3 Killer defects identification: the need for a 3D characterization

Fracture surfaces like the one in Fig.4.2a-b demonstrate that crack initiates from the surface on as-built specimens. However, no defect could be identified and therefore the question remains: which precise defects are responsible for failure?

4.1.3.1 The only defects identifiable using SEM: spatters

Actually, SEM observations enabled the identification of the killer defect in only two specimens in total, one for each build orientation. In both cases, the crack initiated from a large particle that is considered to be a spatter, see Fig.4.7a-d.

Both fracture surfaces are still relatively different and it is interesting to note that in Fig.4.7b, the crack did not seem to initiate from the spatter only. River lines that emanate from the surface suggest indeed that the crack could have initiated from a more extended defect, similar to what can be seen in Fig.4.2a-b. Hence, SEM provides limited clarity on the exact defect causing the failure.

For all other specimens, SEM observations are even less informative, see e.g. Fig.4.2a-b. The crack seems in this case to have started from an extended circular segment rather than from one specific point. With no distinct defect identifiable, **a new strategy is essential for identification**. Incidentally, this also means that it probably is not possible here to quantify defects' severity using the conventional $\sqrt{area}$ parameter. It seems for instance impossible in Fig.4.2a and hazardous in Fig.4.2b. A different approach will therefore be tempted in Chapter 5.

Cette thèse est accessible à l'adresse : https://theses.insa-lyon.fr/publication/2024ISAL0014/these.pdf
© [F. Steinhilber], [2024], INSA Lyon, tous droits réservés

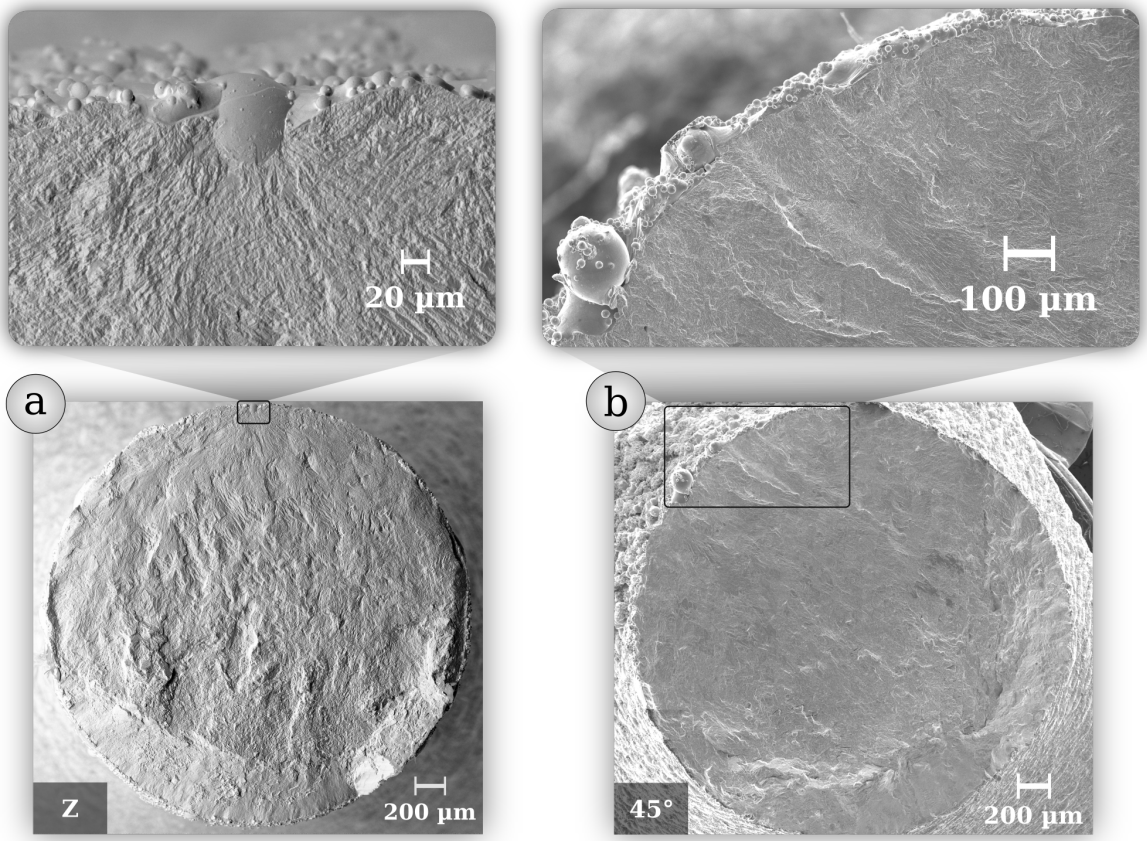

Figure 4.7 | SEM fracture surface observations showing crack initiation from a spatter. (a) Observation of a Z specimen in BSE topological mode. The specimen was tested at 300 MPa and failed after 7 154 298 cycles. (b) Observation of a 45° specimen in SE mode. The specimen was tested at 300 MPa and failed after 125 534 cycles.

4.1.3.2 A 3D workflow for a more extensive initiation site identification

To go further in the initiation site identification, XCT was used to get a broader 3D point of view. To this end, 10 Z and 10 45° fatigue specimens were scanned before and after failure. The workflow for initiation site identification is described in Fig.4.8a-d. The specimen taken as an example is the one that is shown in Fig.4.7b. This allows to check whether river lines emerging from the surface away from the spatter could indicate crack initiation from another defect.

Cette thèse est accessible à l'adresse : https://theses.insa-lyon.fr/publication/2024ISAL0014/these.pdf
© [F. Steinhilber], [2024], INSA Lyon, tous droits réservés

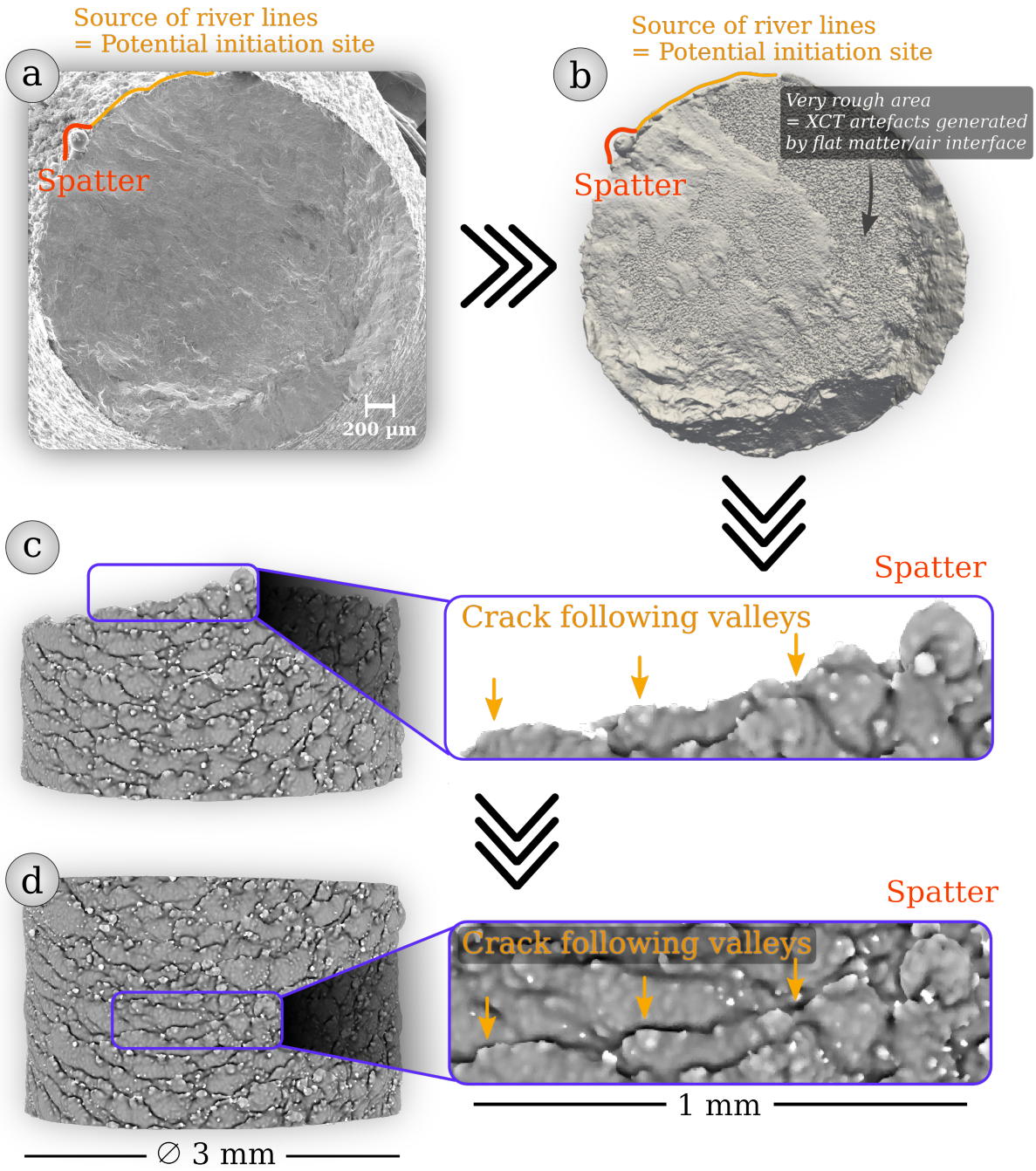

Figure 4.8 | Workflow for crack initiation site identification using both SEM and XCT scans (before and after failure). The specimen used as an example was built at 45° and failed after 125 534 cycles at 300 MPa. (a) SEM-SE fracture surface observation. (b) Surface mesh of the fracture surface obtained from XCT scan. (c) Crack initiation site observed on the fracture surface from the side of the specimen. Gray levels correspond to κ_{min}, estimated using $r_{curv} = 20\,\mu m$. (d) Same area as in (c), trace backed on initial XCT scan before failure.

Cette thèse est accessible à l'adresse : https://theses.insa-lyon.fr/publication/2024ISAL0014/these.pdf
© [F. Steinhilber], [2024], INSA Lyon, tous droits réservés

The fracture surface is first observed by SEM due to its superior resolution, see Fig.4.8a. Even using SEM, initiation site identification can be complex in some cases since initiation was not caused by a clearly delineated defect. To help the identification in such cases, SEM-BSE topographical mode (instead of the conventional SEM-SE mode) was sometimes found very useful. It can help better visualize river marks and trace back the initiation sites at their origin more easily. An example of a BSE topographical image can be seen in Fig.4.7a. In the particular case of Fig.4.8a, only the SEM-SE observation is shown since it is enough to identify both the spatter and the river lines that emerge from the surface a little further.

Once the initiation site is identified on the SEM image, the same fracture surface is observed in 3D using XCT. For this purpose, the surface is extracted from the XCT scan containing the fracture surface. The mesh extracted from the XCT scan using the conventional marching cubes algorithm is for instance shown in Fig.4.8b. By comparing Fig.4.8a and Fig.4.8b, the initiation site is identified on the XCT fracture surface.

Finally, the initial XCT scan before the fatigue test is compared to the XCT fracture surface to identify what surface feature caused crack initiation. This could be done using mesh representations of surfaces before and after failure. But while mesh representations give a good perception of volume, they might not always effectively render the most relevant surface features. On the opposite, it has been shown in Section 2.2.3 that the minimum curvature greatly highlights surface valleys, which, as will be shown, are the surface features of primary interest. Therefore, for the killer defect identification surfaces were rather visualized by using a point cloud of the surface colored using a minimum curvature measurement, see Fig.4.8c-d.

The spatter that was previously seen on the SEM observation can be seen in Fig.4.8b-d obtained from XCT data as well. **The crack path seems to follow a surface valley over a long distance, despite the fact that this valley is not aligned on a horizontal plane.** This is highlighted by the magnifying windows of Fig.4.8c-d. It is precisely the same area that was identified previously as a potential initiation site. Although such a valley can be identified in the 3D representation (especially when they are underlined by the 3D rendering of curvature), it cannot be identified using SEM only, see Fig.4.8a. This **confirms the relevance of such a 3D characterization method for crack initiation site identification** on L-PBF as-built surfaces.

The precise alignment of the crack with valleys indicates their contribution to fatigue failure. Parallel river lines in SEM images, rather than emerging solely from the spatter, suggest crack propagation from the entire area, including the spatter and valleys. Two scenarios could be considered:

1. Valleys and the spatter both served as crack initiation points, leading to simultaneous crack initiation over a vast perimeter. Although the valleys may appear to be less pronounced defects than the spatter, their extent could allow many cracks to initiate along the surface before coalescing, causing rapid damage and short fatigue life, as reported by [PEG 18] in L-PBF Ti64.

2. The crack primarily began at the spatter, but valleys accelerated subsequent crack propagation due to the generated stress concentration.

Cette thèse est accessible à l'adresse : https://theses.insa-lyon.fr/publication/2024ISAL0014/these.pdf
© [F. Steinhilber], [2024], INSA Lyon, tous droits réservés

To confirm these theories, advanced techniques, like in-situ crack propagation in synchrotron XCT, would have been necessary. As of now, no definitive answer can be provided.

Nonetheless, the 3D initiation site characterization in Fig.4.8a-d offers valuable insights. Fig.4.9a magnifies an area where a small detail emerges: a profound, narrow pit-like defect likely present before fatigue cycling. This defect seemingly led to a crack that merged with the primary one, implying it might have contributed to crack initiation.

Conventional pre-failure surface characterization (e.g. using a profilometer or an interferometer) could easily overlook such defects. The XCT characterization, however, accounts for them. As can be seen in Fig.4.9e, the valley located behind the spherical spatter is indeed clearly visible. Furthermore, Fig.4.9d-e show the pit-like defect is visible as well. To see it, one has to look to the surface *from the inside*, i.e. as if one would stand in the core of the material. This point of view is made possible by the XCT characterization and surface extraction. This showcases the capability of 3D XCT in delving deeper into crack initiation mechanisms, especially in potentially uncovering obscured features commonly found in as-built surfaces.

Using the presented workflow, initiation sites were identified for 10 Z and 10 45° specimens. Apart from the two crack initiations caused by spatters — i.e. **in most cases, failure was caused by surface valleys**.

While both build orientations exhibited valleys, their morphologies varied. The morphology of valleys in the 45° specimens is showcased in Fig.4.8d. The focus here, and in subsequent discussions, is on valleys in the down-skin area, as failures in all specimens occurred in this region. Compared to Z specimens, these valleys appear deeper and more irregular.

The Z specimens' valleys, illustrated earlier in Fig.3.19, are generally shallower, horizontal, and regular unless interrupted by prominent protrusions. Fig.4.10a-d depicts the identification of a plate-pile valley as the crack initiation site on a Z specimen. It can be noted that for the specimen chosen as an example, two initiation sites can be identified. This is a frequently encountered case for both Z and 45° specimens, especially at high stresses.

Cette thèse est accessible à l'adresse : https://theses.insa-lyon.fr/publication/2024ISAL0014/these.pdf
© [F. Steinhilber], [2024], INSA Lyon, tous droits réservés

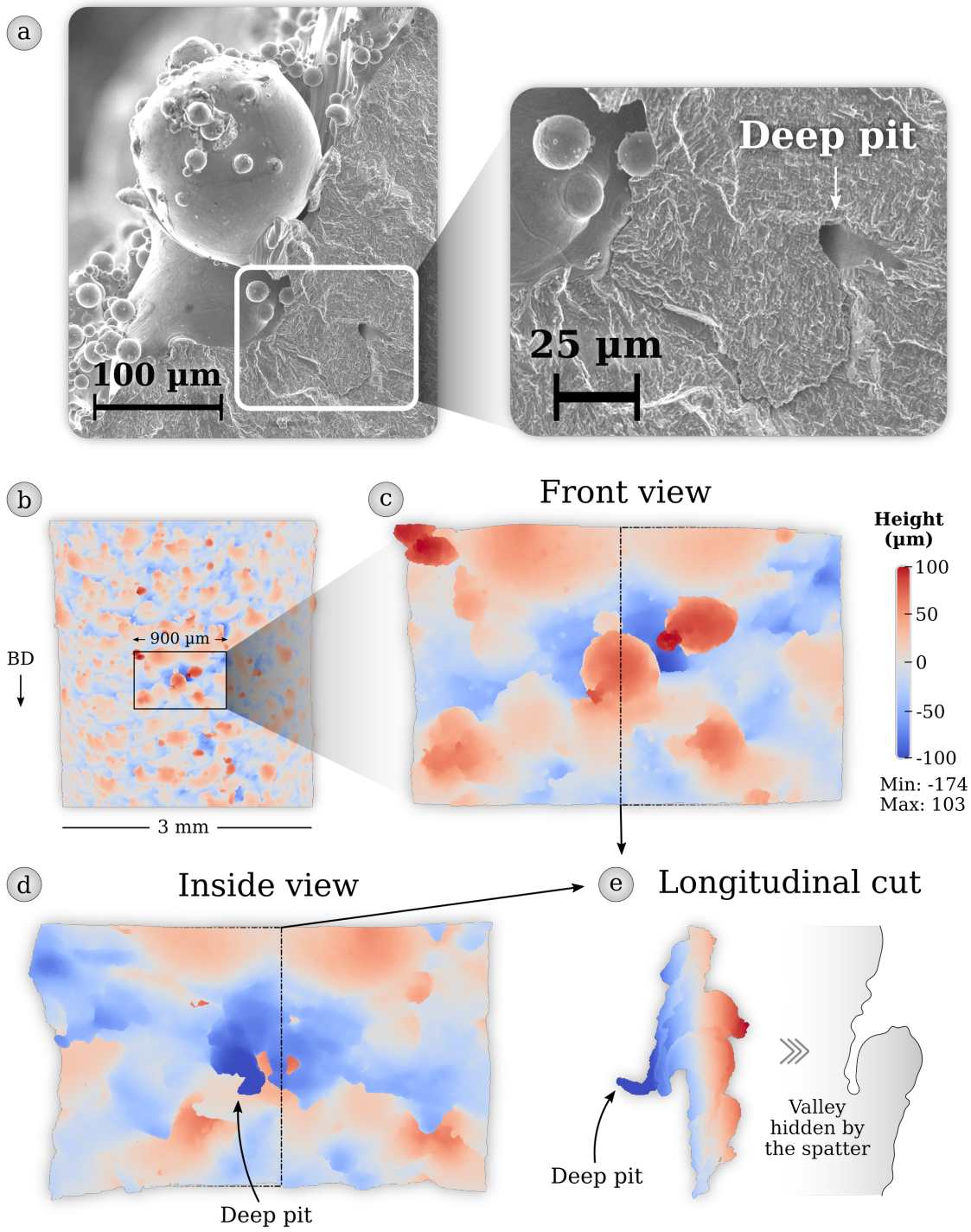

Figure 4.9 | Revealing of deep notches hidden by a spatter using the 3D XCT characterization. The sample characterized is the same 45° specimen as in Fig.4.8. (a) SEM-SE observation of the crack initiation zone, where a spatter can be identified. This spatter hides a deep valley and an even deeper and sharp pit-like defect. (b-e) 3D height maps showing (b) a global view, (c) a magnifying window centered on the initiation site, (d) the crack initiation area observed from the inside, revealing the presence of a deep pit-like defect and (e) a longitudinal cut showing the presence of a valley behind the spatter and the deep pit shown in (d).

Cette thèse est accessible à l'adresse : https://theses.insa-lyon.fr/publication/2024ISAL0014/these.pdf
© [F. Steinhilber], [2024], INSA Lyon, tous droits réservés

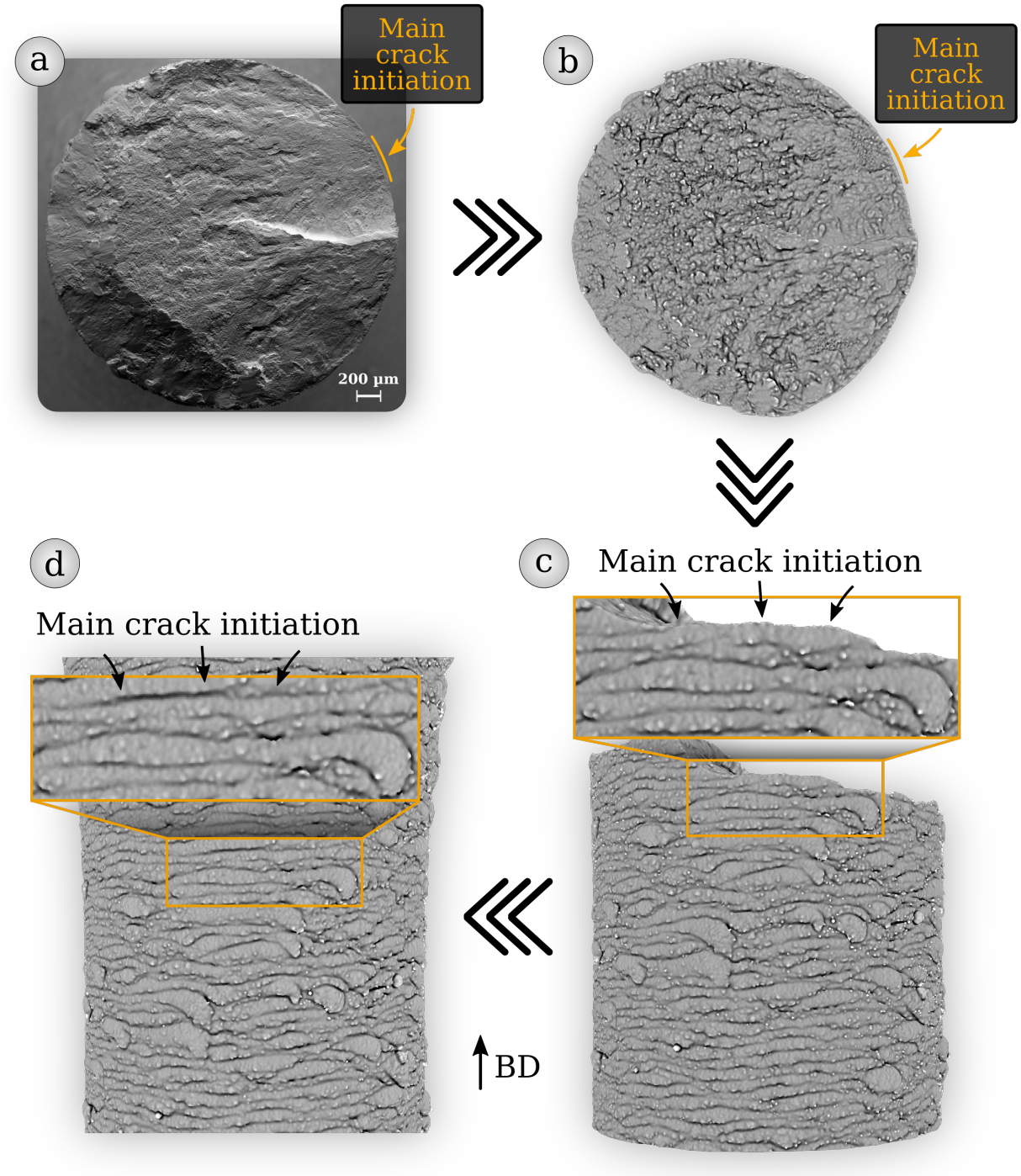

Figure 4.10 | Workflow for crack initiation site identification using both SEM and XCT scans (before and after failure). The specimen used as an example is a vertically built one which failed after 129 339 cycles at 350 MPa. (a) SEM-BSE (topographical mode) fracture surface observation. (b) Fracture surface obtained from XCT scan. Colors correspond to κ_{min} measurements performed using $r_{curv} = 20\,\mu m$ and $\lambda_S = 10$ voxel size. (c) Crack initiation site observed on the fracture surface from the side of the specimen. (d) Same area as in sub-figure c, identified on the initial XCT scan before fatigue failure. A valley is identified to be the cause of crack initiation by comparison with (c).

Cette thèse est accessible à l'adresse : https://theses.insa-lyon.fr/publication/2024ISAL0014/these.pdf
© [F. Steinhilber], [2024], INSA Lyon, tous droits réservés

Further analysis revealed more crack initiations in the specimen, not visible in Fig.4.10a-d. These cracks, termed *secondary cracks*, emerged in the specimen's lower section but did not result in failure. With the provided 3D characterization workflow, one can also identify these secondary cracks if their opening is large enough to be detected using XCT, as displayed in Fig.4.11a-c.

Fig.4.11a shows a view of the crack from the inside (in black), called *internal view*. Fig.4.11b shows the same area but from the outside. This is the "natural" point of view, which would for instance be possible using SEM. Secondary cracks are highlighted by white arrows. A comparison with the surface of the specimen before fatigue testing in Fig.4.11c highlights that **these cracks generally follow the surface valleys**, reinforcing the observations from the 45° specimen in Fig.4.8.

All these results obtained from as-built specimens show that **surface defects, and primarily surface valleys, control fatigue properties**. The impact of surface valleys can probably be explained by the so-called *notch effect*, which results in stress concentrations at valley roots. The extent of this notch effect is known to depend on mechanical properties such as ultimate tensile strength and/or ductility [SCH 09, Ch.7].

Titanium alloys are very sensitive to oxygen content, which has a strong impact on these properties [OGD 55]. Surface oxygen enrichment might happen during heat treatments such as the one used to relieve residual stresses after the L-PBF process. Thus, it may also affect the extent of the notch effect and its consequences on the fatigue properties. This issue is addressed in the following section.

Cette thèse est accessible à l'adresse : https://theses.insa-lyon.fr/publication/2024ISAL0014/these.pdf
© [F. Steinhilber], [2024], INSA Lyon, tous droits réservés

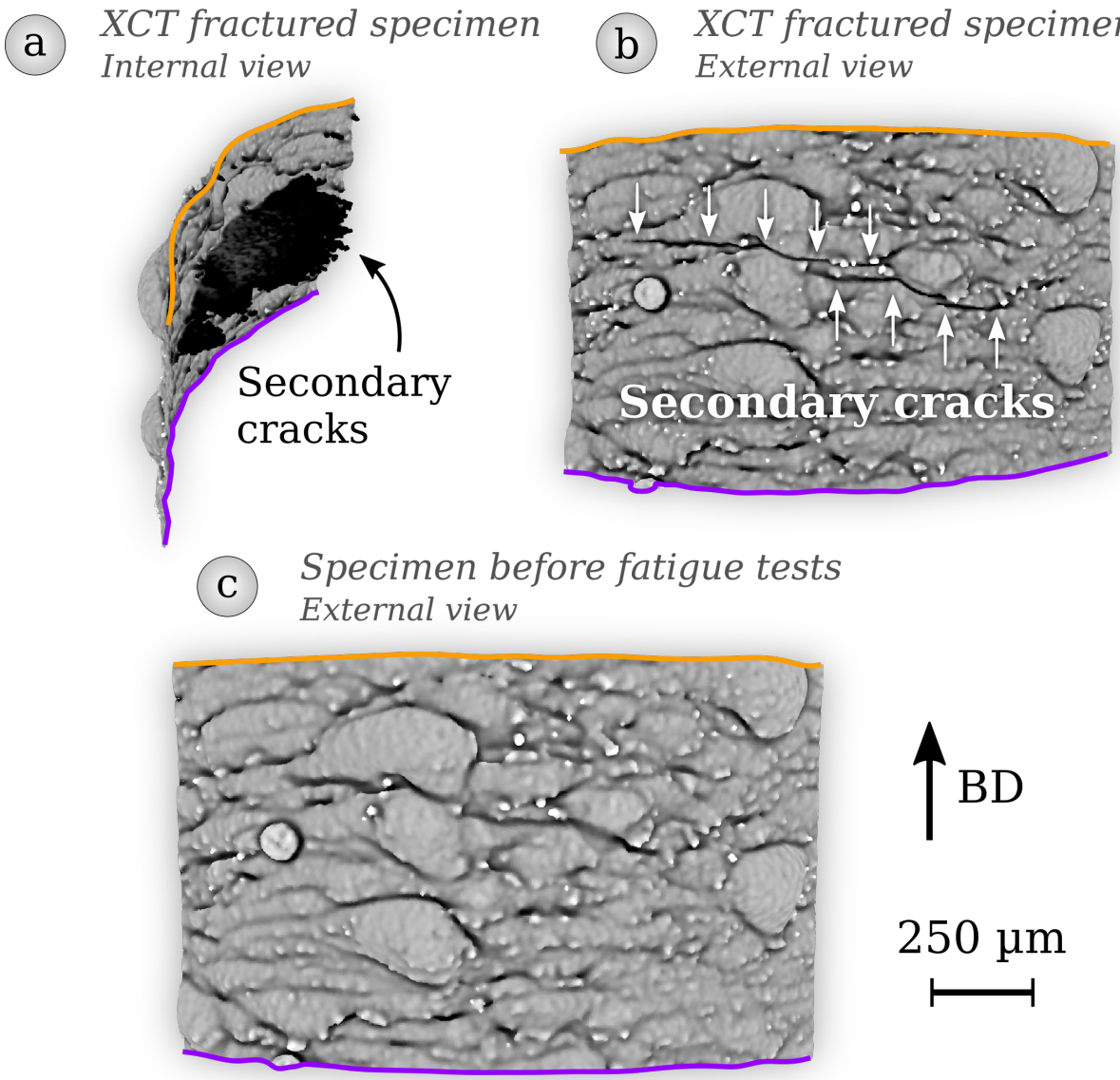

Figure 4.11 | Identification of a secondary crack — i.e. a crack that didn't propagate until failure — in a lower section of the fracture specimen. The fatigue specimen in question is the same as in Fig.4.10. Grey levels in all sub-figures correspond to a minimum curvature measurement. (a) Fractured specimen observed *from the inside* to reveal the partially propagated crack in black. This internal view is possible thanks to the fact that the surface was extracted from XCT data. (b) Fractured specimen observed from the outside, in the same area as in sub-figure a. The crack path is highlighted by white arrows. (c) Same area as in sub-figure b, but before fatigue testing. It can be seen that the secondary crack highlighted in (a) and (b) follows valleys that were initially present.

Cette thèse est accessible à l'adresse : https://theses.insa-lyon.fr/publication/2024ISAL0014/these.pdf
© [F. Steinhilber], [2024], INSA Lyon, tous droits réservés

4.2 Alpha-case formation and surface embrittlement induced by heat treatments

This section focuses on **the effects of the oxygen-enriched surface layer formed during heat treatment, commonly called α-case**, on fatigue properties[1]. First, the discussion will present the main findings obtained by Quentin Gaillard about α-case formation and its influence on tensile properties. For a more in-depth exploration, readers are directed to references [GAI 23b, GAI 23a]. Subsequently, findings from the joint research about its implications on fatigue properties will be presented. As for Section 3.2, the results obtained by Quentin Gaillard can be extended to the material studied in the present PhD work, since he used samples manufactured with the same L-PBF machine, process parameters and Ti64 powders. Industrial heat treatments were also performed by the same company (THERMI-GARONNE), and laboratory heat treatments were performed using the same furnace. In both cases, the same thermal cycles were used.

4.2.1 Alpha-case formation

Two types of heat treatments using different furnaces (an industrial and a laboratory furnace) have been studied by Quentin Gaillard during this PhD [GAI 23b, GAI 23a]. The industrial furnace could reach a nominal vacuum better than 10^{-4} mbar. Yet, instances of α-case formation were observed during the heat treatments in this furnace. Conversely, with the same thermal cycle, the laboratory furnace did not lead to any α-case formation. Such contrasts facilitated a comparative analysis to distinguish between the influences of microstructure changes and α-case emergence, both of which are tied to the selected heat treatment temperature.

Temperatures employed for heat treatments were: 720 °C, 800 °C, 860 °C, 920 °C, and 980 °C, each sustained for 2 h. Additionally, a reference condition was evaluated. It corresponds to samples that did not undergo any heat treatment after printing.

To gauge the depth of the α-case, polished sections of samples were chemically attacked using a Weck reagent, composed of ammonium bifluoride dissolved in ethanol and water. This procedure renders the α-case layer white on polished sections observed with optical microscopy, as illustrated for diverse heat treatments in Fig.4.12a.

No α-case can be seen before any heat treatment, but it can be seen after all heat treatments in the industrial furnace. Its depth ranges from 11 µm for the 720 °C heat treatment to 185 µm for the 980 °C heat treatment. Interestingly, even at the highest temperature of 980 °C, the laboratory furnace treatment did not yield any α-case formation.

4.2.2 Impact on tensile properties

Fig.4.13a-b show the evolution of the yield stress σ_y, the ultimate tensile strength σ_u and the elongation to failure ϵ_f after the different heat treatments.

The main observation that will be discussed here is the evolution of the elongation to failure in Fig.4.13b. It can be seen that it increases steadily as the heat treatment temperature increases when the heat treatment is performed in the laboratory furnace, without the formation of α-case.

[1] Collaborative study conducted with Quentin Gaillard, PhD student, and Amélie Larguier, final year student at INSA Lyon

Cette thèse est accessible à l'adresse : https://theses.insa-lyon.fr/publication/2024ISAL0014/these.pdf
© [F. Steinhilber], [2024], INSA Lyon, tous droits réservés

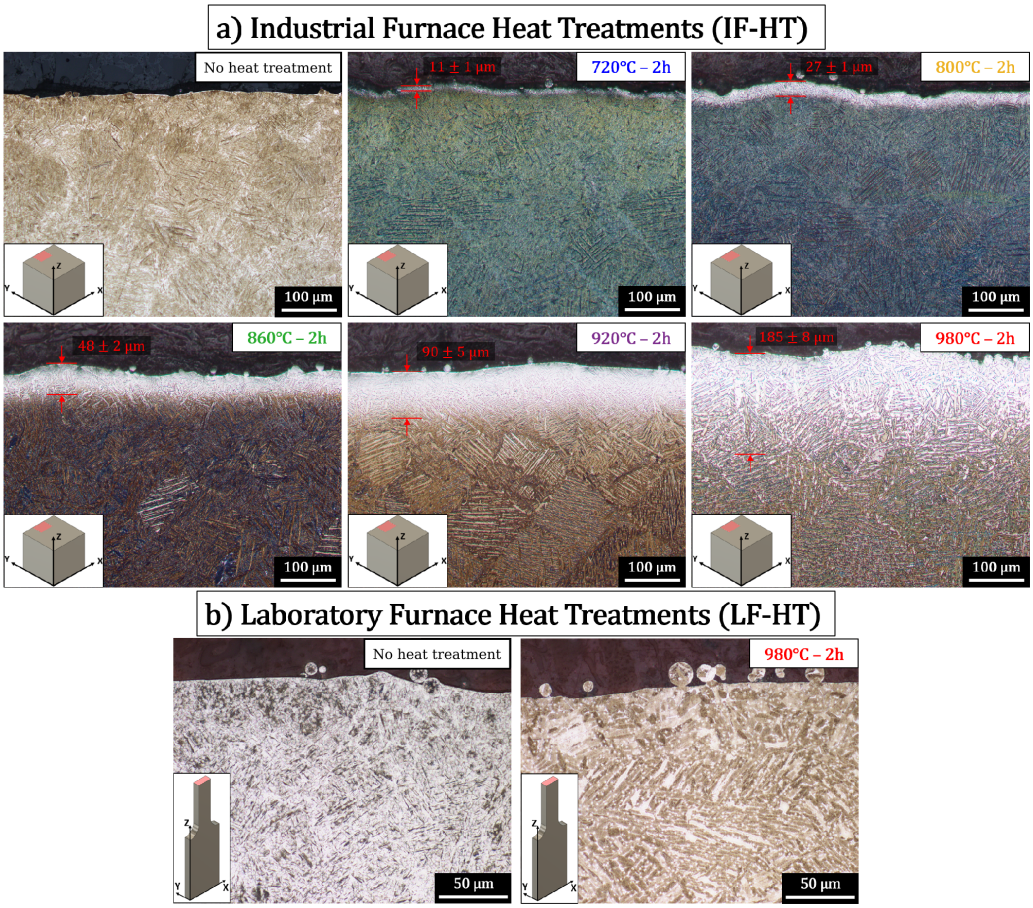

Figure 4.12 | Optical microscope micrographs revealing α-case for different heat treatment conditions , from [GAI 23b, Fig.19]. Micrographs were taken at the edge of cross-sections in the horizontal XY plane of (a) cubes before and after various heat treatments in the industrial furnace, and (b) half tensile specimens before and after heat treatments in the laboratory furnace. The etched material is obtained with a Weck reagent.

When performed in the industrial furnace, the heat treatment leads to comparable results for temperatures lower or equal to 800 °C. Yet, at 860 °C and beyond, there is a reduction in elongation to failure, contrasting with the previous increase. For instance, at 980 °C, the elongation to failure after the industrial treatment is measured at $4.0 \pm 0.8\%$, while a value of $18.7 \pm 0.7\%$ is obtained after the laboratory treatment. **This significant drop in elongation to failure stems from the growth of a pronounced α-case layer**, resulting in surface brittleness.

Evidence of this surface fragility is the profusion of cracks observable on the surfaces of tensile specimens post-failure, as illustrated in Fig.4.14a.

These cracks remain confined to the brittle α-case layer. They likely serve to release the tensile stresses, given the α-case layer's inability to accommodate deformation due to its limited ductility. **The propensity of α-case to initiate cracks prompts questions about its potential influence on fatigue damage**. Consequently, this led to further research into the effects of α-case on fatigue properties.

Cette thèse est accessible à l'adresse : https://theses.insa-lyon.fr/publication/2024ISAL0014/these.pdf
© [F. Steinhilber], [2024], INSA Lyon, tous droits réservés

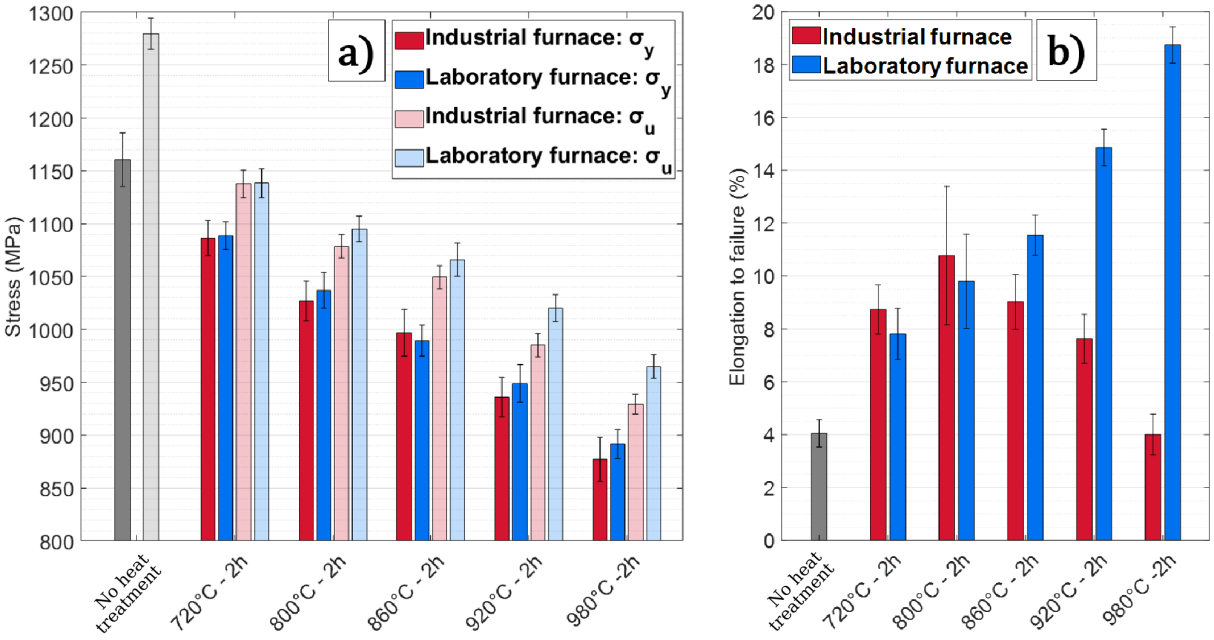

Figure 4.13 | Evolution of tensile properties of the vertically built samples in the as-built condition and subjected to various heat treatments in both the industrial and laboratory furnaces : (a) Yield stress σ_y and ultimate tensile strength σ_u, (b) Elongation to failure ϵ_f. Drawn from [GAI 23b, Fig.19]

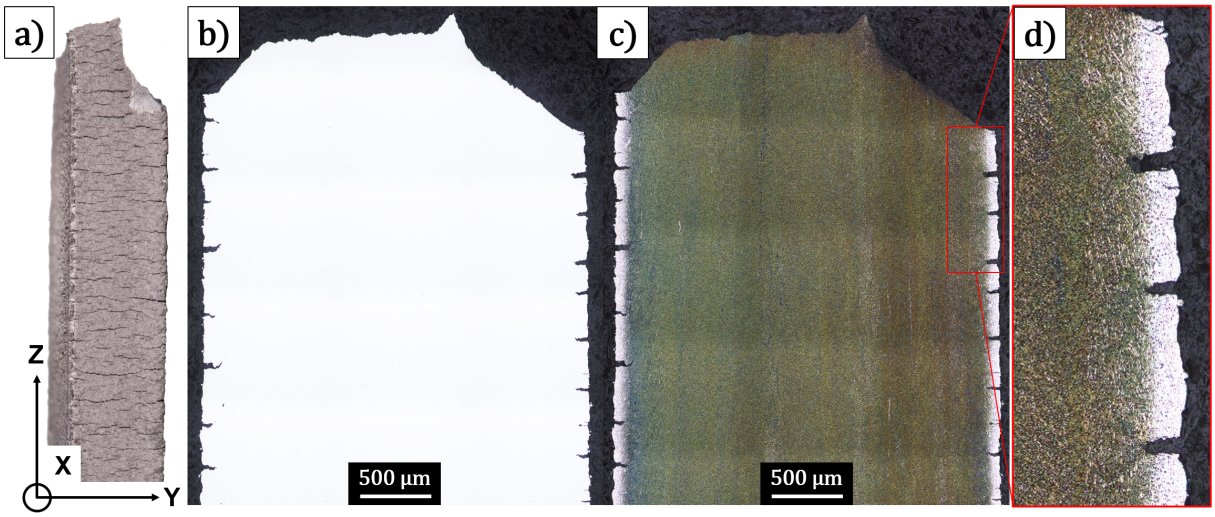

Figure 4.14 | Surface cracks formed in α-case layer during tensile testing. (a) Visualization of cracks on the surface of a broken flat tensile specimen subjected to the industrial heat treatment at 920 °C for 2 h. Visualization of cracks on a cross-section of the same specimen (b) before and (c) after a chemical attack with Weck reagent. (d) Visualization of blunt cracks at the α-case boundary. Drawn from [GAI 23b, Fig.13]

Cette thèse est accessible à l'adresse : https://theses.insa-lyon.fr/publication/2024ISAL0014/these.pdf
© [F. Steinhilber], [2024], INSA Lyon, tous droits réservés

4.2.3 Impact on fatigue properties

4.2.3.1 Heat treatment conditions and resulting α-case and microstructure

Only Z specimens were used for this study, with the same geometry (3 mm diameter cylindrical gauge area) and L-PBF manufacturing conditions as the ones detailed in Section 3.1.

Three heat treatment conditions are compared in this study. They consist of a stress relief possibly followed by a higher-temperature heat treatment:

- The ***stress relieved (SR)*** condition, which consists of a 720 °C|2 h treatment performed in the industrial furnace used in Quentin Gaillard's study. Note that it corresponds to the state called *as-built* elsewhere in this manuscript (same thermal cycle and furnace). It is a convenient denomination in the rest of the manuscript which focuses on the study of surface topography, since it refers to the fact that the surface topography is kept in its as-built state. However, this denomination would not be appropriate for this study which focuses on heat treatments and their impact on α-case formation. Furthermore, the choice has been made to call this condition SR in the present section to prevent confusion with the work of Quentin Gaillard, where the *as-built* state refers to the condition without any heat treatment.
- The ***HT*** condition refers to samples that received a 860 °C|4 h heat treatment in the **laboratory** furnace after the stress-relief treatment in the industrial furnace.
- The ***HT/α-case*** condition pertains to samples treated at 860 °C for 4 h in the **industrial** furnace following stress-relief.

The α-case layers observed for each condition are presented in Fig.4.15a-c.

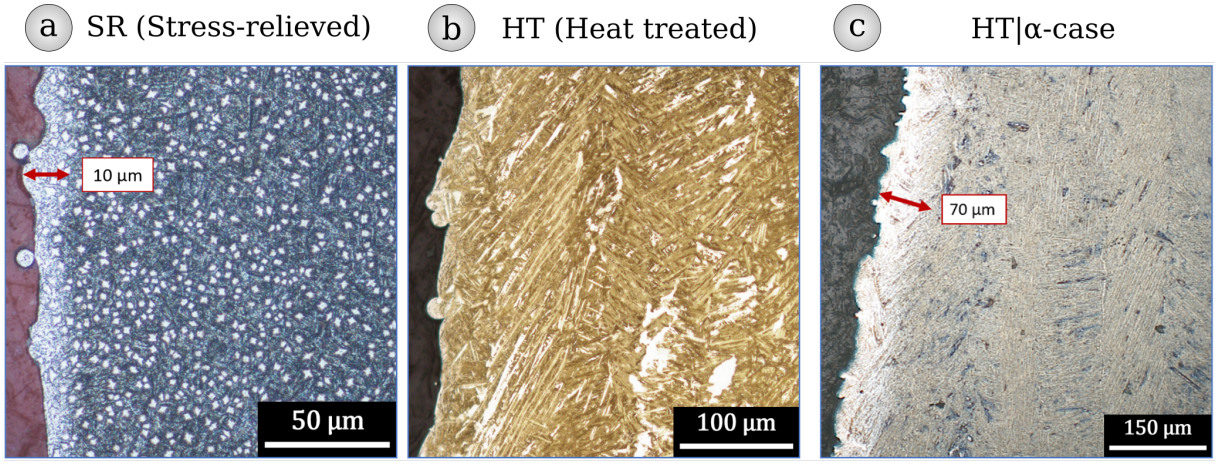

Figure 4.15 | **α-case characterization in SR, HT and HT|α-case conditions.** The optical micrographs were obtained from longitudinal cross-sections of fatigue specimens subjected to a chemical attack with Weck reagent. The Weck reagent reveals the α-case layer which appears in white. (Courtesy of Quentin Gaillard)

Cette thèse est accessible à l'adresse : https://theses.insa-lyon.fr/publication/2024ISAL0014/these.pdf
© [F. Steinhilber], [2024], INSA Lyon, tous droits réservés

Previously, the SR condition revealed an α-case layer approximately 10 µm thick. In the HT|α-case scenario, this layer expands to 70 µm. The HT condition, despite having initially undergone a stress-relief treatment known to induce a 10 µm α-case layer, exhibited no consistent α-case layer. The most likely explanation is that the oxygen from the α-case layer formed during stress-relief treatment further diffused below the surface during the treatment at 860 °C, resulting in its dispersion in the core material.

Section 4.2.2 showed that the thin α-case layer formed in the SR condition did not have any significant impact on tensile properties, including elongation to failure. As a first approach, the influence of α-case in the SR condition is therefore considered to be negligible, even for fatigue properties. The only condition considered to induce a significant α-case layer is the HT|α-case condition. This enables the separation of the influence of microstructure and α-case formation.

Therefore, **a comparison between HT and HT|α-case states will provide insights into the impact of the 70 µm α-case layer** in the latter. In contrast, when comparing SR and HT heat treatments, one can expect only the influence of the microstructure. The microstructure after stress relief and after the 860 °C|4 h heat treatment are shown in Fig.4.16a-b. These figures reveal a thickening of α laths as well as an increase in β phase fraction induced by the 860 °C|4 h heat treatment.

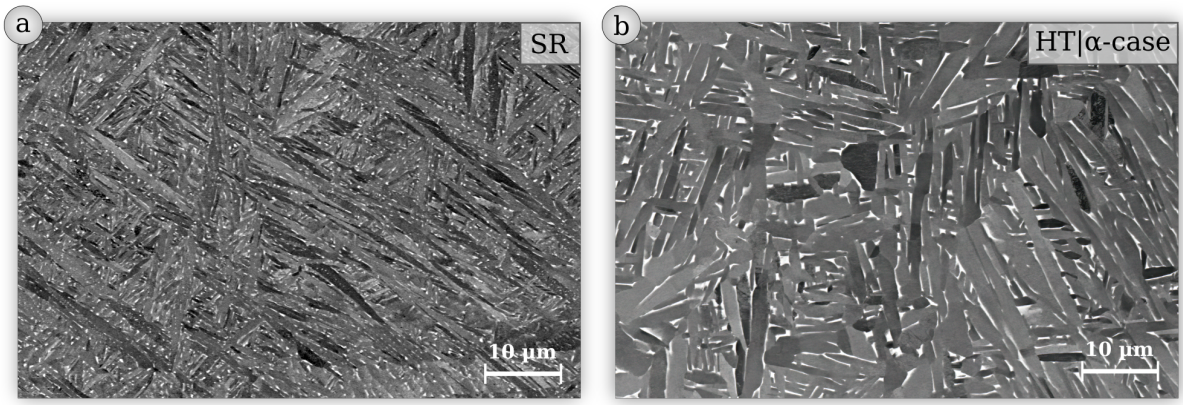

Figure 4.16 | SEM-BSE images showing the microstructure of the bulk material (a) of a SR sample and (b) of an HT|α-case sample. The β phase appears brighter than the α phase. (Courtesy of Quentin Gaillard)

To quantify the α-laths thickening, two EBSD maps were obtained on two fatigue samples in the SR and HT|α-case states (HT|α-case and HT conditions are equivalent in terms of bulk microstructure). The respective EBSD maps were $600 \times 445\,\mu m^2$ and $600 \times 500\,\mu m^2$ in size, captured with a 0.25 µm step size. The determined α-laths thickness shifted from 0.61 µm in the SR state to 1.06 µm for the 860 °C|4 h heat treatment.

Cette thèse est accessible à l'adresse : https://theses.insa-lyon.fr/publication/2024ISAL0014/these.pdf
© [F. Steinhilber], [2024], INSA Lyon, tous droits réservés

4.2.3.2 Influence of α-case on fatigue properties

Fatigue tests on HT and HT|α-case samples were performed under the same conditions as those used for the SR specimens ($R = 0.1$ and $f = 10\,\text{Hz}$). However, due to time constraints, tests were stopped here before 10^7 cycles when no failure occurred.

Fig.4.17 shows the Wöhler curves for the three conditions. Results for M&P specimens presented in Section 4.1.1 are also shown as a reference.

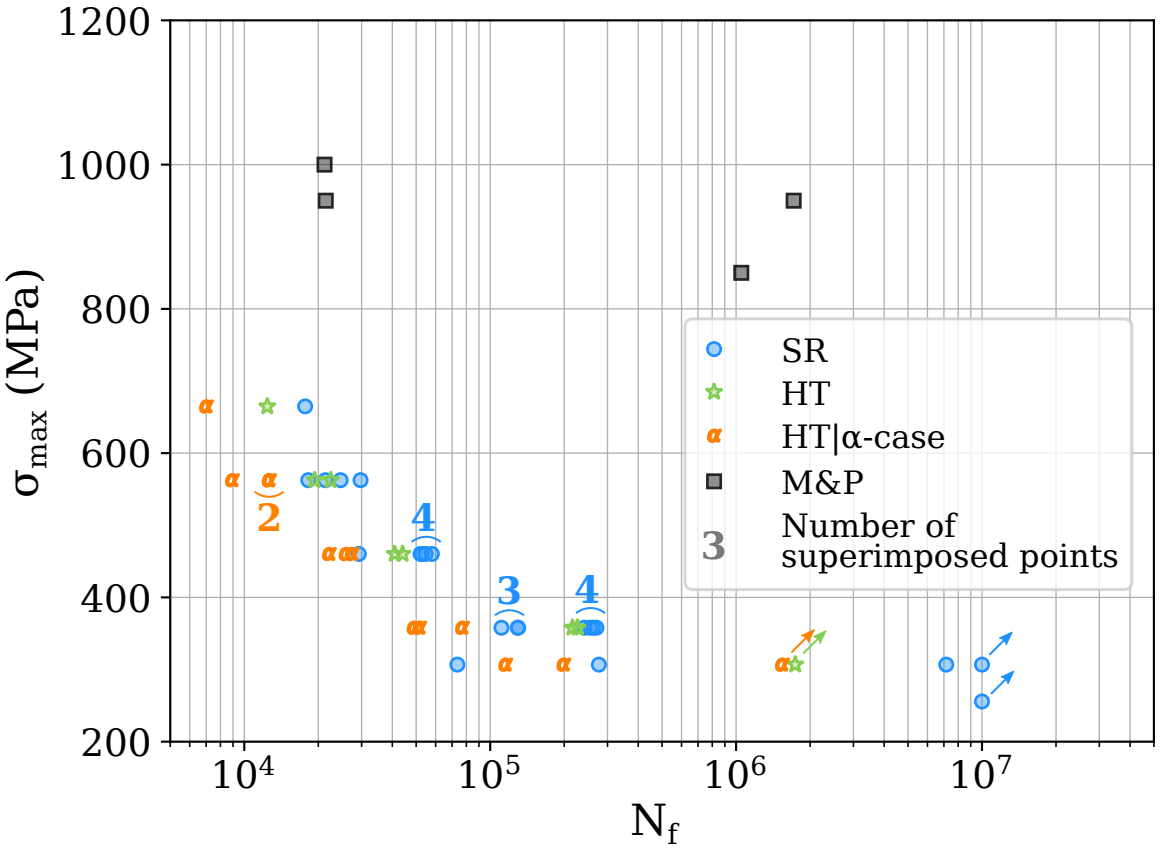

Figure 4.17 | Wöhler curves for SR, HT and HT|α-case conditions. M&P specimens are also represented as a reference. They did undergo a stress-relief treatment after polishing (2 h at 660 °C), ensuring that no residual stress remains from machining. Fatigue tests are performed at $R = 0.1$. All specimens were manufactured vertically.

There seems to be no noticeable difference in fatigue resistance between the SR and HT conditions. This suggests that **the microstructural changes from the 860 °C|4 h heat treatment have a limited influence on the fatigue resistance**. The **small reduction in fatigue life measured for the HT|α-case condition** vanishes at the lowest stress level tested (300 MPa).

It is worth noting that the differences observed among the SR, HT, and HT|α-case conditions are much smaller than those seen with M&P specimens. Still, it would be interesting to study HT and HT|α-case heat treatments on M&P specimens. This may for instance reveal that in the absence of the most detrimental surface defects, microstructure or α-case have a more pronounced influence on the fatigue resistance.

Cette thèse est accessible à l'adresse : https://theses.insa-lyon.fr/publication/2024ISAL0014/these.pdf
© [F. Steinhilber], [2024], INSA Lyon, tous droits réservés

To better understand the influence of α-case on fatigue properties, the fracture surfaces of the specimens were examined using SEM. Some HT|α-case samples were also studied with XCT both before and after failure.

SEM observations revealed that all the cracks that lead to failure started from the surface, regardless of the heat treatment applied. Additionally, XCT characterization showed that most cracks began at surface valleys. Intriguingly, one HT|α-case sample displayed a crack initiation site with no discernible defect on the initially scanned XCT surface, a feature not seen in SR samples. This might indicate a change in crack initiation mechanisms due to the α-case layer, but it may also simply be caused by a lack of resolution which does not enable to capture the killer defect.

Detailed SEM observations revealed traces of the α-case layer in the final failure area of the broken samples, i.e. the part of the fracture surface formed after the fracture toughness K_{IC} is reached. For the three heat treatment conditions, dimples are visible in this region (Fig.4.18a-c), indicating a ductile fracture mechanism. However, near the surface, a transition to a brittle fracture mode can be seen. The width of this zone is of the order of magnitude of the one of the α-case layer. Fig.4.18a-c show the surface in the final failure area for the three heat treatment conditions. One can note from these figures that the width of the fragile fracture layer is not completely homogeneous. This can for instance be seen in Fig.4.18b, where the fragile layer is visible on the left, whereas only cupules are visible on the right.

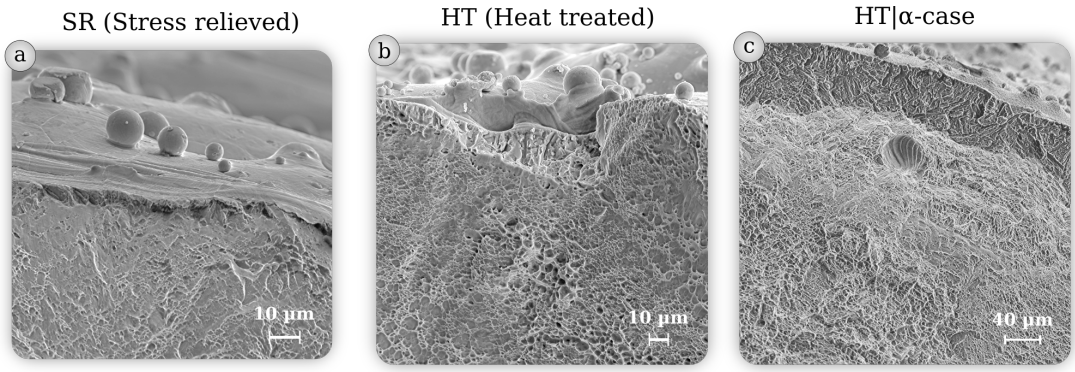

Figure 4.18 | SEM-SE observation of the final failure area of fatigue samples, revealing the brittle behavior of α-case layer (a) for an SR specimen that failed after 262 790 cycles at 350 MPa, (b) an HT specimen that failed after 22 477 cycles at 550 MPa and (c) an HT|α-case specimen that failed after 25 852 cycles at 450 MPa.

The observations indicate that the α-case layer can make the surface more brittle. This effect is especially pronounced for the HT|α-case condition, which has the thickest α-case layer. Thin brittle layers in the SR and HT conditions might also play a role. While it was previously stated in Section 4.2.2 that thin α-case layers do not affect tensile properties, their influence on fatigue could differ. They might, for example, facilitate the early stage of the crack initiation process.

It is interesting here to draw a parallel with the study of [VI 23]. The latter discussed the influence of a 10 µm brittle oxide layer on the fatigue behavior ($R = 0.1$) of 7075-T6 aluminum alloy. By comparing specimens with and without this oxide layer, it has been shown that the fatigue lifetime was reduced by a factor of 3 in the presence of the oxide layer. SEM fractography and acoustic emission analysis during fatigue cycling were used to examine further

Cette thèse est accessible à l'adresse : https://theses.insa-lyon.fr/publication/2024ISAL0014/these.pdf
© [F. Steinhilber], [2024], INSA Lyon, tous droits réservés

the mechanisms behind this observation. The findings suggested two potential mechanisms. The first involves the oxide layer cracking, promoting crack initiation in the underlying material. The second proposes that continuous crack formation in the oxide layer aids in the main crack's propagation, a phenomenon referred to as the *continuous initiation process*.

A parallel can be made here, with the oxide layer corresponding in the present case to the brittle α-case oxygen-enriched metallic layer. In particular, the hypothesis of a continuous initiation process seems coherent when looking at our fracture surfaces, which show comparable appearances as the ones obtained by [VI 23, Fig.13] for specimens with the oxide layer. [VI 23] noticed that when no oxide layer was present, cracks initiated from point defects. However, when the brittle oxide layer was present, cracks seemed to initiate from a large circular segment, possibly due to the occurrence of a continuous initiation process. Such large crack initiations are typically observed in the present work, as can be seen in Fig.4.19a-c.

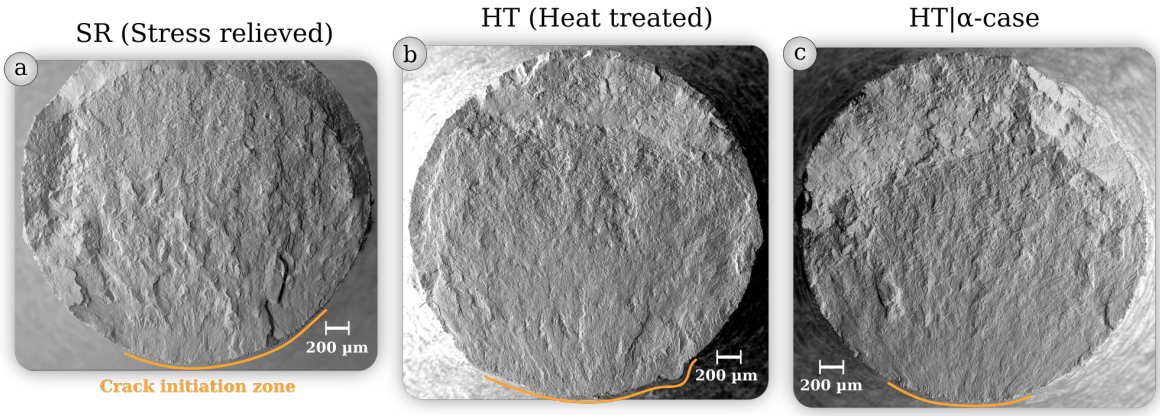

Figure 4.19 | SEM-BSE topological mode observation of fracture surfaces for (a) a SR specimen that failed after 73 547 cycles at 300 MPa, (b) an HT specimen that failed after 40 901 cycles at 450 MPa and (c) an HT|α-case specimen that failed after 198 645 cycles at 300 MPa. In every case, crack initiation seems to occur from a large portion of the surface.

Yet, the observed fracture surface patterns are consistent across all conditions (SR, HT, and HT|α-case) and are not specific to the HT|α-case. One possibility is that α-case always induces a continuous initiation since some α-case layer exists in all treatments, even though it seems discontinuous in the HT condition. A second explanation could be that the particular fracture surface morphology observed comes from the presence of elongated surface valleys rather than α-case. Indeed, it has been shown in 4.1.3.2 that cracks tend to follow surface valleys inherited from the L-PBF process. This suggests that surface valleys could either promote crack initiation or facilitate crack propagation by a continuous initiation-like mechanism. More advanced characterizations would be required to better understand these mechanisms. Acoustic emission analysis, as performed by [VI 23], would for instance have brought valuable information.

To verify if the presence of α-case could promote crack initiation, the crack density within specimens in SR, HT and HT|α-case conditions was studied. For this purpose, the aim was to count the number of cracks that did initiate, even though they did not propagate until failure. In other words, cracks were searched below (or above) the fracture surface.

Cette thèse est accessible à l'adresse : https://theses.insa-lyon.fr/publication/2024ISAL0014/these.pdf
© [F. Steinhilber], [2024], INSA Lyon, tous droits réservés

It is worth mentioning here that two types of cracks can be seen on specimens after fracture. The first one will be referred to as *final failure cracks* and is observed primarily on HT|α-case specimens. Examples of such cracks are given in Fig.4.20a-b.

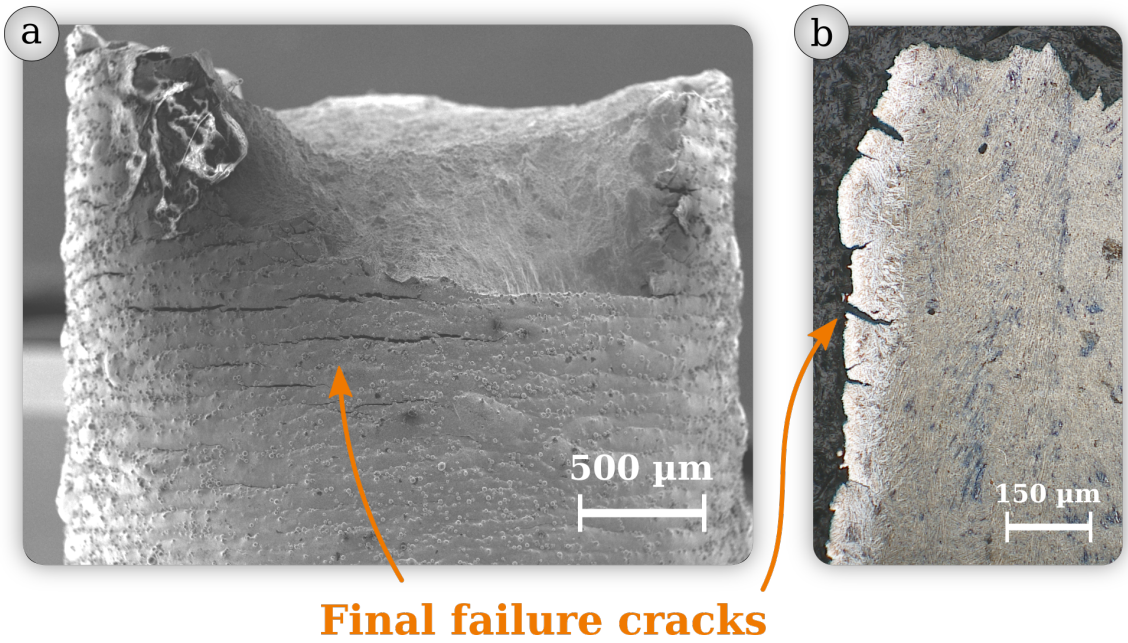

Figure 4.20 | Observation of *final fracture cracks* in HT|α-case specimens. (a) SEM-SE image (b) Optical microscope image of a longitudinal cross-section after a chemical attack with Weck reagent to reveal α-case in white.

Fig.4.20b reveals these cracks to be notably wide but shallow. Their propagation seems to stop at the end of the α-case layer. They are very similar to cracks observed by Quentin Gaillard [GAI 23b, Fig.13] on tensile specimens after failure, as shown in Fig.4.14z=a-d. Interestingly, these cracks reside near the final fracture zone, where the material can be expected to bear very high loads at the end of crack propagation. Towards the end of fatigue life, in the ligament ahead of the propagating main crack, the material is submitted to high levels of stress This likely explains the similarity between the fracture surfaces observed in the final fracture region and the ones found on tensile specimens.

A closer look reveals the densest clustering of these cracks at the fringe of the final failure region, as illustrated in Fig.4.20 and schematically represented in Fig.4.21.

Such cracks underscore the potential of the α-case layer to diminish fracture toughness, accelerating the terminal failure. This behavior mirrors Quentin Gaillard's findings during tensile tests, illustrated in Fig.4.13b. Nevertheless, the presence of these cracks is only related to the final failure phase, excluding the crack initiation or growth phases.

Therefore, in what follows, the focus has been made on a second type of crack. These initiated and propagated during fatigue cycling, even though they did not necessarily propagate through the whole specimen section. They will be referred to as *fatigue cracks* in what follows. Such cracks are much slimmer and straighter, perpendicular to the loading direction, in contrast to the final failure cracks. Moreover, their propagation often extends beyond the α-case layer, as can be seen on the longitudinal cross-section in Fig.4.22.

Cette thèse est accessible à l'adresse : https://theses.insa-lyon.fr/publication/2024ISAL0014/these.pdf
© [F. Steinhilber], [2024], INSA Lyon, tous droits réservés

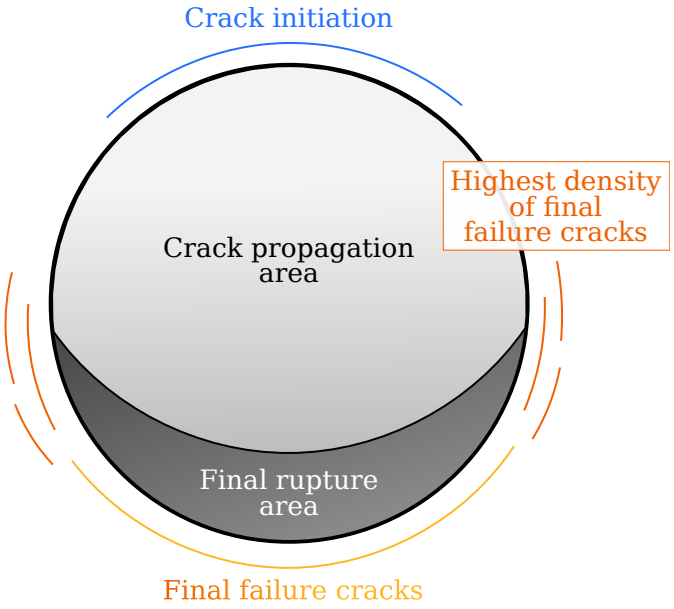

Figure 4.21 | Schematic representation of an HT|α-case fracture surface, showing the preferential locations of final failure cracks. Adapted from [LAR 23].

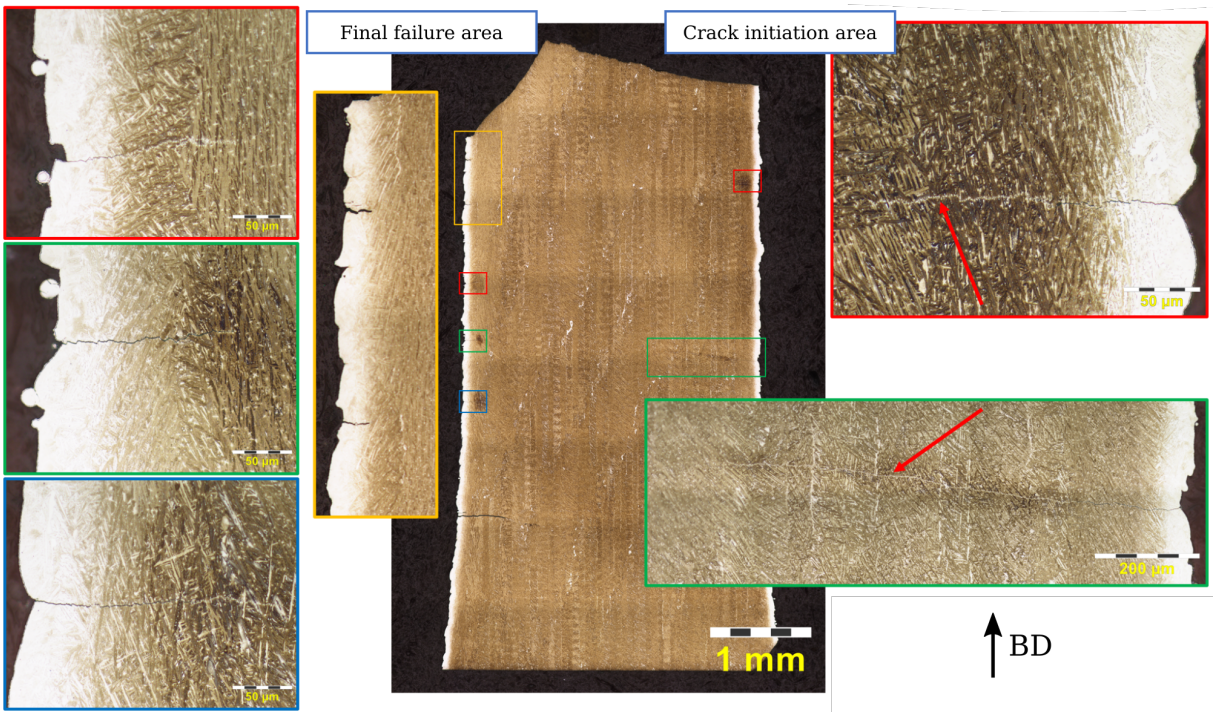

Figure 4.22 | Fatigue cracks observed by optical microscopy on an HT|α-case specimen longitudinal cross-section. The cross section was polished and subjected to Weck reagent, which best revealed thin cracks.

Cette thèse est accessible à l'adresse : https://theses.insa-lyon.fr/publication/2024ISAL0014/these.pdf
© [F. Steinhilber], [2024], INSA Lyon, tous droits réservés

An extensive study was conducted using 11 SR, 9 HT and 11 HT|α-case specimens tested at different stress levels. After failure, a longitudinal cross-section was obtained from one-half of each specimen. This cross-section was polished, and the Weck reagent was applied. This proved effective in highlighting thin cracks, as illustrated in Fig.4.22. Within a specified distance h from the fracture surface (see Fig.4.23a), fatigue cracks were counted. The resulting count was normalized by the length of the inspected surface, yielding a crack linear density in mm^{-1}, as presented in Fig.4.23b.

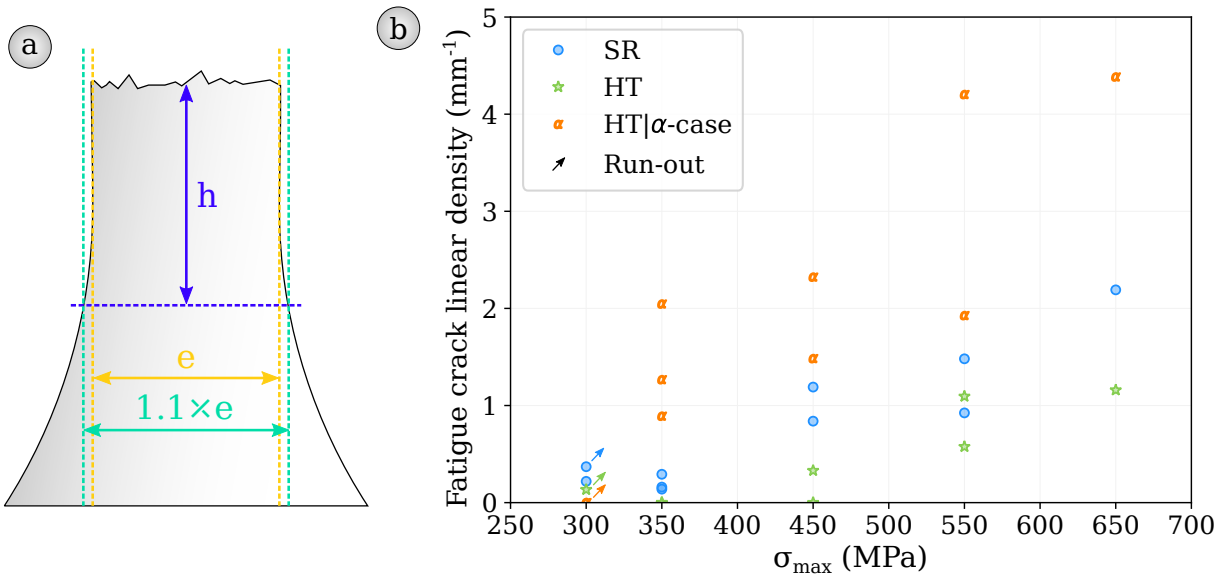

Figure 4.23 | Fatigue crack linear density measurements on SR, HT and HT|α-case specimens at different stress levels. (a) Scheme specifying the height h over which cracks are counted for each specimen. (b) Cracks densities measured for all specimens, as a function of the maximum stress during fatigue test.

The results shown in Fig.4.23b indicate that the crack density increases with the value of maximum cyclic stress for all SR, HT, and HT|α-case specimens. Such a trend is anticipated, aligning with findings that a greater number of nucleated cracks appear at elevated stress levels [SCH 09, Fig.2.20].

Further analysis of Fig.4.23b reveals that, excluding the readings at 300 MPa, the HT|α-case specimens exhibit considerably higher fatigue crack densities. This supports the theory that **the 70 µm α-case layer in HT|α-case specimens promotes crack initiation during cycling**, potentially reducing fatigue lifespan. Densities for SR and HT specimens are similar, with a marginally elevated count for SR. This could be due to the wider and more regular α-case layer present in SR specimens, although it is only 10 µm wide.

A deeper exploration could shed light on how the α-case affects fatigue properties. For instance, testing specimens with thicker α-case layers or M&P specimens with an equivalent α-case layer would provide complementary information. Alternative characterization techniques could have also proven useful. For instance, using acoustic emission, as explored by [VI 23], could provide insights into the timing of crack initiation during cyclic loading and its relationship with the α-case presence.

Cette thèse est accessible à l'adresse : https://theses.insa-lyon.fr/publication/2024ISAL0014/these.pdf
© [F. Steinhilber], [2024], INSA Lyon, tous droits réservés

This research establishes that the 70 µm α-case layer developed during heat treatment slightly diminishes the fatigue resistance of L-PBF Ti64 specimens. Combined with the surface roughness considerations discussed in Section 4.1, it underscores the significance of L-PBF Ti64's surface integrity on fatigue properties. M&P specimens' superior properties hint that strategic surface polishing might significantly enhance fatigue attributes by both smoothing the surface and eliminating the α-case layer. Although the impact of surface roughness seems much more pronounced than the one of the α-case layer, the use of surface polishing could still be interesting regarding the α-case issue. Indeed, one of the advantages of using material-removal polishing is that it would enable heat treatments to be carried out with fewer constraints on the vacuum to be achieved in the furnace, as the α-case layer (if of a reasonable depth) would be eliminated by polishing.

However, polishing additively manufactured components poses challenges. Such components typically have rougher surfaces than their machined counterparts. Moreover, additive manufacturing techniques like L-PBF are prized for making parts with intricate designs, making most polishing methods unsuitable due to inaccessibility. Despite these issues, various technologies aim to address these challenges [MAL 21, KHA 21, NUT 19, BOB 21]. In this PhD work, a specific technique, Plasma Electrolytic Polishing (PeP), was explored to enhance fatigue properties.

4.3 Improvement of fatigue properties by Plasma electrolytic Polishing (PeP)

4.3.1 Principle of PeP surface treatment

Plasma electrolytic Polishing (PeP) is a surface finishing method for metals and alloys. It was first introduced in 1979 [DUR 79] and has since aroused increasing interest. Several studies and reviews mention its application to AM parts [CUT 22, SEO 21, NAV 22, ZEI 22, HEN 18, BAS 22]. This can be partly explained by its ability to treat surfaces of complex geometries.

As an example, Fig.4.24a-b show results from a study that characterized titanium additive manufactured parts before and after PeP [NAV 22]. Significant improvements can be seen, both in terms of roughness and fatigue properties.

Fig.4.25 shows schematically the PeP process principle. PeP setup is at first sight similar to the one that could be used in conventional Electrolytic Polishing (EP). The metallic part to polish is placed in a temperature-controlled electrolytic bath and connected to a cathode. A voltage difference is then applied between the workpiece (acting as an anode) and the cathode. However, PeP differs from EP in many aspects.

Firstly, **polishing mechanisms are different**. They are multiple and complex in the case of PeP, and still a topic of discussion nowadays [BAS 22, HUA 21, BEL 20]. Without going into too much detail, the reactions occurring at the anode produce gas (O_2) which rapidly forms an insulating gas layer around the workpiece – see Fig.4.25. Due to the high potential difference between the anode and the electrolyte, this so-called vapour-gaseous envelope (VGE) is ionized which leads to the formation of a plasma. The polishing action comes both from the chemical reaction with the electrolyte and the action of this plasma layer.

Cette thèse est accessible à l'adresse : https://theses.insa-lyon.fr/publication/2024ISAL0014/these.pdf
© [F. Steinhilber], [2024], INSA Lyon, tous droits réservés

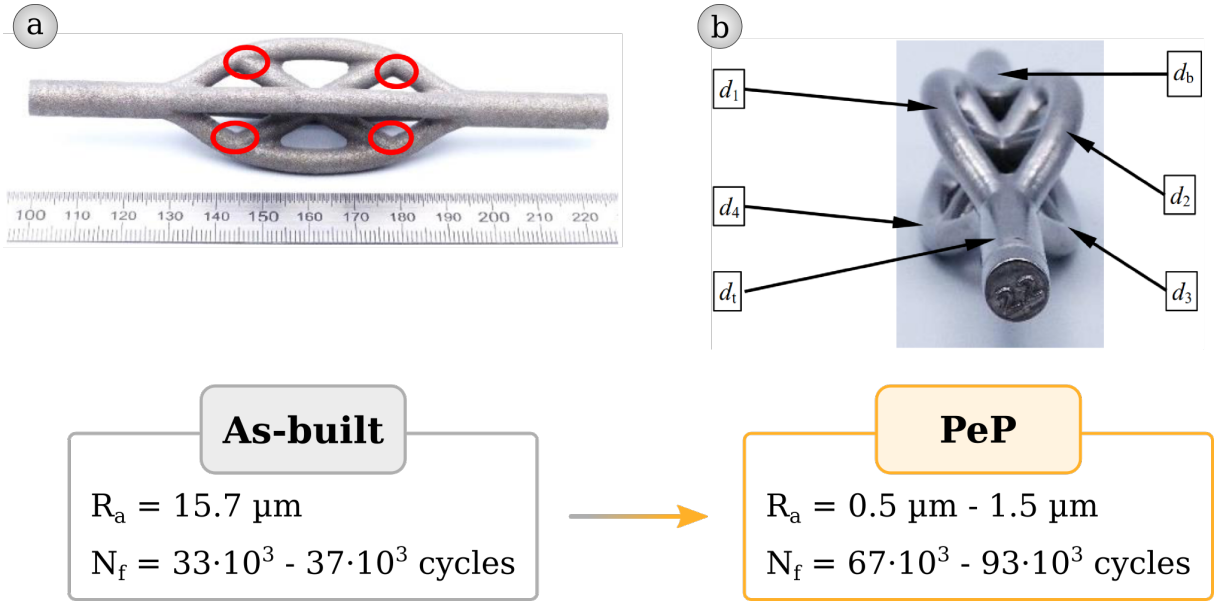

Figure 4.24 | Roughness and fatigue characterization of titanium additive manufactured parts (a) before and (b) after PeP [NAV 22]. Parts present eight tensile stress concentration spots that are highlighted in (a). They were tested with a constant amplitude at $R = 0.1$ and a peak load of 11.793 kN. Fatigue data is estimated from [NAV 22, Fig.6].

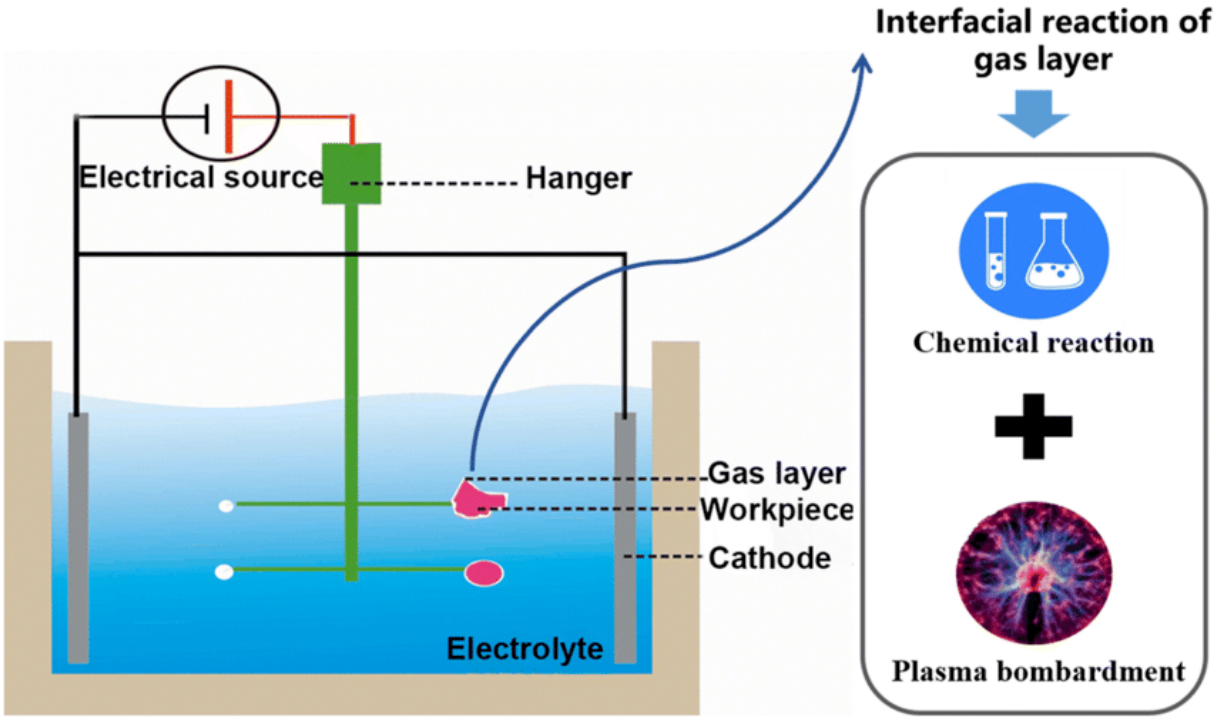

Figure 4.25 | Principle scheme of PeP process drawn from [HUA 21].

Cette thèse est accessible à l'adresse : https://theses.insa-lyon.fr/publication/2024ISAL0014/these.pdf
© [F. Steinhilber], [2024], INSA Lyon, tous droits réservés

Because polishing mechanisms are different from the ones active in EP, **PeP does not require the use of a cathode whose geometry is similar to the one of the workpiece**. Simple geometries such as rings or plates can therefore be used [ZEI 22], which is a huge advantage for the treatment of parts of complex geometry. Some constraints still exist, like the need for the cathode to be of significantly larger size than the workpiece [ZEI 22, NAV 22, HUA 21] which could be limiting for large industrial parts. Furthermore, **material removal rate directly depends on the immersion depth** [ALE 05, BEL 20]. This issue comes from the effect of hydrostatic pressure on the gas layer. Some inhomogeneity can therefore be expected, especially for large parts. However, some solutions could exist in those cases, such as the use of electrolyte jet PeP [HUA 21] where the electrolyte is used in the form of a jet propelled towards the workpiece rather than a bath.

One of the characteristics of PeP is the **high applied voltage and current density** which are needed for the gas layer to form and the polishing to occur. Typical voltage values range from 200 to 350 V and current densities from 0.2 to 0.5 A/cm^2 [HUA 21]. This makes PeP much more demanding than conventional EP and can require the use of costly and energy-consuming generators for large parts.

On a more positive side, electrolytes used for PeP (e.g. made of low-concentration salt solutions) are generally considered to be **less harmful to the environment** than the ones used in conventional EP [BAS 22, ZEI 22, NAV 22, HUA 21]. For titanium alloys, the most commonly used electrolyte is a (low concentrated) fluorine salt-based aqueous solution [HUA 21].

On the whole, PeP presents interesting perspectives for the surface treatment of metallic additive manufactured parts of complex geometries. However, as it is more recent than other methods such as (electro-)chemical polishing or shot-peening, more studies are needed to estimate its practical relevance.

4.3.2 Conditions of PeP treatments applied to fatigue specimens

To investigate the effect of PeP treatment on fatigue properties, specimens with as-built surfaces were utilized. These specimens only underwent a 720 °C|2 h stress-relief heat treatment after production. Given the shallow depth of the α-case layer in this state (10 µm), it is believed that PeP's effects on fatigue properties are not due to the α-case layer's removal.

PeP treatments were performed by the French company Ineosurf on several Z and 45° specimens. Specific PeP operational details remain confidential. To assess the evolution of surface roughness, specimens underwent XCT scanning both before and after PeP. The XCT acquisition and data processing conditions are the same as those of the as-built specimens, as outlined in 3.4.1.

Different surface treatment conditions were applied depending on the build orientation. **Two treatment durations were assigned for Z specimens**: 40 min and 1 h 20 min. All 45° specimens received a 40 min polish. However, **some of the 45° specimens were oriented at 45°** in the electrolyte bath. The positioning of the specimens in the electrolyte during treatment is illustrated in Fig.4.26. Treatment conditions in subsequent discussions will be labeled as $Z|^{\text{Vertical}}_{\text{40min}}$, $Z|^{\text{Vertical}}_{\text{1h20}}$, $45°|^{\text{Vertical}}_{\text{40min}}$, and $45°|^{\text{45°}}_{\text{40min}}$.

Fig.4.28 shows a polished specimen and the number of specimens available for each condition. It also indicates by a red cross specimens for which PeP treatment failed and led to a clear degradation of surface state on part or the whole specimen – see Fig.4.27 for an example. The reason behind these dysfunctions remains unknown.

Cette thèse est accessible à l'adresse : https://theses.insa-lyon.fr/publication/2024ISAL0014/these.pdf
© [F. Steinhilber], [2024], INSA Lyon, tous droits réservés

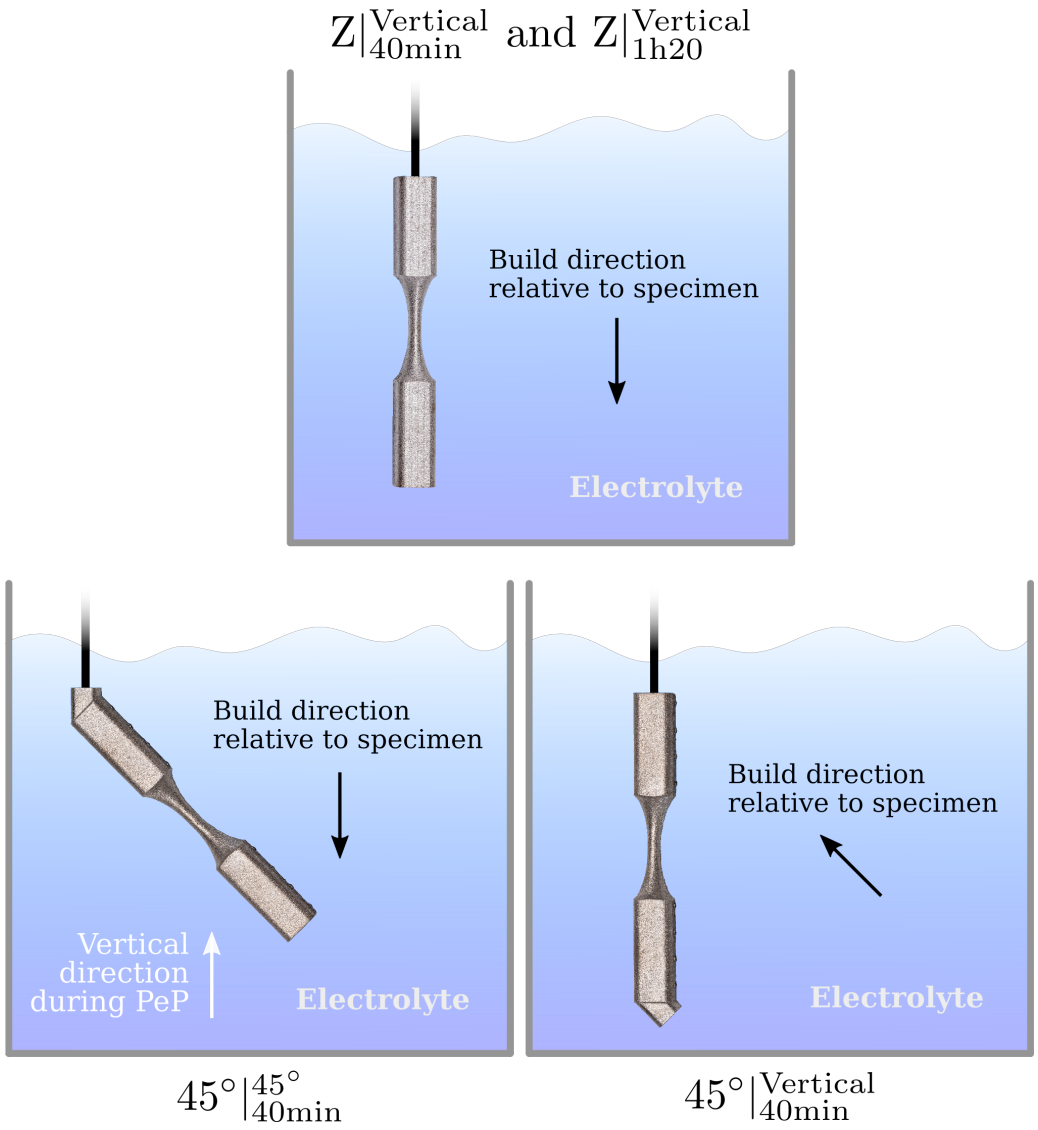

Figure 4.26 | Position of the specimens in the electrolyte bath during PeP treatment.



Figure 4.27 | $45°|^{\text{Vertical}}_{\text{40min}}$ specimen surface after a failed PeP treatment.

Cette thèse est accessible à l'adresse : https://theses.insa-lyon.fr/publication/2024ISAL0014/these.pdf
© [F. Steinhilber], [2024], INSA Lyon, tous droits réservés

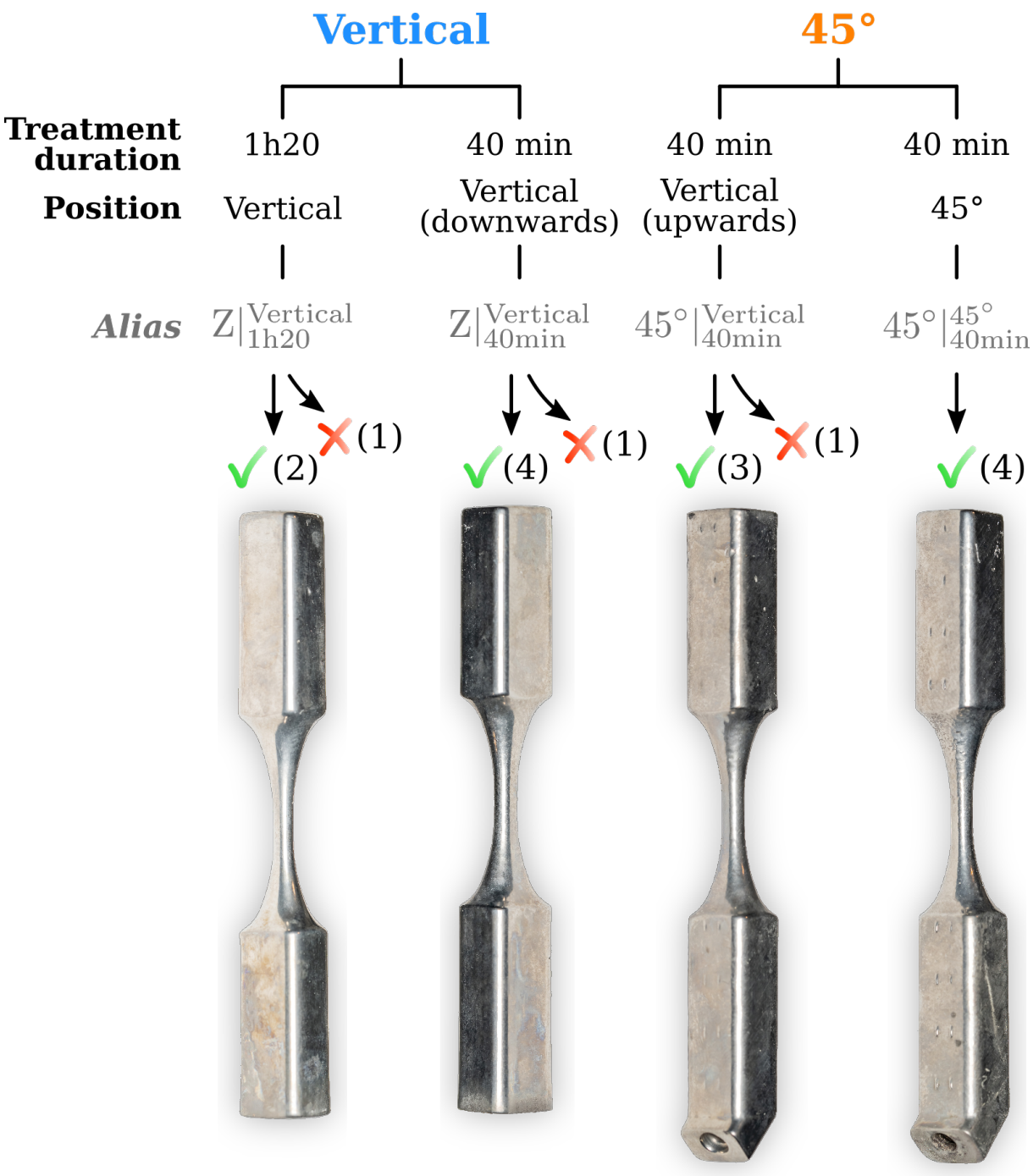

Figure 4.28 | PeP conditions for Z and 45° fatigue specimens. "Position" refers to the specimen orientation of the specimen in the electrolytic bath. Red crosses indicate the number of specimens for which treatment failed, see Fig.4.27 for an example. Note that the hole used to hold the specimens in the bath is visible on the 45° specimen support structures. The hole was mistakenly made for the 45° specimen in the vertical condition, but another hole was made on the opposite head to allow the treatment to be performed in the vertical position.

Cette thèse est accessible à l'adresse : https://theses.insa-lyon.fr/publication/2024ISAL0014/these.pdf
© [F. Steinhilber], [2024], INSA Lyon, tous droits réservés

4.3.2.1 Analysis of material removal

Tab.4.1 indicates the thickness of removed material for all the treatment conditions. For a given specimen, it corresponds to the difference between the minimum radius of the as-built specimen and the minimum radius of the polished specimen, both measured from XCT data.

Treatment condition	$Z\|^{Vertical}_{40min}$	$Z\|^{Vertical}_{1h20}$	$45°\|^{Vertical}_{40min}$	$45°\|^{45°}_{40min}$
Matter removal (µm)	182 ± 22	345 ± 3	171 ± 7	223 ± 15

Table 4.1 | Matter removals measured for the different PeP treatment conditions. It corresponds to the difference between the minimum radius of the as-built specimens and the minimum radius of the polished specimen, both measured from XCT data. The values shown are the average and standard deviation for all specimens treated with the same condition.

The thickness of removed material is approximately 180 µm for specimens treated for 40 min (i.e. $Z|^{Vertical}_{40min}$, $45°|^{Vertical}_{40min}$, and $45°|^{45°}_{40min}$ conditions). For the $Z|^{Vertical}_{1h20}$ condition, material removal is nearly double, at approximately 340 µm.

Polishing at 45° resulted in a slightly higher matter removal than polishing in the vertical position for 45° specimens, although the difference is small and could be considered within the measurement uncertainty. Although no clear explanation was found, it could be attributed to the specimen's position in the bath. The position might alter the gas layer behavior around the samples during PeP, influencing the material removal rate.

It should be noted that the polishing is not homogeneous across the specimen surfaces. Fig.4.29 demonstrates that material removal thickness evolves along the specimen axis. Note that each curve in Fig.4.29 represents a single specimen, not an average as in Fig.4.28.

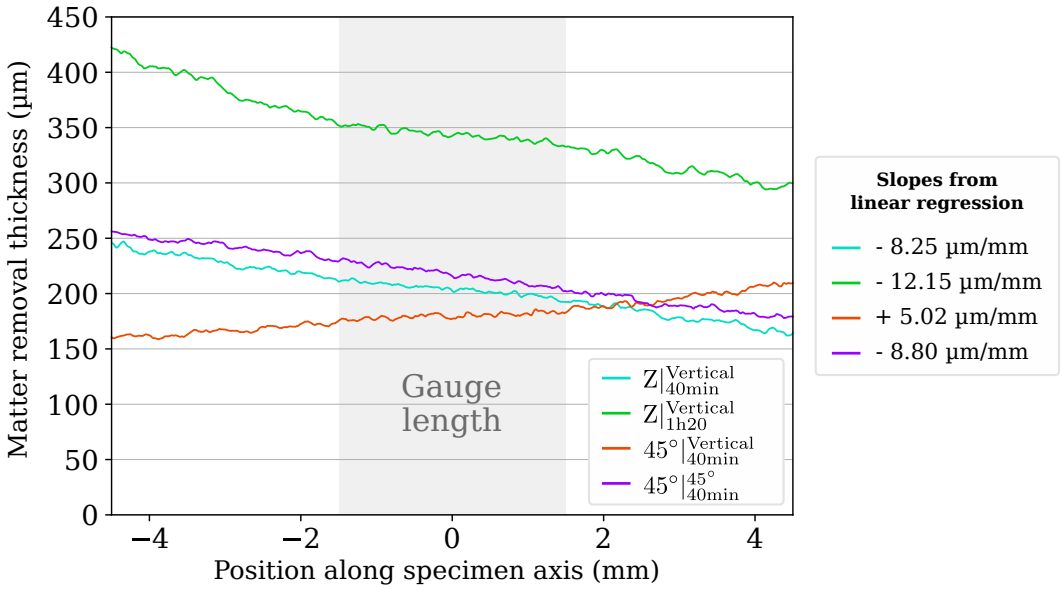

Figure 4.29 | Matter removal thicknesses measured along the specimen axis of 4 specimens which underwent PeP with different treatment conditions. By convention, the position along the specimen axis decreases in the direction of the built plate (for instance in the direction of the residual support structures for 45° specimens.)

Cette thèse est accessible à l'adresse : https://theses.insa-lyon.fr/publication/2024ISAL0014/these.pdf
© [F. Steinhilber], [2024], INSA Lyon, tous droits réservés

Material removal appears to have a linear trend along the specimen axis. Maybe the most striking point here is that the slope of the linear regression is negative for the $Z|^{Vertical}_{40min}$, $Z|^{Vertical}_{1h20}$ and $45°|^{45°}_{40min}$ conditions, whereas it is positive for the $45°|^{Vertical}_{40min}$ one. This can be correlated to the position of the specimens during the PeP treatment. For the $Z|^{Vertical}_{40min}$, $Z|^{Vertical}_{1h20}$ and $45°|^{45°}_{40min}$ conditions, the specimens are pointing downwards. Hence, the matter removal rate is at its maximum for the smallest immersion depth. For the $45°|^{Vertical}_{40min}$ condition, specimens are pointing upwards and therefore the positive slope shows that here again, the matter removal rate is at its maximum for the smallest immersion depth.

However, these results seem difficult to explain regarding the existing literature. Indeed, the effects of immersion depth on the material removal rate were found to be explained by variations in the hydrostatic pressure. Hydrostatic pressure is an important parameter since it influences the shape and width of the gas layer, which itself conditions the treatment efficiency. Such an effect makes the material removal rate higher for higher immersion depths [ALE 05, BEL 20], which is the exact opposite of what is observed in the present work.

Furthermore, the effect of hydrostatic pressure seem much less pronounced in the study of [ALE 05] on a 12Cr-18Ni-10Ti steel than what is seen here. For instance, assuming a treatment of 40 min, the evolution of the thickness of removed material with immersion depth was according to their measurements of 0.15 µm/mm, which is about 50 times less than what is observed in the present study. One can also add that the material removal thickness evolution seems very similar between the $Z|^{Vertical}_{40min}$ and the $45°|^{45°}_{40min}$ conditions, although for this specimen the immersion depth variation is smaller than for the $45°|^{45°}_{40min}$ condition where the specimen is oriented at 45°. Inversely, the slope is smaller of the $45°|^{Vertical}_{40min}$ condition. All these observations suggest that the material removal rate variations along the specimens' axis are likely induced by another factor than hydrostatic pressure variation. Since no other explanation could be found, **the observed material removal inhomogeneity will be simply taken into account as they are in the subsequent analysis**.

Chapter 3 highlighted that a unique microstructure and pore distribution are observed near the surface. It is thus relevant to analyze the relationship between material removal thickness and these distributions under different polishing conditions. Key findings are compiled in Fig.4.30. Only the average matter removal presented in Tab.4.1 is shown here, but it is worth keeping in mind that matter removal can vary among specimens and within a specimen itself.

Fig.4.30 superimposes:

- the distributions of the pores distance to the surface for both Z and 45° specimens
- a crystallographic orientation map (EBSD) of the reconstructed β_0 grains close to the surface
- vertical lines showing the mean value of the thickness of the removed material for each PeP treatment condition

Comparing average material removals with pore distance distributions, the $Z|^{Vertical}_{1h20}$ treatment seems to entirely eliminate sub-surface porosity. For other conditions, the removal depth aligns with the tail-end of sub-surface porosity. This could imply that **residual sub-surface pores could get exposed during polishing**, forming new surface flaws that would negatively impact fatigue resistance.

Cette thèse est accessible à l'adresse : https://theses.insa-lyon.fr/publication/2024ISAL0014/these.pdf
© [F. Steinhilber], [2024], INSA Lyon, tous droits réservés

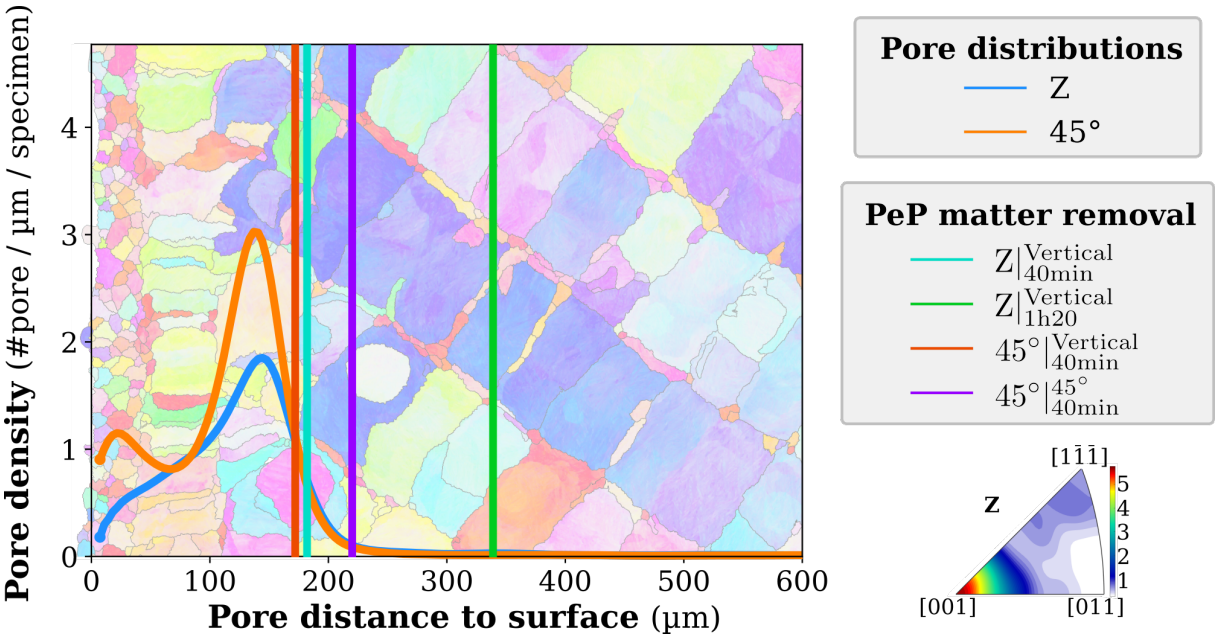

Figure 4.30 | Relation between matter removal during PeP, pores distance to surface and near-surface microstructure. Pore distance to surface distributions is a zoomed view of Fig.3.14. Similarly, the near-surface microstructure in the background is an EBSD orientation map of prior β_0 grains that has been shown in Fig.3.10.

Similarly, for the $Z|^{\text{Vertical}}_{\text{1h20}}$ condition, polishing exceeds the microstructural contour region discussed in 3.2. The surface microstructure after PeP resembles the border chessboard microstructure referenced in 3.2. For other conditions, the end of polishing can be expected to lie astride the boundary between contour and border regions. EBSD analyses were conducted on $Z|^{\text{Vertical}}_{\text{40min}}$ and $Z|^{\text{Vertical}}_{\text{1h20}}$ specimens to verify these observations and ensure PeP did not alter surface microstructure. As expected, the surface microstructure after PeP corresponds to the border region that has been characterized on as-built samples. Detailed results are available in Appendix C.

Lastly, residual stress measurements were also performed on one of the specimens' heads and led to the conclusion that PeP did not generate any residual stress.

4.3.3 Roughness of specimens polished by PeP

Due to roughness inhomogeneity in as-built specimens (Z vs 45°; up-skin vs down-skin) and in the subsequent PeP treatment, different surface states are obtained after PeP. They will be presented for each treatment condition, and finally summarized in terms of roughness parameters.

Fig.4.31 displays the surface of a Z specimen before and after a 40 min PeP treatment ($Z|^{\text{Vertical}}_{\text{40min}}$ condition). Notably, the original surface roughness disappears. The deepest valley, however, remains at 38 µm. At greater magnification, tiny sharp pits become visible, contributing to this measured depth. **These pits are due to sub-surface pores exposed during polishing**, as highlighted in Section 4.3.2.1. Such defects could compromise fatigue performance despite the otherwise smooth surface.

Cette thèse est accessible à l'adresse : https://theses.insa-lyon.fr/publication/2024ISAL0014/these.pdf
© [F. Steinhilber], [2024], INSA Lyon, tous droits réservés

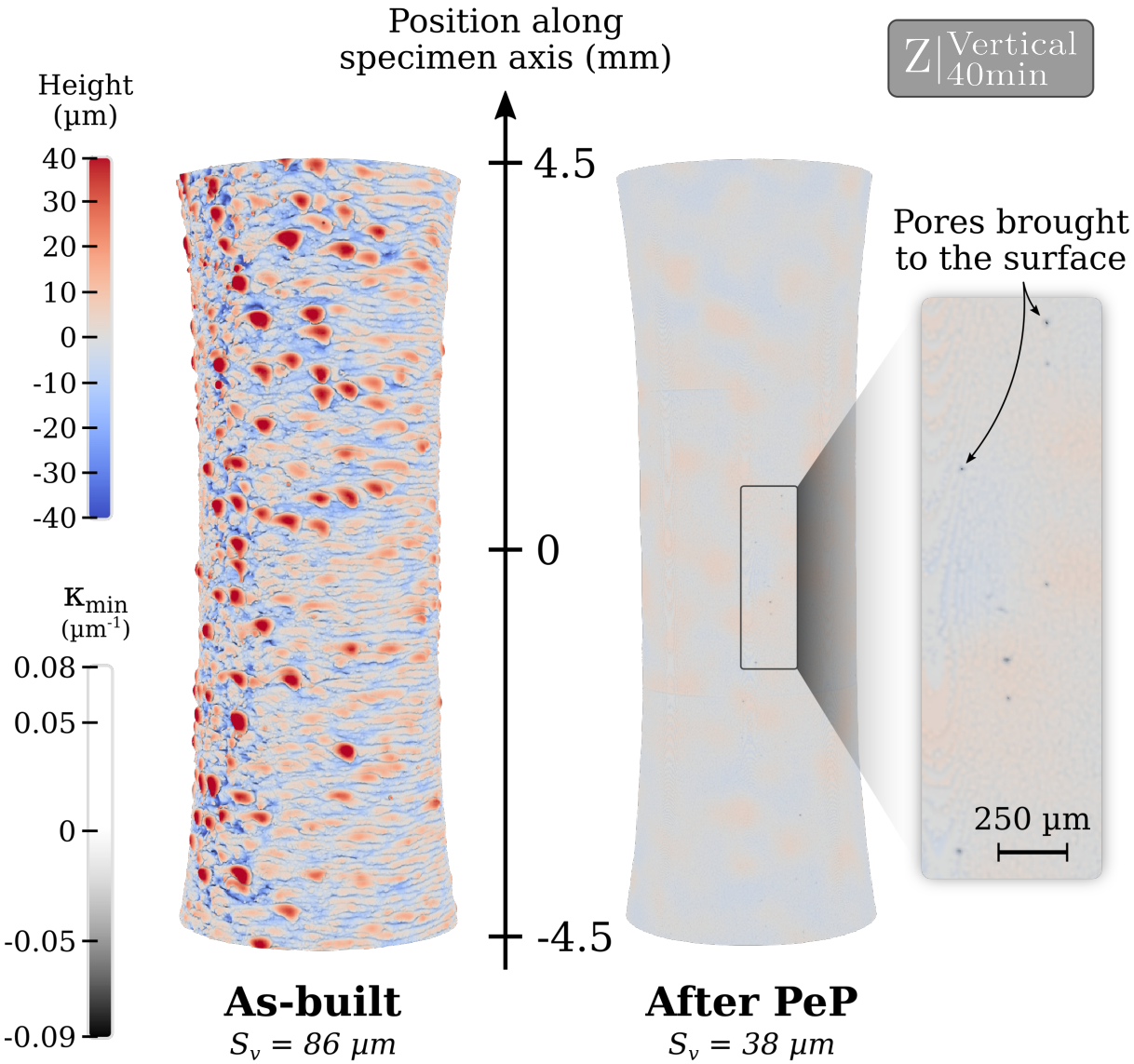

Figure 4.31 | Surface of a Z specimen before and after a 40 min PeP treatment ($\mathbf{Z}|^{\mathbf{Vertical}}_{\mathbf{40min}}$ condition). The color used to represent the surface combines the roughness (using $\lambda_c = 0.8\,\text{mm}$) as well as the minimum curvature (using $r_{curv} = 20\,\mu\text{m}$) to exacerbate valleys and details in general. Although PeP completely smoothed the original surface roughness, a few small pits can be identified on the surface. They are attributed to pores that were brought to the surface by polishing.

Cette thèse est accessible à l'adresse : https://theses.insa-lyon.fr/publication/2024ISAL0014/these.pdf
© [F. Steinhilber], [2024], INSA Lyon, tous droits réservés

Fig.4.32 shows that after a longer treatment (1 h 20 min), **surface pits can no longer be seen**. The maximum S_v value measured in this condition is accordingly low (6 µm). This comforts the hypothesis that those defects originate from sub-surface pores in $Z|^{Vertical}_{40min}$ specimens, since they are all eliminated for $Z|^{Vertical}_{1h20}$ specimens. Due to the higher matter removal, the specimen section is however greatly reduced, which may cause other dimensional issues.

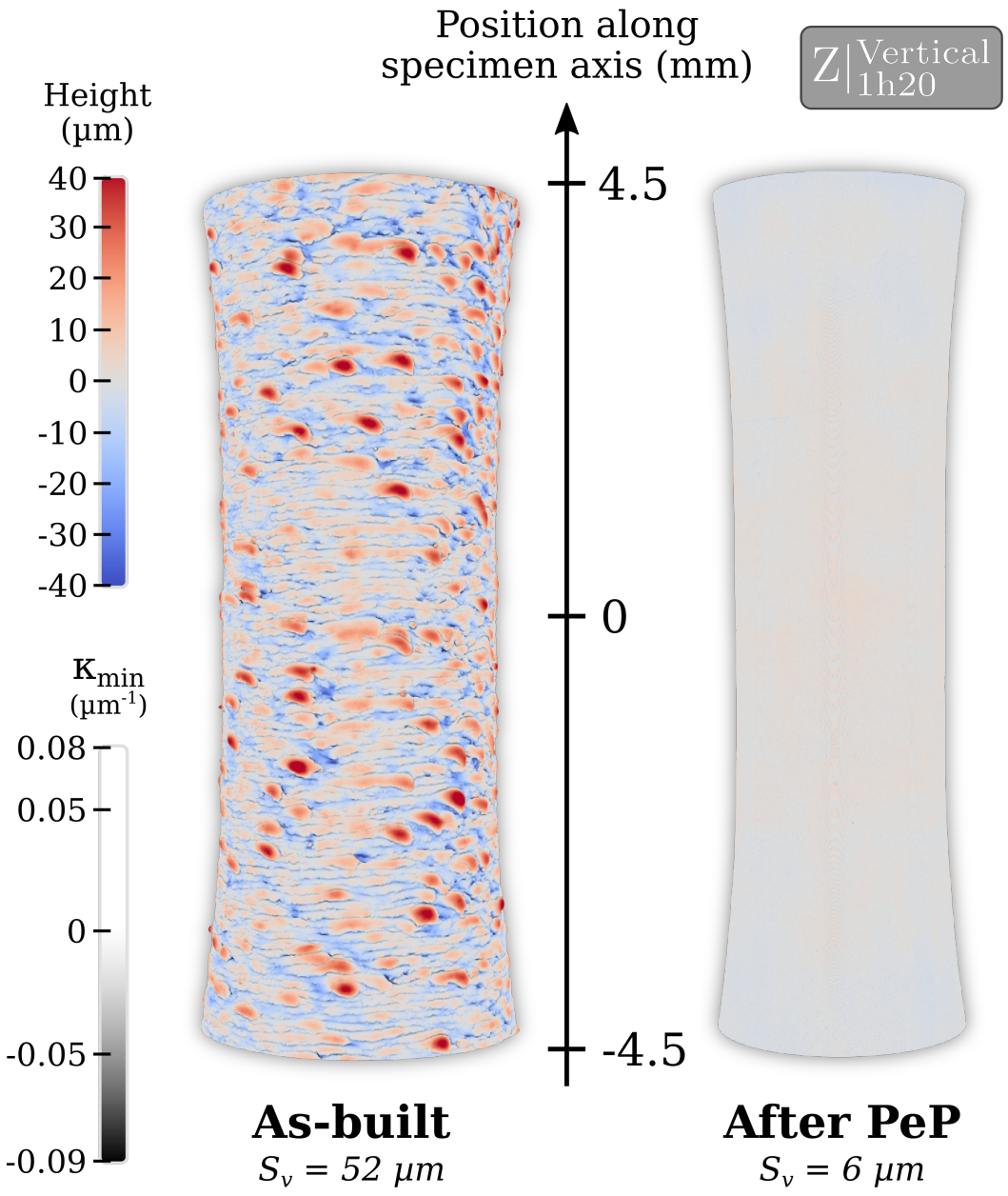

Figure 4.32 | Surface of a Z specimen before and after a 1 h 20 min PeP treatment ($Z|^{Vertical}_{1h20}$ condition). The color used to represent the surface combines the roughness (using $\lambda_c = 0.8$ mm) as well as the minimum curvature (using $r_{curv} = 20$ µm) to exacerbate valleys and details in general. This 1 h 20 min treatment enables to erase all the initial roughness, and no surface holes caused by pores can be seen as in Fig.4.31 for $Z|^{Vertical}_{40min}$ condition.

Cette thèse est accessible à l'adresse : https://theses.insa-lyon.fr/publication/2024ISAL0014/these.pdf
© [F. Steinhilber], [2024], INSA Lyon, tous droits réservés

The influence of PeP on the $45°|^{\text{Vertical}}_{\text{40min}}$ condition is demonstrated in Fig.4.33. Polishing yields a uniformly smooth surface, but upon closer inspection, the down-skin region reveals some pits. They bear resemblance in depth and form to those seen in the $Z|^{\text{Vertical}}_{\text{40min}}$ condition. Since the matter removal thickness for the $45°|^{\text{Vertical}}_{\text{40min}}$ condition (171 ± 7µm) is much larger than the maximum valley depth of the as-built specimen (88 µm), it is considered here that these defects originate as well from sub-surface pores that were brought to the surface by PeP.

Looking at the two magnifying windows, it is possible to notice that most of the surface pits are found in the bottom region of the sample. This observation is consistent with the results shown in 4.3.2.1. Indeed, Fig.4.30 showed that the polishing was done until the near-end of the sub-surface pores. Fig.4.29 showed on its part that the matter removal thickness was lower at the bottom of the specimen. Thus, the higher density of defect at the bottom in Fig.4.33 may be explained by the lower matter removal in this region, which did not enable the complete removal of the surface layer where most pores are located.

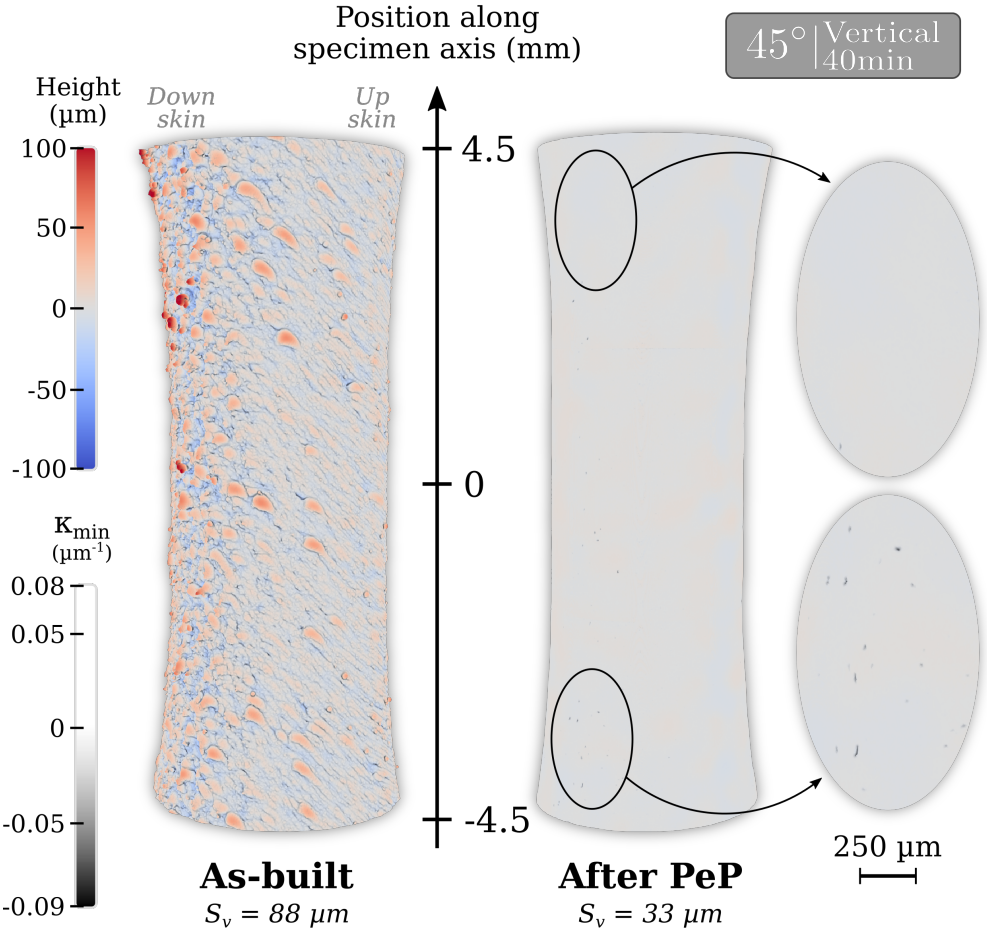

Figure 4.33 | Surface of a 45° specimen before and after a 40 min PeP treatment performed vertically ($45°|^{\text{Vertical}}_{\text{40min}}$ condition). The color used to represent the surface combines the roughness (using $\lambda_c = 0.8$ mm) as well as the minimum curvature (using $r_{curv} = 20$ µm) to exacerbate valleys and details in general. A few small pits can still be identified on the surface after PeP, especially at the bottom of the specimen.

Cette thèse est accessible à l'adresse : https://theses.insa-lyon.fr/publication/2024ISAL0014/these.pdf
© [F. Steinhilber], [2024], INSA Lyon, tous droits réservés

Fig.4.34 shows that for $45°|^{45°}_{40min}$ specimens, PeP leaves significant defects, particularly at the top of the down-skin region. Their presence here, and not in $45°|^{Vertical}_{40min}$ specimens, likely stems from different material removal profiles between the conditions. As evidenced in Fig.4.29, the $45°|^{45°}_{40min}$ condition has minimal material removal at the top of the down-skin area. Additionally, this region is nearly horizontal during fabrication, resulting in maximal roughness. The combination of this initial roughness and minimal material removal explains **the presence of residual valleys after PeP**.

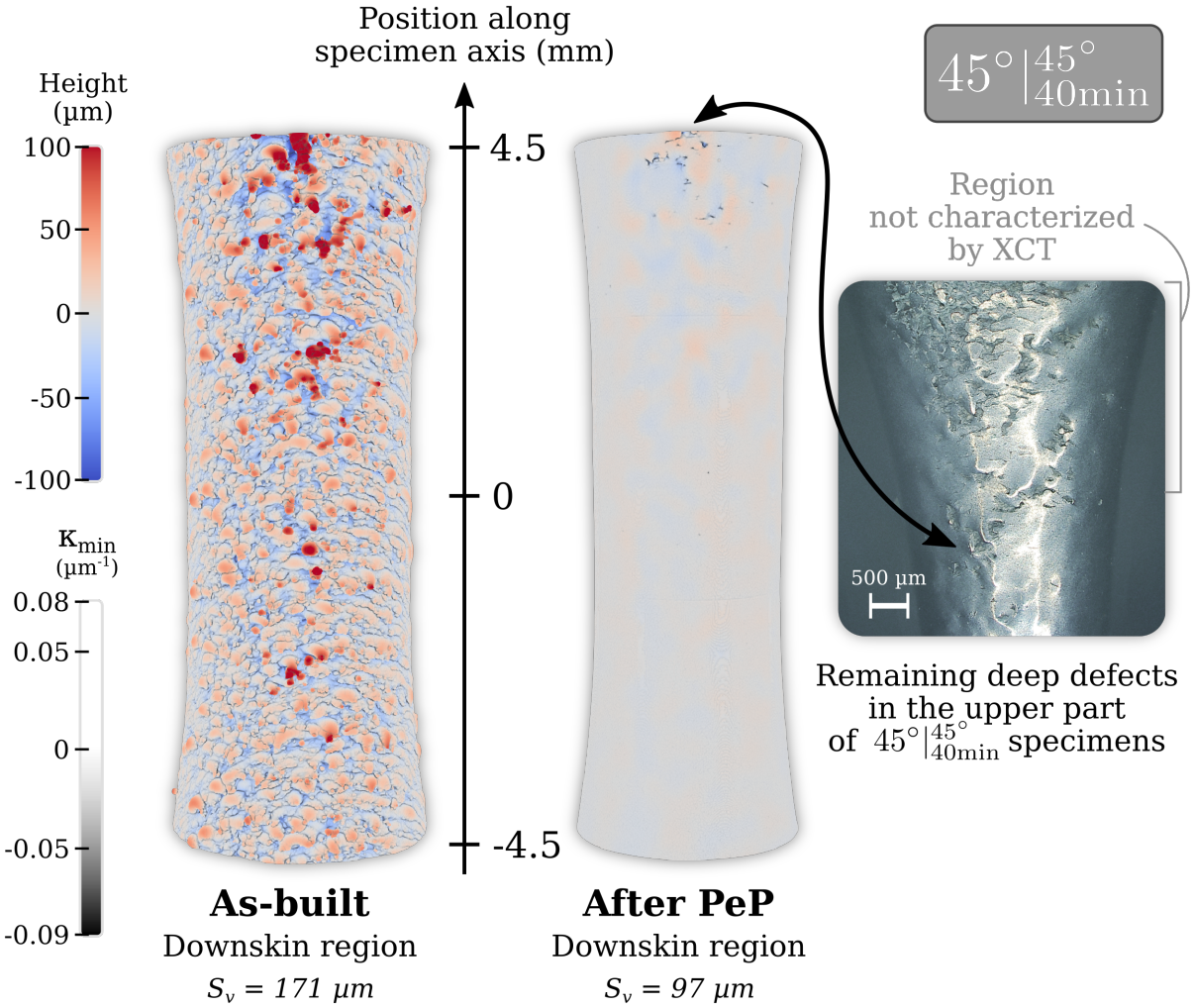

Figure 4.34 | Surface of a 45° specimen before and after a 40 min PeP treatment at 45° ($45°|^{45°}_{40min}$ condition). The color used to represent the surface combines the roughness (using $\lambda_c = 0.8\,mm$) as well as the minimum curvature (using $r_{curv} = 20\,µm$) to exacerbate valleys and details in general. Large and deep valleys can still be identified at the top of the specimen. They are remains of the down-skin surface roughness. Most of the valleys in question are not taken into account by roughness measurements since they are out of the zone characterized by XCT. An optical microscopy image shows that defects grow even larger outside this zone.

Cette thèse est accessible à l'adresse : https://theses.insa-lyon.fr/publication/2024ISAL0014/these.pdf
© [F. Steinhilber], [2024], INSA Lyon, tous droits réservés

However, since XCT scans only enable the characterization of a 9 mm high portion of the specimens, these large defects are mostly not accounted for. The optical microscope observation in Fig.4.34 shows that even larger defects can be seen in higher parts of the specimens that are not characterized by XCT. Yet, as they are far away from the specimens' gauge area, their impact on fatigue tests might be minimal.

Finally, $45°|^{45°}_{40\text{min}}$ specimens are the only ones for which large defects remain after PeP. These defects are located in the upper part of the down-skin region. As evidenced in Fig.4.29, the $45°|^{45°}_{40\text{min}}$ condition has minimal material removal at the top of the down-skin area. Additionally, this region is closest to horizontal during creation, resulting in maximal roughness (see Fig.4.6c). The combination of this initial roughness and minimal removal can explain the residual valleys after PeP and their location in the upper part of the down-skin region.

It is important to notice here that the XCT characterization is limited to a height of 9 mm, which is barely enough to reach the beginning of those defects. The optical microscope image in Fig.4.34 shows indeed that many defects can be seen further in the radius fillet. Although these defects are very large, the fact they are not situated in the specimens' gauge length may lead in practice to a limited impact on fatigue tests.

To understand PeP's impact on roughness evolution more broadly, the evolution of S_a and S_v roughness parameters were analyzed for each specimen. Vertical specimens' roughness evolution ($\text{Z}|^{\text{Vertical}}_{40\text{min}}$ and $\text{Z}|^{\text{Vertical}}_{1\text{h}20}$ conditions) is showcased in Fig.4.35. Each specimen's roughness parameters, before and after PeP, are illustrated. The arithmetical mean height S_a on the x-axis reflects the overall average surface condition, while the maximum valley depth S_v on the y-axis sheds light on the deepest remaining surface defects.

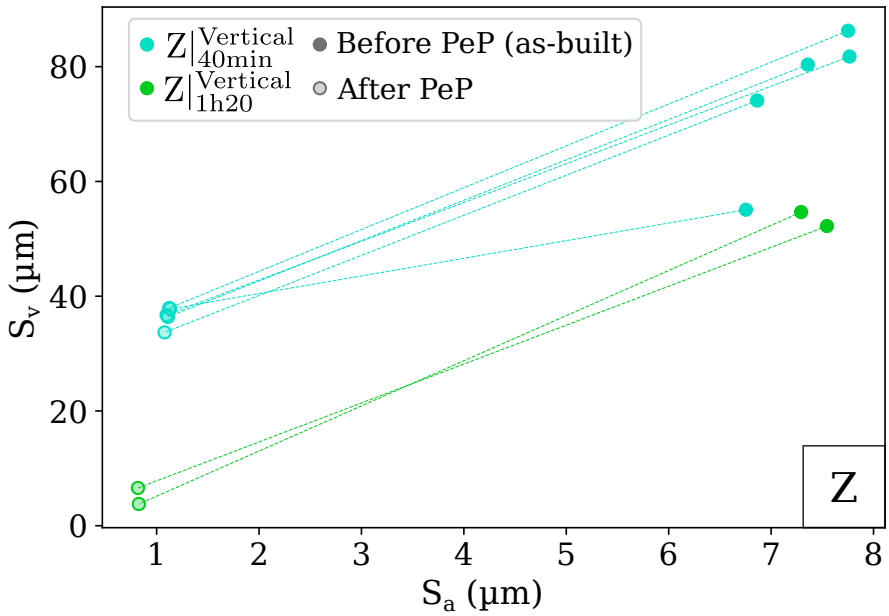

Figure 4.35 | Evolution of S_a and S_v roughness parameters induced by the PeP treatment of Z specimens. Roughness was computed using $\lambda_c = 0.8$ mm and $\lambda_S = 0.03$ mm. Dashed lines are represented only to enable the identification of points that were obtained before and after the PeP treatment of a given specimen. They do not mean that a linear relationship exists between S_a and S_v parameters.

Cette thèse est accessible à l'adresse : https://theses.insa-lyon.fr/publication/2024ISAL0014/these.pdf
© [F. Steinhilber], [2024], INSA Lyon, tous droits réservés

It can be seen on Fig.4.35 that S_a and S_v values are very reproducible for both $\mathrm{Z}|_{40\mathrm{min}}^{\mathrm{Vertical}}$ and $\mathrm{Z}|_{1\mathrm{h}20}^{\mathrm{Vertical}}$ conditions. Similar S_a values are reached in both cases. This is in good agreement with a preceding discussion concerning Fig.4.31 and Fig.4.32 where it could be seen that on average, very smooth surface states are reached for both conditions.

However, using the S_v parameter which is more sensitive to the deepest defects, a clear distinction appears between the two conditions. $\bar{S_v}$ equals to 5 µm for the $\mathrm{Z}|_{1\mathrm{h}20}^{\mathrm{Vertical}}$ condition, which is less than two voxels. In other words, no actual notch-like defect could be detected. On the other side, $\bar{S_v}$ equals to 37 µm for the $\mathrm{Z}|_{40\mathrm{min}}^{\mathrm{Vertical}}$ condition, revealing the presence of pores brought to the surface after polishing as identified in Fig.4.31.

Considering 45° specimens, Fig.4.36 reveals that after polishing, down-skin areas remain comparatively rougher. For instance, in the $45°|_{40\mathrm{min}}^{45°}$ condition, $\bar{S_a}$ equals to 2.36 µm in down-skin and to 0.88 µm in up-skin.

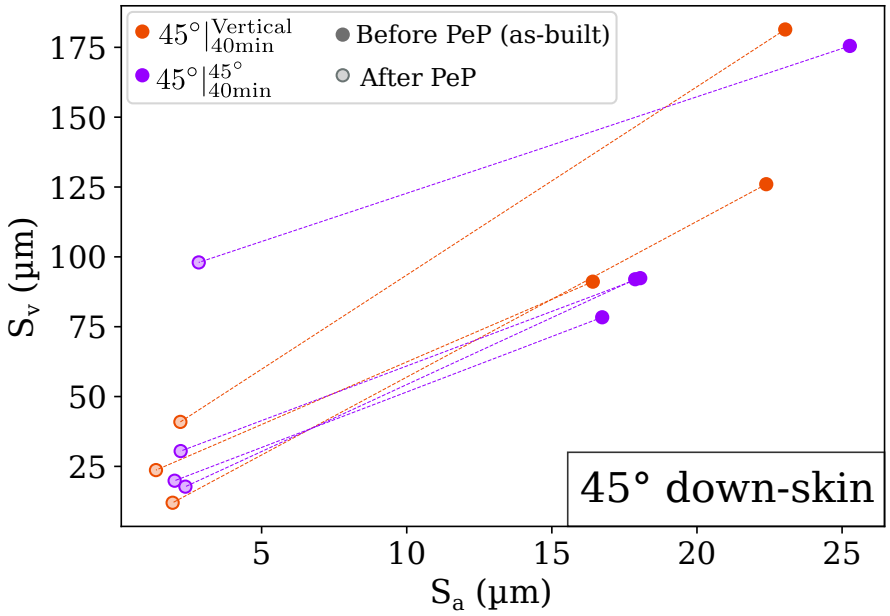

Figure 4.36 | Evolution of S_a and S_v roughness parameters induced by the PeP treatment of 45° specimens in the down-skin region. Roughness was computed using $\lambda_c = 0.8\,\mathrm{mm}$ and $\lambda_S = 0.03\,\mathrm{mm}$. Dashed lines are represented only to enable the identification of points that were obtained before and after the PeP treatment of a given specimen. They do not mean that a linear relationship exists between S_a and S_v parameters.

Results are also more scattered, especially for S_v. For example, the $45°|_{40\mathrm{min}}^{45°}$ specimen illustrated in Fig.4.34 shows an abnormally high S_v value of 97 µm. Fig.4.34 showed the existence of large remaining valleys in the upper part of the down-skin region, responsible for this high measured S_v. Furthermore, the optical microscope observation has shown that even larger and deeper defects are present further away from the gauge length. The same is true for other $45°|_{40\mathrm{min}}^{45°}$ specimens, which means that their relatively low value is due to the fact that the Z span of the XCT scan is not sufficient to capture these defects. S_v values for the $45°|_{40\mathrm{min}}^{45°}$ condition **can thus be considered to be underestimated**. However, one may also argue that the large defects in question should not be taken into account, since they are too far from the gauge length. This makes crack initiation unlikely in this area.

Cette thèse est accessible à l'adresse : https://theses.insa-lyon.fr/publication/2024ISAL0014/these.pdf
© [F. Steinhilber], [2024], INSA Lyon, tous droits réservés

On the contrary, $45°|^{45°}_{40min}$ specimens are smoother in the up-skin region than $45°|^{Vertical}_{40min}$ specimens, see Fig.4.37. They even show results comparable to $Z|^{Vertical}_{1h20}$ specimens with an average $\bar{S_v}$ of 5 µm. These results may indicate that surfaces oriented downwards during PeP are better polished than surfaces oriented upwards, since for the $45°|^{45°}_{40min}$ condition, the up-skin region is oriented downwards.

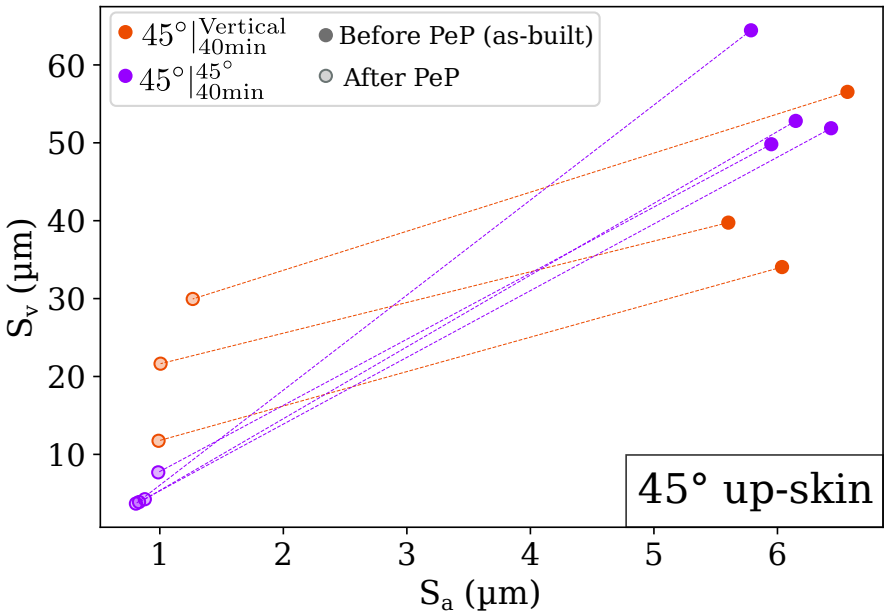

Figure 4.37 | Evolution of S_a and S_v roughness parameters induced by the PeP treatment of 45° specimens in the up-skin region. Roughness was computed using λ_c = 0.8 mm and λ_S = 0.03 mm. Dashed lines are represented only to enable the identification of points that were obtained before and after the PeP treatment of a given specimen. They do not mean that a linear relationship exists between S_a and S_v parameters.

Table 4.2 presents a variety of roughness parameters calculated after PeP across the four tested conditions. For a more detailed description of roughness parameter computations, refer to Chapter 2 and Section 3.4.3.2.

While many key insights from these results are highlighted in previous figures, a notable observation is the predominance of negative skewness S_{sk} in most cases. This contrasts with the mainly positive skewness seen in as-built specimens. This difference arises because, post-PeP, the surface mostly consists of smooth areas interspersed with occasional notches that have negative local heights. Such a pattern is characteristic of surfaces dominated by valleys, which result in negative skewness.

Regarding kurtosis, elevated values in some conditions can be correlated to the existence of occasional, yet notably deep, defects. The observed variability suggests that the occurrence and depth of these defects can differ significantly between specimens. **As a result, variations in fatigue behavior might also be anticipated**. Conversely, the low kurtosis value for conditions like $Z|^{Vertical}_{1h20}$ signifies the lack of exceptionally deep surface irregularities. It indicates that PeP effectively produces a consistently smooth and even surface. **Such a surface is anticipated to exhibit superior fatigue resistance**.

Cette thèse est accessible à l'adresse : https://theses.insa-lyon.fr/publication/2024ISAL0014/these.pdf
© [F. Steinhilber], [2024], INSA Lyon, tous droits réservés

	$\mathbf{Z}\vert^{\text{Vertical}}_{\text{40min}}$	$\mathbf{Z}\vert^{\text{Vertical}}_{\text{1h20}}$	$\mathbf{45°}\vert^{\text{Vertical}}_{\text{40min}}$		$\mathbf{45°}\vert^{\text{45°}}_{\text{40min}}$	
			Down-skin	**Up-skin**	**Down-skin**	**Up-skin**
S_a (µm)	1.11 ± 0.02	0.82	1.83 ± 0.35	1.09 ± 0.13	2.36 ± 0.31	0.88 ± 0.07
S_q (µm)	1.43 ± 0.02	1.03	2.30 ± 0.50	1.41 ± 0.18	3.22 ± 0.69	1.08 ± 0.10
S_z (µm)	43 ± 2	9	34 ± 14	26 ± 7	59 ± 42	8 ± 2
S_v (µm)	37 ± 2	5	26 ± 12	21 ± 7	42 ± 33	5 ± 2
S_{sk}	-0.12 ± 0.11	-0.03	-0.38 ± 0.06	-0.44 ± 0.48	-0.54 ± 0.81	0.02 ± 0.06
S_{ku}	4.78 ± 1.01	-0.10	1.01 ± 0.82	5.65 ± 4.57	8.41 ± 12.52	-0.35 ± 0.05

Table 4.2 | Roughness parameters measured for specimens polished by PeP. Roughness was computed from XCT data using the 3D characterization workflow introduced in Chapter 2. The cut-off values for filters were set to $\lambda_c = 0.8\,\text{mm}$ and $\lambda_S = 0.03\,\text{mm}$. Roughness parameter values are presented in the format (mean $\pm$ std) for conditions where at least 3 specimens were available. Otherwise, only the mean value is given.

4.3.4 Fatigue resistance improvement and change in crack initiation mechanism

Having characterized the surface state post-PeP, the next step is to assess its impact on fatigue properties. Uniaxial fatigue tests were conducted under conditions identical to those of as-built specimens, with details available in Section 4.1.1. Unlike as-built specimens, the PeP specimens' fatigue tests were stopped at 2×10^6 cycles when no failure occurred. Non-failed specimens underwent further testing at elevated stresses for 2×10^6 cycles, increasing the maximum stress value until failure and starting again the cycle count from zero at each stress level. On Wöhler curves, 2×10^6 cycles run-outs get marked by an arrow, and points from the same specimen tested under varying stresses are connected with a dashed line.

Due to the substantial material removal by PeP, XCT was used to measure the specimen's section to set stress levels correctly. The average section across the gauge length was used. Results from M&P and as-built specimens are shown to allow for comparison and better gauge the enhancements resulting from PeP.

The S-N diagram in Fig.4.38 displays results for 45° specimens. It can be seen from Fig.4.38 that PeP significantly enhances fatigue life. A comparable enhancement was observed for both $45°\vert^{\text{Vertical}}_{\text{40min}}$ and $45°\vert^{\text{45°}}_{\text{40min}}$ conditions, though this would require further specimen testing for validation.

Considering available data, the fatigue strength for 45° specimens post-PeP polishing is estimated between 450 MPa and 550 MPa. This translates to **an 80%-120% improvement over as-built specimens**. Although significant, this enhancement is still far from the one provided by machining and manual polishing. The limited improvement can be primarily attributed to **pores either exposed on the surface or slightly beneath it by PeP**. Fig.4.39a-b illustrate two examples of crack initiation sites on $45°\vert^{\text{Vertical}}_{\text{40min}}$ specimen fractures where such defects can be identified.

Cette thèse est accessible à l'adresse : https://theses.insa-lyon.fr/publication/2024ISAL0014/these.pdf
© [F. Steinhilber], [2024], INSA Lyon, tous droits réservés

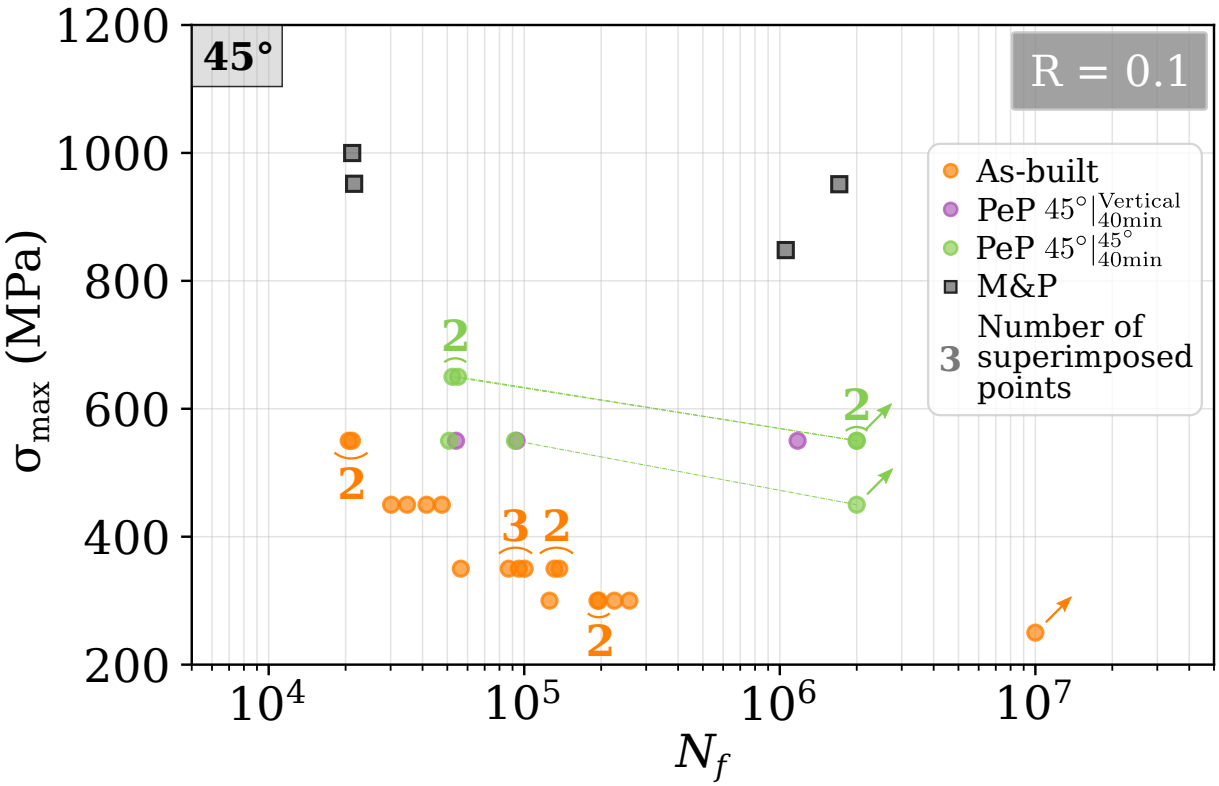

Figure 4.38 | Wöhler for 45° specimens before and after PeP in both 45°|$^{\text{Vertical}}_{\text{40min}}$ and 45°|$^{\text{45°}}_{\text{40min}}$ conditions. Results for 45° as-built specimens and M&P specimens are also shown for comparison.

Fig.4.39a corresponds to the failure on a pore brought to the surface by PeP. It is the most frequent initiation site observed. It can be seen that the inner surface of the defect is somehow degraded, probably under the effects of PeP treatment (see Fig.4.39b for comparison with a subsurface pore with a smooth wall/inner surface).

Fig.4.39b shows another case, where the failure occurred from a sub-surface pore that was brought just beneath the surface by PeP. These two examples confirm the detrimental effect of the few remaining defects on the fatigue properties of specimens polished after PeP, especially if the polishing depth falls close to the sub-surface layer where most pores are located.

For one 45°|$^{\text{45°}}_{\text{40min}}$ specimen, the main crack initiated from a residual surface valley which was not entirely suppressed after PeP. The specimen is the one shown in Fig.4.34, which presented the largest defect among all 45°|$^{\text{45°}}_{\text{40min}}$ specimens. The initiation site can be seen in the SEM-SE observation in Fig.4.40a.

One crack initiation site found on another 45°|$^{\text{45°}}_{\text{40min}}$ specimen, shown in Fig.4.40b, could also correspond to a residual surface valley, although its origin could not be precisely identified. It may as well be a pore brought to the surface as the ones in Fig.4.39a-b. Nonetheless, this shows that insufficient polishing, especially in down-skin areas, residual valleys can facilitate fatigue failure. However, similar fatigue lives for both 45°|$^{\text{Vertical}}_{\text{40min}}$ and 45°|$^{\text{45°}}_{\text{40min}}$ suggests this is not a major influence on fatigue resistance in our case. This can be explained by the fact that residual valleys are mostly located in the upper part of the specimen, far away from the gauge area.

Cette thèse est accessible à l'adresse : https://theses.insa-lyon.fr/publication/2024ISAL0014/these.pdf
© [F. Steinhilber], [2024], INSA Lyon, tous droits réservés

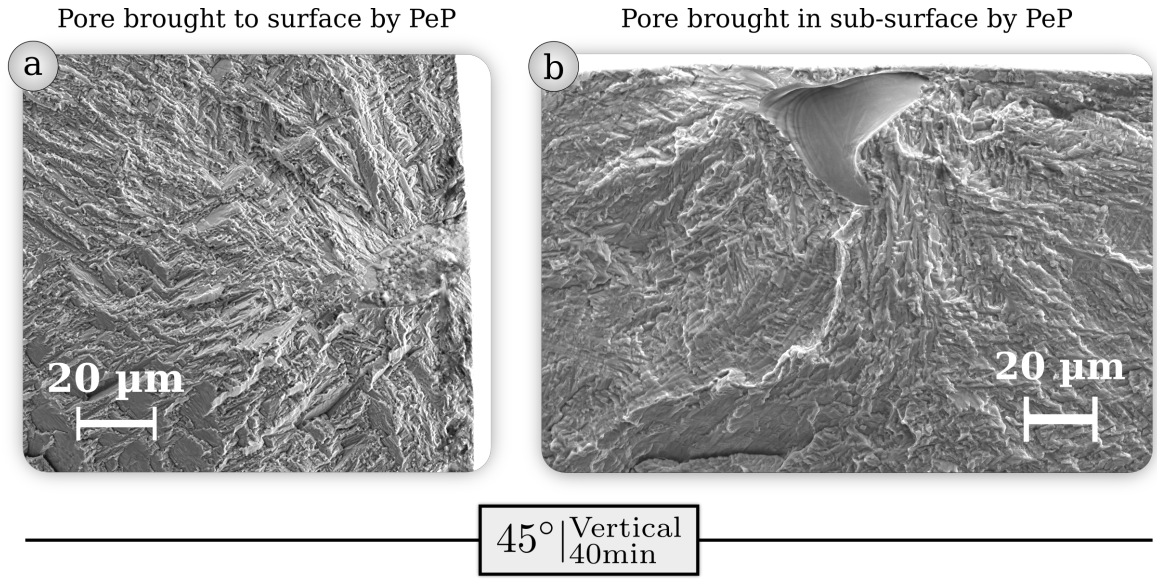

Figure 4.39 | Crack initiation sites of $45°|^{\text{Vertical}}_{\text{40min}}$ specimens, observed by SEM-SE. (a) Pore brought to the surface by PeP. The specimen failed after 54 092 cycles at 550 MPa. (b) Pore brought in sub-surface by PeP. Only a thin ligament separates the pore from the surface. The specimen failed after 1 173 759 cycles at 550 MPa.

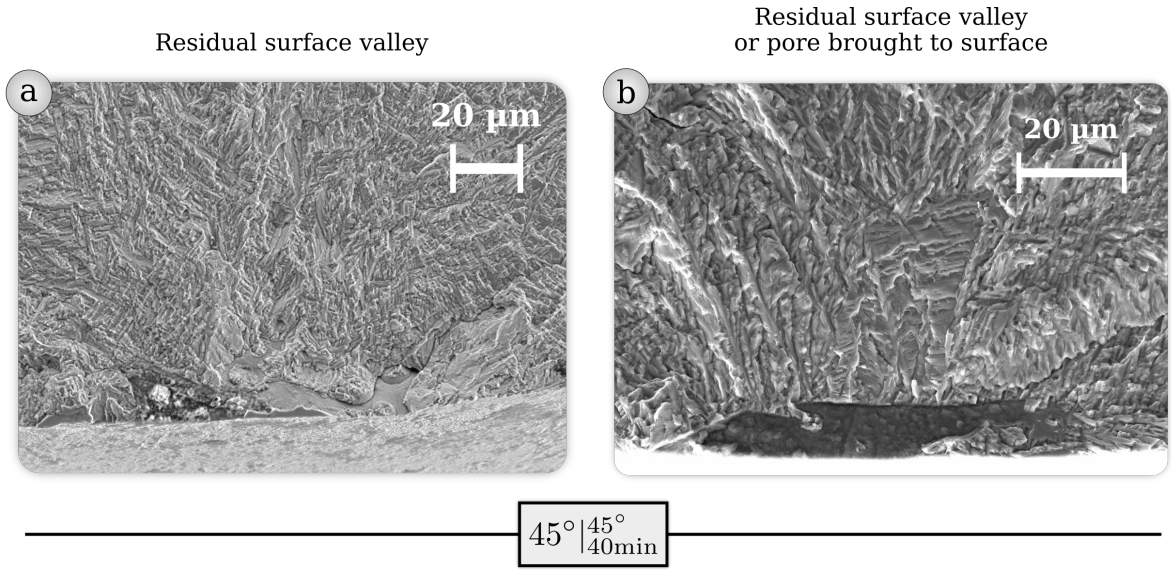

Figure 4.40 | Crack initiation sites of $45°|^{45°}_{\text{40min}}$ specimens, observed by SEM-SE. (a) Residual surface valley in the upper part of the down-skin region. This observation has been observed on the same specimen that was used for Fig.4.34. The specimen failed after 2×10^6 cycles at 450 MPa followed by 91 990 cycles at 550 MPa. (b) Crack initiation site whose origin could not be found with certainty. It corresponds most probably to a residual surface valley or a pore brought to the surface by PeP. The specimen failed after 2×10^6 cycles at 550 MPa followed by 55 086 cycles at 650 MPa.

Cette thèse est accessible à l'adresse : https://theses.insa-lyon.fr/publication/2024ISAL0014/these.pdf
© [F. Steinhilber], [2024], INSA Lyon, tous droits réservés

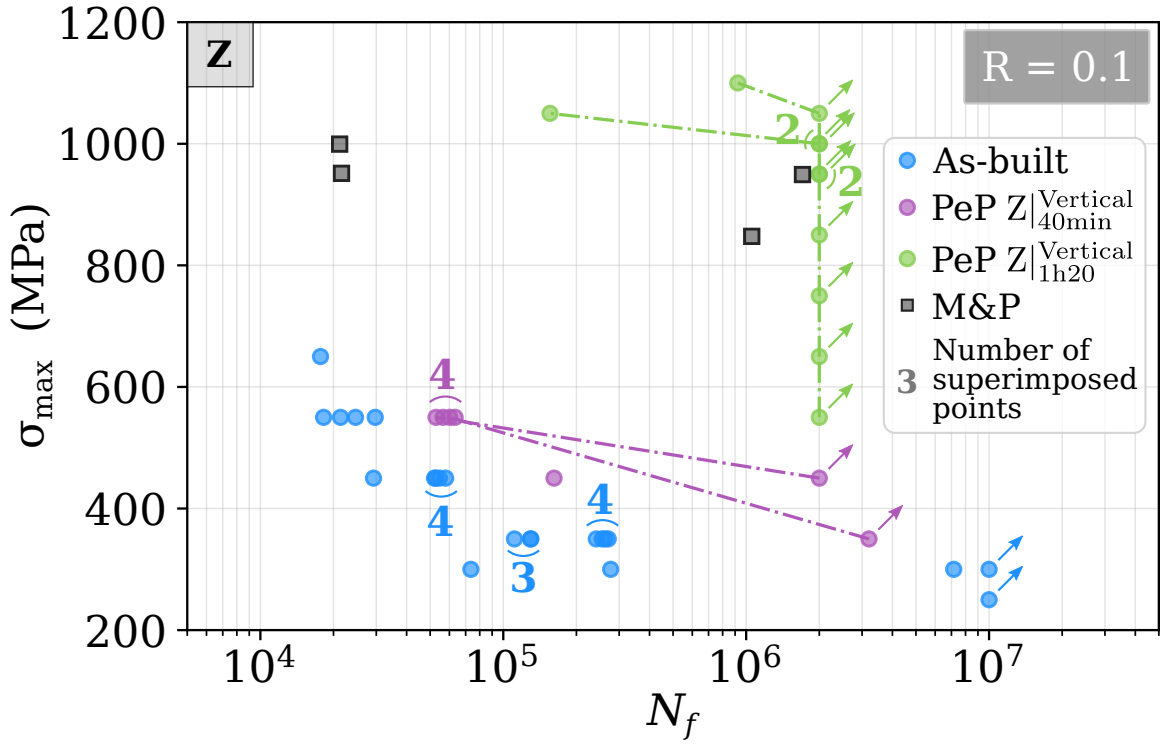

Figure 4.41 | Wöhler for Z specimens before and after PeP in both $Z|^{Vertical}_{40min}$ and $Z|^{Vertical}_{1h20}$ conditions. Results for Z as-built specimens and M&P specimens are also shown for comparison.

Fig.4.41 presents the S-N diagram for Z specimens. The data indicates that the $Z|^{Vertical}_{40min}$ polishing yields lesser improvements than observed for $45°|^{Vertical}_{40min}$ specimens. The enhancement in terms of fatigue strength at 2×10^6 cycles can be estimated to be around 150 MPa. In terms of initiation site, all failures of $Z|^{Vertical}_{40min}$ specimens occurred from pores brought to the surface by PeP, similarly to what has been shown in Fig.4.39a.

However, **the $Z|^{Vertical}_{1h20}$ condition displayed impressive fatigue resistance**, as evidenced by one specimen enduring successive cycles at increasing stresses and finally failing at 1100 MPa. As a reminder, tensile tests in Section 3.3 enabled to estimate the yield strength of Z specimens to be about 1098 MPa. This exceptional resistance might result from the gauge section being particularly small in the $Z|^{Vertical}_{1h20}$ condition, reducing the probability of having a large defect.

Thus, Fig.4.35 showed for instance that no significant surface defects could be found on $Z|^{Vertical}_{1h20}$ using the XCT scan with a 3 µm voxel size. As a result, the crack leading to failure initiated from internal defects in this case.

In terms of porosity, only a few pores could be identified on XCT scans in both $Z|^{Vertical}_{1h20}$ specimens. For instance, only 5 pores could be identified within the specimen that showed the highest fatigue resistance. Apart from one having an equivalent diameter of 32 µm, all have equivalent diameters inferior to 13 µm. The sub-surface pore that caused crack initiation could not even be identified on the XCT scan due to resolution limitation. It is shown on the SEM-SE fractography in Fig.4.42a.

Cette thèse est accessible à l'adresse : https://theses.insa-lyon.fr/publication/2024ISAL0014/these.pdf
© [F. Steinhilber], [2024], INSA Lyon, tous droits réservés

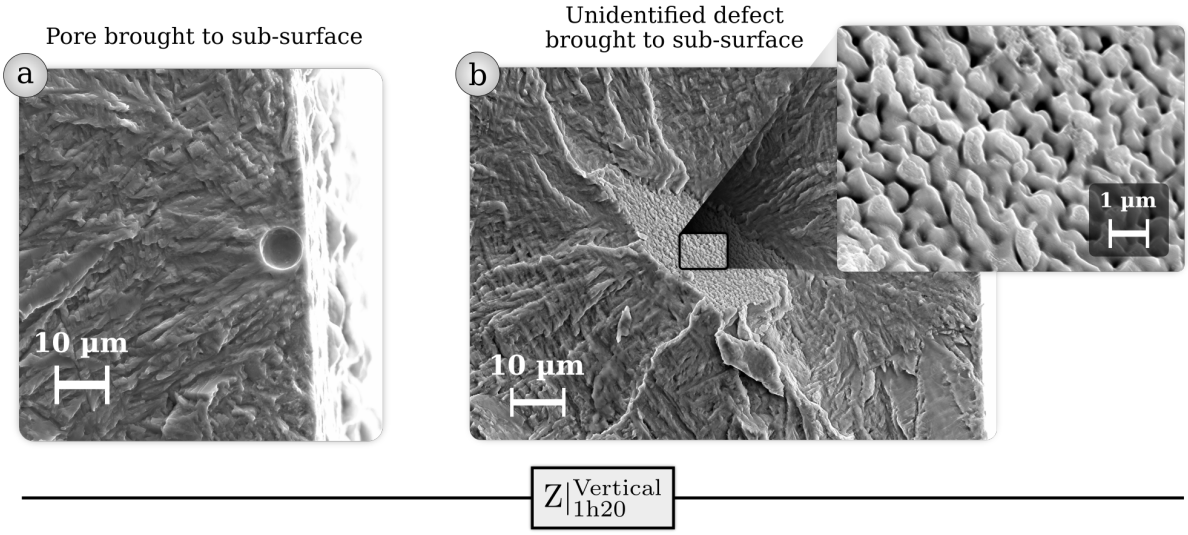

Figure 4.42 | Crack initiation sites of $Z|^{\text{Vertical}}_{\text{1h20}}$ specimens, observed by SEM-SE. (a) 9 µm spherical sub-surface pore. The specimen underwent 2×10^6 cycles successively at 550 MPa, 650 MPa, 750 MPa, 850 MPa, 950 MPa, 1000 MPa, 1050 MPa and failed after 924 055 cycles at 1100 MPa. (b) Unidentified flat defect. The specimen underwent 2×10^6 cycles successively at 950 MPa and 1000 MPa, and failed after 155 739 cycles at 1050 MPa.

Even fewer pores could be identified on the second $Z|^{\text{Vertical}}_{\text{1h20}}$ specimen, with **3 pores in total and a maximum equivalent diameter of 17 µm**. However, crack initiation still occurred from a larger sub-surface defect, as can be seen in Fig.4.42b. This defect could however not be identified on the XCT scan either, probably because of its very flat shape. The nature of this defect is very puzzling due to its very particular rough aspect. No convincing hypothesis could be found to explain its origin.

Fig.4.43 offers a summarized view of the fatigue results for PeP specimens. While as-built specimens mostly show crack initiation on surface valleys, PeP-treated specimens for $45°|^{\text{Vertical}}_{\text{40min}}$, $45°|^{45°}_{\text{40min}}$ and $Z|^{\text{Vertical}}_{\text{40min}}$ conditions exhibit initiation primarily on surface or near-surface pores. This change in the crack initiation site is associated with a limited gain in terms of fatigue resistance. When material removal goes beyond the sub-surface layer that gathers most pores, as is the case for $Z|^{\text{Vertical}}_{\text{1h20}}$ specimens, a drastic increase of fatigue resistance is observed. Only a few defects remain in this condition, often of reduced size. However, a high scatter can be expected in this condition, since a single larger defect would certainly significantly reduce the fatigue resistance.

To give a better idea of predominant initiation sites for each PeP condition, Tab.4.3 counts the number of surface and sub-surface crack initiations for each PeP condition. Results were obtained by analyzing both SEM fractography and XCT scans before/after failure.

Cette thèse est accessible à l'adresse : https://theses.insa-lyon.fr/publication/2024ISAL0014/these.pdf
© [F. Steinhilber], [2024], INSA Lyon, tous droits réservés

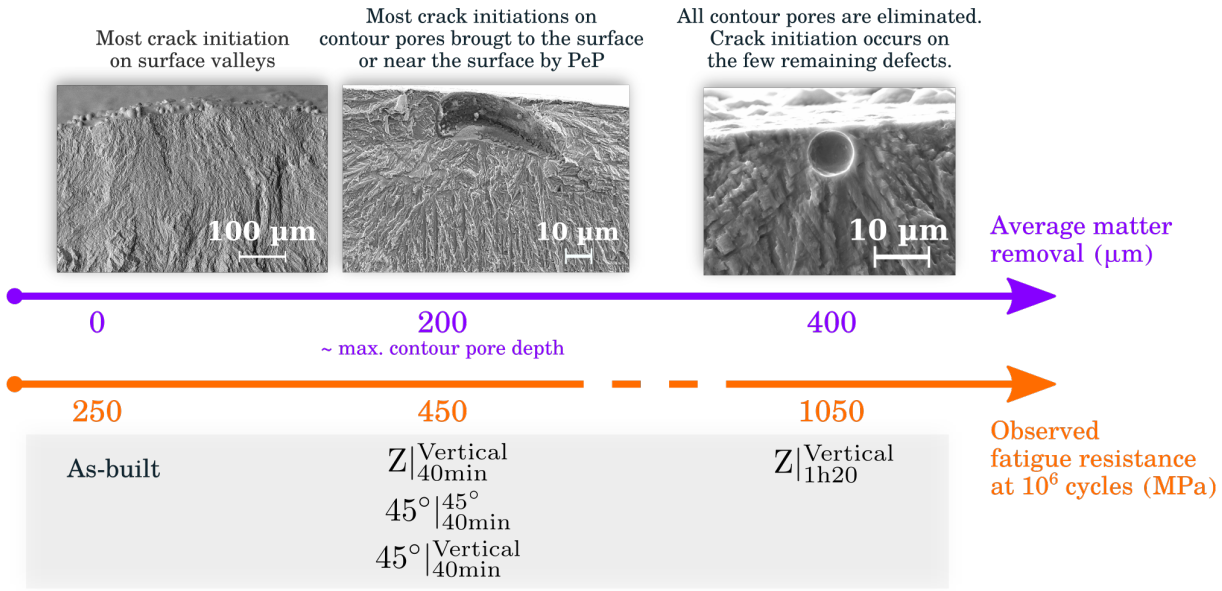

Figure 4.43 | Evolution of fatigue resistance and crack initiation mechanisms with increases PeP matter removal. *Contour pores* refer to the pores located at about 140 µm from the surface, between the contour scans and the bulk material (see Section 3.4.2).

	$Z|^{Vertical}_{40min}$	$Z|^{Vertical}_{1h20}$	$45°|^{Vertical}_{40min}$	$45°|^{45°}_{40min}$
Pore brought to the surface	5		2	2
Pore brought near the surface		1	1	
Residual valley				1
Unidentified nature		1		1

Table 4.3 | Number of crack initiation on surface defects (mostly pores brought to the surface by PeP) and sub-surface pores for each PeP condition. The number of defects that could not be identified on the surface extracted from the XCT scan is also specified. This issue comes either from a lack of resolution or simply from the fact that the sub-surface defect had no connection on the surface and was therefore not present in the extracted surface.

Cette thèse est accessible à l'adresse : https://theses.insa-lyon.fr/publication/2024ISAL0014/these.pdf
© [F. Steinhilber], [2024], INSA Lyon, tous droits réservés

Intermediate summary

This chapter focused on assessing the uni-axial ($R = 0.1$) fatigue properties of L-PBF Ti64 with different post-treatment conditions. Initial tests targeted specimens with as-built surfaces, which had only been subjected to a stress-relief heat treatment for 2 h at 720 °C. Specimens were manufactured both vertically and at 45°, to gauge the influence of build orientation.

For as-built specimens, all failures originated from the surface. Detailed insights from 3D XCT characterization before and after failure reveal that killer defects are primarily surface valleys. These drastically reduced the fatigue resistance of the material, evident when comparing against the fatigue resistance of vertically built, machined and manually polished (M&P) specimens. Fatigue strength at 2×10^6 cycles for as-built specimens, regardless of build orientation, is found close to 250 MPa. In contrast, M&P specimens reached a fatigue strength of roughly 850 MPa. There is a small yet notable difference in the fatigue life between vertically built and 45° specimens. The latter display shorter fatigue lives, likely due to the increased roughness in their down-skin area, which consistently was the site of failure.

Another part of the study concerned specimens subjected to a more intense heat treatment (4 h at 860 °C). This focused on the effects of the α-*case*, a brittle oxygen-contaminated surface layer forming during heat treatments. In our case, the treatment yielded a 70 µm layer. This layer further compromised the fatigue resistance of as-built specimens, though possibly not as seriously as surface roughness. The diminished fatigue life could be due to the α-case's tendency to promote crack initiation.

Plasma Electrolytic Polishing (PeP), a recent surface polishing method, was tested as a solution to mitigate both roughness and α-case in as-built surfaces. While some specimens experienced uneven material removal or unexplained polishing failures, the process effectively minimized initial surface roughness. Because material removal during a 40 min PeP treatment was insufficient (about 180 µm), sub-surface pores were brought to the surface, leading to the formation of surface pits. Consequently, cracks emerged from these exposed pores, limiting the improvement in fatigue resistance. The fatigue resistance at 2×10^6 cycles after such treatment improved from 250 MPa to approximately 400 to 550 MPa. A more prolonged PeP treatment (1 h 20 min) polished beyond this porosity overconcentration layer, significantly enhancing fatigue resistance. Thus, the fatigue strength at 2×10^6 cycles for these specimens was larger than 1000 MPa, slightly surpassing M&P samples.

While PeP offers enhanced fatigue properties, it may not be feasible for many practical scenarios. Factors such as complex part shapes or prohibitive post-processing costs and time considerations might hinder its adoption. Hence, understanding, modeling, and predicting the influence of as-built surface defects on fatigue properties remain crucial. Traditional models, like the Murakami parameter $\sqrt{area}$, fall short when addressing the complexities of surface valleys leading to failure. Thus, the search for alternative methods is explored in Chapter 5.

Cette thèse est accessible à l'adresse : https://theses.insa-lyon.fr/publication/2024ISAL0014/these.pdf
© [F. Steinhilber], [2024], INSA Lyon, tous droits réservés

Chapter 5

Quantitative analysis of surface defects harmfulness

Contents

5.1 Surface defects segmentation 154

5.1.1 Detailed methodology 155

5.1.2 Segmentation of valleys and pit-like defects 158

5.1.3 Segmentation of protrusions/peaks 160

5.2 Relationships between fatigue resistance and parameters derived from the surface characterization using XCT 160

5.2.1 Parameters selected to reflect surface defects harmfulness 161

5.2.2 Correlation between the selected parameters and the fatigue lifetime 163

5.3 Killer defect prediction 168

5.3.1 Application to surface-treated specimens (PeP) 169

5.3.2 Application to specimens with as-built surfaces 178

Intermediate summary 183

Chapter 4 primarily focused on the description of fatigue properties and defects at the origin of failure. This chapter aims at rationalizing the impact of surface defects on fatigue, based on the analysis of XCT data. Specimens in their as-built state and those polished by PeP will be analyzed. Specimens subjected to a heat treatment at 860 °C have been excluded from our analysis to alleviate the effect of α-case formation or changes in microstructure.

The first section introduces the methodology employed to segment surface defects, i.e. to identify them. In other words, this step consists of going from a description of the surface as a scalar field (= values such as K_t^* at each surface voxel) to a defect-based description (= a single K_t^* value associated with each segmented defect). This defect segmentation will be used in the subsequent sections.

Cette thèse est accessible à l'adresse : https://theses.insa-lyon.fr/publication/2024ISAL0014/these.pdf
© [F. Steinhilber], [2024], INSA Lyon, tous droits réservés

The second section is dedicated to the study of the relationship between parameters measured from XCT data (e.g. K_t^*) and the experimentally measured fatigue resistance of samples with different surface conditions (as-built Z and 45°, PeP...). The aim is to evaluate whether the parameters measured from XCT such as K_t^* can give quantitative and reliable information about the fatigue lifetime at a given stress level, or about the maximum stress level that can be reached for a targeted fatigue lifetime.

Finally, the third section evaluates the ability of the methodology to predict the location of killer defects, similarly to what has been shown for chemically etched E-PBF specimens in Chapter 2, in Section 2.4.

5.1 Surface defects segmentation

The main objective of this section is to **provide a tool to segment surface defects that are likely to initiate cracks during fatigue loading**. It concerns mainly valleys in as-built specimens and pit-like defects (= pores brought to the surface) in specimens polished by PeP. The developed methodology has also been used to segment protrusions/peaks, i.e. the highest surface features. Although they are unlikely to initiate a crack, their segmentation is required for some calculations in the subsequent sections. This explains why this topic is addressed here.

Fundamentally, the same method has been used to segment all kinds of surface defects in specimens with different surface states (vertical or 45° specimens, before or after PeP). However, the method requires to adjust several parameters to take into account the particularities of each case.

Identifying pit-like defects in PeP-polished specimens and protrusions in as-built specimens turned out to be relatively straightforward. These defects are usually well-identified. However, isolating valleys in as-built specimens is more challenging due to several reasons discussed hereafter:

- The very elongated (and sometimes tortuous) shape of valleys.
- The fact that valleys are not well separated from each other. They often form a sort of *valley network* that can make it difficult to define separated defects, especially in down-skin regions in 45° specimens.
- The resolution of XCT scans is often too low to accurately capture the valleys' depth and morphology. This likely leads to underestimating their depth and curvature, further complicating their separation from the rest of the surface. Moreover, the underestimation of valley depth and curvature is not necessarily homogeneous along valleys. As a result, a single valley can appear from the XCT scan as several fragments of valleys that are separated because the resolution was not high enough to properly capture the entire valley. Finally, the limited resolution makes results (especially curvature) noisy, which further hinders the segmentation of such defects.

The segmentation method was chosen to best overcome these difficulties. Its different steps are detailed hereafter for an as-built (45°) specimen. Examples are then shown for the segmentation of potential killer defects (i.e. valleys or pit-like defects) for all surface states, and finally, other examples are given for the segmentation of protrusions.

Cette thèse est accessible à l'adresse : https://theses.insa-lyon.fr/publication/2024ISAL0014/these.pdf
© [F. Steinhilber], [2024], INSA Lyon, tous droits réservés

5.1.1 Detailed methodology

The defect segmentation is achieved in 3 steps:

1. **Thresholding** of the *defects points* (i.e. surface points that are considered to belong to a defect) based on their curvature or height value.
2. **Clustering** of these points to define defects.
3. **Cleaning** the identified defects by removing the smallest ones.

As shown in Section 4.1.3.2, valleys are most easily identified based on their low κ_{min} or κ_{σ} values (the sign being taken into account). Thus, defect points are first separated from the rest of the surface by thresholding, based on the local curvature.

While κ_{min} successfully reveals valleys, it does not seem suited for their segmentation since it does not allow to differentiate those that are parallel to the specimens' axis from those that are perpendicular to it. Therefore, using κ_{min} would make it very difficult to segment individual valleys, as many of the valleys perpendicular to the specimen axis would be connected by valleys that are parallel to the specimen axis. This would lead to the segmentation of valley networks, especially in down-skin regions of 45° specimens, see Fig.5.2c.

To avoid this problem, the curvature oriented in the direction of the specimens' axis, **κ_{σ}, is used instead of κ_{min}**. A drawback of this method is that when computed at a fine scale, κ_{σ} is more noisy than κ_{min}. For this reason, the curvature is computed here at a relatively large scale, i.e. using $r_{curv} = 50\,\mu m$.

The value for the threshold is determined automatically based on the histogram of the κ_{σ} values. The method is **similar to that of the triangle threshold for bimodal histograms (TTBH)** introduced in Section 2.2.1. The definition of the threshold is schematically illustrated in Fig.5.1.

As for the TTBH, the value of the threshold is determined by maximizing the distance d between the hypotenuse of the triangle (orange dashed lines in Fig.5.1) and the normalized histogram. This enables the separation of the main histogram peak and the left tail, which contains points with the lowest κ_{σ}, i.e. defect points. However, the obtained threshold value is not always the most suitable. In some cases, slightly increasing or decreasing the threshold value allows to achieve better results. To allow for such flexibility, an *offset* parameter is included and can be set between -1 and 1. This modifies the final threshold value as schematized in Fig.5.1.

Fig.5.2a-f show the surface before and after thresholding of a 45° specimens (*offset* = +0.4), in both down-skin and up-skin regions. The surface is represented in grayscale using the minimum curvature computed at a rather low scale ($r_{curv} = 20\,\mu m$) to provide a detailed visualization of the surface. Fig.5.2c shows the complex network of interconnected valleys that would be identified if κ_{min} was used instead of κ_{σ}. Contrariwise, **the use of κ_{σ} breaks this network and results in separated defects**, see Fig.5.2d,f.

A clustering algorithm called DBSCAN is then used to gather defect points together, and thus obtain a set of isolated and well-identified defects. Details on how this algorithm works can be found in [EST 96]. Two parameters are required in this model: *Eps* and *MinPts*. The meaning of the *MinPts* will not be discussed extensively here, since its value has always been set to 1 in our case. With *MinPts*= 1, the DBSCAN algorithm simply clusters together all points that are separated by a distance shorter than *Eps*.

Cette thèse est accessible à l'adresse : https://theses.insa-lyon.fr/publication/2024ISAL0014/these.pdf
© [F. Steinhilber], [2024], INSA Lyon, tous droits réservés

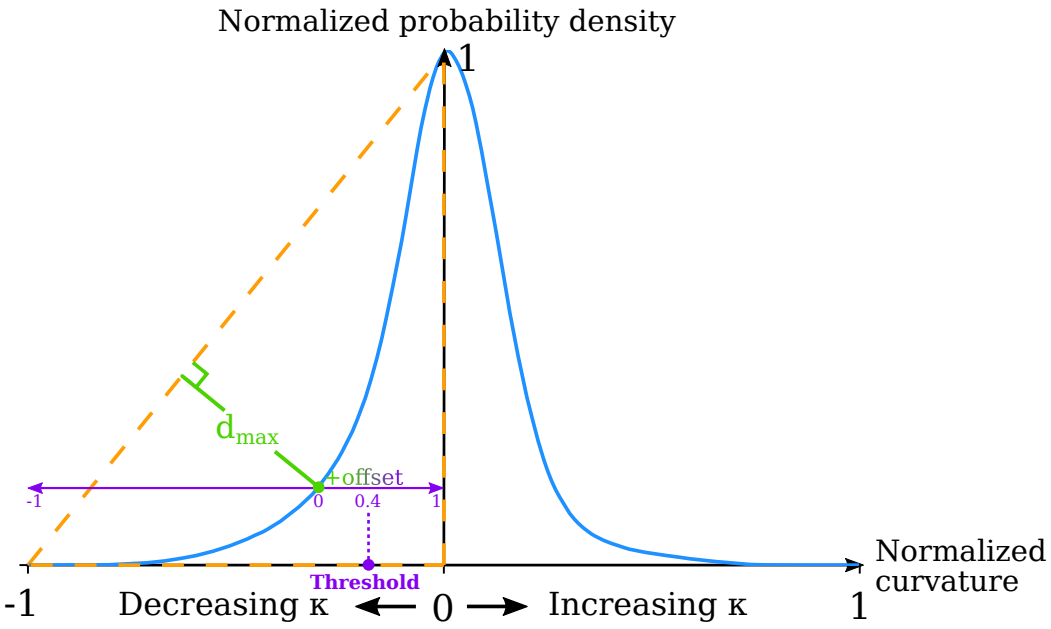

Figure 5.1 | Definition of the method for the automatic determination of the threshold for valleys thresholding, based on κ_σ values. The threshold is computed using the normalized histogram computed for $\kappa_\sigma(r_{curv} = 50\,\mu m)$ by KDE.

A small adjustment is introduced here to further improve the ability of the model to cluster elongated valleys that are perpendicular to the specimen axis, without connecting two parallel transverse valleys that are close to one another. To do this, all points are dilated along the specimen axis by a factor *aspect_ratio*, e.g. equal to 5 for as-built 45° specimens. In other words, the component of each point along the specimen axis (i.e. the Z component for vertical specimens) is multiplied by *aspect_ratio*, which artificially increases the distance between points along the specimen axis. This **prevents to some extent the algorithm from merging two parallel valleys** that are very close to each other at some point.

After clustering, many of the identified clusters are small in size. This leads to high numbers of clusters that are not necessarily significant. For instance, 2949 clusters were found for the specimen shown in Fig.5.2. To reduce this number and keep only the most significant clusters, only the ones having a size greater than *min_cluster_size* were kept. The minimum cluster size was set at 500 for as-built 45° specimens, which resulted in a final number of clusters of 692.

Cette thèse est accessible à l'adresse : https://theses.insa-lyon.fr/publication/2024ISAL0014/these.pdf
© [F. Steinhilber], [2024], INSA Lyon, tous droits réservés

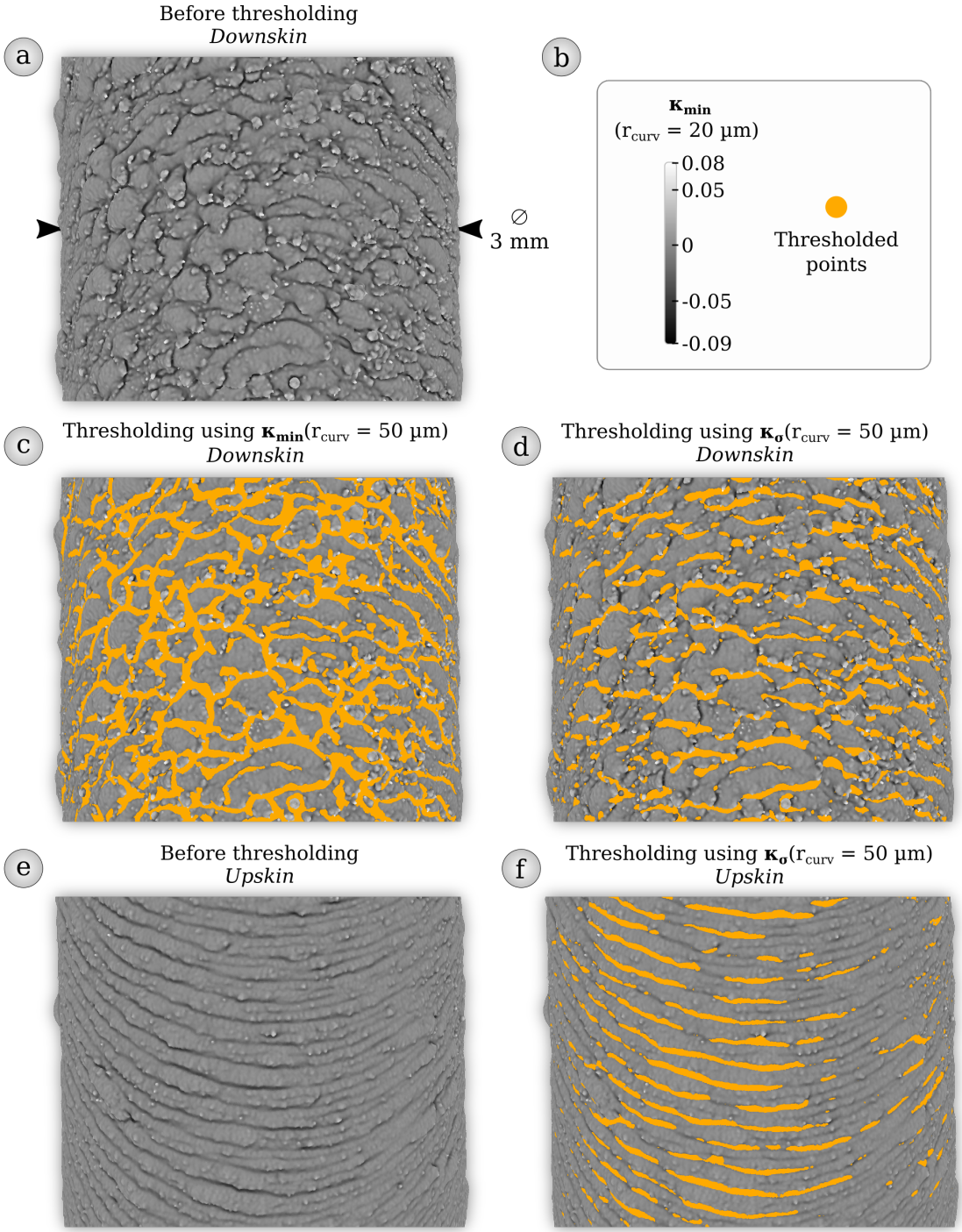

Figure 5.2 | Identification of surface defects (valleys) by thresholding the local curvature. Example based on the surface of an as-built 45° specimen. (a) Downskin area represented by $\kappa_{min}(r_{curv} = 20\,\mu m|\lambda_S = 0.03\,mm)$. (b) Color code for all other subfigures. (c) Thresholded points (in orange) using as threshold $\kappa_{min}(r_{curv} = 50\,\mu m) = -0.0071\,\mu m^{-1}$. (d) Thresholded points (in orange) in down-skin using as threshold $\kappa_{\sigma}(r_{curv} = 50\,\mu m) = -0.0071\,\mu m^{-1}$. (e) Upskin area represented by $\kappa_{min}(r_{curv} = 20\,\mu m|\lambda_S = 0.03\,mm)$. (f) Thresholded points (in orange) in up-skin using as threshold $\kappa_{\sigma}(r_{curv} = 50\,\mu m) = -0.0071\,\mu m^{-1}$.

Cette thèse est accessible à l'adresse : https://theses.insa-lyon.fr/publication/2024ISAL0014/these.pdf
© [F. Steinhilber], [2024], INSA Lyon, tous droits réservés

5.1.2 Segmentation of valleys and pit-like defects

The parameters used for each surface state for the segmentation of valleys or pit-like defects are given in Tab.5.1. They were all chosen manually.

	as-built Z	**as-built 45°**	**PeP**
offset	+0.5	+0.4	-0.1
Eps	20	10	2
aspect_ratio	5	5	1
min_cluster_size	500	500	20

Table 5.1 | Parameters used for the main valleys segmentation in each surface state condition: as-built Z or 45°, as well as specimens polished by PeP (all conditions included).

The result of the clustering for the as-built 45° specimen shown in Fig.5.2 is presented in Fig.5.3a-b. Likewise, the results of the clustering for an as-built Z specimen and for a Z specimen polished by PeP are shown in Fig.5.4a-b and Fig.5.5a-b respectively.

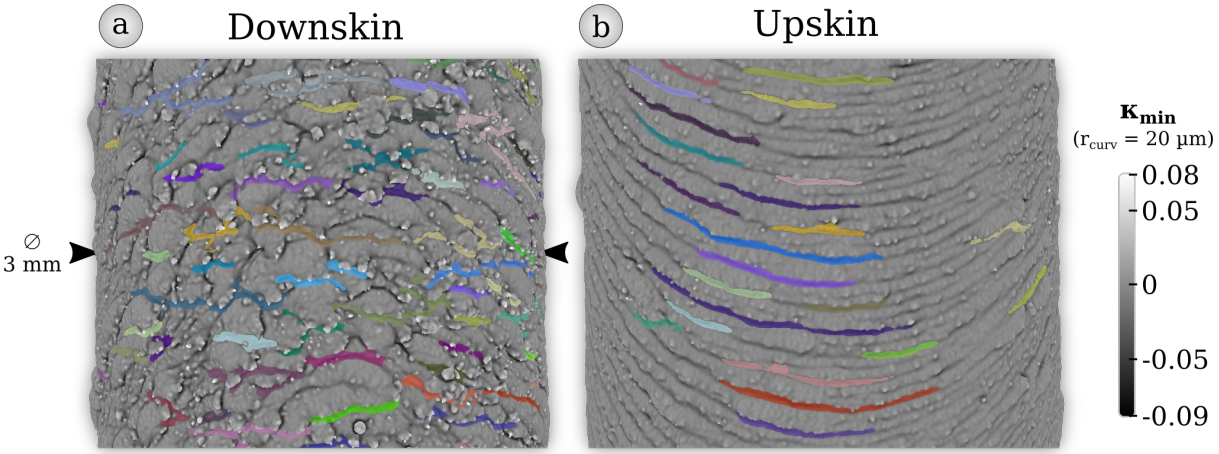

Figure 5.3 | Final valleys segmentation in (a) down-skin and (b) up-skin regions of an as-built 45° specimens. A random color is attributed to each cluster.

Overall, the quality of the segmentation seems **reasonable given the resolution** of the 3D images. However, we can see in Fig.5.3a-b and Fig.5.4a-b that **a significant proportion of the valleys are not or only partially captured**, a problem that could be circumvented by using more advanced segmentation techniques and/or higher resolution XCT scans.

Cette thèse est accessible à l'adresse : https://theses.insa-lyon.fr/publication/2024ISAL0014/these.pdf
© [F. Steinhilber], [2024], INSA Lyon, tous droits réservés

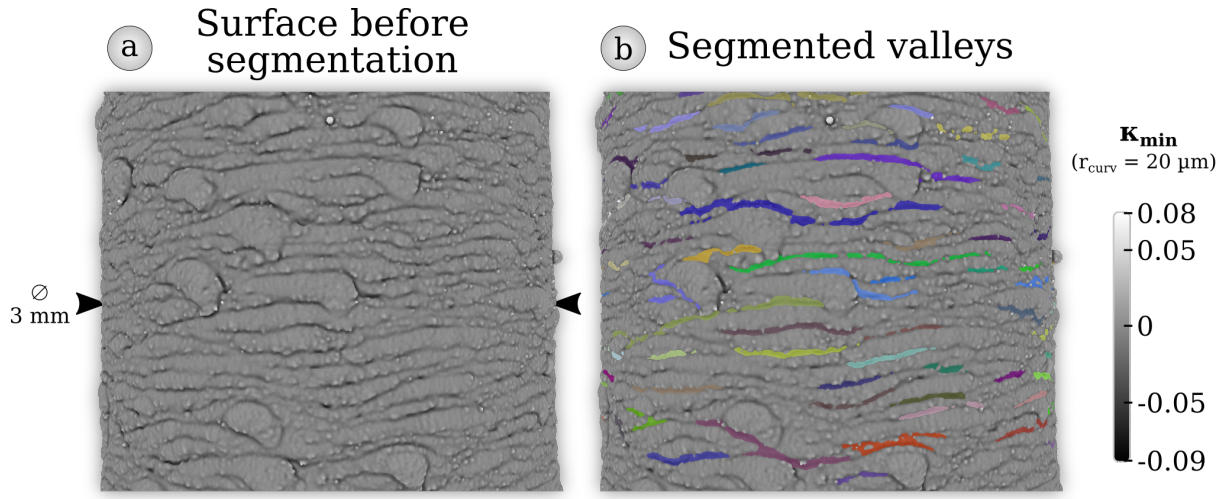

Figure 5.4 | Valleys segmentation on a Z specimen. (a) Surface before segmentation. (b) Segmentation result. A random color is attributed to each cluster.

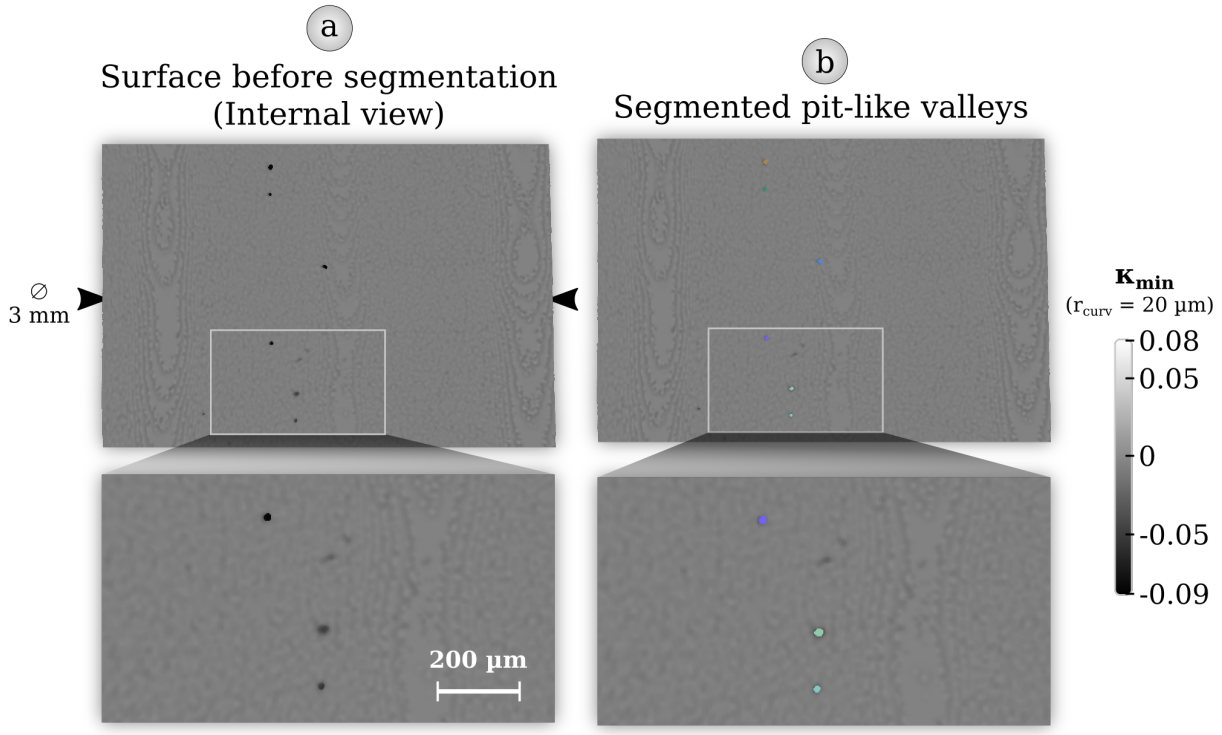

Figure 5.5 | Pit-like defects segmentation on a Z specimen polished by PeP ($Z|^{Vertical}_{40min}$ condition). (a) Surface before segmentation. (b) Surface after segmentation. A random color is attributed to each cluster.

Cette thèse est accessible à l'adresse : https://theses.insa-lyon.fr/publication/2024ISAL0014/these.pdf
© [F. Steinhilber], [2024], INSA Lyon, tous droits réservés

5.1.3 Segmentation of protrusions/peaks

Since protrusions have much larger width and height, and exhibit a more rounded morphology, their segmentation is easier than that of valleys. The κ_σ parameter is not necessarily the most suited in such a case. A more simple roughness measurement is contrariwise very well adapted. Thus, the methodology presented for valley segmentation can simply be applied, using the roughness measurement instead of κ_σ. Clusters will thus be formed from surface points that have the highest height. To do that, the thresholding method illustrated in Fig.5.1 is adapted to isolate the right tail of the height distribution (highest values) instead of the left tail.

Eps and *aspect_ratio* parameters were taken equal to 2 and 1 respectively, which roughly means that only points in direct contact will be clustered together, without any preferential direction. *offset* and *min_cluster_size* parameters are taken equal to -0.25 and 1000 respectively, for both as-built Z and 45° specimens. The segmentation of protrusions has not been performed on specimens polished by PeP, since none is left after polishing.

As an example, the result of protrusions segmentation in the same area of the Z specimen shown in Fig.5.4 is presented in Fig.5.6a-b. All the main protrusions are identified.

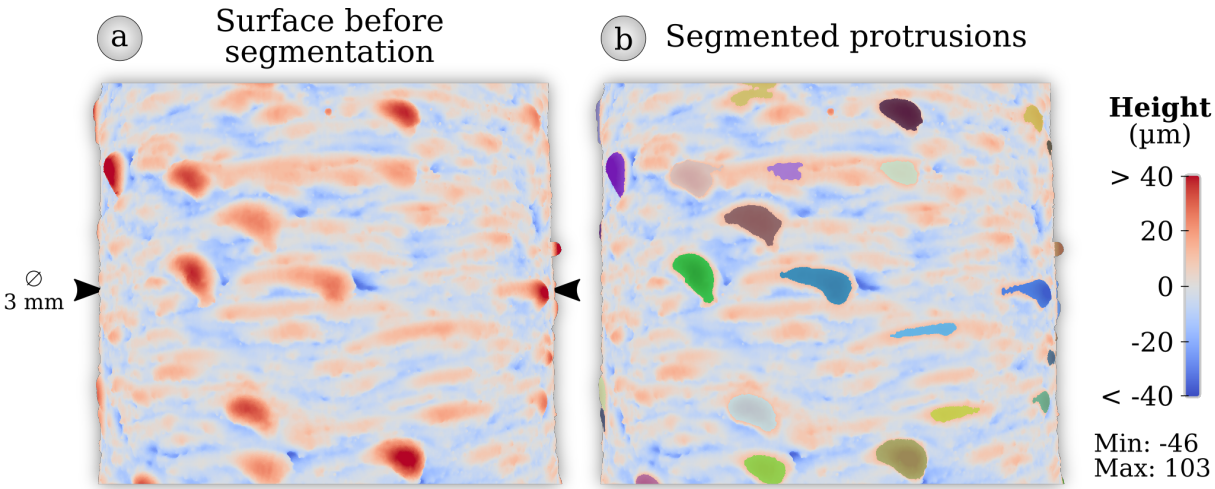

Figure 5.6 | Protrusions segmentation on a Z specimen. (a) Surface before segmentation. (b) Surface after segmentation. A random color is attributed to each cluster.

5.2 Relationships between fatigue resistance and parameters derived from the surface characterization using XCT

The aim of this section is to test the ability of different parameters (e.g. the roughness parameter S_a), calculated for a given specimen, to inform about the impact of surface defects on the fatigue resistance.

Cette thèse est accessible à l'adresse : https://theses.insa-lyon.fr/publication/2024ISAL0014/these.pdf
© [F. Steinhilber], [2024], INSA Lyon, tous droits réservés

5.2.1 Parameters selected to reflect surface defects harmfulness

Several parameters possibly reflecting the surface defects' harmfulness were evaluated, all computed using roughness and curvature measurements based on XCT data. Roughness and curvature were measured using $\lambda_c = 0.8\,\text{mm}$, $r_{curv} = 20\,\mu\text{m}$ and $\lambda_S = 0.03\,\text{mm}$. All parameters were computed over a height of 9 mm centered on the specimens' gauge area. Here, all the surface is used, i.e. **measurements are not restricted to the down-skin area for 45° specimens**.

First, conventional S_a **and** S_v **roughness parameters** were used. An additional parameter was evaluated, in an attempt to combine several roughness parameters in a more comprehensive way than considering each roughness parameter alone. This parameter is based on a model proposed by [ARO 99] that has been introduced in Section 1.4.2.2. The model derives an *effective stress concentration factor* from roughness measurements, a value that should quantify the notch effect generated by the surface roughness. This parameter is conventionally used to predict the fatigue limit of specimens based on roughness data. However, here, it was used as an index reflecting the impact of surface roughness on the fatigue resistance.

Since this model was defined for 2D roughness profile measurements, some adjustments were made here to extend it in 3D. The obtained formula for the **effective stress concentration factor** $\bar{K}_t^{AR}$ is given by the following equation:

$$\bar{K}_t^{AR} = 1 + 2\left(\frac{S_a}{\bar{\rho}}\right)\left(\frac{S_z^*}{S_{10z}^*}\right) \tag{5.1}$$

S_a is the arithmetic mean roughness. S_z^* and S_{10z}^* definitions are close to the ones of standard ISO parameters S_z and S_{10z} [Int 21]. Still, it is slightly different because the method used in our case for valley segmentation (presented in the previous section) is different from the one advised in the ISO standard [Int 21]. Thus, in the present case, S_z^* is the sum of the highest peak height and the deepest valley depth, whereas S_{10z}^* is the sum of the average depth of the five deepest valleys and the average height of the five highest peaks. Finally, $\bar{\rho}$ is the average radius of curvature measured on the five deepest valleys. The radius of curvature is calculated here as the inverse of the curvature along the loading direction. Valleys and peaks are segmented using the method presented in the previous section. When less than 5 valleys or 5 peaks are detected, the average is computed from the few detected ones.

The last parameter that is evaluated is **the maximum value of the estimated stress concentration factor** K_t^* **measured on a whole specimen, denoted** $K_{t,max}^*$. A slight modification was made compared to the definition of K_t^* given in Section 2.2.4. This modification aims to **take into account the variation of the section along its axis**. Since the specimen section is larger within a fillet radius, the stress experienced by the material is reduced in this area. K_t^* is thus corrected at each point of the surface by the ratio of the minimum section along the whole specimen (i.e. within the gauge length) S_{min} and the section S at this point. The resulting formula for K_t^* is given in Eq.5.2:

$$K_t^* = \frac{S_{min}}{S} \cdot \left(1 + 2\sqrt{\text{height} \cdot \kappa_\sigma}\right) \tag{5.2}$$

Fig.5.7a-d show the K_t^* values before and after correction, as well as the $\frac{S_{min}}{S}$ factor, measured on a 45° specimen.

Cette thèse est accessible à l'adresse : https://theses.insa-lyon.fr/publication/2024ISAL0014/these.pdf
© [F. Steinhilber], [2024], INSA Lyon, tous droits réservés

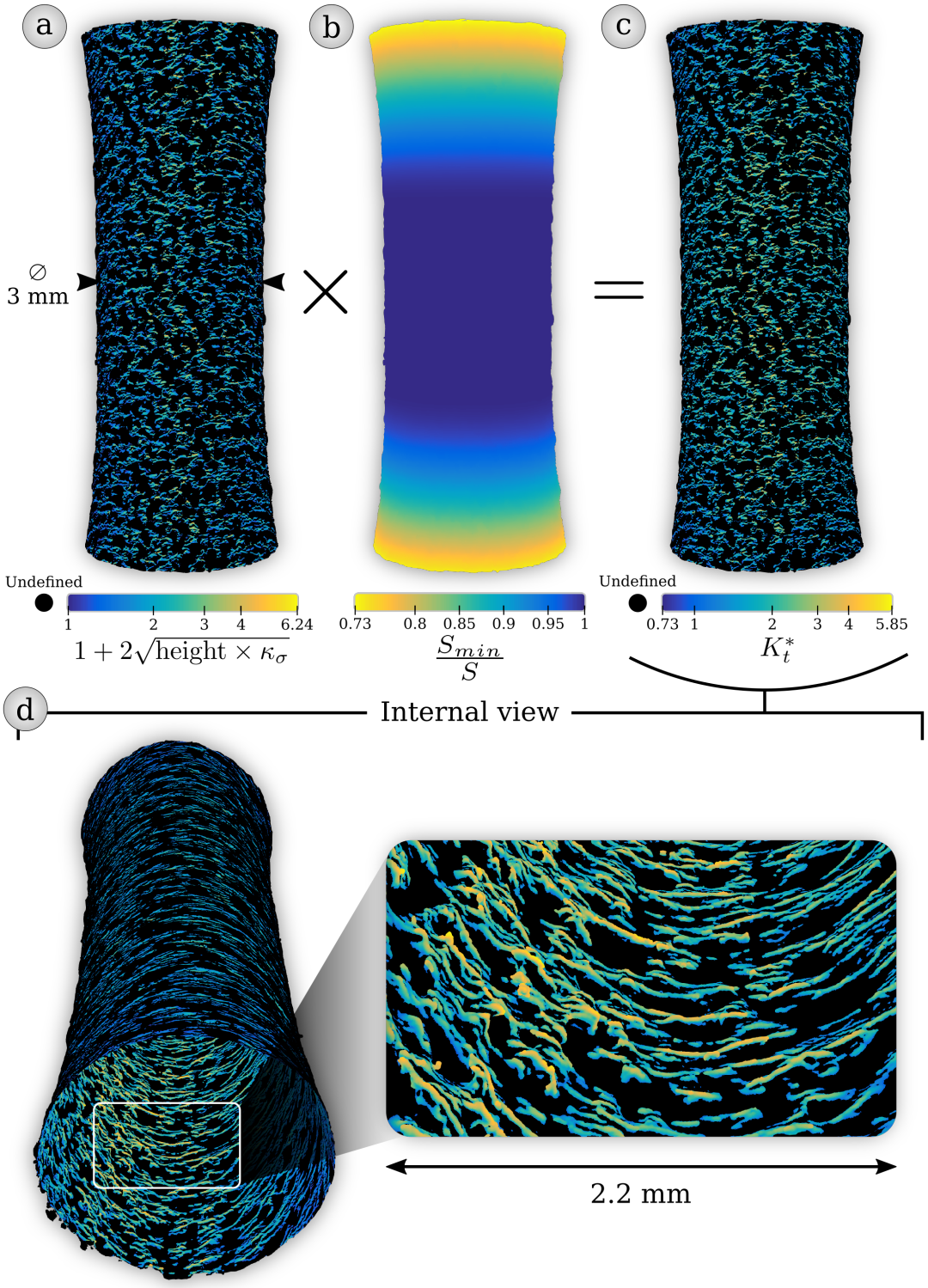

Figure 5.7 | Correction of the K_t^* parameter to take into account the variation of the section along the specimens' axis. (a) K_t^* map before correction, (b) $\frac{S_{min}}{S}$ correction factor, (c) K_t^* map after correction, and (d) Internal view of the K_t^* map after correction.

Cette thèse est accessible à l'adresse : https://theses.insa-lyon.fr/publication/2024ISAL0014/these.pdf
© [F. Steinhilber], [2024], INSA Lyon, tous droits réservés

Note that theoretically, the stress concentration at the intersection of the gauge area and the fillet radii (which is different from the simple impact of section variation mentioned previously) could also be taken into account. However, FEM calculations were conducted from the specimens' CAD geometry and the measured stress concentration reached a maximum of 1.03. It was considered negligible here and was thus not taken into account.

5.2.2 Correlation between the selected parameters and the fatigue lifetime

To evaluate the correlation between the four parameters defined previously (S_a, S_v, $\bar{K}_t^{AR}$ and $K_{t,max}^*$) and the fatigue resistance, S-N diagrams are created for each parameter, with data points color-coded according to the parameter value. Figure 5.8a provides an ideal example of such a diagram, assuming a strong correlation between the investigated parameter and the fatigue resistance.

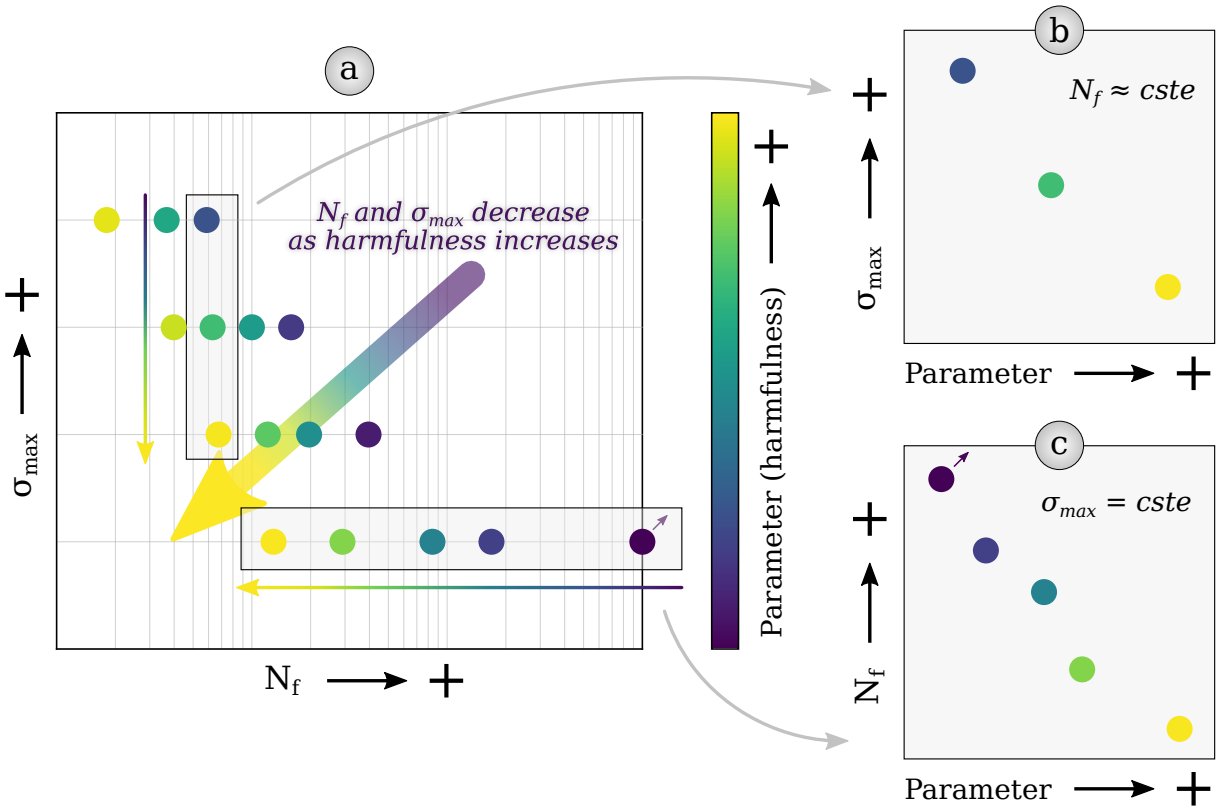

Figure 5.8 | Schematic representation of an ideal correlation between fatigue resistance and a given parameter representative of surface defects harmfulness. (a) Hypothetical S-N diagram that would be obtained if the fatigue lifetime of specimens was directly correlated to the harmfulness parameter. (b) Plot of σ_{max} as a function of the harmfulness parameter, for specimens that failed after a given number of cycles. (c) Plot of N_f as a function of the harmfulness parameter, at a given maximum stress level.

In Fig.5.8a, specimens with defects that are not severe (low harmfulness, reflected by the selected parameter) tend to have longer lifespans or endure higher maximum stresses. This unified graph representation allows for a comprehensive overview.

Cette thèse est accessible à l'adresse : https://theses.insa-lyon.fr/publication/2024ISAL0014/these.pdf
© [F. Steinhilber], [2024], INSA Lyon, tous droits réservés

To assess possible correlations, the detailed plots in Fig.5.8b-c are helpful. These graphs plot the maximum stress σ_{max} or the number of cycles to failure N_f against the harmfulness parameter. A strong correlation in these plots indicates the parameter's reliability in predicting fatigue resistance. However, caution is needed when generalizing these results, as they require plotting data for a single σ_{max} or N_f value only.

Plots are first shown for S_a in Fig.5.9a-c. All surface states (e.g. as-built and PeP) are represented on the same plot. This enables to evaluate whether S_a is relevant to reflect defects harmfulness for very different surfaces.

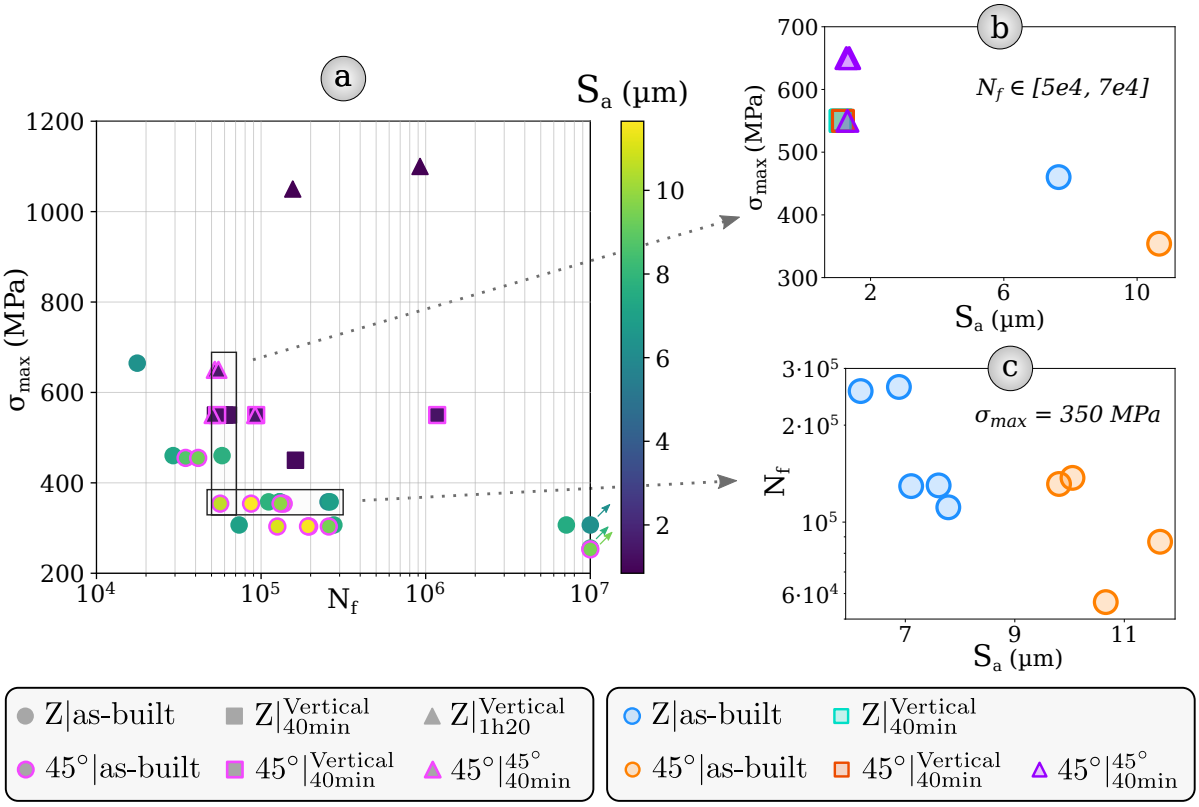

Figure 5.9 | Correlation between S_a and the fatigue resistance of specimens with different surface states. (a) S-N curve with points coloring according to the specimens' S_a. (b) σ_{max} vs. S_a plot for point with $N_f \in [5 \times 10^5, 7 \times 10^4]$. (c) N_f vs. S_a plot for $\sigma_{max} = 350\,\text{MPa}$.

The S-N diagram in Fig.5.9a shows that some correlation exists between S_a and the fatigue resistance. Specifically, specimens with a lower S_a, such as those polished by PeP, tend to have longer fatigue lives and withstand higher stresses.

Additionally, the plot of fatigue life (N_f) against S_a in Fig.5.9c shows a fairly good correlation at 350 MPa. S_a **effectively captures the fact that, on average, as-built Z specimens reach higher fatigue lives than as-built 45° specimens** which exhibit higher S_a values. However, there is a **noticeable scatter**: for example, some Z specimens have similar fatigue lives in comparison with 45° specimens, despite having significantly different S_a values. The quality of the correlation also depends on the stress levels. For instance, at 300 MPa, an as-built

Cette thèse est accessible à l'adresse : https://theses.insa-lyon.fr/publication/2024ISAL0014/these.pdf
© [F. Steinhilber], [2024], INSA Lyon, tous droits réservés

45° specimen failed after 193 381 cycles with S_a = 6.4 µm, while an as-built Z specimen failed after only 125 534 cycles while S_a = 11.0 µm. Therefore, while a correlation between N_f and S_a is observed, especially for as-built surfaces, it should be interpreted cautiously due to the observed scatter and limited number of specimens.

The σ_{max} vs. S_a graph in Fig.5.9b shows a stronger correlation of S_a with σ_{max}. This plot is based on specimens with fatigue lives between 5×10^4 and 7×10^4 cycles. However, all PeP-polished specimens show similar S_a values, even though they sustained different stress levels. This trend is also noticeable in Fig.5.9a, where PeP-polished specimens are distinctly separated in dark blue (indicating low S_a) from as-built specimens in green/yellow (higher S_a). Hence, S_a might not be the best parameter for polished surfaces which are smooth but may contain a few harmful defects.

In such cases, S_v, which better represents the most critical defect across the entire surface, might be more appropriate. Corresponding plots for S_v are presented in Fig.5.10a-c.

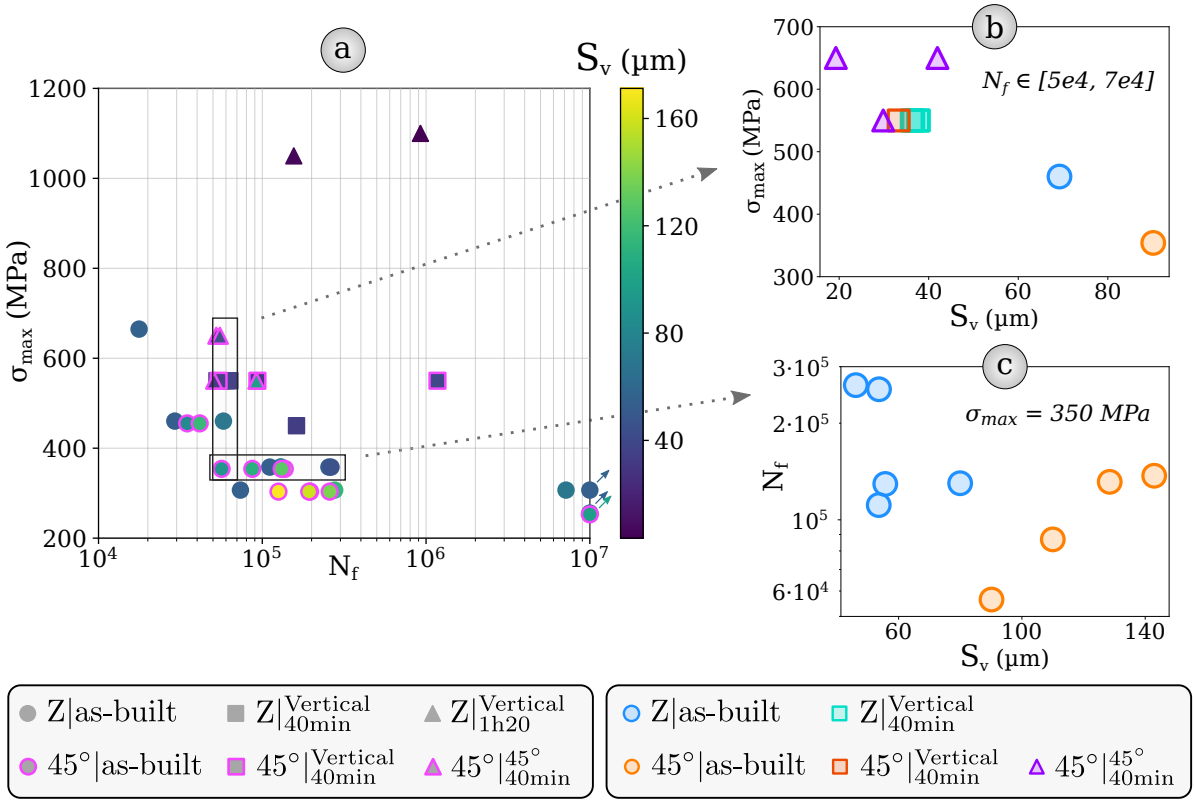

Figure 5.10 | Correlation between S_v and the fatigue resistance of specimens with different surface states. (a) S-N curve with points coloring according to the specimens' S_v. (b) σ_{max} vs. S_v plot for point with $N_f \in [5 \times 10^5, 7 \times 10^4]$. (c) N_f vs. S_v plot for σ_{max} = 350 MPa.

In Fig.5.10b, the use of S_v avoids the saturation effect seen with S_a for PeP-polished specimens. However, **the correlation of S_v with fatigue life (N_f) is not as good as that of S_a**. Notably, for as-built 45° specimens at 350 MPa, the highest fatigue lives paradoxically correspond to the higher S_v values. Thus, while S_v generally shows that as-built Z specimens have higher fatigue lives and lower S_v values on average than as-built 45° specimens, it fails to adequately explain the scatter in fatigue lives among specimens with similar surface states.

Cette thèse est accessible à l'adresse : https://theses.insa-lyon.fr/publication/2024ISAL0014/these.pdf
© [F. Steinhilber], [2024], INSA Lyon, tous droits réservés

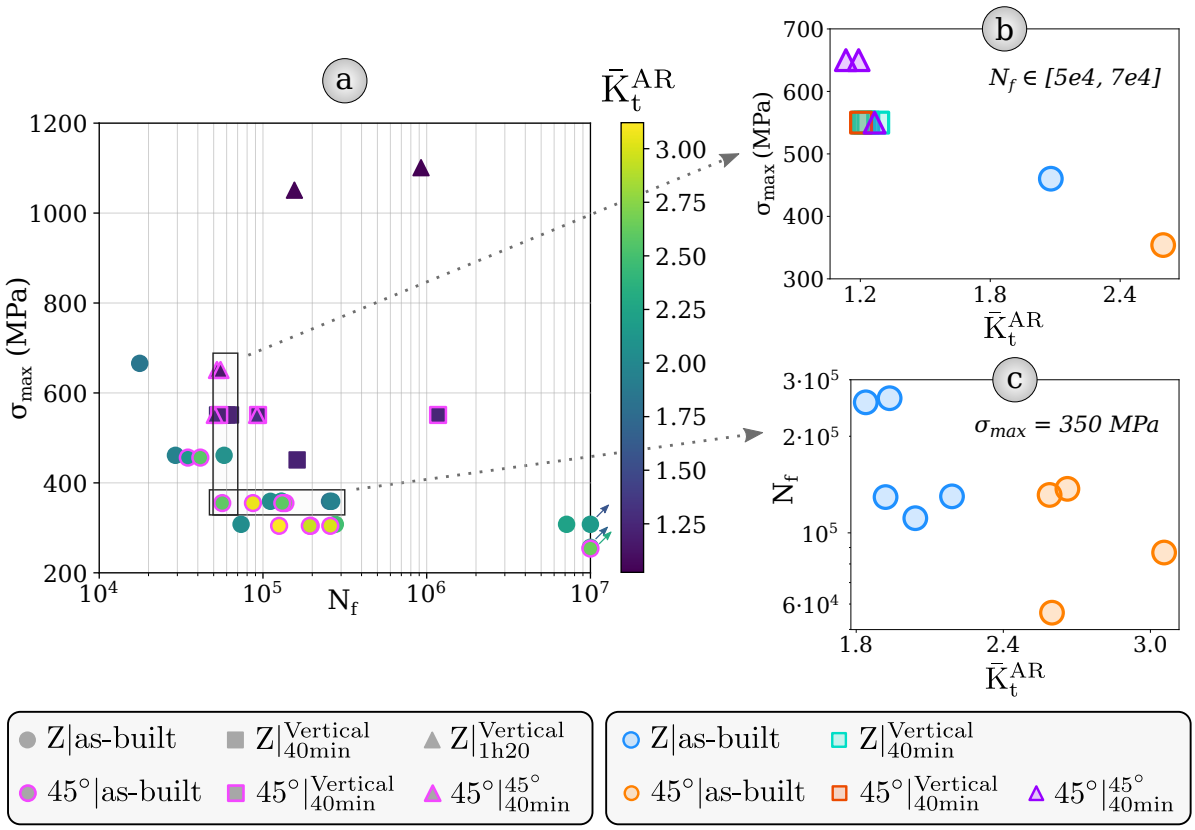

Figure 5.11 | Correlation between $\bar{K}_t^{AR}$ and the fatigue resistance of specimens with different surface states. (a) S-N curve with points coloring according to the specimens' $\bar{K}_t^{AR}$. (b) σ_{max} vs. $\bar{K}_t^{AR}$ plot for point with $N_f \in [5 \times 10^5, 7 \times 10^4]$. (c) N_f vs. $\bar{K}_t^{AR}$ plot for $\sigma_{max} = 350\,\text{MPa}$.

Fig.5.11a-c presents results for $\bar{K}_t^{AR}$ which lie between those of S_a and S_v, leaning more towards S_a. This was somewhat expected, since $\bar{K}_t^{AR}$ is derived from S_a and S_z^* (S_z^* is the average of the deepest valley depth and the highest peak height and is thus close to S_v). **The contribution of curvature (at least with a convolution radius of 20 µm) appears to be limited in this case.**

Fig.5.12a-c displays plots for $K_{t,max}^*$, showing trends similar to those for S_v. This similarity is likely due to the fact that $K_{t,max}^*$, like S_v, is a parameter that mainly characterizes the most critical defect. Thus, the correlation of $K_{t,max}^*$ with N_f at 350 MPa (Fig.5.12c) is not very good, despite the clear distinction between the average behaviors of as-built Z and 45° specimens.

In contrast, **the correlation between σ_{max} and $K_{t,max}^*$ in Fig.5.12b is much more pronounced and effectively differentiates between varying surface states**, i.e. for both as-built and PeP-polished specimens. It could be expected that a parameter such as $K_{t,max}^*$ yields a better correlation with σ_{max} than N_f, since $K_{t,max}^*$ quantifies a stress concentration effect. Fig.5.12a also shows that $K_{t,max}^*$ allows to better account for the transition between as-built and PeP specimens, without the distinct separation between the two as was noticed with S_a.

Cette thèse est accessible à l'adresse : https://theses.insa-lyon.fr/publication/2024ISAL0014/these.pdf
© [F. Steinhilber], [2024], INSA Lyon, tous droits réservés

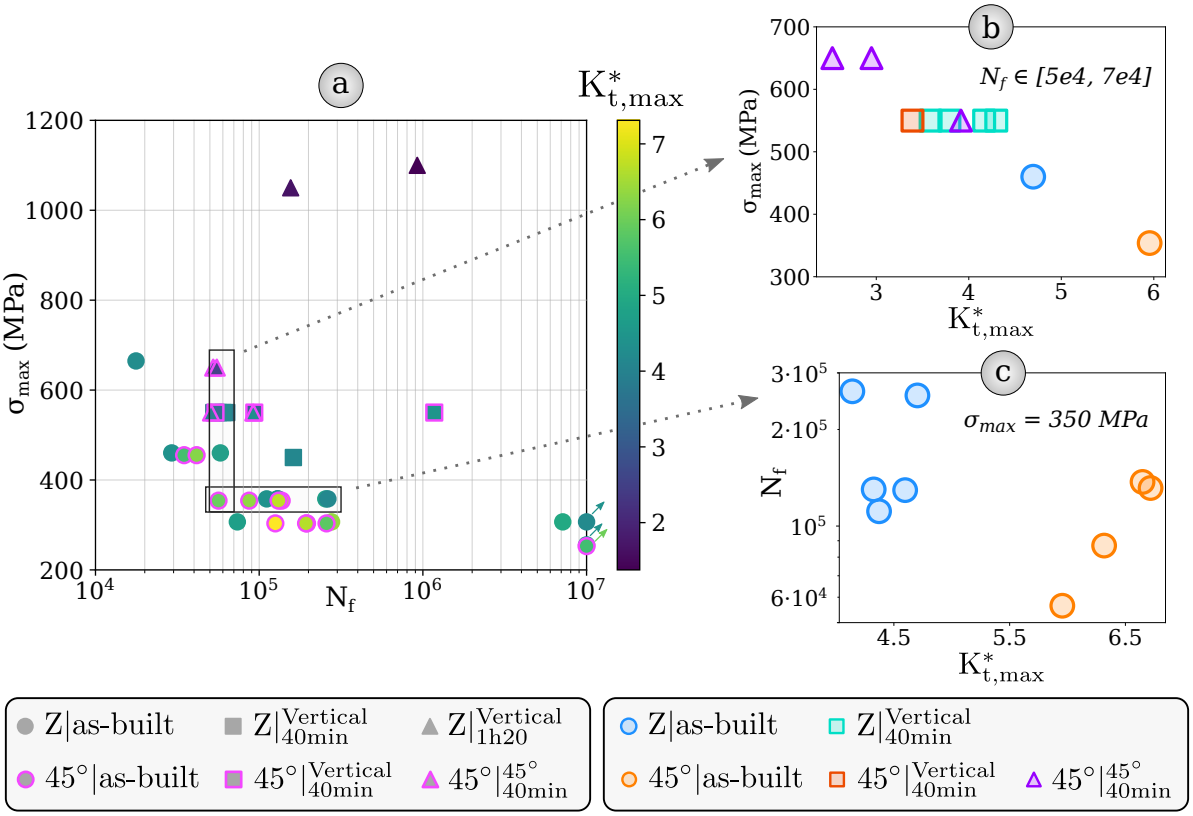

Figure 5.12 | Correlation between $K^*_{t,max}$ and the fatigue resistance of specimens with different surface states. (a) S-N curve with points coloring according to the specimens' $K^*_{t,max}$. (b) σ_{max} vs. $K^*_{t,max}$ plot for point with $N_f \in [5 \times 10^5, 7 \times 10^4]$. (c) N_f vs. $K^*_{t,max}$ plot for $\sigma_{max} = 350\,\text{MPa}$.

A possible solution to improve these results, especially the correlation between parameters and N_f, would be to consider the shape of surface defects, particularly for as-built specimens. For example, $K^*_{t,max}$ being a local measurement, it does not account for the lengths of surface valleys. Yet, as discussed in Section 4.1.3.2, the elongated nature of valleys might be a critical factor in fatigue failure. To estimate whether taking this factor into account could improve predictions, the length of the crack initiation zone (ℓ_{CIZ}) was manually measured on the fracture surfaces of as-built specimens using SEM. ℓ_{CIZ} represents the length of the surface perimeter from which river lines appear to originate. Assessing whether including valley length improves the predictive accuracy of $K^*_{t,max}$ could be an interesting pathway in the future.

Fig.5.13a demonstrates that at higher maximum stress levels, the values of ℓ_{CIZ} (length of the crack initiation zone) tend to be higher. This trend is likely because increased stress levels promote the initiation of multiple cracks [SCH 09, Fig.2.20], leading to larger ℓ_{CIZ} values. Additionally, there is a noticeable trend because specimens with smaller crack initiation zones achieve longer fatigue lives at a given stress level, as shown in Fig.5.13b. This observation suggests that **considering the length of valleys might be essential for a more accurate prediction of their impact on fatigue resistance**.

Cette thèse est accessible à l'adresse : https://theses.insa-lyon.fr/publication/2024ISAL0014/these.pdf
© [F. Steinhilber], [2024], INSA Lyon, tous droits réservés

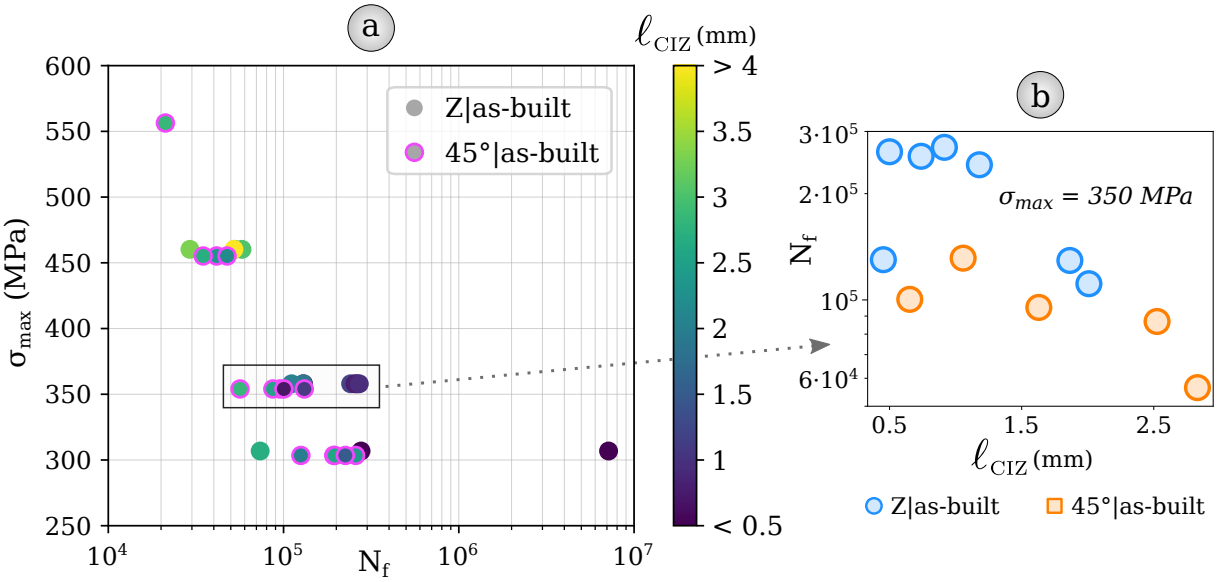

Figure 5.13 | Correlation between ℓ_{CIZ} and the fatigue resistance of as-built specimens. (a) S-N curve with points coloring according to ℓ_{CIZ}. (b) N_f vs. ℓ_{CIZ} plot for $\sigma_{max} = 350\,\text{MPa}$.

5.3 Killer defect prediction

Roughness, curvature and K_t^* measurements are now used for the prediction of killer defects. As in the previous section, the analysis has been conducted solely on as-built specimens that were subjected to a stress relief (no high-temperature heat treatment) as well as specimens polished by PeP.

The methodology followed here is similar to the one used in the study conducted on chemically polished E-PBF specimens, see Section 2.4. The main difference is that the defects segmentation presented in Section 5.1.1 has been applied to achieve more meaningful results for as-built specimens.

Each specimen was scanned by XCT before and after failure. The most harmful defects (valleys for as-built specimens and pit-like defects for PeP specimens) were automatically segmented from the initial scan before fatigue testing using the methodology described in Section 5.1.1. Among them, the killer(s) defect(s) were manually identified from the (SEM and XCT) fracture surface observation as detailed in Section 4.1.3.2. Note that if several defects were thought to play a significant role in fatigue failure (i.e. in the case of multiple crack initiations), those defects were merged and considered as one for the subsequent analysis. For example, the maximum K_t^* value of the killer defect will be considered to be the maximum value among all defects that lead to the initiation of a crack of significant size. For some specimens, the killer defect could not be identified due to the insufficient resolution of XCT scans.

Roughness, κ_σ, and K_t^* were calculated using $\lambda_c = 0.8\,\text{mm}$, $r_{curv} \in \{10, 20, 50, 100, 150\}\mu\text{m}$ and $\lambda_S = 0.03\,\text{mm}$. Note that K_t^* has been calculated using the section correction presented in Section 5.2. For each defect segmented from the initial XCT scan, the most critical value is computed for each parameter. This value corresponds to the highest one for the K_t^* parameter and to the lowest one for roughness and κ_σ.

Cette thèse est accessible à l'adresse : https://theses.insa-lyon.fr/publication/2024ISAL0014/these.pdf
© [F. Steinhilber], [2024], INSA Lyon, tous droits réservés

At this step of the analysis, we have, for each specimen, a set of defects automatically segmented from the 3D image. Each defect is characterized by a single value of depth, as well as a value of κ_σ and K_t^* for five different values of r_{curv} (hence $1 + (2 \cdot 5) = 11$ values in total for a given defect). Among these defects, we also know which ones were responsible for failure in experimental fatigue tests based on the fracture surface observation using SEM.

Two scores were then calculated to inform about the ability of the model to predict the killer defect. The first one is the ***rank***, which corresponds to the number of defects initially segmented from the XCT scan that is expected to have a more detrimental effect on the fatigue lifetime compared to the killer defect(s). A rank of 1 means that the killer defect is well-predicted with our approach. A rank of 10 means that 9 defects were predicted to be more harmful than the actual killer defect(s). The second score is a ***percentage*** that corresponds to the ratio of the maximum K_t^* value measured at the killer defect(s) and the maximum K_t^* value measured all over the characterized surface. This percentage score has been calculated for the K_t^* parameter only, since it is the one showing the most physical meaning.

The results will be first shown for specimens polished by PeP. It is the most advantageous situation since defects can be segmented more easily than valleys in as-built specimens. This case is similar to that of chemically polished E-PBF specimens presented in Section 2.4. In a second part, results will then be shown for as-built specimens.

5.3.1 Application to surface-treated specimens (PeP)

5.3.1.1 Ranks and percentage

Fig.5.14 shows the influence of r_{curv} on the median rank for κ_σ and K_t^*. The median rank is calculated from the ranks obtained for all specimens when the methodology could be applied (i.e. when the killer defect could effectively be captured by XCT).

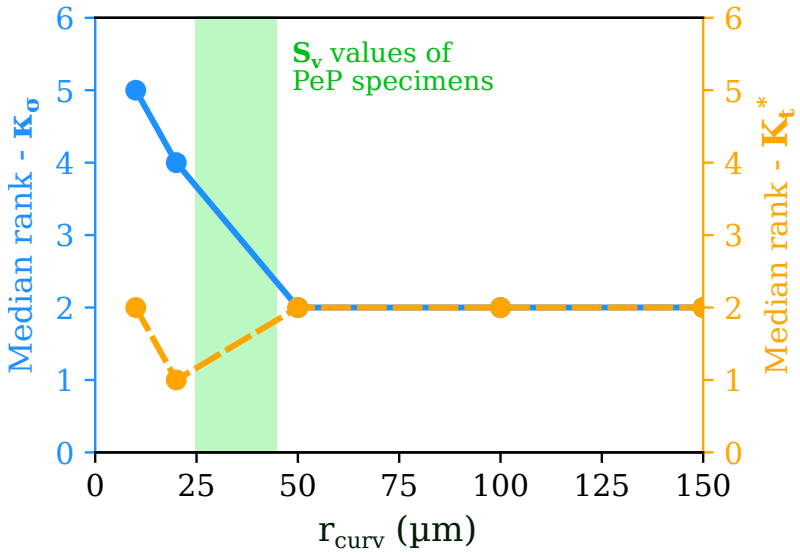

Figure 5.14 | Median ranks obtained for κ_σ and K_t^* for the different values tested for r_{curv}. The range of S_v values obtained for PeP specimens (except the $Z|_{1h20}^{Vertical}$ condition) is given in green.

Cette thèse est accessible à l'adresse : https://theses.insa-lyon.fr/publication/2024ISAL0014/these.pdf
© [F. Steinhilber], [2024], INSA Lyon, tous droits réservés

For κ_σ, the median rank decreases when r_{curv} increases and reaches a plateau between 20 µm and 50 µm. This is consistent with the observation made in Section 2.4, where the optimum r_{curv} value was found to be close to the maximum valley depth S_v. Indeed, S_v values lie between 20 µm and 50 µm for specimens polished by PeP, except $\mathrm{Z}|_{1h20}^{\mathrm{Vertical}}$ ones which could anyway not be part of this analysis since the killer defect could not be found in the XCT scan before failure. Given these results, ranks of PeP specimens considering the κ_σ metric will be studied using $r_{curv} = 50\,\mu m$.

For specimens polished by PeP, r_{curv} does not have a strong influence on the ranks obtained based on the K_t^* parameter. Slightly better results are yet obtained for $r_{curv} = 20\,\mu m$, which is why ranks and percentage scores for K_t^* will be presented using this value.

Fig.5.15 provides a visual representation to help understand rank and percentage scores. It shows in blue the Probability Density Function (PDF ≈ continuous histogram) of K_t^* values obtained for all surface points where this parameter is defined (i.e. where $height < 0$ and $\kappa_\sigma < 0$). Most surface points exhibit K_t^* values below 1.5. The distribution extends into a very long tail, for a large part representing points within pit-like defects. Thus, the orange points, corresponding to the maximum K_t^* value found among all points of each defect, are found in this tail section of the distribution.

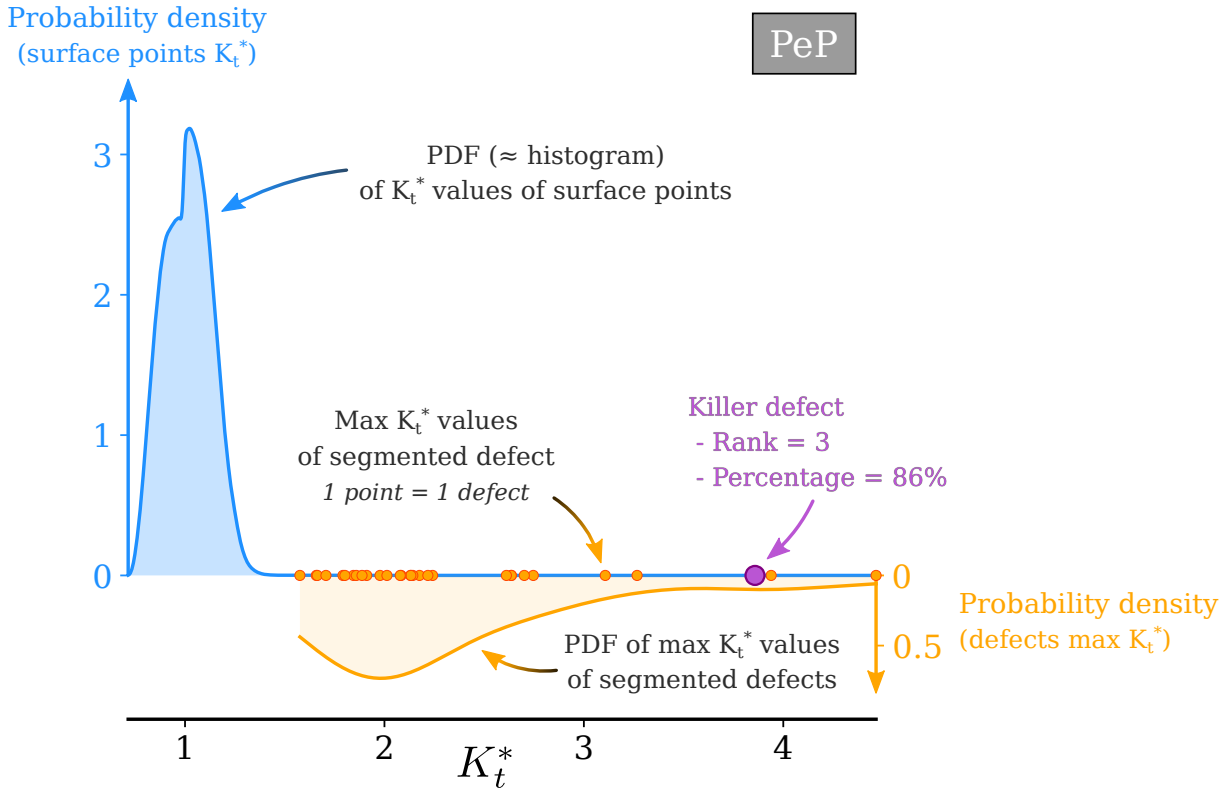

Figure 5.15 | Distributions of surface points and defects K_t^* values for $45°|_{40min}^{Vertical}$-2 specimen. The blue line shows the PDF for K_t^* values of surface points, considering only points with negative heights and κ_σ. The orange points and curve represent the maximum K_t^* value for each segmented defect and its PDF. The killer defect is marked in purple. PDFs are calculated using the KDE method with Silverman's rule of thumb for bandwidth selection.

Cette thèse est accessible à l'adresse : https://theses.insa-lyon.fr/publication/2024ISAL0014/these.pdf
© [F. Steinhilber], [2024], INSA Lyon, tous droits réservés

Additionally, an orange PDF illustrates the maximum K_t^* values distribution for the segmented defects, and the killer defect is distinctly marked in purple, with its rank/percentage scores. In the given example, two defects exhibit higher maximum K_t^* values than the killer defect, placing its rank at 3. For a detailed description of the results, specific values for each specimen are summarized in Tab.5.2.

PeP		**Rank**			**Percentage**
		Height	κ_σ	K_t^*	K_t^*
Specimen	$n_{defects}$	$\lambda_c = 800\,\mu m$	$r_{curv} = 50\,\mu m$	$\lambda_c = 800\,\mu m$ $r_{curv} = 20\,\mu m$	$\lambda_c = 800\,\mu m$ $r_{curv} = 20\,\mu m$
$Z\|^{Vertical}_{40min}$ - 1	29	7	9	8	75
$Z\|^{Vertical}_{40min}$ - 2	41	1	1	1	100
$Z\|^{Vertical}_{40min}$ - 3	12	2	2	1	100
$Z\|^{Vertical}_{40min}$ - 4	10	5	4	5	74
$Z\|^{Vertical}_{40min}$ - 5	21	1	1	1	100
$Z\|^{Vertical}_{1h20}$ - 1	×	Killer defect not captured by XCT			
$Z\|^{Vertical}_{1h20}$ - 2	×	Killer defect not captured by XCT			
$45°\|^{Vertical}_{40min}$ - 1	43	11	12	8	85
$45°\|^{Vertical}_{40min}$ - 2	30	2	2	3	86
$45°\|^{Vertical}_{40min}$ - 3	×	Killer defect not captured by XCT			
$45°\|^{45°}_{40min}$ - 1	11	1	1	1	100
$45°\|^{45°}_{40min}$ - 2	×	Killer defect not captured by XCT			
$45°\|^{45°}_{40min}$ - 3	×	Killer defect not captured by XCT			
$45°\|^{45°}_{40min}$ - 4	×	Killer defect not captured by XCT			
Median	25	2	2	1	93

Table 5.2 | Killer defect predictions scores (*rank & percentage*) for specimens polished by PeP using roughness, κ_σ and K_t^* parameters. The *Specimen* column refers to the name of individual specimens and the $n_{defects}$ column gives the total number of defects that were automatically segmented. Colors are given for guidance, the color tending to green for a successful killer defect prediction while it tends to red for a less accurate prediction.

First, we can notice that **for 5 specimens out of 14, the killer defect could not be captured by XCT due to a lack of resolution**. Therefore, the analysis could not be conducted for those specimens. For the remaining specimens, the ranks obtained using roughness, κ_σ or K_t^* are all very similar. This is likely due to the small and point-like shape of the defects in PeP specimens. Notably, their point-like shape reduces the benefit of using the curvature oriented in the direction of the specimen axis.

Among the 8 specimens that could be analyzed, the killer defect could be successfully predicted in 4 cases using the K_t^* parameter. These results are comparable to or even slightly better than the ones obtained on chemically polished E-PBF samples in Section 2.4. This may be because the surface obtained for L-PBF polished by PeP is smoother and the few remaining defects show a more regular/globular morphology.

Cette thèse est accessible à l'adresse : https://theses.insa-lyon.fr/publication/2024ISAL0014/these.pdf
© [F. Steinhilber], [2024], INSA Lyon, tous droits réservés

For specimens that showed higher ranks (e.g. $Z|_{40min}^{Vertical}$ - 1 and $45°|_{40min}^{Vertical}$ - 1), the bad scores could be at least partly explained by other factors such as microstructure are not taken into account. For example, crack formation has been reported to be more frequent along basal and prismatic planes in α phase of Ti64 alloy [BRI 08], which means that the local crystallographic orientation of surface grains can be expected to play a role. The percentage scores for $Z|_{40min}^{Vertical}$ - 1 and $45°|_{40min}^{Vertical}$ - 1 specimens being relatively high (75% and 85% respectively), crystallographic orientation inhomogeneity may have caused crack initiation to occur at a defect that does not generate the highest stress concentration.

Nonetheless, it is also very likely that a lack of resolution also plays a major role as already emphasized. This is evidenced by the fact that the killer defect could not even be found (even by visual inspection) on the surface extracted from the XCT scan for 5 specimens out of 14. Since the resolution of XCT scans seems to be a major issue regarding critical defects' characterization, a more detailed analysis has been conducted on a few specimens.

5.3.1.2 The impact of XCT scan resolution on the prediction of killer defect

The objective here is to compare the killer defect as characterized by XCT with its characterization with SEM. Since SEM provides a better resolution than XCT, it is considered as a ground truth. This is possible for specimens polished by PeP since defects can be unambiguously delineated on SEM observations, which is not possible for valleys in as-built specimens.

Four cases will be successively discussed:

- a case where the killer defect is effectively captured by XCT, leading to a successful prediction (example 1);
- a case showing that the method can also be used to account for near-surface internal pores (example 2);
- a case where the limited XCT scan resolution enables to only partially capture the killer defect, leading to a much less accurate prediction (example 3);
- a case where the killer defect could not even be found in the surface extracted from XCT scans (example 4).

Example 1: successful prediction

Fig.5.16a-e show a first example where the killer defect could be successfully identified on the surface extracted from the XCT scan. The defect is, in this case, a pore that was brought to the surface by PeP, leading to the formation of a pit-like defect.

Fig.5.16c shows the killer defect on the 3D height map of the initial surface, but the external point of view barely enables one to see it. The defect can be observed much more accurately when looking from inside the sample, see Fig.5.16d-e. In Fig.5.16e, one can recognize the particular shape of the defect that can be seen with more detail in the SEM image shown in Fig.5.16a. Moreover, the dimensions of the defect are in good agreement with the ones found using SEM. **As a result of this relatively good defect segmentation, the killer defect is successfully identified** (rank = 1) regardless of the parameter used (height, κ_σ, or K_t^*). However, even for such a large defect, it can be seen that due to the limited XCT scan resolution, the 3D morphology appears smoother/rounder than the one visible on the fracture surface observed by SEM.

Cette thèse est accessible à l'adresse : https://theses.insa-lyon.fr/publication/2024ISAL0014/these.pdf
© [F. Steinhilber], [2024], INSA Lyon, tous droits réservés

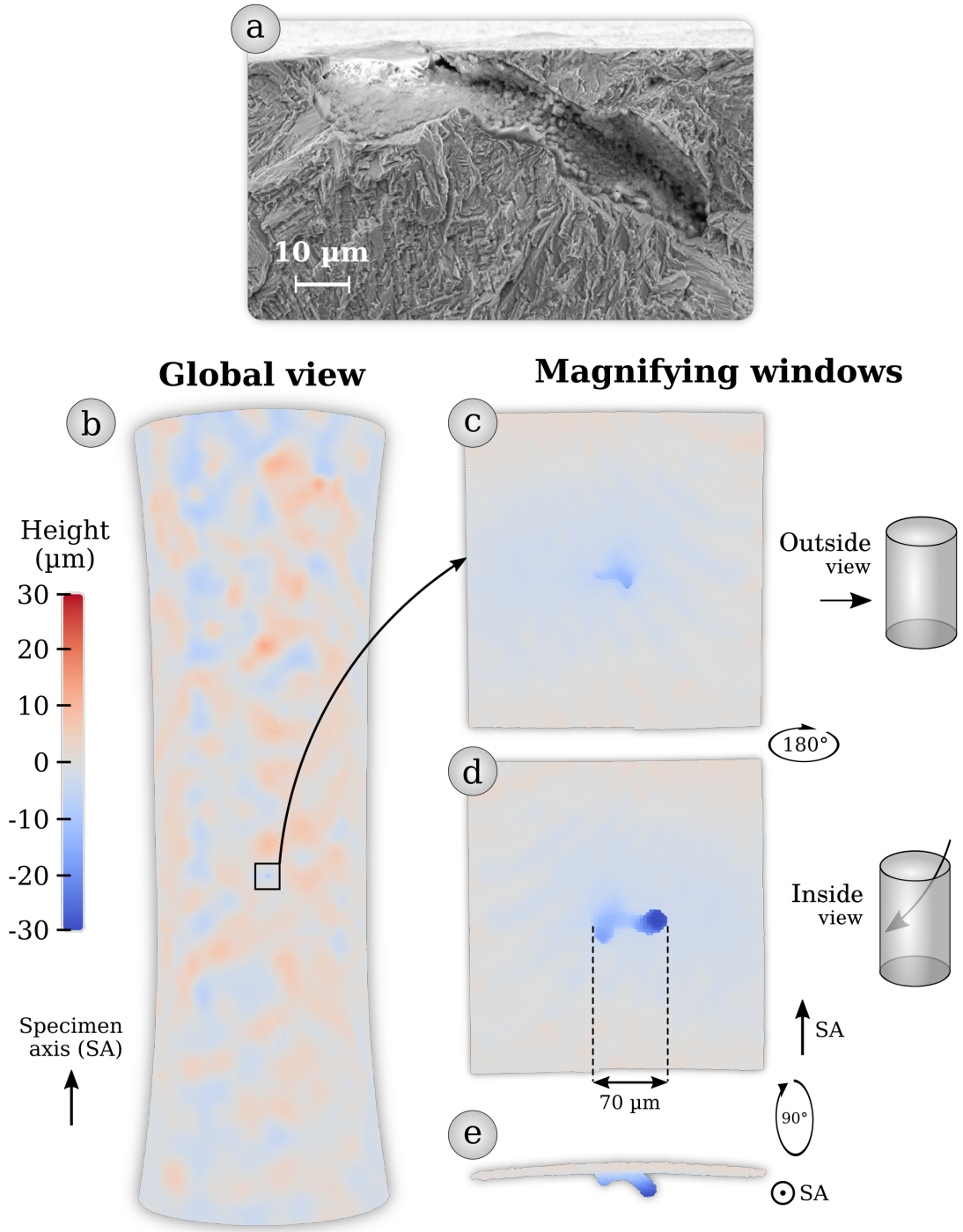

Figure 5.16 | Crack initiation site identification on the $45°|^{45°}_{40min}$-1 specimen. The specimen failed after 50 780 cycles at 550 MPa. The killer defect is a sub-surface pore that was brought to the surface during PeP. (a) SEM-SE observation of the initiation site on the fracture surface. (b) Global 3D height map of the specimen before fatigue testing. (c) Zoom on the killer defect. (d) Same area as in (c), observed from the inside, revealing the morphology of the killer defect that cannot be seen from the outside. (e) Killer defect observed from above, showing a similar geometry as in the SEM observation.

Cette thèse est accessible à l'adresse : https://theses.insa-lyon.fr/publication/2024ISAL0014/these.pdf
© [F. Steinhilber], [2024], INSA Lyon, tous droits réservés

It is worth noting here that **the killer defect could be successfully segmented from the XCT scan thanks to the use of the Triangle Threshold for Bimodal Histograms (TTBH)**. As shown in the transverse slices of the XCT scan containing the defect in Fig.5.17a-c, a conventional threshold obtained from Otsu's method fails to capture this defect due to its limited width.



Figure 5.17 | Comparison of the abilities of Otsu's threshold and TTBH to capture the killer defect shown in Fig.5.16. (a) Transverse XCT slice (voxel size = 3 µm). (b) Application of Otsu's threshold, which does not capture the defect. (c) Successful segmentation of the killer defect using the TTBH.

Example 2: prediction for a sub-surface pore

Another example of the benefits of using the TTBH is illustrated by the second example shown in Fig.5.18a-e. It shows the analysis of the crack initiation site on another $45°|^{45°}_{40\text{min}}$ specimen.

The killer defect is a sub-surface pore that has no direct connection with the surface, although the ligament that separates the two is very thin. Fig.5.18c shows that Otsu's threshold does partially segment the pore, but that the resulting defect is not connected to the surface. Since only surface defects are taken into account in the methodology used here, such a defect will be ignored in the analysis, and the killer defect would not be possible to identify. Conversely, the use of a higher threshold (in terms of gray level) **erodes the surface and enables to erase the ligament that separates the pore from the surface**, see Fig.5.18d. It is advantageous here, as a pore so close to the surface can reasonably be considered equivalent from a mechanical point of view to the same defect located at the surface.

In this regard, the surface segmentation could be adapted to take into account all subsurface pores and consider them as equivalent surface defects. A simple way would be to artificially remove the ligaments that separate sub-surface pores from the surface, and then characterize the obtained surface defect. Fig.5.18e shows an example, where the ligament is erased in the case of Otsu's threshold. Here, this operation was performed manually, but it could be automatized fairly easily.

Finally, it can be seen that even if the defect can be segmented from XCT data using the TTBH, its exact morphology cannot be extracted. This highlights, once again, that the use of laboratory XCT with a voxel size of 3 µm reaches its limits, especially considering the small size of the observed defects.

Cette thèse est accessible à l'adresse : https://theses.insa-lyon.fr/publication/2024ISAL0014/these.pdf
© [F. Steinhilber], [2024], INSA Lyon, tous droits réservés

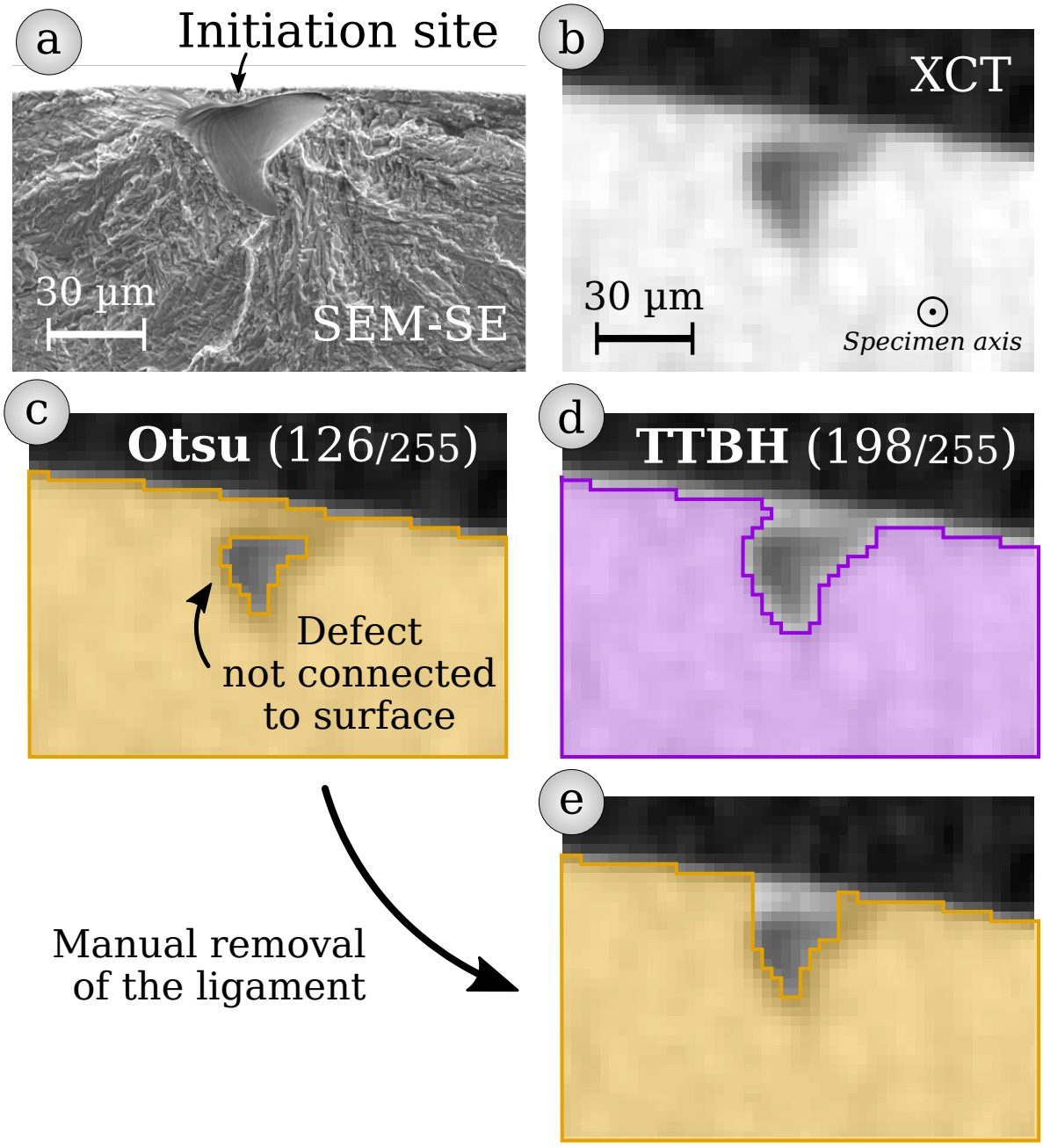

Figure 5.18 | Comparison of the abilities of Otsu's threshold and TTBH to capture the killer defect on the 45°$|^{\text{Vertical}}_{\text{40min}}$-2 specimen. The specimen failed after 1 173 759 cycles at 550 MPa, and the killer defect is a sub-surface pore that was brought just beneath the surface by the PeP treatment. (a) SEM-SE observation of the initiation site on the fracture surface. (b) Transverse XCT slice (voxel size = 3 µm). (c) Application of Otsu's threshold, which enables capturing some part of the defect only. Since the defect is not connected to the surface, it would not be considered a surface defect. (d) Successful segmentation of the defect using the TTBH. The small ligament that separated the pore from the surface was removed by the TTBH. (e) An alternative solution to take into account sub-surface pores in the present workflow dedicated to surface defects analysis. The ligament that separates the pore from the surface is artificially removed, revealing the underlying defect even when using Otsu's threshold.

Cette thèse est accessible à l'adresse : https://theses.insa-lyon.fr/publication/2024ISAL0014/these.pdf
© [F. Steinhilber], [2024], INSA Lyon, tous droits réservés

Example 3: defect only partially captured due to an insufficient resolution

This is even clearer in the third example shown in Fig.5.19a-d, where the killer defect is significantly blurred due to this lack of resolution. As a result, its depth is significantly underestimated when it is measured from the XCT scan, even using the TTBH for the surface segmentation, see Fig.5.19a,d. Its shape is not well described since it is only a few voxels large. This will necessarily lead to erroneous estimations of the depth and curvature measurements. This is probably the major reason accounting for the unsuccessful killer defect prediction in this peculiar case (rank = 8 – 12).

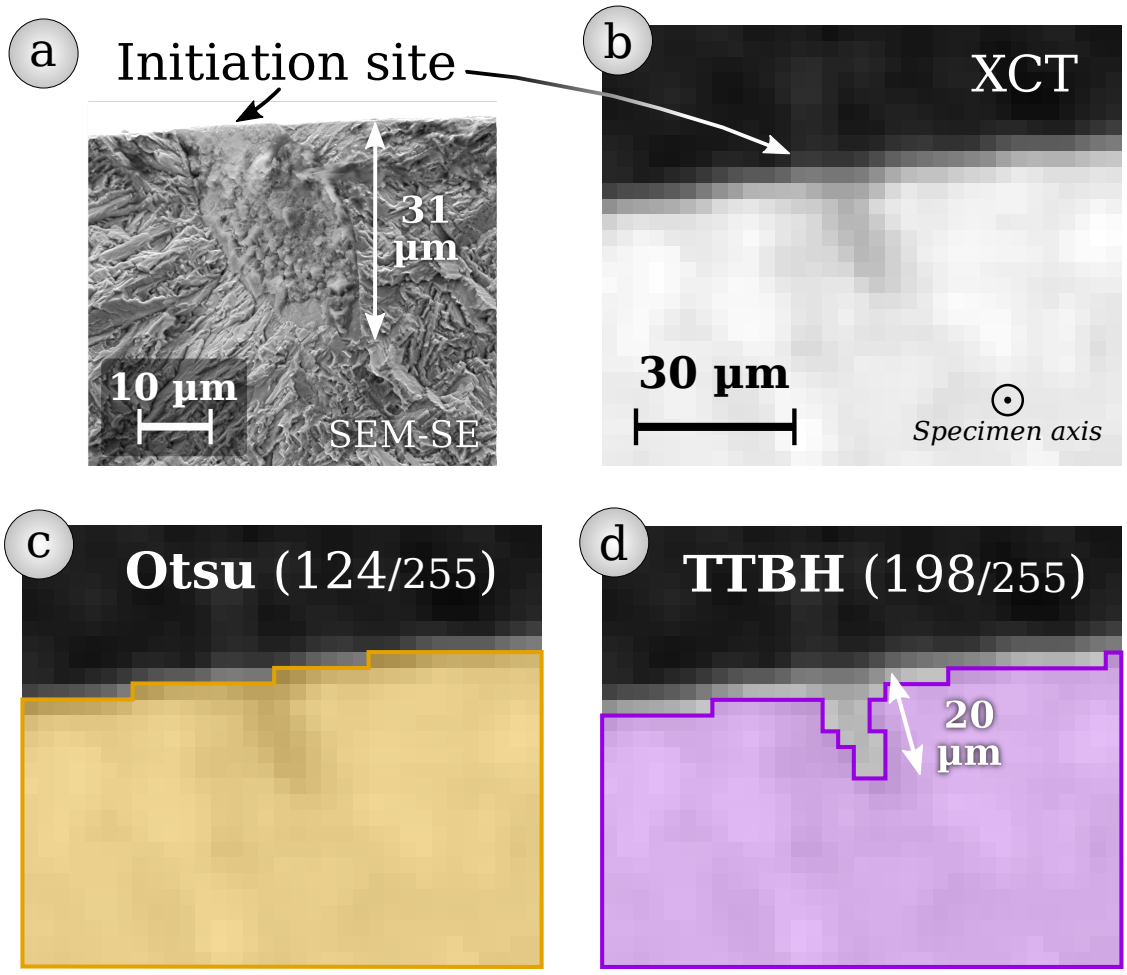

Figure 5.19 | Comparison of the killer defect observed by SEM and the segmentation from the XCT scan on the 45°$|^{\text{Vertical}}_{\text{40min}}$-1 specimen. The specimen failed after 54 092 cycles at 550 MPa, and the killer defect is a sub-surface pore that was brought to the surface by the PeP treatment. (a) SEM-SE observation of the initiation site on the fracture surface. (b) Transverse XCT slice (voxel size = 3 µm). (c) Surface segmentation using Otsu's threshold. (d) Surface segmentation using the TTBH.

Cette thèse est accessible à l'adresse : https://theses.insa-lyon.fr/publication/2024ISAL0014/these.pdf
© [F. Steinhilber], [2024], INSA Lyon, tous droits réservés

Example 4: defect not captured at all due to an insufficient resolution

Finally, Fig.5.20a-d show the last case where the killer defect could not be captured at all from XCT data at all because of insufficient resolution.

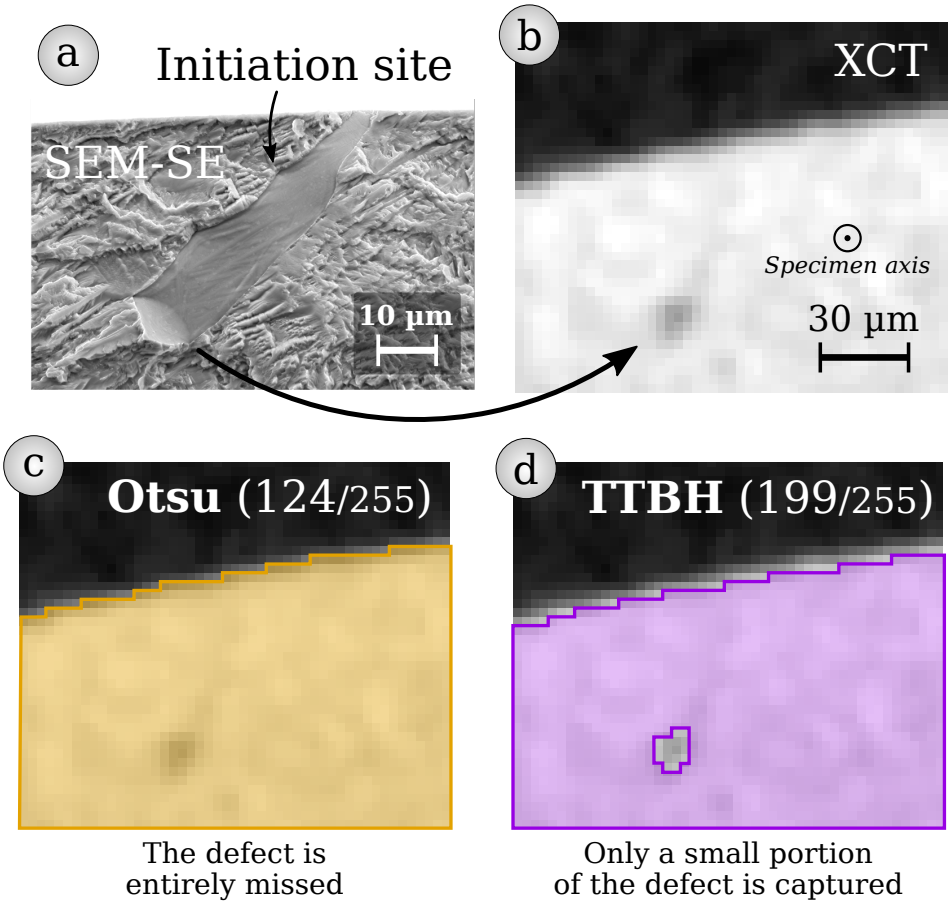

Figure 5.20 | Unsuccessful segmentation of the killer defect on the 45°$|^{45°}_{40min}$-3 specimen due to a lack of resolution. The specimen failed after 2×10^6 cycles at 550 MPa followed by 52 369 cycles at 650 MPa. The killer defect is a subsurface pore that was brought to the surface by PeP, although its connection to the surface is very small. (a) SEM-SE observation of the initiation site on the fracture surface. (b) Transverse XCT slice (voxel size = 3 µm). (c) Application of Otsu's threshold, which entirely misses the killer defect. (d) Application of the TTBH which enables capturing some part of the defect only, and fails at establishing its connection with the surface.

The SEM observation in Fig.5.20a shows that the killer defect is a pore that is barely connected to the surface. Moreover, the portion of the defect close to the surface seems very thin, making its characterization by XCT very difficult. As a result, Fig.5.20b shows that only a limited portion of the defect can be detected in the XCT scan. It corresponds to the bottom of the defect, which is larger. This portion of the defect is successfully segmented using the TTBH threshold, see Fig.5.20d. However, most of the defect is not captured, and in particular its connection to the surface is not accounted for. Thus, the methodology for killer defect prediction could not be applied.

Cette thèse est accessible à l'adresse : https://theses.insa-lyon.fr/publication/2024ISAL0014/these.pdf
© [F. Steinhilber], [2024], INSA Lyon, tous droits réservés

In light of the four examples discussed above, the quality of the killer defect prediction seems well correlated with the ability of XCT to properly capture defects. In other words, the resolution of XCT scans plays a major role, and even a 3 µm voxel size is often insufficient given the small size of the defects. This resolution issue can also be expected to play a major role for as-built specimens and the ability of XCT to properly capture the roots of surface valleys.

5.3.2 Application to specimens with as-built surfaces

For the sake of simplicity, the measurements of roughness, κ_σ, and K_t^* for the as-built specimens were conducted using the same parameters (λ_c, r_{curv}, and λ_S) as those used for PeP-polished specimens. Despite testing other values, no significant improvements or changes in interpretation were observed.

As-built specimens have markedly different surface topologies compared to PeP specimens, leading to distinct K_t^* PDFs and a greater number of segmented defects. This is illustrated in Fig.5.21, which shows for Z-7 specimen the surface points' K_t^* distribution in blue and the maximum K_t^* distribution for segmented defects in orange.

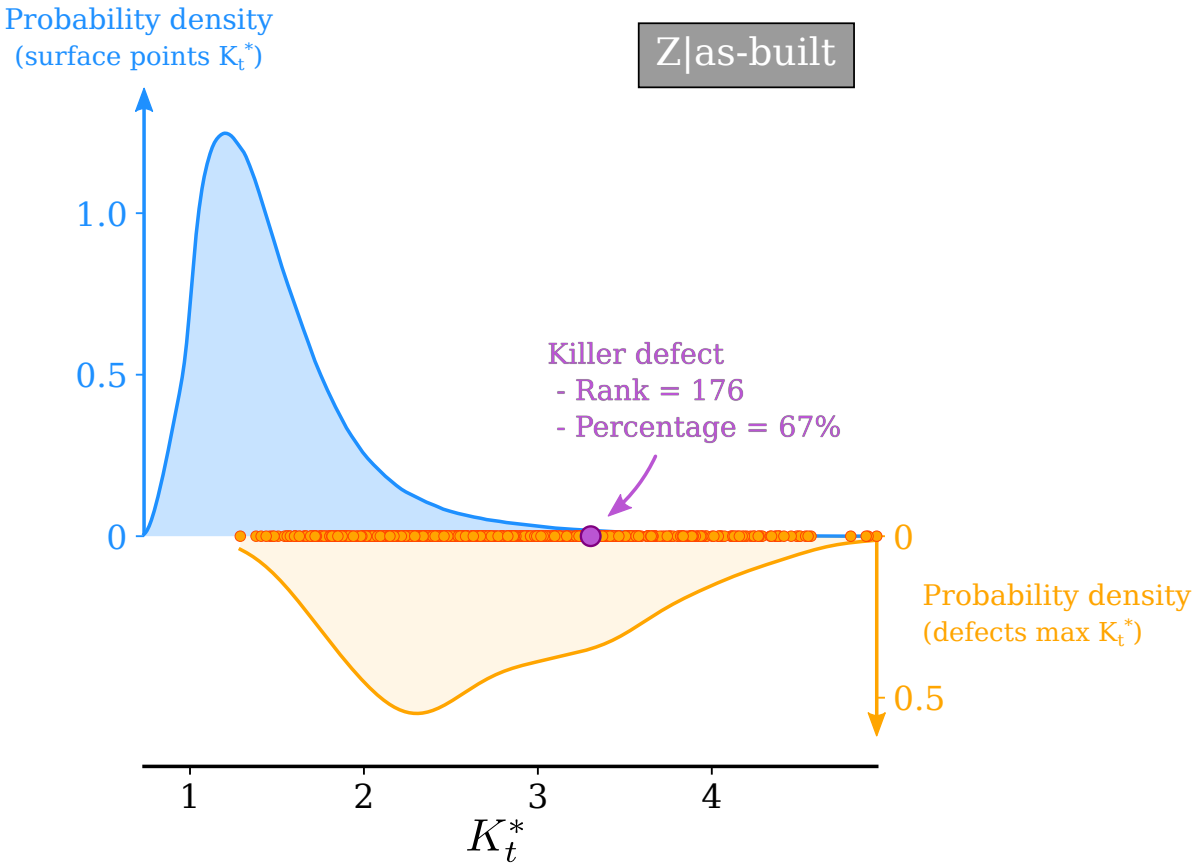

Figure 5.21 | Distributions of surface points and defects K_t^* values for as-built Z-7 specimen. The blue line shows the PDF for K_t^* values of surface points, considering only points with negative heights and κ_σ. The orange points and curve represent the maximum K_t^* value for each segmented defect and its PDF. The killer defect is marked in purple. PDFs are calculated using the KDE method with Silverman's rule of thumb for bandwidth selection.

Cette thèse est accessible à l'adresse : https://theses.insa-lyon.fr/publication/2024ISAL0014/these.pdf
© [F. Steinhilber], [2024], INSA Lyon, tous droits réservés

The surface points' K_t^* distribution has a less extended tail than that observed in PeP specimens. While the killer defect appears in the tail of the surface points' K_t^* distribution, its rank is quite high (176), which illustrates the more complex killer defect prediction for as-built specimens. The rank and percentage scores for the killer defect predictions across all as-built Z specimens are detailed in Tab.5.3.

Z		**Rank**			**Percentage**
		Height	κ_σ	K_t^*	K_t^*
Specimen	$n_{defects}$	$\lambda_c = 800\,\mu m$	$r_{curv} = 50\,\mu m$	$\lambda_c = 800\,\mu m$ $r_{curv} = 20\,\mu m$	$\lambda_c = 800\,\mu m$ $r_{curv} = 20\,\mu m$
Z-1	725	323	234	215	51
Z-2	654	287	140	200	55
Z-3	710	181	198	187	67
Z-4	732	316	217	271	59
Z-5	752	26	11	1	100
Z-6	719	318	200	242	71
Z-7	739	301	87	176	67
Z-8	709	49	20	5	93
Z-9	730	53	31	28	82
Z-10	761	114	60	57	84
Median	728	234	114	182	69

Table 5.3 | Killer defect prediction scores (rank & percentage) for as-built Z specimens using roughness, κ_σ and K_t^* parameters. The *Specimen* column refers to the name of individual specimens and the $n_{defects}$ column gives the total number of defects that were automatically segmented. Colors are given for guidance, the color tending to green for a successful killer defect prediction while it tends to red for a failed prediction.

First, it can be noticed that **the number of segmented defects is much higher for as-built specimens** (≈ 700) in comparison with specimens polished by PeP (< 50). This is, of course, linked to the much higher density of surface defects in as-built specimens.

A second observation is that ranks are much higher for as-built Z specimens compared to those polished by PeP. Thus, for most as-built Z specimens, the method **clearly fails to properly predict the killer defect**. In this context, it seems hazardous to try determining which parameter among the roughness, κ_σ, and K_t^* is the most relevant.

Nonetheless, **results for as-built 45° specimens are much more encouraging** than those for as-built Z specimens. They are shown in the form of PDFs for one specimen in Fig.5.22, followed by a more comprehensive analysis for all specimens in Tab.5.4.

As-built 45° specimens consistently achieve much lower ranks compared to as-built Z specimens. For instance, the median rank for the K_t^* parameter across 10 analyzed 45° specimens is 21. The relatively better results obtained for the 45° specimens might be because defects in 45° specimens are larger. This may facilitate their identification using XCT with the resolution employed here (voxel = 3 µm). The difference between Z and 45° specimens might also arise due to the very different valley morphologies in either case.

Cette thèse est accessible à l'adresse : https://theses.insa-lyon.fr/publication/2024ISAL0014/these.pdf
© [F. Steinhilber], [2024], INSA Lyon, tous droits réservés

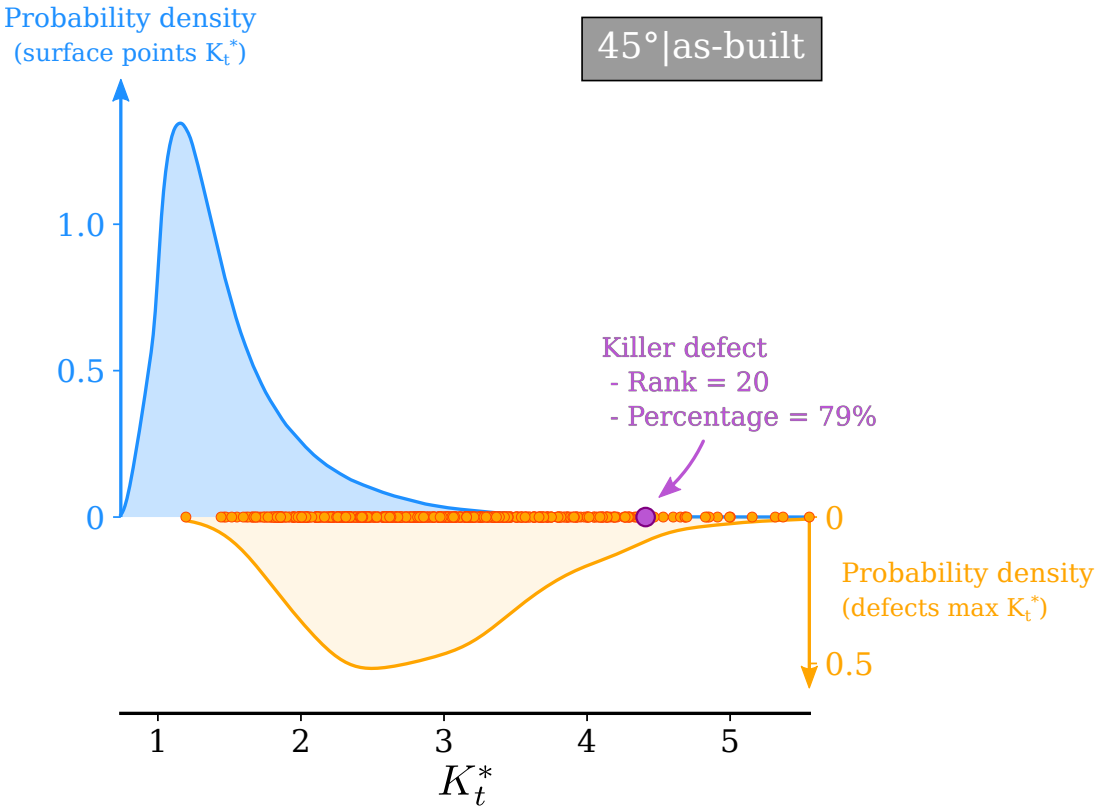

Figure 5.22 | Distributions of surface points and defects K_t^* values for as-built 45°-7 specimen. The blue line shows the PDF for K_t^* values of surface points, considering only points with negative heights and κ_σ. The orange points and curve represent the maximum K_t^* value for each segmented defect and its PDF. The killer defect is marked in purple. PDFs are calculated using the KDE method with Silverman's rule of thumb for bandwidth selection.

As for PeP specimens, it is also worth noting that although very high ranks are obtained for some specimens, **the percentage score can remain reasonably high**. For instance, a rank of 242 is obtained but a relatively high percentage of 71% is found for the Z-6 specimen.

Given all these observations, the following points might at least partially explain the inability of the model to provide an accurate prediction of the killer defects in as-built specimens:

- The resolution of XCT scans is insufficient to properly capture surface defects.
- Due to the higher density of defects in as-built specimens, it seems logical that it is more challenging to find the killer defect among ≈700 segmented defects than it was to find it among ≈30 defects in the case of specimens polished by PeP.
- Other factors such as the microstructure may play a role and promote crack initiation at spots where the stress concentration is not maximal.
- The model does not take into account the defects' morphology. Yet, the particularly elongated shape of surface valleys may play a significant role in crack initiation and/or propagation. Properly taking into account the defects' shape would probably require improving the method used for defect segmentation together with the resolution of XCT scans.

Cette thèse est accessible à l'adresse : https://theses.insa-lyon.fr/publication/2024ISAL0014/these.pdf
© [F. Steinhilber], [2024], INSA Lyon, tous droits réservés

45°		Rank			Percentage
		Height	κ_σ	K_t^*	K_t^*
Specimen	$n_{defects}$	$\lambda_c = 800\,\mu m$	$r_{curv} = 50\,\mu m$	$\lambda_c = 800\,\mu m$ $r_{curv} = 20\,\mu m$	$\lambda_c = 800\,\mu m$ $r_{curv} = 20\,\mu m$
45°-1	799	1	32	1	100
45°-2	788	12	30	3	93
45°-3	774	23	37	22	87
45°-4	706	97	2	78	64
45°-5	685	130	81	73	60
45°-6	670	85	68	51	68
45°-7	692	35	2	20	79
45°-8	766	22	15	9	77
45°-9	724	35	15	14	82
45°-10	655	58	5	41	75
Median	715	35	23	21	78

Table 5.4 | Killer defect prediction scores (rank & percentage) for as-built 45° specimens using roughness, κ_σ and K_t^* parameters. The *Specimen* column refers to the name of individual specimens and the $n_{defects}$ column gives the total number of defects that automatically were segmented. Colors are given for guidance, the color tending to green for a successful killer defect prediction while it tends to red for a failed prediction.

Cette thèse est accessible à l'adresse : https://theses.insa-lyon.fr/publication/2024ISAL0014/these.pdf
© [F. Steinhilber], [2024], INSA Lyon, tous droits réservés

Regarding the issue of lack of resolution, it has already been discussed extensively for specimens polished by PeP since it was possible in such a case to compare with the defect shape observed by SEM. The task is much more difficult for as-built specimens because the killer defects cannot be clearly identified on fracture surfaces.

Still, simply looking at the XCT scan and the surface extracted from it already shows that resolution is a significant issue. For instance, Fig.5.23c-e present the segmentation for one of the two killer defects found in the Z-3 specimen. Although the valley can be identified on the 3D minimum curvature map in Fig.5.23a, Fig.5.23c reveals that the resolution is not good enough to properly capture its root. In such a case, regardless of the threshold used for surface segmentation, it leads to **a significant smoothing of the valley root**, inevitably altering the roughness, curvature, and K_t^* measurements. Thus, here again, improvements in the resolution of XCT scans seem to be a key axis for improvement.

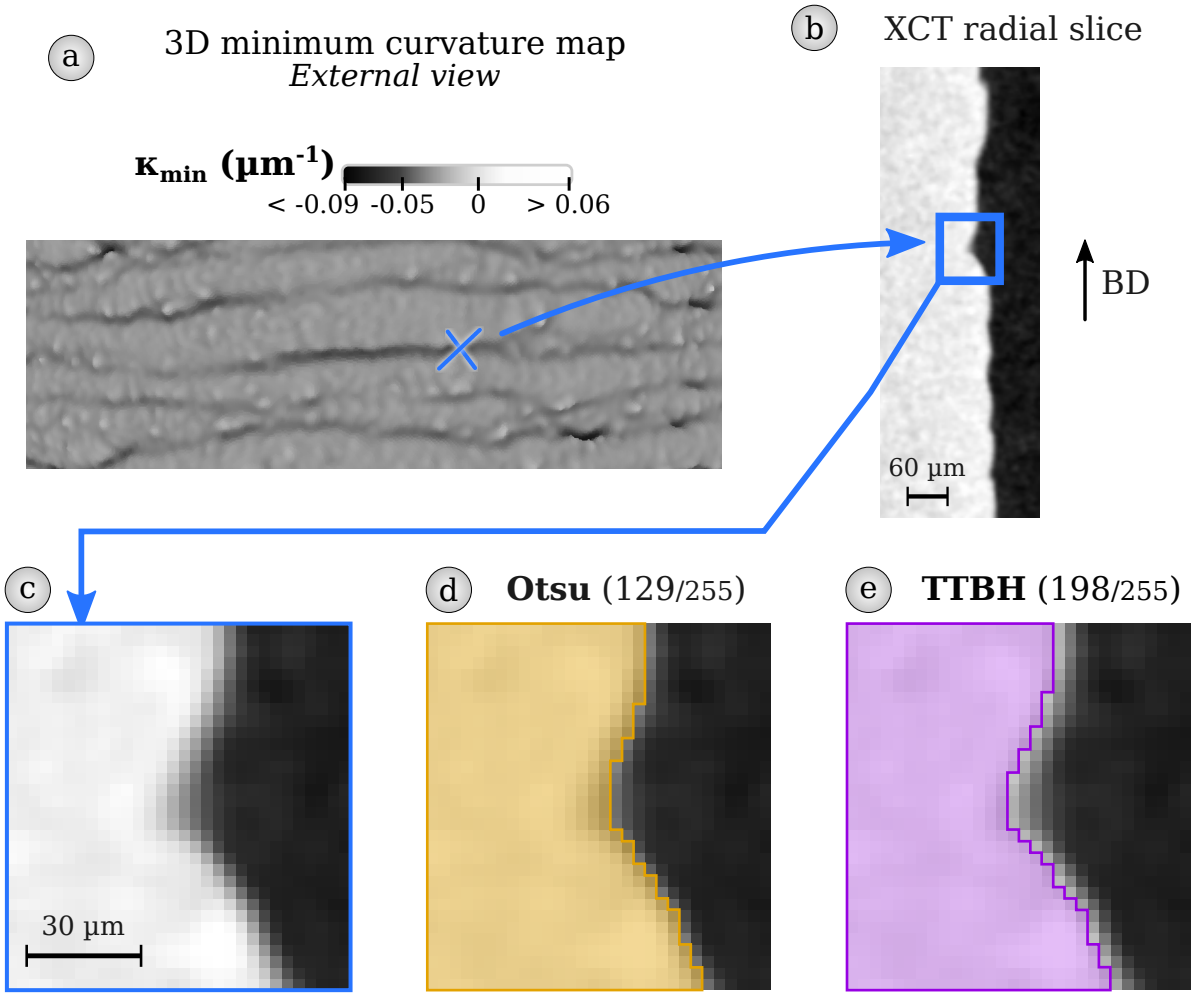

Figure 5.23 | Detailed inspection of the surface segmentation on a radial slice of a killer defect in the Z-3 specimen. (a) Valley responsible for failure, observed on a 3D minimum curvature map. (b) XCT radial slice at a given point of the valley, marked by a blue cross in (a). (c) Enlarged view of (b) centered on the killer defect. (d) Segmentation of the killer defect using Otsu's threshold. (e) Segmentation of the defect using the TTBH.

Cette thèse est accessible à l'adresse : https://theses.insa-lyon.fr/publication/2024ISAL0014/these.pdf
© [F. Steinhilber], [2024], INSA Lyon, tous droits réservés

Intermediate summary

This chapter aimed at testing to which extent the roughness, curvature and K_t^* measurements are representative of the harmfulness of surface defects on fatigue properties. First, a method to segment defects and in particular surface valleys from the surface extracted from XCT scans was described. Although it can segment valleys with particularly elongated shapes, valleys are often only partially captured. A major reason is the limited resolution of XCT scans, which does not always enable full capture of them.

Qualitatively, roughness parameters such as S_a and S_v, along with the maximum estimated stress concentration factor $K_{t,max}^*$, exhibited some correlation with the fatigue resistance of as-built and PeP-polished specimens. In terms of the fatigue life reached at a given maximum stress level, these parameters effectively differentiate between significantly different surface states (like as-built vs PeP). However, they fall short in explaining the variations in fatigue life among specimens with similar surface states, such as between different as-built Z specimens. Surprisingly, a better correlation was still found for the S_a parameter. Conversely, at a fixed fatigue lifetime, the maximum stress that specimens can endure appears to correlate better with the parameters tested, particularly K_t^*.

A perspective to improve these results for as-built specimens would be to take into account the length of the surface valleys. Indeed, a correlation was also found between the fatigue resistance of as-built specimens and the length of the initiation zone measured on the fracture surface observed by SEM. The latter is related to the length of the valley at the origin of fatigue failure.

The results obtained for the prediction of the killer defects using the K_t^* parameter calculated from XCT scans were encouraging for specimens polished by PeP. For 4 specimens out of the 8 where the killer defect could be identified on the XCT scan before failure, the killer defect could be successfully predicted. For the 4 other specimens, the killer defect was among the 10 defects considered to be the most harmful based on their K_t^* value. However, due to the lack of resolution of XCT scans, the killer defect could not be identified on the surface extracted from XCT scans for 6 specimens (out of the 14 that were analyzed).
The killer defect predictions have proved to be a far more complex task for specimens with an as-built surface. Defects have much more complex geometries than in the case of PeP specimens, making accurate segmentation more difficult. The high density of defects (≈700/specimen compared to ≈30/specimen for PeP specimens) also contributes to making the task more difficult.
Hence, the killer defect predictions clearly failed for as-built Z specimens. The median rank of the killer defect is thus 182 when using the K_t^* parameter. Even though the killer defect could not be successfully predicted in most cases, the results are much better for as-built 45° specimens. This could be due to the larger depth and different shape of valleys in 45° specimens.

Cette thèse est accessible à l'adresse : https://theses.insa-lyon.fr/publication/2024ISAL0014/these.pdf
© [F. Steinhilber], [2024], INSA Lyon, tous droits réservés

In all cases, the ability of the roughness, curvature, and K_t^* measurements to quantify surface defects' harmfulness is thought to be strongly limited by the resolution of XCT scans. Several examples were presented to show that even with a 3 µm voxel size, the XCT characterization could lead to a significant blurring which can affect its depth and curvature measurement. Although the use of the Triangle Threshold for Bimodal Histograms (TTBH) instead of a more conventional Otsu's threshold for surface segmentation helps to better capture critical defects, it seems difficult to achieve significantly better results without having access to higher resolution scans.

Still, further improvements could be achieved, for instance by taking into account the length of the surface valleys. This would require improvements in the method used for the surface defects segmentation, which has been done here essentially by thresholding surface points based on the local curvature. Also, if higher resolutions are difficult to obtain, it would be interesting to apply this methodology to specimens with larger surface defects which would be better captured by XCT at an equivalent resolution. This could, for instance, be the case by studying as-built samples manufactured by other AM processes such as E-PBF or Wire Arc Additive Manufacturing (WAAM).

Cette thèse est accessible à l'adresse : https://theses.insa-lyon.fr/publication/2024ISAL0014/these.pdf
© [F. Steinhilber], [2024], INSA Lyon, tous droits réservés

Conclusion and Perspectives

Conclusion

This work aimed at better understanding the impact of defects on fatigue properties of the Ti64 alloy manufactured by Laser Powder Bed Fusion (L-PBF). The extensive literature on this subject reveals that the large surface roughness inherited from this process significantly reduces the fatigue properties. This roughness is caused by surface defects such as valleys that generate stress concentrations and promote crack initiation under cyclic loading. Characterizing these defects is challenging because additively manufactured surfaces can show complex 3D shapes and topography. Traditional surface characterization methods often fall short in these scenarios, requiring new developments.

A methodology for a thorough 3D surface characterization

To address these challenges, **Chapter 2** describes the methodology developed for a thorough 3D characterization of surfaces based on X-ray Computed Tomography (XCT) data. This approach enables the calculation of roughness and curvature in 3D. Thus, the methodology could be applied on various components that would have been impossible to characterize using conventional methods (e.g. a 2.5 characterization using a white light interferometers), namely additively manufactured architected structures and an impeller produced by L-PBF. This 3D characterization also makes possible to capture critical defects such as notches hidden by partially melted powder particles at the surface. The methodology proposed makes use of *volumetric* operations (e.g. 3D Gaussian filters) and has thus the advantage of being possible to perform rather easily on a software such as Image. Thus, an ImageJ implementation of the 3D roughness measurement is available in an online repository [STE 23]. A Python implementation is provided as well.

This methodology developed here could be used in a wide variety of contexts, such as studying surfaces inherited from different processes (conventional casting, etc.) and in different applications (mechanical, biomedical, etc.). Here, we illustrate how this methodology can be applied to investigate the effect of notch-like defects on fatigue properties. For this purpose, a simple model has been proposed to combine roughness and curvature so as to derive a parameter representative of the stress concentration induced by defects, denoted K_t^*. Enhancements in XCT data analysis were also explored to improve the identification of critical defects, including the use of a particular threshold for surface segmentation and the use of 3D curvature analysis to specifically highlight notches oriented perpendicularly to the loading direction.

Cette thèse est accessible à l'adresse : https://theses.insa-lyon.fr/publication/2024ISAL0014/these.pdf
© [F. Steinhilber], [2024], INSA Lyon, tous droits réservés

A case study was conducted on specimens with rather simple surface states (i.e. few isolated defects) to test the ability of the methodology to predict the defect responsible for the fatigue failure (referred to as the *killer defect*). It showed promising results and has the advantage of being fully automated, with the potential for further improvements. Additionally, this methodology applies to more complex surfaces, as demonstrated in subsequent chapters on L-PBF Ti64 specimens with as-built surface states.

Material characterization

Chapter 3 describes the samples used in this work. These are Ti64 mechanical specimens manufactured by L-PBF using several build orientations: vertical (Z), at 45°, and horizontal (for tensile specimens only). Samples were stress relieved for 2 h at 720 °C to remove all residual stresses. After stress relief, the microstructure is composed of a mixture of fine α laths (with an average thickness of 0.5 µm) along with a small fraction of β phase (2.2 ± 0.3%).

It results in a rather high yield strength ($\bar{YS}$ = 1098 MPa for Z specimens) but a rather low elongation to failure (7.8% for Z specimens, and only 0.8% for horizontal specimens). The strong anisotropy in elongation to failure seems to be partly due to the preferential failure at prior β_0 columnar grain boundaries.

The defects characterization showed that samples have a high density (> 99.998%) and that residual pores are both small (over 80% smaller than 30 µm) and have a high sphericity. Most pores are located in a sub-surface layer at approximately 140 µm from the surface, which corresponds to the boundary between contour laser scans and the bulk material (hatching).

Several surface defects could be identified on the 3D surface characterization, the defects that are expected to cause the most damage in fatigue being valleys. Valleys were found to be deeper and more tortuous in down-skin areas of specimens built at a 45° angle with respect to the built plate, in comparison with vertically built specimens.

Fatigue properties of as-built specimens

Chapter 4 assesses the effect of surface defects on fatigue properties. Specimens were first studied with a stress relief treatment only. The objective was to preserve the as-built surface.

100% of crack initiations take place from surface defects, which emphasizes their crucial role, much more than internal pores. Conventional fracture surface observations by Scanning Electron Microscopy (SEM) did not enable the systematic identification of the killer defects, the latter being shallow and difficult to delineate. The use of the 3D XCT characterization presented in Chapter 2 allowed to overcome this limitation and demonstrated that most killer defects are shallow valleys running along the specimens' surface. Furthermore, it showed that cracks tend to follow surface valleys over large distances, which is thought to play a role in their detrimental impact on fatigue resistance.

Quantitatively speaking, the fatigue strength at 10^6 cycles of as-built specimens is estimated to be approximately 250 MPa. It is the case for both Z and 45° orientations, although 45° specimens show on average slightly lower fatigue lives than Z specimens. In any case, the fatigue strength of as-built specimens is much lower than that of Machined and manually Polished specimens (M&P), which is around 850 MPa. This confirms the critical impact of surface defects, as well as the possibility of reaching a very high fatigue resistance if defects are properly controlled.

Cette thèse est accessible à l'adresse : https://theses.insa-lyon.fr/publication/2024ISAL0014/these.pdf
© [F. Steinhilber], [2024], INSA Lyon, tous droits réservés

Fatigue properties after a heat treatment leading to surface oxygen contamination

Some vertically built specimens were subjected to a subsequent higher temperature heat treatment (860 °C for 4 h). The latter leads to the formation of an oxygen-contaminated surface layer, referred to as α-case, of about 70 µm in depth. This layer was found to be responsible for a slight decrease in fatigue resistance. This is most probably caused by the brittleness of the α-case layer which promotes crack initiation, as suggested by the high density of initiated cracks observed in those specimens.

Fatigue properties improvements after a surface finishing treatment

Some as-built specimens underwent Plasma electrolytic Polishing (PeP) to enhance fatigue properties. Several polishing conditions led to different polishing depths, either around 180 µm or 340 µm. A 180 µm removal improved fatigue strength at 2×10^6 cycles to approximately 400 to 550 MPa. This improvement was limited due to the exposure of sub-surface pores (particularly numerous at about 140 µm from the surface), creating pit-like defects that led to fatigue failure. In contrast, a more extensive 340 µm removal that goes beyond the subsurface layer containing a high density of pores significantly increased fatigue strength at 2×10^6 cycles, above 1000 MPa.

Correlation between fatigue resistance and parameters derived from the 3D surface characterization

In **Chapter 5**, the quantitative and predictive capabilities of the surface characterization method introduced in Chapter 2 were evaluated. Specifically, it tested whether this method could give interesting indicators of a specimen's fatigue resistance and accurately predict the killer defect.

Conventional roughness parameters such as S_a capture the difference between very different surface states, e.g. they capture the fact that as-built specimens have lower fatigue lives on average than specimens polished by PeP. However, they are unable to account for the fatigue lives scatter observed between similar surface states, e.g. between two as-built Z specimens. These parameters seem better correlated with the maximum stress that can be endured by a specimen for a targeted lifetime, the K_t^* parameter yielding, in this case, the most promising results. Results could be improved by taking into account other factors such as the length of valleys.

Prediction of the killer defect

The prediction of killer defects using the K_t^* parameter showed good results for specimens polished by PeP. However, it seems strongly limited by the resolution of the XCT scans. Thus, for 6 out of 14 specimens, XCT could not detect the killer defect due to an insufficient resolution. Over the remaining 8 specimens, the method accurately identified the killer defect in 50% of the cases.

Predicting killer defects in as-built Z specimens turned out to be more challenging and did not lead to conclusive results. However, results for as-built 45° specimens were much more encouraging.

Cette thèse est accessible à l'adresse : https://theses.insa-lyon.fr/publication/2024ISAL0014/these.pdf
© [F. Steinhilber], [2024], INSA Lyon, tous droits réservés

Improving XCT resolution could potentially yield better predictions, as valleys in as-built specimens were often too shallow to be adequately captured with the 3 µm voxel size used in this study. Considering the shape and length of surface valleys might also enhance the predictions. Furthermore, as-built surfaces present a large population of valleys with similar shapes and mechanical harmfulness. Thus, the exact location of the killer defect within this population could depend on other factors such as the local surface microstructure.

Perspectives

This work opens various avenues for future developments and a deeper understanding of the impact of surface defects on fatigue properties. Below are some key areas for potential improvements.

Enhancing XCT scan resolution

One of the main challenges in correlating 3D roughness and curvature characterization with fatigue resistance or killer defect location is the insufficient resolution of XCT scans. Thus, the most obvious (and maybe the most promising) lever for improvement is the access to higher-resolution scans. These could be obtained with advanced laboratory X-ray tomographs capable of smaller voxel sizes or by using synchrotron XCT facilities.

An experiment was conducted to evaluate the impact of improved resolution. The Z-10 (as-built Z) specimen, was scanned at the I12 Beamline of the Diamond synchrotron (UK), thanks to Thomas Connoley, James Ball, and David Collins. The killer defect was identified, and its detection using laboratory XCT (with a voxel size of 3 µm) was compared to that using synchrotron XCT (with a voxel size of 1.3 µm), see Fig.5.24a-e.

The 3D κ_{min} map in Fig.5.24a illustrates that a better resolution of the surface is achieved with synchrotron XCT compared to what could be obtained using laboratory XCT in this work. The radial slices (Fig.5.24b-c) centered on the killer defect, a valley, further highlight this difference. Enlarged views (Fig.5.24d-e) provide a closer look at the killer defect, with surface segmentation performed using the TTBH.

Although laboratory XCT partially captures the killer defect, synchrotron XCT offers a more detailed and accurate description of the defect. This suggests that improved resolution could significantly enhance surface characterization, especially in measuring curvature at the notch root. Hence, pursuing higher-resolution scans could potentially yield better results and predictions in future studies. However, it is worth keeping in mind that accessing synchrotron XCT can be difficult and that higher resolutions may lead to large amounts of data that require significant computing resources for analysis.

Cette thèse est accessible à l'adresse : https://theses.insa-lyon.fr/publication/2024ISAL0014/these.pdf
© [F. Steinhilber], [2024], INSA Lyon, tous droits réservés

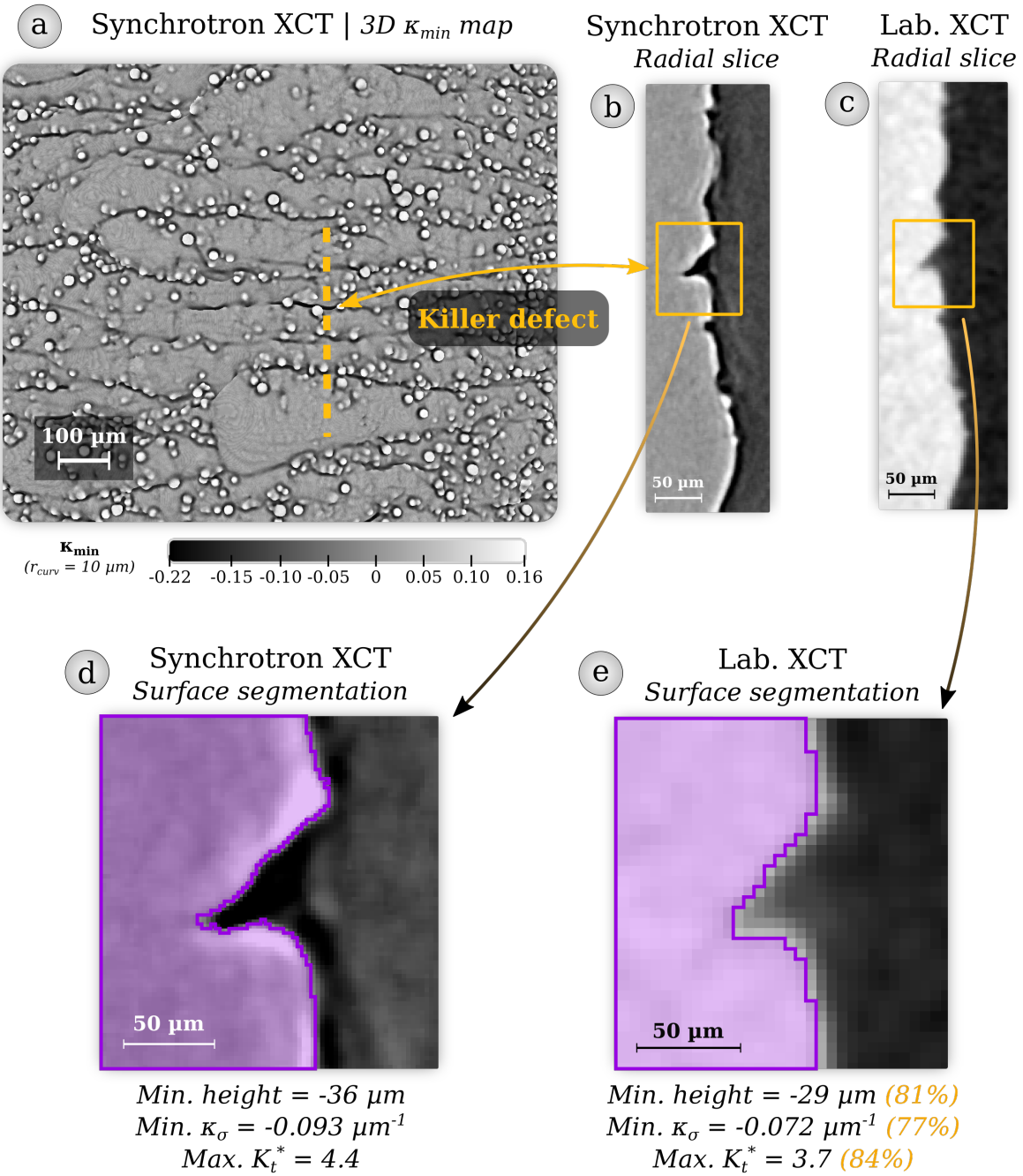

Figure 5.24 | Comparaison of killer defect identification using laboratory XCT (vox. = 3 µm) and synchrotron XCT (vox. = 1.3 µm) on Z-10 specimen. (a) 3D minimum curvature map centered on the killer defect. (b) and (c) show radial slices centered on the killer defect using either laboratory or synchrotron XCT. (d) and (e) show enlarged views of (b) and (e) with the surface segmentation achieved in both cases using the TTBH.

Cette thèse est accessible à l'adresse : https://theses.insa-lyon.fr/publication/2024ISAL0014/these.pdf
© [F. Steinhilber], [2024], INSA Lyon, tous droits réservés

Comparing 2.5D and 3D characterization methods

Given the challenges in obtaining high-resolution XCT scans, a practical alternative could involve using high-resolution 2.5D instruments like white light interferometry. These instruments typically offer better resolutions than XCT [VIL 19]. This suggestion might appear counterintuitive, given that part of this research underscores the necessity of true 3D characterization for adequately capturing critical surface defects typical of as-built surfaces in additive manufacturing. However, the higher resolution that can be achieved using 2.5D instruments may justify the trade-off depending on the case. Consequently, conducting further studies to compare the predictive accuracy (e.g. regarding fatigue properties) of 3D XCT measurements and higher-resolution 2.5D measurements could be worthwhile.

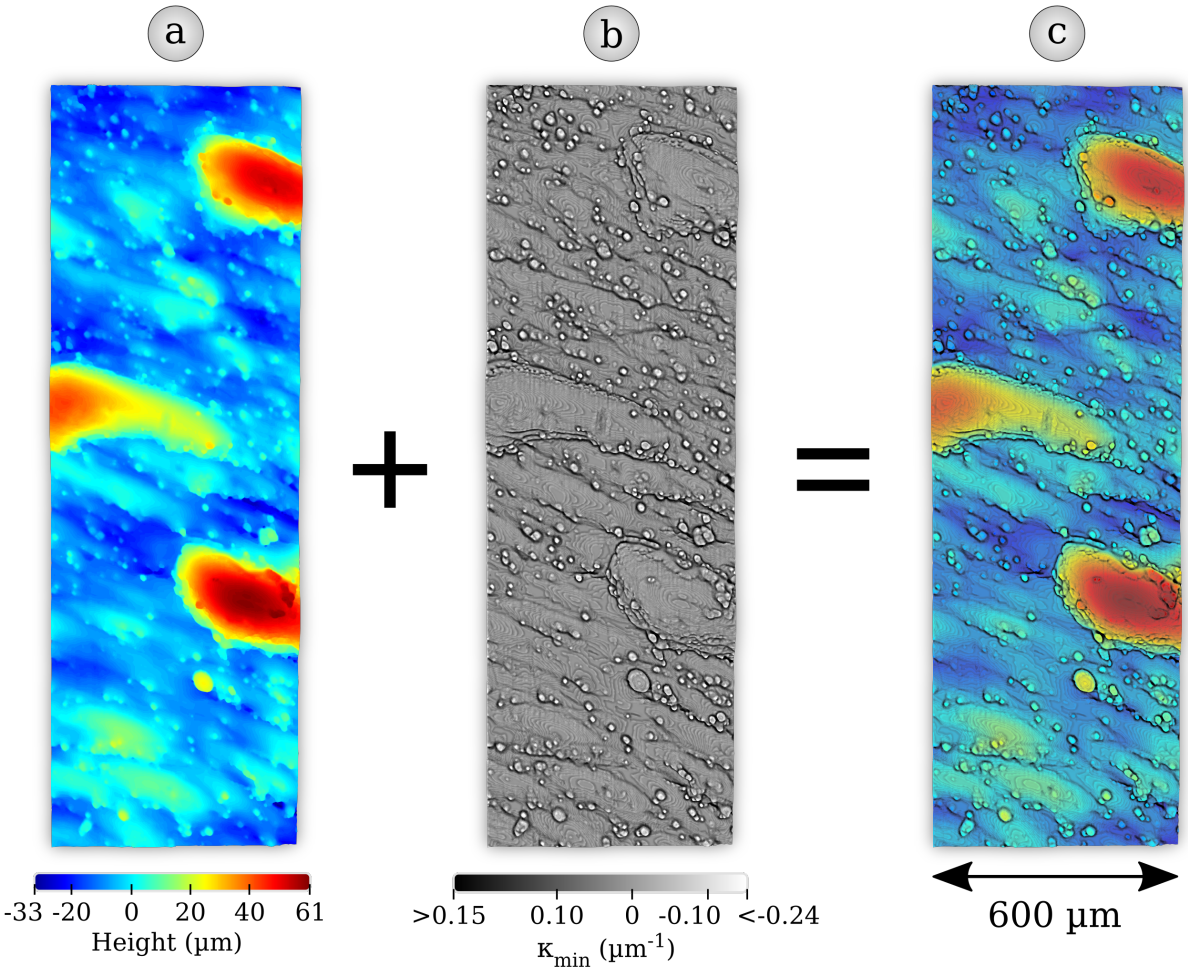

Figure 5.25 | Surface roughness and curvature characterization from 2.5D data. (a) 2.5D roughness measurement obtained using a chromatic confocal sensor (HiroX NPS) and a lateral spacing for measurement of 1 µm. (b) Minimum curvature map, computed using $r_{curv} = 10\,\mu m$. (c) Superposition of (a) and (b).

Cette thèse est accessible à l'adresse : https://theses.insa-lyon.fr/publication/2024ISAL0014/these.pdf
© [F. Steinhilber], [2024], INSA Lyon, tous droits réservés

As an example, Fig.5.25a-c present a 2.5D surface characterization of an as-built Z specimen. Fig.5.25a displays the roughness map, from which curvature is computed using the same integral invariant method described in Chapter 2. Fig.5.25b shows the resulting minimum curvature map, and Fig.5.25c combines the roughness and curvature maps for a comprehensive surface representation of both details and larger scale variations. The lateral measurement spacing here is 1 µm, achieving a detailed surface representation comparable to the one obtained with synchrotron XCT, see Fig.5.24a. Thus, the accuracy of the surface characterization may be improved accordingly. Of course, despite the improved resolution, the 2.5D characterization might miss or only partially capture hidden features, potentially leading to inaccuracies, particularly in curvature estimation.

Enhancing defects segmentation and considering defects' shape and neighborhood

If enhancing the spatial resolution of surface characterization is not an option, alternative avenues for improvement remain. Thus, Chapter 5 highlights the potential for more accurately assessing the impact of valley-type defects by considering their shape, particularly their length. Additionally, the neighborhood of a defect, and in particular nearby valleys, can also influence its harmfulness. A well-known phenomenon, the *shielding effect*, suggests that a single valley can generate higher stress concentration compared to multiple valleys close to one another [BAR 23, BAR 21].

Improving the defect segmentation methodology could lead to a better understanding and quantification of these effects. While enhanced XCT scan resolution, as discussed in Chapter 5, would most probably be of great help, exploring other segmentation techniques could also be effective. The watershed method, combined with Wolf pruning, is the method outlined in ISO standards [Int 21, LOU 20] and could be an interesting choice. One of the few examples of watershed-based segmentation on a free-form surface found in the literature is shown in Fig.5.26a-d.

However, it might be necessary to adapt the watershed and Wolf pruning algorithms to better take into account the elongated shape of valley-type defects and break the *valleys network* mentioned in Section 5.1.1, for example by using directional curvature measurement besides roughness.

Alternative techniques could be explored for more precise segmentation of valley roots, as the watershed method typically segments the entire surface, categorizing all points as part of a defect (see Fig.5.26d). For instance, the works of [COE 16, LEV 15] introduce segmentation methods that rely on estimations of curvature or normal fields. These approaches could potentially offer a more targeted segmentation, specifically focusing on the critical areas of the valleys. An example of sharp feature segmentation (here, edges instead of notches) using this method is shown in Fig.5.27.

Cette thèse est accessible à l'adresse : https://theses.insa-lyon.fr/publication/2024ISAL0014/these.pdf
© [F. Steinhilber], [2024], INSA Lyon, tous droits réservés

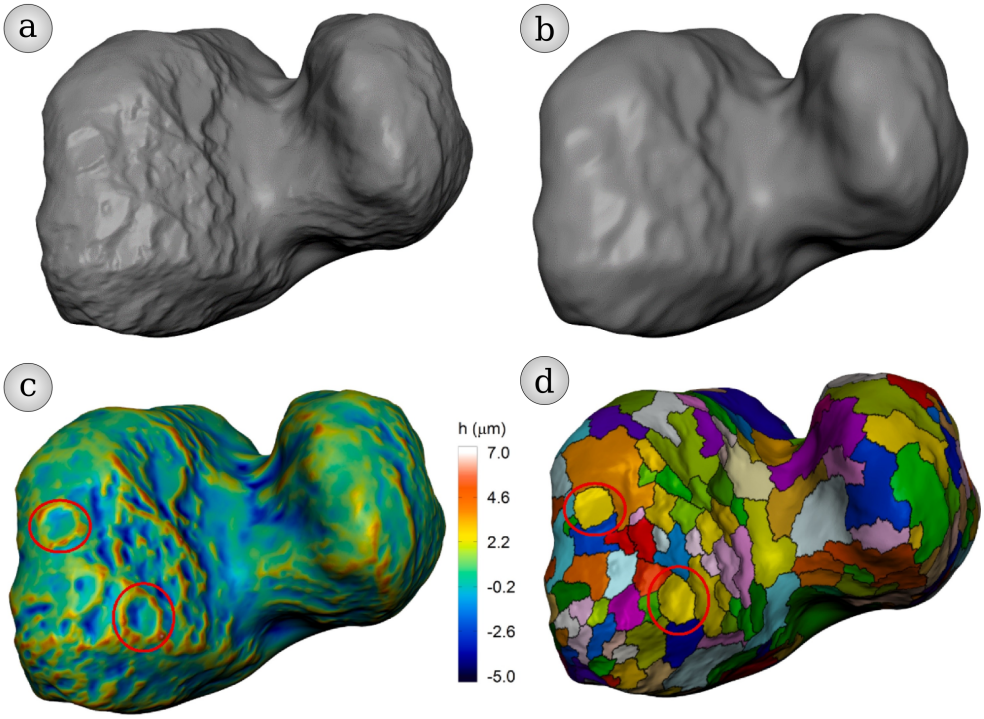

Figure 5.26 | Surface valleys segmentation on a free-form surface using watershed method together with Wolf pruning, adapted from [LOU 20]. (a) Initial surface mesh, derived from the Rosetta comet model developed by the European Space Agency. (b) Smoothed mesh obtained by Laplacian smoothing and used as a reference for roughness computation. (c) 3D roughness map obtained by computing the distance between (a) and (b). (d) Result of the watershed segmentation after Wolf pruning.

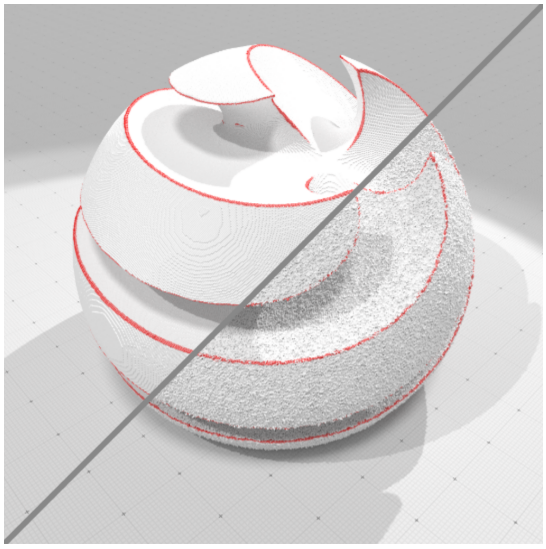

Figure 5.27 | Sharp features extraction using the approach of [COE 16], based on normal vector field regularization. Sharp edges are successfully segmented in red, even when some noise is added to the data (see the lower right half of the image).

Cette thèse est accessible à l'adresse : https://theses.insa-lyon.fr/publication/2024ISAL0014/these.pdf
© [F. Steinhilber], [2024], INSA Lyon, tous droits réservés

Selecting the appropriate scale for surface analysis

Another option to improve results regardless of the spatial resolution of XCT scans would be to gain a deeper understanding of the role of the scale at which the analysis is conducted. In our study, the roughness measurement scale is defined by the cut-off wavelength λ_c, and the curvature measurement scale by the convolution radius r_{curv}. The results in Section 2.4 and Section 5.3 have shown that the prediction ability of our model heavily depends on these parameters.

Setting these parameters appropriately can be challenging, a complexity only partially addressed in this work. As highlighted in Section 2.4, fully understanding and describing surface features may even require characterizing the surface at multiple scales. This concept of *multi-scale analysis* has been explored in various studies for both roughness [JIA 20a, GO 16] and curvature [BRO 18, BAR 19, VUL 14].

In fact, our comparison of killer defect predictions for various values of r_{curv} in Sections 2.4 and 5.3 already ludes elements of multi-scale analysis. This is somewhat analogous to the approach of [VUL 14], who calculated surface curvature at multiple scales on machined steel specimens to find the scale where the maximal mean curvature correlates best with the experimental fatigue resistance. This approach could be further studied in our case by computing curvature (and/or roughness) at an increased number of scales and trying to link the most relevant scales to the observed surface defects, particularly those causing fatigue failure.

Further work could also focus on integrating measurements from different scales, possibly requiring more complex modeling approaches. For instance, [LEV 15] suggests a method for segmenting surface features (like sharp edges) using the slope of curvature change with respect to the convolution radius r_{curv}, rather than the curvature at a fixed scale. This method can identify features existing at varying scales on the same surface, offering a more comprehensive characterization.

Applying the 3D characterization method to various materials and processes

Besides the influence of the resolution of XCT scans and the methodology used for data analysis, the accuracy of predictions may also depend on the manufacturing processes used for sample manufacturing. Exploring the fatigue properties of samples made using different additive manufacturing techniques, such as Electron Beam Powder Bed Fusion (E-PBF), Wire Arc Additive Manufacturing (WAAM), or conventional casting, could therefore be insightful. Notably, these methods often result in larger defects, potentially simplifying the characterization and providing more conclusive results even with a limited spatial resolution.

Investigating materials different from Ti64, with different properties (e.g. different notch sensitivities) could also provide valuable insights, as they might respond differently to fatigue loading with a similar defect population. A preliminary study on IN718 bending fatigue specimens produced by L-PBF has shown promising results, see Fig.5.28a-d.

The K_t^* maps before and after the fatigue test are displayed in Fig.5.28b and Fig.5.28c, respectively. They are shown from an internal point of view (i.e. from under the surface). This allows to better observe hidden features such as the notch at point A shown in the enlarged view in Fig.5.28a.

Cette thèse est accessible à l'adresse : https://theses.insa-lyon.fr/publication/2024ISAL0014/these.pdf
© [F. Steinhilber], [2024], INSA Lyon, tous droits réservés

Fig.5.28c shows the propagated crack's location, and comparison with Fig.5.28b helps identify major defects along the crack path. The defect at point A shows the highest K_t^* value along this path. Fig.5.28d is an observation of this defect on an XCT scan slice. Only one other surface location, point B in Fig.5.28b, exhibits higher K_t^* values. Therefore, the actual killer defect was the second most critical based on the K_t^* parameter, indicating a reasonably good prediction.

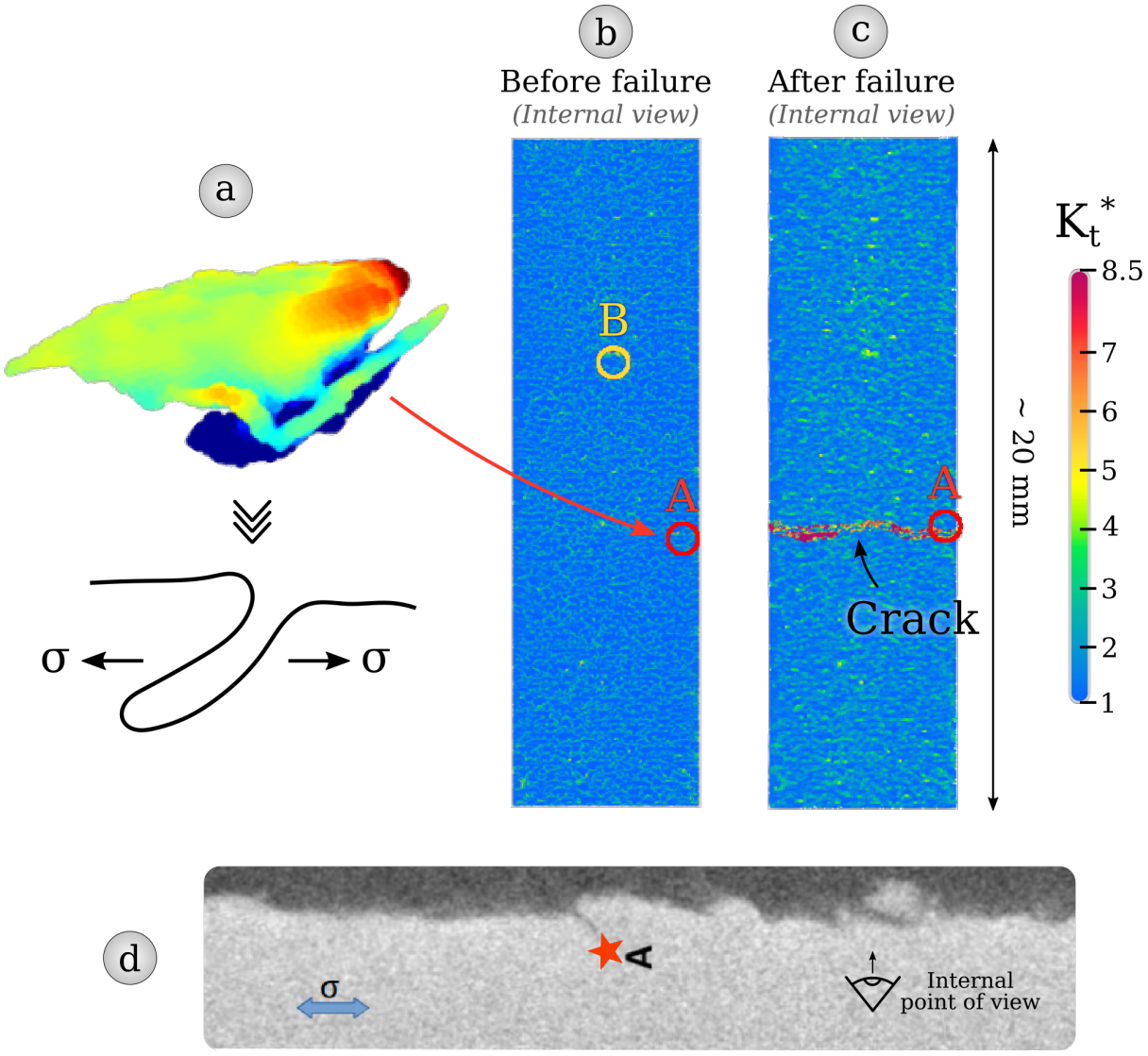

Figure 5.28 | Comparing the killer defect prediction to the actual crack location after failure in an IN718 bending fatigue specimen manufactured by L-PBF. The surface subjected to fatigue loading is the down-skin part of a specimen built a 45°. The characterization was done using XCT scans with a voxel size of 4 µm. (a) Enlarged view of the K_t^* map of the defect at point A, belonging to the crack path. Point B is the only location of the surface where K_t^* values superior to those in point A were found. (b) Internal view of the surface K_t^* map before fatigue testing. (c) Internal view of the surface K_t^* map after fatigue testing. The propagated crack is characterized by high K_t^* values and can thus be seen in red. (d) XCT slice revealing the notch defect at point A.

Cette thèse est accessible à l'adresse : https://theses.insa-lyon.fr/publication/2024ISAL0014/these.pdf
© [F. Steinhilber], [2024], INSA Lyon, tous droits réservés

Combining Hot Isostatic Pressing (HIP) with surface finishing

In parallel to enhancing our understanding and predictive capabilities regarding the impact of defects on fatigue properties, exploring ways to improve the fatigue properties themselves through various post-treatments would be interesting. Although not explored in this study, Hot Isostatic Pressing (HIP) treatment has for example the potential to offer significant benefits, particularly if properly combined with a subsequent surface finishing step.

Chapter 4 demonstrated that surface finishing significantly enhances the fatigue properties of L-PBF Ti64, provided it does not expose internal pores to the surface. A polishing depth of 340 µm was particularly effective, completely removing the subsurface layer where most pores were found to be located. To avoid the issues associated with such extensive polishing (like dimensional inaccuracies), a preliminary HIP treatment to close internal pores might be more advantageous. Following HIP, a milder polishing with a reduced polishing depth of around 200 µm could be sufficient to remove surface valleys and achieve excellent material properties.

However, it is important to note that HIP, typically conducted at high temperatures (e.g., 920 °C for 2 hours for Ti64 alloy), can also alter the microstructure, potentially affecting mechanical properties or causing surface contamination. Additionally, HIP significantly adds to the manufacturing cost. Thus, a comprehensive study assessing the pros and cons and finding an optimal balance for this treatment could be valuable.

Cette thèse est accessible à l'adresse : https://theses.insa-lyon.fr/publication/2024ISAL0014/these.pdf
© [F. Steinhilber], [2024], INSA Lyon, tous droits réservés

Cette thèse est accessible à l'adresse : https://theses.insa-lyon.fr/publication/2024ISAL0014/these.pdf
© [F. Steinhilber], [2024], INSA Lyon, tous droits réservés

Appendix A

Comparison of different distance calculation methods

Measuring roughness on free-form surfaces involves calculating the distance between the original rough surface and a reference surface. In this study, the original surface is defined by what we call the *sample mask* or *surface mask*, as introduced in Chapter 2. The reference surface is identified as the *smooth mask* in the same chapter. Additionally, we can introduce here the concept of the *smooth surface mask*, which is to the smooth mask what the surface mask is to the sample mask.

Different methods can calculate this distance, and while they often yield similar results, some may introduce more errors, especially in specific scenarios. This appendix focuses on comparing two distinct methods.

The method presented in Chapter 2 involves the use of a Signed Euclidean Distance Transform (SEDT). Its advantage is that it is a 3D operation, directly available on software such as ImageJ.

Alternatively, a Nearest Neighbor Search (NNS) technique can be more appropriate in certain cases. NNS seeks the closest point(s) in a point cloud for a given point. In our context, it can be used to identify the nearest point on the smooth surface for each point on the (rough) surface. The local height, or roughness, is then the distance between these two points. Practically, NNS is often executed using a kd-tree data structure [SKR 19], as used in this study. In terms of computing time, the NNS approach is similar to SEDT, but better than SEDT in terms of memory usage. However, unlike SEDT or Gaussian filters, it is not a volumetric operation and is not readily available in software like ImageJ without custom implementation. In this work, the NNS computation was done using the *scipy-spatial* Python library. The SEDT method was also conducted using Python, utilizing the *edt* library, which offers an efficient multi-threaded implementation. Note that the Python implementation for 3D roughness measurement provided in [STE 23] proposes the two methods for distance calculation. In the script, the SEDT method is referred to as the *'edt'* method, while the NNS method is referred to as the *'kdtree'* method.

Fig.A.1a-e presents a comparison of roughness measurements obtained using SEDT and NNS methods on a straightforward example: a perfect cylinder with a radius of 3.5 voxels. In this scenario, both the sample mask and the smooth mask are identical, as they represent the same perfect cylinder (shown in Fig.A.1a). Similarly, the surface mask and the smooth surface mask are also the same (see Fig.A.1b).

Cette thèse est accessible à l'adresse : https://theses.insa-lyon.fr/publication/2024ISAL0014/these.pdf
© [F. Steinhilber], [2024], INSA Lyon, tous droits réservés

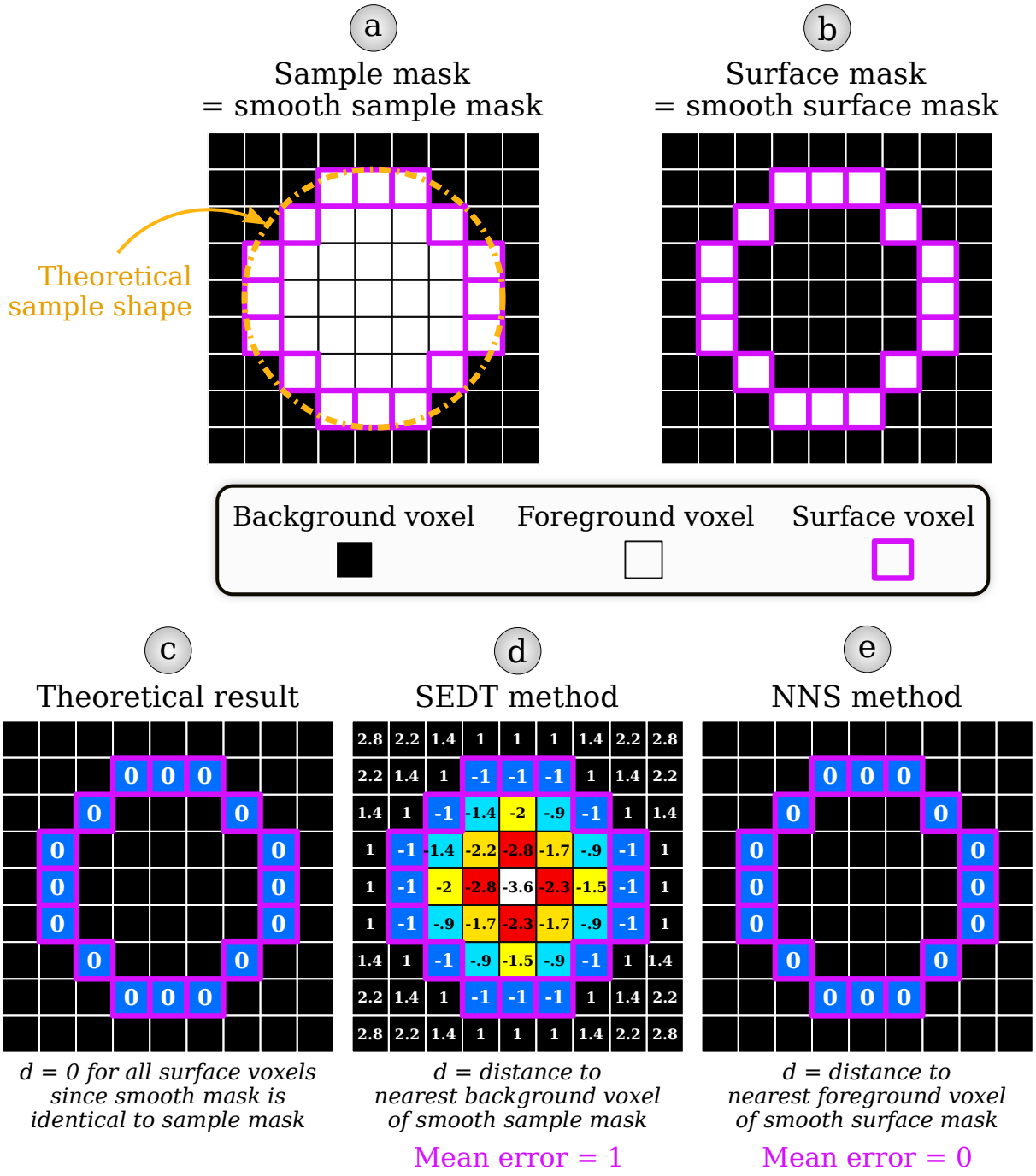

Figure A.1 | Comparing mean errors in roughness measurement between SEDT and NNS methods for a perfect cylinder. Each subfigure displays a cross-sectional slice of the cylinder. (a) Sample mask showing the cylinder's theoretical shape and surface voxels. This also represents the ideal sample mask as the smooth version of a perfect cylinder is identical. (b) Surface mask, identical to the smooth surface mask in this case. (c) Expected theoretical roughness values for each surface voxel. (d) SEDT results, with roughness values of -1 for all surface voxels. (e) Roughness values, determined by the NNS method for each surface voxel.

Cette thèse est accessible à l'adresse : https://theses.insa-lyon.fr/publication/2024ISAL0014/these.pdf
© [F. Steinhilber], [2024], INSA Lyon, tous droits réservés

In this example, where the surface and its smooth reference are the same, the anticipated local height for all surface voxels should be zero (as seen in Fig.A.1c). However, SEDT calculates the distance from each surface voxel to the nearest background voxel of the smooth sample mask, resulting in a -1 value. Consequently, this leads to an error of 1 for each voxel, and an overall mean error of 1, defined as:

$$\text{Mean error} = \underset{\text{surface voxels}}{mean} |\text{height} - \text{theoretical height}| \tag{A.1}$$

In this specific case, the error can be corrected by subtracting the mean height from all surface voxels post-calculation, a process that will be referred to as *zero-centering*. This correction step is recommended in Chapter 2, notably for situations like this.

For a more in-depth comparison, we used a cylinder with an artificial sinusoidal roughness on its surface. The cylinder is 4 mm in height and has an average diameter of 1 mm, with the sinusoidal roughness featuring a wavelength of $\lambda = 100\,\mu m$ and amplitude A varying from 0 to 30 µm. Figure A.2 provides a schematic representation of a 2D segment of this surface. The sample mask, used for calculations, is generated from the analytical formula of this shape, using a voxel size of 2.5 µm.

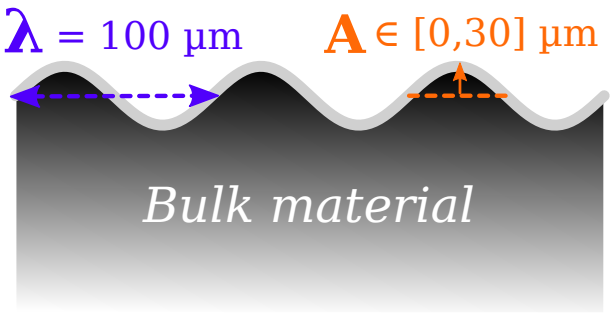

Figure A.2 | Illustration of a section of the sinusoidal roughness used for the example.

3D roughness maps for this cylinder with $A = 15\,\mu m$ are depicted in Fig.A.3a-c.

Fig.A.3a serves as a reference, showing the ideal results one would get by directly computing the local height at each surface voxel based on the analytical formula. Figures A.3b and A.3c display the results from the SEDT and NNS methods, respectively. Both methods produce roughness maps that closely resemble the theoretical ones. However, enlarged views reveal that the discrete nature of distance calculations results in abrupt local height changes, unlike the smoother theoretical results in Fig.A.3a.

Fig.A.4a-b quantitatively compare the mean error and the average arithmetic roughness S_a for amplitude values A from 0 to 30 µm. These figures assess which method, SEDT or NNS, yields more accurate results compared to the theoretical values. Additionally, both methods are evaluated with and without the zero-centering step to determine its effectiveness in reducing errors.

Fig.A.4a indicates that generally, the NNS method outperforms the SEDT method, particularly for smaller amplitude values (A), similar to the smooth cylinder case seen in Fig.A.1. However, applying the zero-centering step allows to reduce to some extent the error generated by the SEDT method. For the NNS method, at least in our example of a sinusoidally roughened cylinder, zero-centering does not improve accuracy.

Cette thèse est accessible à l'adresse : https://theses.insa-lyon.fr/publication/2024ISAL0014/these.pdf
© [F. Steinhilber], [2024], INSA Lyon, tous droits réservés

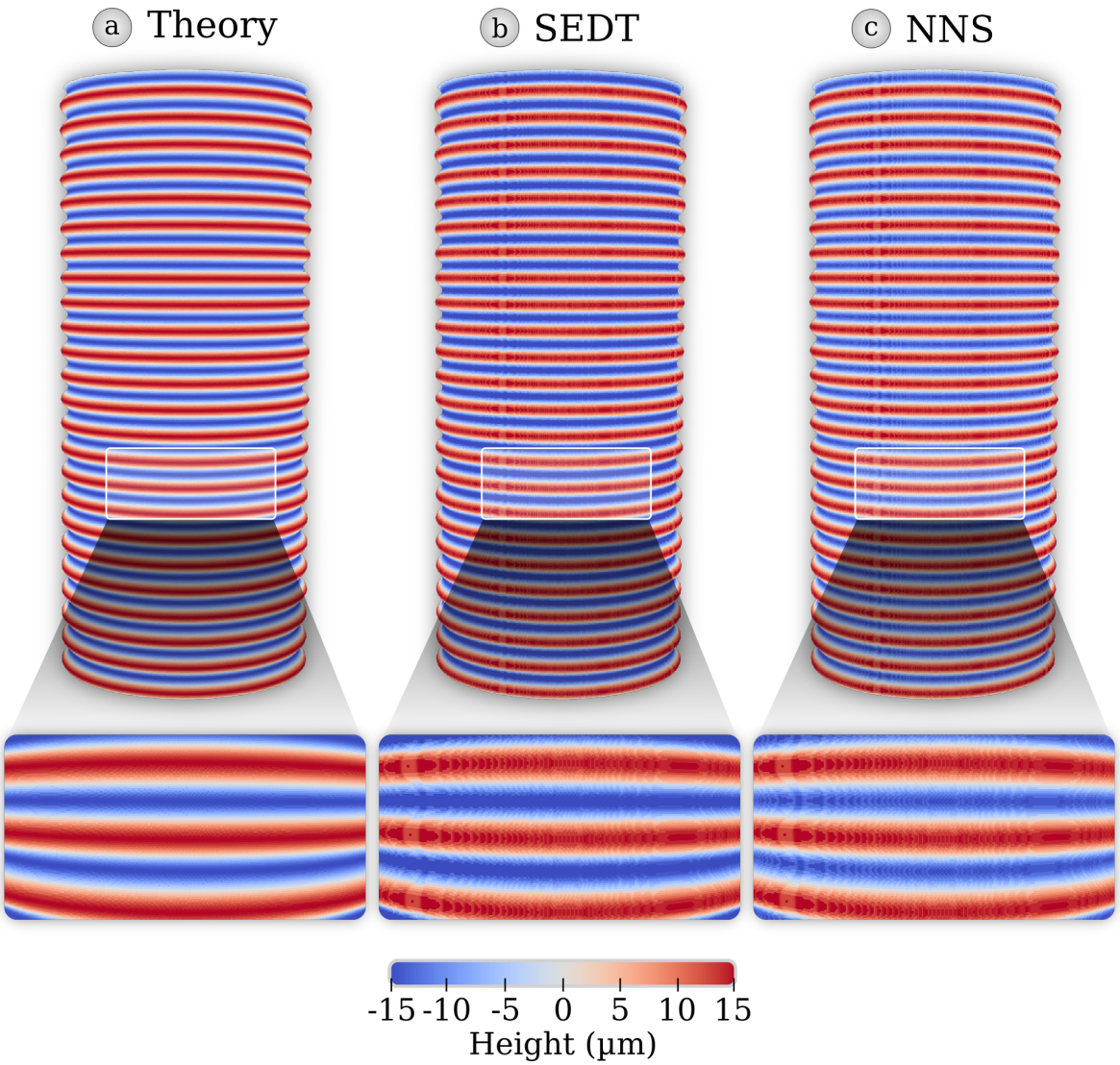

Figure A.3 | 3D roughness maps of the cylinder with sinusoidal roughness. (a) Displays the ideal, analytically derived roughness values. (b) Shows results using the SEDT method. (c) Presents results obtained with the NNS method.

These findings suggest that while the choice between SEDT and NNS methods may not be critical for surfaces with significant roughness, it becomes crucial for smoother surfaces. This is for example the case for PeP-polished samples from Chapter 4, where the SEDT method was found to cause substantial errors in some roughness measurements.

The error from using SEDT, as opposed to a method like NNS, will typically be around the voxel size. While this may not seem substantial for single voxel height measurements or for calculating roughness parameters like S_z or S_v, it can significantly affect average parameters such as S_a. This is because a consistent 2.5 µm negative error (as seen in Fig.A.1d) will substantially skew the S_a value.

Cette thèse est accessible à l'adresse : https://theses.insa-lyon.fr/publication/2024ISAL0014/these.pdf
© [F. Steinhilber], [2024], INSA Lyon, tous droits réservés

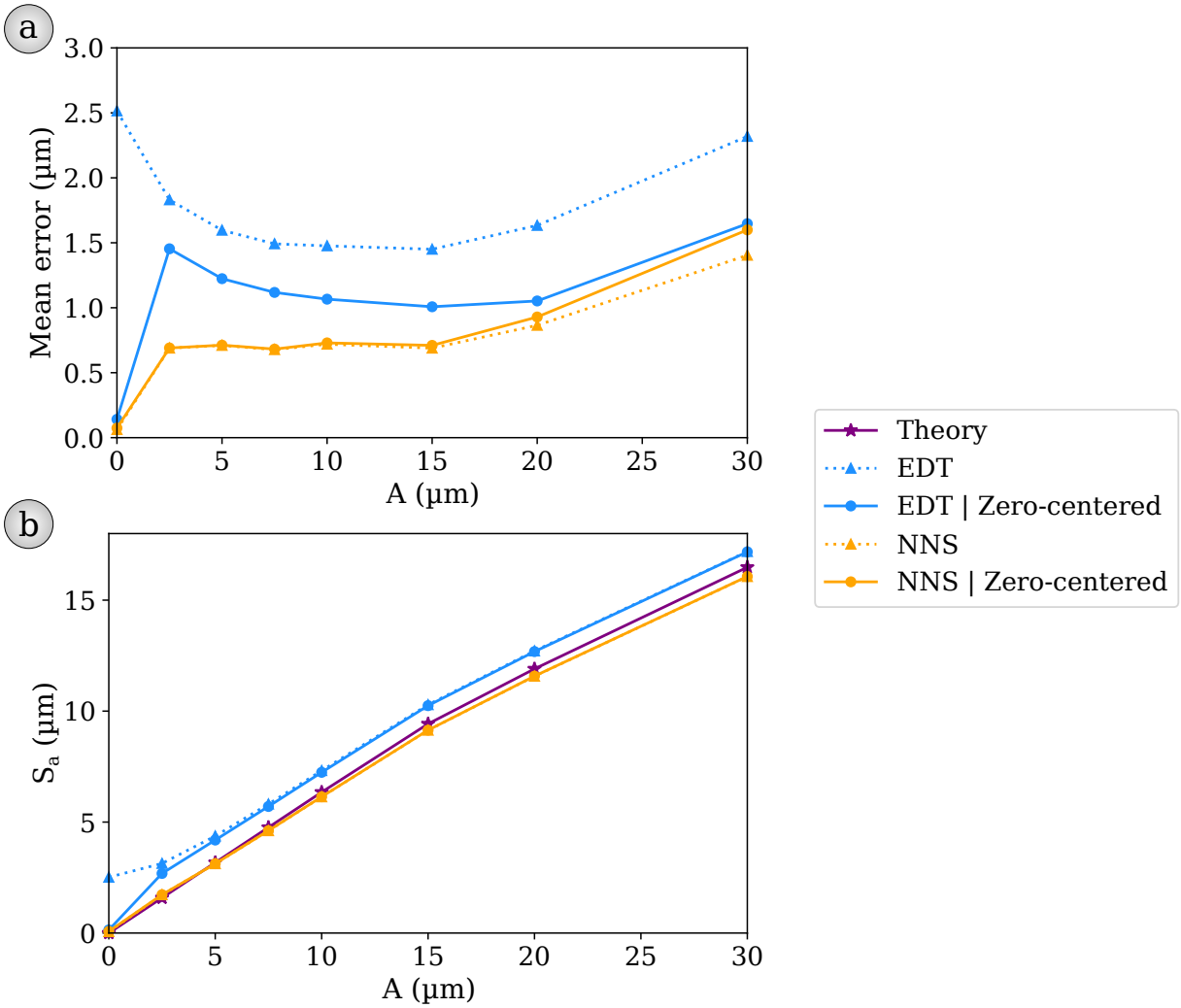

Figure A.4 | Comparing roughness measurements from SEDT and NNS methods with theoretical calculations. (a) Theoretical results with analytically calculated roughness values. (b) Roughness measurements using the SEDT method. (c) Measurements from the NNS method.

This effect is visible in Fig.A.4b, where using the SEDT method without zero-centering results in S_a values markedly higher than theoretical ones, particularly at small A values. This discrepancy persists even at larger A values. In contrast, the NNS method delivers S_a values very close to the theoretical results.

In summary, the NNS method is preferable to SEDT where possible. If SEDT must be used, the zero-centering step can reduce errors. However, caution is advised when characterizing very smooth surfaces, particularly if S_a values are close to the voxel size.

Cette thèse est accessible à l'adresse : https://theses.insa-lyon.fr/publication/2024ISAL0014/these.pdf
© [F. Steinhilber], [2024], INSA Lyon, tous droits réservés

Cette thèse est accessible à l'adresse : https://theses.insa-lyon.fr/publication/2024ISAL0014/these.pdf
© [F. Steinhilber], [2024], INSA Lyon, tous droits réservés

Appendix B

3D Gaussian S-Filter using normalized convolution

The following methodology can be used to apply any 3D linear filter on a set of voxels. In particular, it can be used to apply a Gaussian S-filter (or L-filter) to roughness values calculated following the workflow described in Section 2.2.2. It can be considered as a particular application case of the concept of normalized convolution introduced by [KNU 93]. Unlike a conventional convolution where all voxels are taken into account, normalized convolution can be used to ignore certain voxels. Here, it will be used to ignore background voxels and thus filter only the ones that carry actual information – i.e. the surface voxels that carry roughness values.

A linear filter is an operation where the value at a given voxel is replaced by a linear combination of the value at the given point and its neighbors. Each neighbor has a specific weight w, i.e. the weight of its contribution to the final filtered value. The matrix assigning the weights for the central voxel and its neighbors is called the filter kernel. For a uniform (= mean) filter, all weights in the kernel will have the same weight. In the case of a Gaussian filter, weights decrease as the distance to the central voxel increases following a Gaussian law, see Fig.B.1. In both cases, weights are generally normalized, meaning the sum of all kernel weights equals 1. For example, this ensures that applying a Gaussian filter to a uniform volume made of 1 will result in a uniform volume made of 1. This is the standard "global" normalization illustrated in Fig.B.1 and employed in common Gaussian filter implementations.

However, the situation is a bit different when applying a S-filter to a set of surface voxels. In such a case, to compute the filtered value at a given voxel, only neighbor surface voxels should be taken into account instead of all neighbor voxels. The solution would be to explicitly loop over surface voxels only, and never visit background voxels. This can be done in programming languages such as C++. However, this still requires some programming skills, especially to achieve reasonable computation times. Conversely, there are already many efficient implementations of the standard Gaussian filter, including ones accelerated via GPU of FFT computations. The idea here is thus to use such optimized implementations ingeniously to compute indirectly the S-filter.

Cette thèse est accessible à l'adresse : https://theses.insa-lyon.fr/publication/2024ISAL0014/these.pdf
© [F. Steinhilber], [2024], INSA Lyon, tous droits réservés

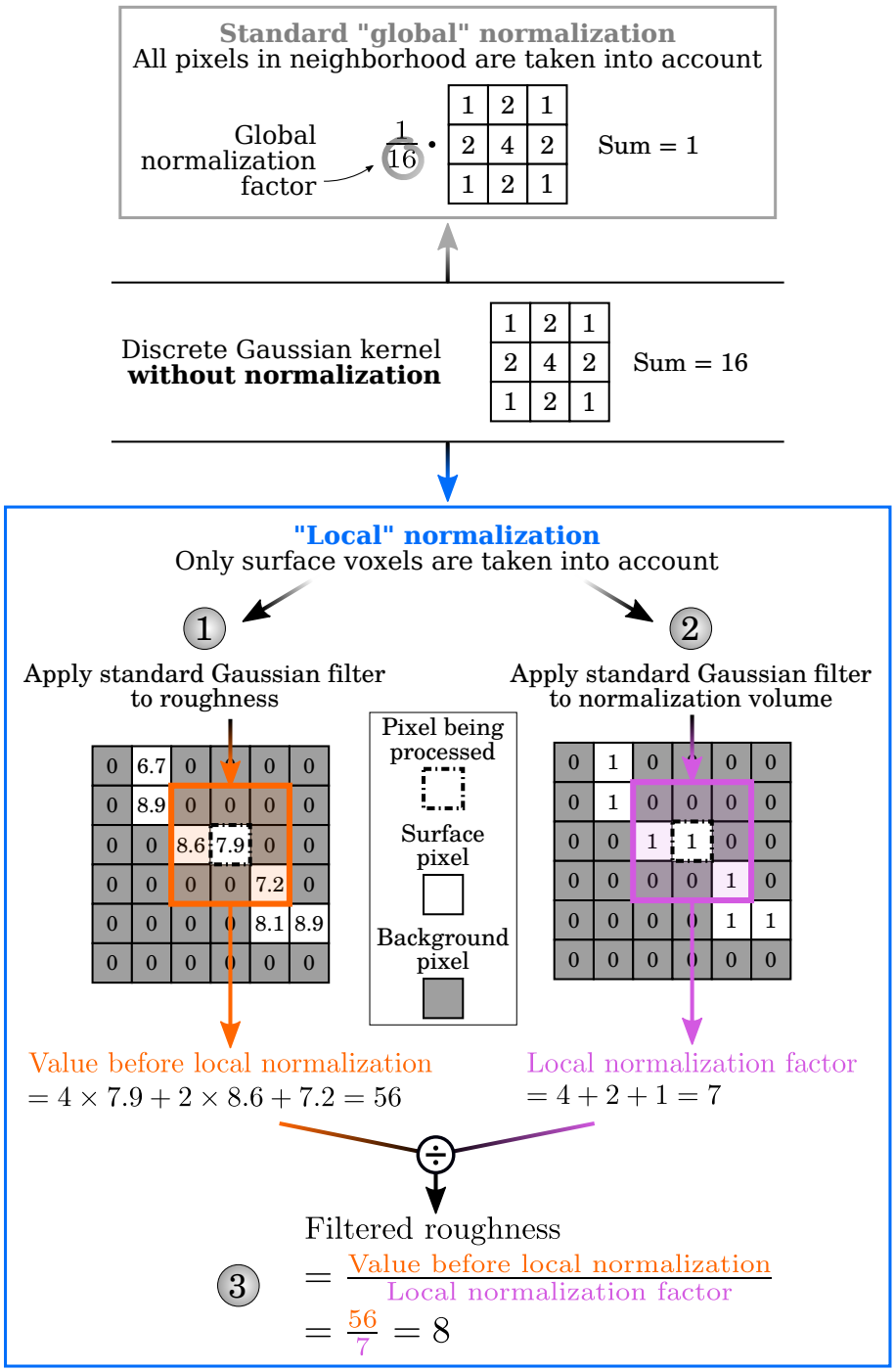

Figure B.1 Workflow proposed for the application of a 3D Gaussian S-filter. All calculations are done using operations on digital volumes, just as the rest of the roughness computation workflow. The example provided in the present figure is restricted to 2D, which means voxels are replaced by pixels. This choice is made to facilitate understanding and visualization, considering the adaptation to a 3D case is straightforward. Note that in steps 1 and 2 of the "local normalization" in Fig.B.1, a non-normalized Gaussian filter is used for the sake of clarity only. The same steps can therefore be followed using a conventional Gaussian filter.

Cette thèse est accessible à l'adresse : https://theses.insa-lyon.fr/publication/2024ISAL0014/these.pdf
© [F. Steinhilber], [2024], INSA Lyon, tous droits réservés

To do so, the first step consists of applying a conventional Gaussian filter to the volume where surface voxels contain roughness values, while background voxels contain 0 − see step 1 in Fig.B.1. Thus, background voxels do not contribute to the final filtered value. Even though, the obtained filter is not properly normalized. Indeed, the sum of the weights of all neighbors that are taken into account (i.e. all neighbor surface voxels) should equal 1. However, this sum will be in general much lower than one, because most neighbor voxels are background ones (equal to 0). To correct this bias, one simply needs to compute the same conventional Gaussian filter to a volume containing 0 at background voxels and 1 at surface voxels, see step 2 in Fig.B.1.

The resulting value at each point is the sum of all the Gaussian kernel weights that effectively come across surface voxels. It can be considered as a "local normalization factor", since by dividing the filtered value obtained in step 1 by this value, we obtain a properly normalized S-filter, see step 3 in Fig.B.1. This method is equivalent to use at each voxel a specific kernel. The latter contains 0 at background voxels, and at other voxels, a weight decreasing according to a Gaussian law with the distance to the central voxel. To be normalized, the sum of all weights must be equal to one. The trick here is to achieve such a (non-linear) computation using only linear filtration steps − i.e. using the same unique kernel for all voxels.

Cette thèse est accessible à l'adresse : https://theses.insa-lyon.fr/publication/2024ISAL0014/these.pdf
© [F. Steinhilber], [2024], INSA Lyon, tous droits réservés

Cette thèse est accessible à l'adresse : https://theses.insa-lyon.fr/publication/2024ISAL0014/these.pdf
© [F. Steinhilber], [2024], INSA Lyon, tous droits réservés

Appendix C

Near-surface microstructure after PeP treatment

The following figures show EBSD characterizations on vertical specimens before and after PeP treatment. Average α-laths thickness for the as-built (Z), $Z|_{40min}^{Vertical}$ and $Z|_{1h20}^{Vertical}$ specimens characterized were measured to be 0.609 µm, 0.593 µm and 0.594 µm respectively.

Acquisition and analysis were done by Quentin Gaillard. For a more detailed analysis of the near-surface microstructure, see Section 3.2.2 or the PhD thesis of Quentin Gaillard [GAI 23a].

Cette thèse est accessible à l'adresse : https://theses.insa-lyon.fr/publication/2024ISAL0014/these.pdf
© [F. Steinhilber], [2024], INSA Lyon, tous droits réservés

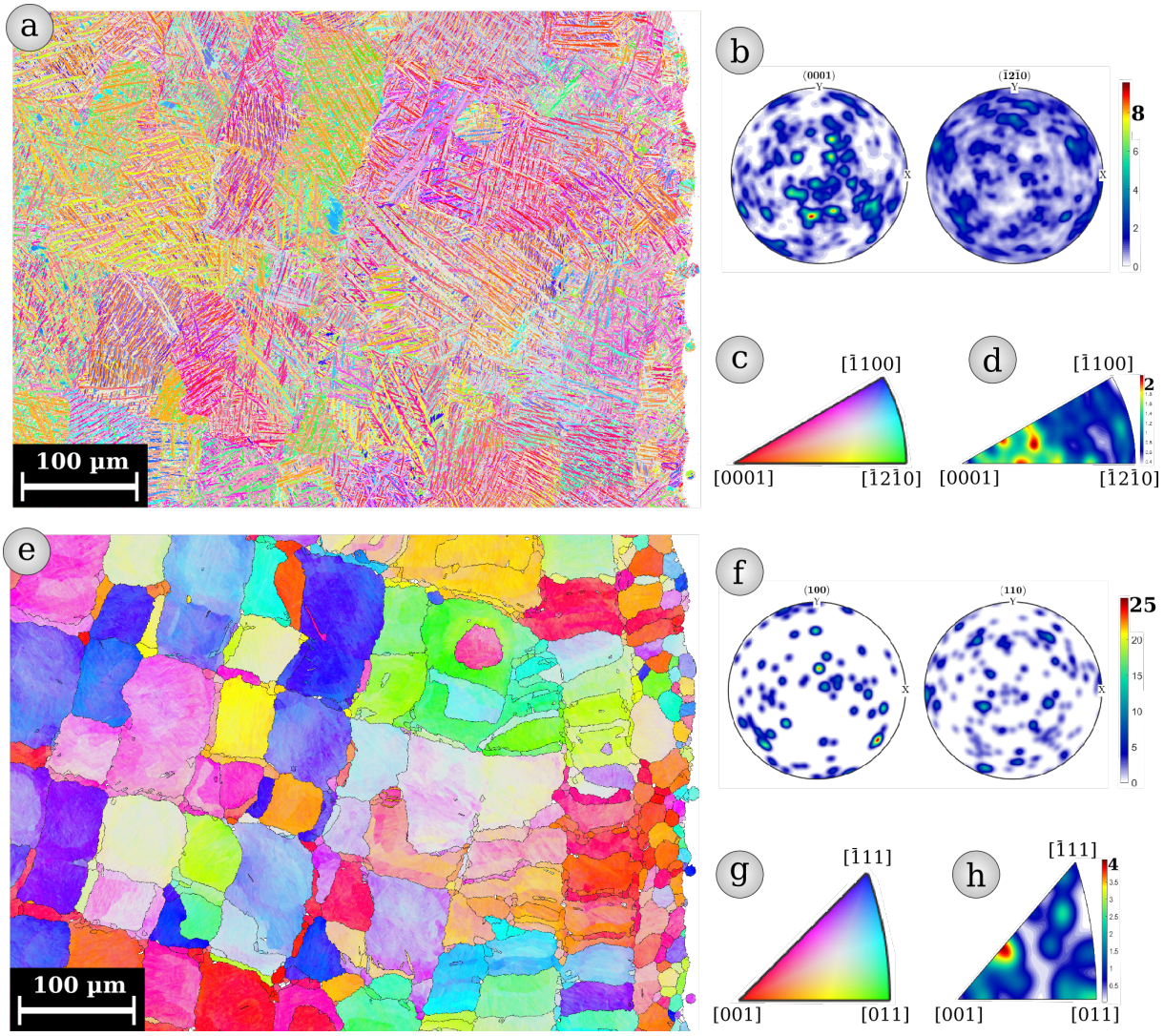

Figure C.1 | EBSD analysis of the microstructure near the surface in a transverse cross-section of a vertical fatigue specimen before PeP treatment. Crystallographic orientation maps of (a) α and (e) prior β_0 phases. Pole figures of (b) α and (f) prior β_0 phases in the border area. Inverse pole figures color maps for (c) α and (g) prior β_0 phases. Inverse pole figures of (d) α and (h) prior β_0 phases in the border area. The build direction Z is taken as a reference. The maps are 600 µm × 445 µm wide and are collected with a step size of 0.25 µm.

Cette thèse est accessible à l'adresse : https://theses.insa-lyon.fr/publication/2024ISAL0014/these.pdf
© [F. Steinhilber], [2024], INSA Lyon, tous droits réservés

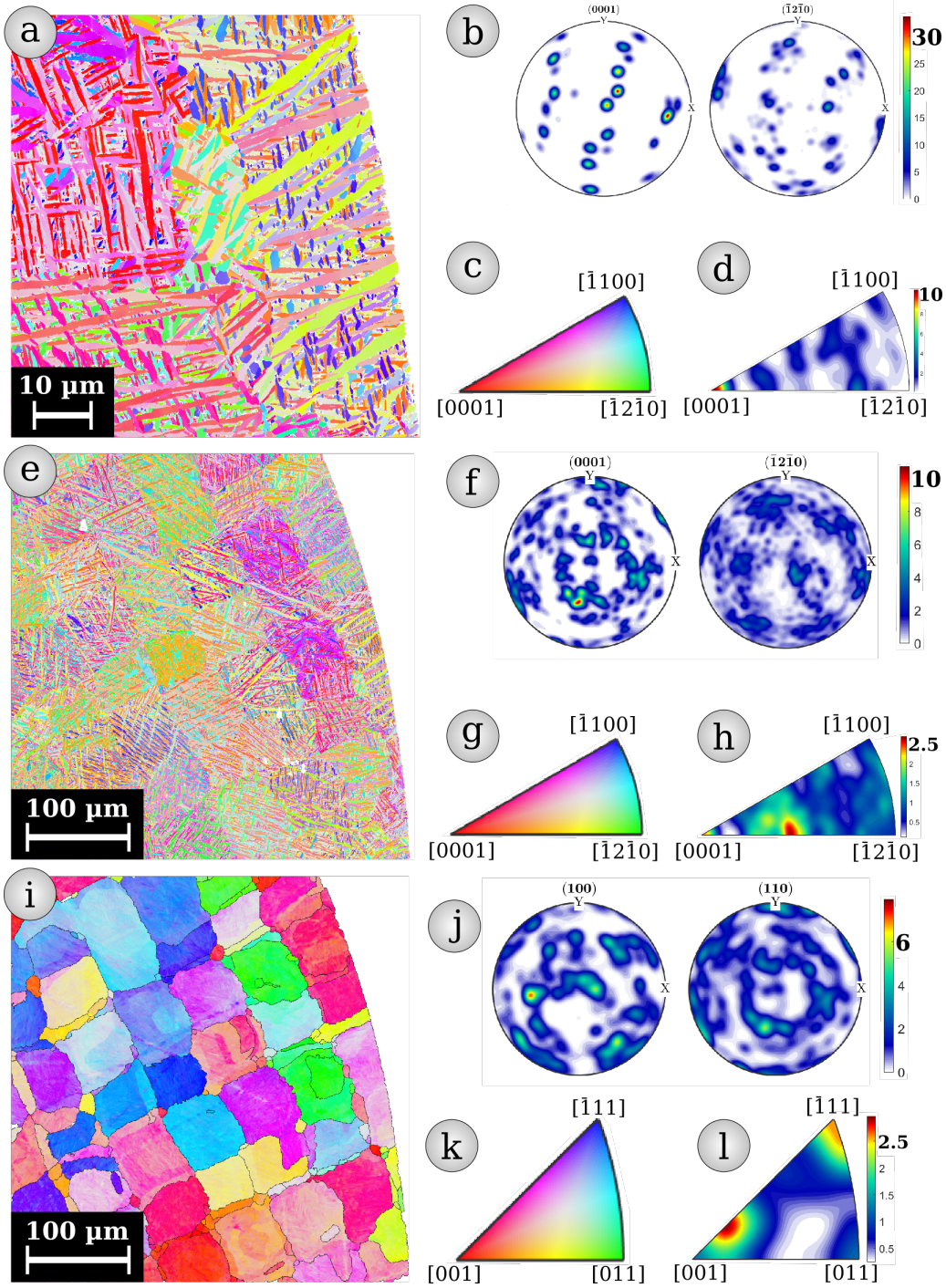

Figure C.2 | EBSD analysis of the microstructure near the surface in a transverse cross-section of a vertical fatigue specimen after a 40 min PeP treatment. Crystallographic orientation maps of (a,e) α and (i) prior β_0 phases. Pole figures of (b,f) α and (j) prior β_0 phases in the border area. Inverse pole figures color maps for (c,g) α and (k) prior β_0 phases. Inverse pole figures of (d,h) α and (l) prior β_0 phases in the border area. The build direction Z is taken as a reference. The map in (a) is 75 µm × 75 µm wide and is done with a step size of 0.06 µm. The map in (e) and (i) are 400 µm × 400 µm wide and are collected with a step size of 0.25 µm.

Cette thèse est accessible à l'adresse : https://theses.insa-lyon.fr/publication/2024ISAL0014/these.pdf
© [F. Steinhilber], [2024], INSA Lyon, tous droits réservés

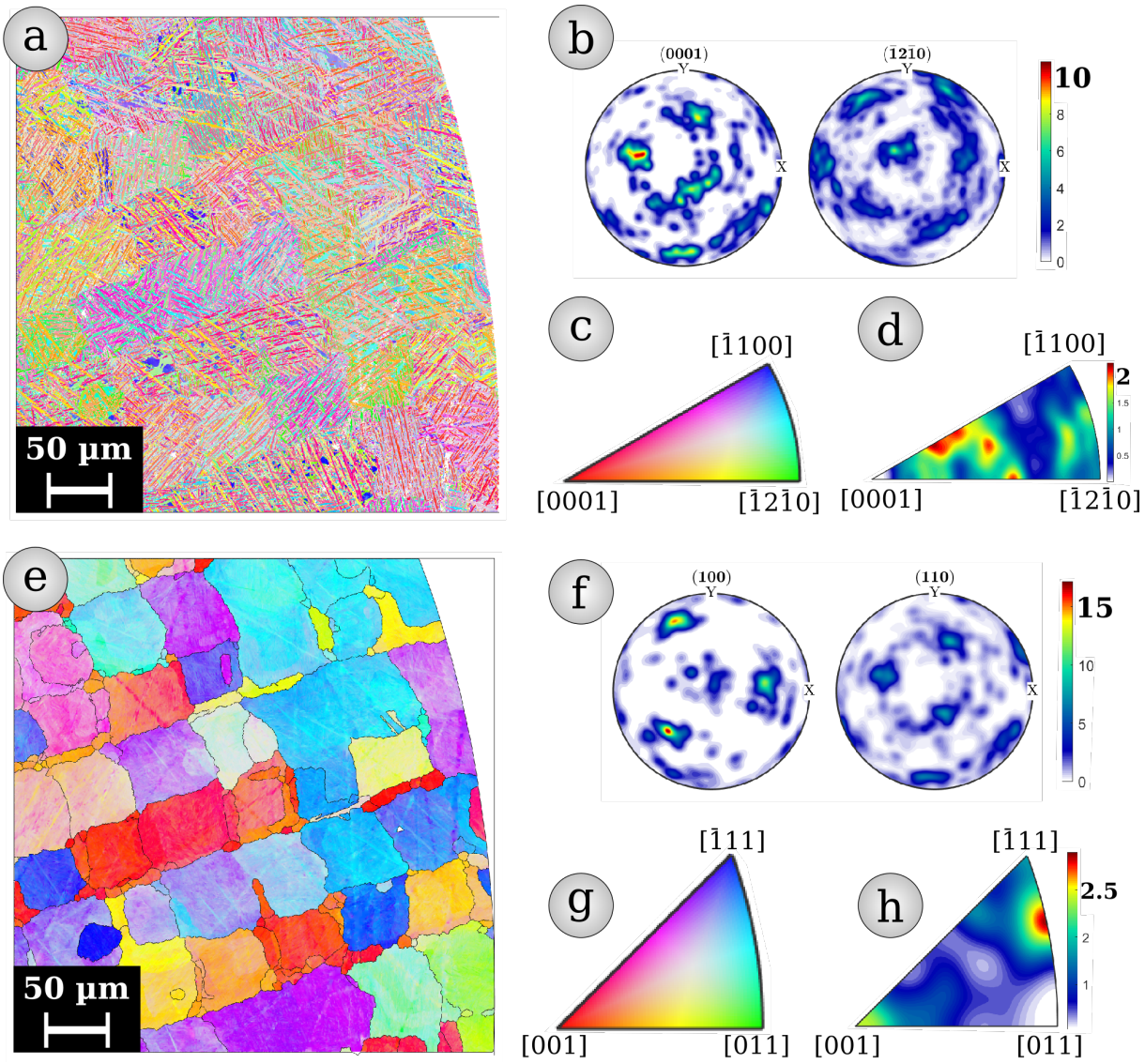

Figure C.3 | EBSD analysis of the microstructure near the surface in a transverse cross-section of a vertical fatigue specimen after a 1 h 20 min PeP treatment. Crystallographic orientation maps of (a) α and (e) prior β_0 phases. Pole figures of (b) α and (f) prior β_0 phases in the border area. Inverse pole figures color maps for (c) α and (g) prior β_0 phases. Inverse pole figures of (d) α and (h) prior β_0 phases in the border area. The build direction Z is taken as a reference. The maps are 400 µm × 400 µm wide and are collected with a step size of 0.25 µm.

Cette thèse est accessible à l'adresse : https://theses.insa-lyon.fr/publication/2024ISAL0014/these.pdf
© [F. Steinhilber], [2024], INSA Lyon, tous droits réservés

References

[ABD 13] Abdul-Rahman H. S., Jiang J., Scott P. J.
A Gaussian-like Filtering algorithm for Freeform Surfaces Represented by Triangular Meshes. , 2013. Publisher: Unpublished. 35

[ABO 14] Aboulkhair N. T.
Reducing porosity in AlSi10Mg parts processed by selective laser melting. *Additive Manufacturing*, , 2014, Page 10. 15

[AHM 20] Ahmed Obeidi M., Mussatto A., Groarke R., Vijayaraghavan R. K., Conway A., Rossi Kaschel F., McCarthy E., Clarkin O., OConnor R., Brabazon D.
Comprehensive assessment of spatter material generated during selective laser melting of stainless steel. *Materials Today Communications*, vol. 25, 2020. 13

[ALE 05] Alekseev Y., Kosobutsky A., Korolev A., Niss V., Kucheryavy V., Povszhik A.
Features of the processes of dimensional processing of metal products by the electrolyte-plasma method. *Litye. Metall.*, vol. 4, 2005, p. 188–195. 133, 137

[ALI 20] Ali U.
Internal surface roughness enhancement of parts made by laser powder-bed fusion additive manufacturing. *Vacuum*, vol. 177, 2020. 35

[ALL 11] Alla R. K., Ginjupalli K., Upadhya N., Shammas M., Krishna R., Sekhar R.
Surface Roughness of Implants: A Review. *Trends in Biomaterials & Artificial Organs*, vol. 25, n° 3, 2011, p. 112–118. 39

[AND 19a] Andreau O.
Nocivité en fatigue et contrôle de défauts produits par fabrication additive. Doctoral thesis, Ecole Nationale Supérieure d'Arts et Métiers, 2019. 12, 30, 62

[AND 19b] Andreau O., Pessard E., Koutiri I., Penot J.-D., Dupuy C., Saintier N., Peyre P.
A competition between the contour and hatching zones on the high cycle fatigue behaviour of a 316L stainless steel: Analyzed using X-ray computed tomography. *Materials Science and Engineering: A*, vol. 757, 2019, p. 146–159. 18, 28

[ARO 99] Arola D., Ramulu M.
An Examination of the Effects from Surface Texture on the Strength of Fiber Reinforced Plastics. *Journal of Composite Materials*, vol. 33, n° 2, 1999, p. 102–123. 33, 161

[ARO 02] Arola D., Williams C.
Estimating the fatigue stress concentration factor of machined surfaces. *International Journal of Fatigue*, vol. 24, n° 9, 2002, p. 923–930. 33

Cette thèse est accessible à l'adresse : https://theses.insa-lyon.fr/publication/2024ISAL0014/these.pdf
© [F. Steinhilber], [2024], INSA Lyon, tous droits réservés

[ATZ 12] Atzeni E., Salmi A.
Economics of additive manufacturing for end-usable metal parts. *The International Journal of Advanced Manufacturing Technology*, vol. 62, n° 9-12, 2012, p. 1147–1155. 2

[BAG 17] Bagehorn S., Wehr J., Maier H.
Application of mechanical surface finishing processes for roughness reduction and fatigue improvement of additively manufactured Ti-6Al-4V parts. *International Journal of Fatigue*, vol. 102, 2017, p. 135–142. 21, 22

[BAR 19] Bartkowiak T., Brown C. A.
Multiscale 3D Curvature Analysis of Processed Surface Textures of Aluminum Alloy 6061 T6. *Materials*, vol. 12, n° 2, 2019. 69, 193

[BAR 21] Barricelli L., Beretta S.
Analysis of prospective SIF and shielding effect for cylindrical rough surfaces obtained by L-PBF. *Engineering Fracture Mechanics*, vol. 256, 2021. 26, 191

[BAR 23] Barricelli L., Patriarca L., du Plessis A., Beretta S.
Orientation-dependent fatigue assessment of Ti6Al4V manufactured by L-PBF: Size of surface features and shielding effect. *International Journal of Fatigue*, vol. 168, 2023. 27, 191

[BAS 22] Basha M., Basha S., Jain V., Sankar M.
State of the art on chemical and electrochemical based finishing processes for additive manufactured features. *Additive Manufacturing*, vol. 58, 2022. 3, 131, 133

[BAT 99] Bathias C.
There is no infinite fatigue life in metallic materials. *Fatigue & Fracture of Engineering Materials & Structures*, vol. 22, n° 7, 1999, p. 559–565. 9

[BAY 19] Bayat M., Thanki A., Mohanty S., Witvrouw A., Yang S., Thorborg J., Tiedje N. S., Hattel J. H.
Keyhole-induced porosities in Laser-based Powder Bed Fusion (L-PBF) of Ti6Al4V: High-fidelity modelling and experimental validation. *Additive Manufacturing*, vol. 30, 2019. 15

[BEL 20] Belkin P., Kusmanov S., Parfenov E.
Mechanism and technological opportunity of plasma electrolytic polishing of metals and alloys surfaces. *Applied Surface Science Advances*, vol. 1, 2020. 131, 133, 137

[BEN 17] Benedetti M., Torresani E., Leoni M., Fontanari V., Bandini M., Pederzolli C., Potrich C.
The effect of post-sintering treatments on the fatigue and biological behavior of Ti-6Al-4V ELI parts made by selective laser melting. *Journal of the Mechanical Behavior of Biomedical Materials*, vol. 71, 2017, p. 295–306. 14, 31

[BEN 18] Benedetti M., Fontanari V., Bandini M., Zanini F., Carmignato S.
Low- and high-cycle fatigue resistance of Ti-6Al-4V ELI additively manufactured via selective laser melting: Mean stress and defect sensitivity. *International Journal of Fatigue*, vol. 107, 2018, p. 96–109. 82

[BER 17] Beretta S., Romano S.
A comparison of fatigue strength sensitivity to defects for materials manufactured by AM or traditional processes. *International Journal of Fatigue*, vol. 94, 2017, p. 178–191. 12, 27

[BEZ 20] Bezuidenhout M.
The effect of HF-HNO3 chemical polishing on the surface roughness and fatigue life of laser powder bed fusion produced Ti6Al4V. *Materials Today Communications*, , 2020, Page 10. 3

Cette thèse est accessible à l'adresse : https://theses.insa-lyon.fr/publication/2024ISAL0014/these.pdf
© [F. Steinhilber], [2024], INSA Lyon, tous droits réservés

[BHA 23] Bhandari L., Gaur V.
Different post-processing methods to improve fatigue properties of additively built Ti-6Al-4V alloy. *International Journal of Fatigue*, vol. 176, 2023. 33

[BIA 11] Biamino S., Penna A., Ackelid U., Sabbadini S., Tassa O., Fino P., Pavese M., Gennaro P., Badini C.
Electron beam melting of Ti48Al2Cr2Nb alloy: Microstructure and mechanical properties investigation. *Intermetallics*, vol. 19, n° 6, 2011, p. 776–781. 15

[BLU 19] Blunt M. J., Lin Q., Akai T., Bijeljic B.
A thermodynamically consistent characterization of wettability in porous media using high-resolution imaging. *Journal of Colloid and Interface Science*, vol. 552, 2019, p. 59–65. 52

[BOB 21] Boban J., Ahmed A.
Improving the surface integrity and mechanical properties of additive manufactured stainless steel components by wire electrical discharge polishing. *Journal of Materials Processing Technology*, vol. 291, 2021, Page 117013. 131

[BOO 16] Book T. A., Sangid M. D.
Strain localization in Ti-6Al-4V Widmanstätten microstructures produced by additive manufacturing. *Materials Characterization*, vol. 122, 2016, p. 104–112. 10

[BOR 02] Borbély A., Mughrabi H., Eisenmeier G., Höppel H. W.
A finite element modelling study of strain localization in the vicinity of near-surface cavities as a cause of subsurface fatigue crack initiation. *International Journal of Fatigue*, vol. 115, n° 3, 2002, p. 227–232. 17

[BRI 08] Bridier F., Villechaise P., Mendez J.
Slip and fatigue crack formation processes in an / titanium alloy in relation to crystallographic texture on different scales. *Acta Materialia*, vol. 56, n° 15, 2008, p. 3951–3962. 172

[BRO 18] Brown C. A., Hansen H. N., Jiang X. J., Blateyron F., Berglund J., Senin N., Bartkowiak T., Dixon B., Le Goïc G., Quinsat Y., Stemp W. J., Thompson M. K., Ungar P. S., Zahouani E. H.
Multiscale analyses and characterizations of surface topographies. *CIRP Annals*, vol. 67, n° 2, 2018, p. 839–862. 193

[CAB 18] Cabanettes F., Joubert A., Chardon G., Dumas V., Rech J., Grosjean C., Dimkovski Z.
Topography of as built surfaces generated in metal additive manufacturing: A multi scale analysis from form to roughness. *Precision Engineering*, , 2018, Page 17. 2, 13

[CAI 15] Cain V., Thijs L., Van Humbeeck J., Van Hooreweder B., Knutsen R.
Crack propagation and fracture toughness of Ti6Al4V alloy produced by selective laser melting. *Additive Manufacturing*, vol. 5, 2015, p. 68–76. 82

[CAL 14] Calignano F.
Design optimization of supports for overhanging structures in aluminum and titanium alloys by selective laser melting. *Materials & Design*, vol. 64, 2014, p. 203–213. 13

[CAR 19] Carrion P. E., Soltani-Tehrani A., Phan N., Shamsaei N.
Powder Recycling Effects on the Tensile and Fatigue Behavior of Additively Manufactured Ti-6Al-4V Parts. *JOM*, vol. 71, n° 3, 2019, p. 963–973. 16, 19

Cette thèse est accessible à l'adresse : https://theses.insa-lyon.fr/publication/2024ISAL0014/these.pdf
© [F. Steinhilber], [2024], INSA Lyon, tous droits réservés

[CAZ 05] Cazals F., Pouget M.
Estimating differential quantities using polynomial fitting of osculating jets. *Computer Aided Geometric Design*, vol. 22, n° 2, 2005, p. 121–146. 51

[CHA 15] Chan K. S.
Characterization and analysis of surface notches on Ti-alloy plates fabricated by additive manufacturing techniques. *Surface Topography: Metrology and Properties*, vol. 3, n° 4, 2015. 13

[CHA 17] Chastand V.
Etude du comportement mécanique et des mécanismes d'endommagement de pièces métalliques réalisées par fabrication additive. Doctoral thesis, Centrale Lille, 2017. 19

[CHA 18] Chastand V.
Comparative study of fatigue properties of Ti-6Al-4V specimens built by electron beam melting (EBM) and selective laser melting (SLM). *Materials Characterization*, vol. 143, 2018, p. 76–81. 16, 18, 21

[CHA 22] Charles A., Bayat M., Elkaseer A., Thijs L., Hattel J. H., Scholz S.
Elucidation of dross formation in laser powder bed fusion at down-facing surfaces: Phenomenon-oriented multiphysics simulation and experimental validation. *Additive Manufacturing*, vol. 50, 2022. 13, 34

[CHI 21] Childerhouse T., Hernandez-Nava E., Tapoglou N.
The influence of finish machining depth and hot isostatic pressing on defect distribution and fatigue behaviour of selective electron beam melted Ti-6Al-4V. *International Journal of Fatigue*, vol. 147, 2021, Page 106169. 19

[COE 14] Coeurjolly D., Lachaud J.-O., Levallois J.
Multigrid convergent principal curvature estimators in digital geometry. *Computer Vision and Image Understanding*, vol. 129, 2014, p. 27–41. 51, 55

[COE 16] Coeurjolly D., Foare M., Gueth P., Lachaud J.-O.
Piecewise smooth reconstruction of normal vector field on digital data. *Computer Graphics Forum*, vol. 35, n° 7, 2016, p. 157–167. 191, 192

[CUT 22] Cutolo A., Elangeswaran C., Muralidharan G. K., Van Hooreweder B.
On the role of building orientation and surface post-processes on the fatigue life of Ti-6Al-4V coupons manufactured by laser powder bed fusion. *Materials Science and Engineering: A*, vol. 840, 2022. 131

[DEP 18] DePond P. J., Guss G., Ly S., Calta N. P., Deane D., Khairallah S., Matthews M. J.
In situ measurements of layer roughness during laser powder bed fusion additive manufacturing using low coherence scanning interferometry. *Materials & Design*, vol. 154, 2018, p. 347–359. 13, 15

[DGt 22] DGtal Team
. DGtal, 2022. 51

[DIA 22] Dias Corpa Tardelli J., Duarte Firmino A. C., Ferreira I., Cândido Dos Reis A.
Influence of the roughness of dental implants obtained by additive manufacturing on osteoblastic adhesion and proliferation: A systematic review. *Heliyon*, vol. 8, n° 12, 2022. 39

Cette thèse est accessible à l'adresse : https://theses.insa-lyon.fr/publication/2024ISAL0014/these.pdf
© [F. Steinhilber], [2024], INSA Lyon, tous droits réservés

[DUR 79] Duradzhi V., Bryantsev I., Tokarov A.
Investigation of erosion of the anode under the action of an electrolytic plasma on it. *Elektronnaya Obrabotka Materialov*, , 1979. 131

[EDW 14] Edwards P., Ramulu M.
Fatigue performance evaluation of selective laser melted Ti6Al4V. *Materials Science*, , 2014, Page 11. 21

[EST 96] Ester M., Kriegel H.-P., Sander J., Xu X.
A Density-Based Algorithm for Discovering Clusters in Large Spatial Databases with Noise. *Proceedings of the 2nd International Conference on Knowledge Discovery and Data Mining (KDD-96)*, , 1996. 63, 155

[FEL 84] Feldkamp L. A., Davis L. C., Kress J. W.
Practical cone-beam algorithm. *Journal of the Optical Society of America A*, vol. 1, n° 6, 1984. 41

[FEN 21] Feng S., Kamat A. M., Sabooni S., Pei Y.
Experimental and numerical investigation of the origin of surface roughness in laser powder bed fused overhang regions. *Virtual and Physical Prototyping*, vol. 16, 2021. 13

[FIN 02] Findlay S., Harrison N.
Why aircraft fail. *Materials Today*, vol. 5, n° 11, 2002, p. 18–25. 2

[FOR 16] de Formanoir C., Suard M., Dendievel R., Martin G., Godet S.
Improving the mechanical efficiency of electron beam melted titanium lattice structures by chemical etching. *Additive Manufacturing*, vol. 11, 2016, p. 71–76. 34

[FOX 18] Fox J. C., Kim F., Reese Z., Evans C.
Complementary use of optical metrology and X-ray computed tomography for surface finish and defect detection in laser powder bed fusion additive manufacturing. *American Society for Precision Engineering*, vol. 69, 2018, p. 195–200. 35

[GAI 22] Gaillard Q., Cazottes S., Boulnat X., Dancette S., Desrayaud C.
Microstructure, texture and mechanical properties with raw surface states of Ti-6Al-4V parts built by L-PBF. *Procedia CIRP*, vol. 108, 2022, p. 698–703. 82, 83

[GAI 23a] Gaillard Q.
Optimisation des propriétés de composants en TA6V élaborés par Laser Beam Melting. Doctoral thesis, Ecole des Mines de St Etienne, 2023. 4, 71, 72, 76, 77, 78, 79, 80, 81, 84, 101, 120, 207

[GAI 23b] Gaillard Q., Boulnat X., Cazottes S., Dancette S., Desrayaud C.
Strength/ductility trade-off of Laser Powder Bed Fusion Ti-6Al-4V: Synergetic effect of alpha-case formation and microstructure evolution upon heat treatments. *Additive Manufacturing*, vol. 76, 2023, Page 103772. 76, 101, 107, 120, 121, 122, 128

[GAL 17] Galarraga H., Warren R. J., Lados D. A., Dehoff R. R., Kirka M. M.
Fatigue crack growth mechanisms at the microstructure scale in as-fabricated and heat treated Ti-6Al-4V ELI manufactured by electron beam melting (EBM). *Engineering Fracture Mechanics*, vol. 176, 2017, p. 263–280. 107

[Gen 18] General Electric
. New manufacturing milestone: 30,000 additive fuel nozzles | GE Additive, 2018. 1

[GIL 22] Gillham B., Yankin A., Shipley H., McNamara F., Tomonto C., O'Donnell G., Trimble D., Yin S., Taylor D., Lupoi R.

Cette thèse est accessible à l'adresse : https://theses.insa-lyon.fr/publication/2024ISAL0014/these.pdf
© [F. Steinhilber], [2024], INSA Lyon, tous droits réservés

The Analysis of Small-Scale Notches on the Fatigue Performance of SLM Ti-6Al-4V; A Theory of Critical Distances Approach. *Key Engineering Materials*, vol. 926, 2022, p. 250–267. 26

[GOC 19] Gockel J., Sheridan L., Koerper B., Whip B.
The influence of additive manufacturing processing parameters on surface roughness and fatigue life. *International Journal of Fatigue*, vol. 124, 2019, p. 380–388. 32

[GON 15] Gong H., Rafi K., Gu H., Janaki Ram G., Starr T., Stucker B.
Influence of defects on mechanical properties of Ti6Al4V components produced by selective laser melting and electron beam melting. *Materials & Design*, vol. 86, 2015, p. 545–554. 18, 22

[GO 16] Goïc G. L., Bigerelle M., Samper S., Favrelière H., Pillet M.
Multiscale roughness analysis of engineering surfaces: A comparison of methods for the investigation of functional correlations. *Mechanical Systems and Signal Processing*, vol. 66-67, 2016, p. 437–457. 69, 193

[GRA 23] Grazia Guerra M., Lavecchia F.
Measurement of additively manufactured freeform artefacts: The influence of surface texture on measurements carried out with optical techniques. *Measurement*, vol. 209, 2023. 35, 46

[GRE 17] Greitemeier D., Palm F., Syassen F., Melz T.
Fatigue performance of additive manufactured TiAl6V4 using electron and laser beam melting. *International Journal of Fatigue*, vol. 94, 2017, p. 211–217. 21, 22, 82

[GUN 18] Gunenthiram V.
Compréhension de la formation de porosités en fabrication additive (LBM). Analyse expérimentale de linteraction laser - lit de poudre - bain liquide. Doctoral thesis, Ecole Nationale Supérieure d'Arts et Métiers, 2018. 13, 15

[HAI 13] Haitjema H.
Uncertainty estimation of 2.5-D roughness parameters obtained by mechanical probing. *International Journal of Precision Technology*, vol. 3, n° 4, 2013, p. 403–412. 35

[HAM 20] Hamidi Nasab M., Romano S., Gastaldi D., Beretta S., Vedani M.
Combined effect of surface anomalies and volumetric defects on fatigue assessment of AlSi7Mg fabricated via laser powder bed fusion. *Additive Manufacturing*, vol. 34, 2020. 26, 35

[HEN 18] Henning Z., Falko B.-H.
Surface Finish of Additively Manufactured Parts using Plasma Electrolytic Polishing. *WCMNM 2018 World Congress on Micro and Nano Manufacturing*, Slovenia, 2018 Research Publishing Services, p. 385–388. 131

[HU 20a] Hu Y., Wu S., Withers P., Zhang J., Bao H., Fu Y., Kang G.
The effect of manufacturing defects on the fatigue life of selective laser melted Ti-6Al-4V structures. *Materials & Design*, vol. 192, 2020. 15

[HU 20b] Hu Y., Wu S., Wu Z., Zhong X., Ahmed S., Karabal S., Xiao X., Zhang H., Withers P.
A new approach to correlate the defect population with the fatigue life of selective laser melted Ti-6Al-4V alloy. *International Journal of Fatigue*, vol. 136, 2020. 28

[HUA 21] Huang Y., Wang C., Ding F., Yang Y., Zhang T., He X., Zheng L., Li N.
Principle, process, and application of metal plasma electrolytic polishing: a review. *The International Journal of Advanced Manufacturing Technology*, vol. 114, 2021. 131, 132, 133

Cette thèse est accessible à l'adresse : https://theses.insa-lyon.fr/publication/2024ISAL0014/these.pdf
© [F. Steinhilber], [2024], INSA Lyon, tous droits réservés

[ING 13] Inglis C.
Stresses in plates due to the presence of cracks and sharp corners. *Spie Milestone series MS*, vol. 137, 1913, p. 3–17. 24, 54

[Int 12] International Organisation for Standardization
. ISO 25178-3:2012 Geometrical product specifications (GPS) - Surface texture: Areal - Part 3: Specification operators, 2012. 44, 46, 47

[Int 15] International Organisation for Standardization
. ISO 16610-60:2015 Geometrical product specification (GPS) - Filtration - Part 60: Linear areal filters - Basic concepts, 2015. 46

[Int 16] International Organisation for Standardization
. ISO 16610-28:2016 Geometrical product specifications (GPS) Filtration Part 28: Profile filters: End effects, 2016. 47

[Int 21] International Organisation for Standardization
. ISO 25178-2:2012 Geometrical product specifications (GPS) Surface texture: Areal Part 2: Terms, definitions and surface texture parameters, 2021. 31, 32, 49, 161, 191

[IRV 74] Irving P. E., Beevers C. J.
The effect of air and vacuum environments on fatigue crack growth rates in Ti-6Al-4V. *Metallurgical Transactions*, vol. 5, n° 2, 1974, p. 391–398. 17

[JAI 16] Jain P., Tyagi V.
A survey of edge-preserving image denoising methods. *Information Systems Frontiers*, vol. 18, n° 1, 2016, p. 159–170. 41

[JAN 12] Janecki D.
Edge effect elimination in the recursive implementation of Gaussian filters. *Precision Engineering*, vol. 36, n° 1, 2012, p. 128–136. 47

[JIA 10] Jiang X., Zhang X., Scott P. J.
Template matching of freeform surfaces based on orthogonal distance fitting for precision metrology. *Measurement Science and Technology*, vol. 21, n° 4, 2010. 44

[JIA 11] Jiang X., Cooper P., Scott P. J.
Freeform surface filtering using the diffusion equation. *Proceedings of the Royal Society A: Mathematical, Physical and Engineering Sciences*, vol. 467, n° 2127, 2011, p. 841–859. 44

[JIA 20a] Jiang X. J., Scott P. J.
Advanced metrology: freeform surfaces. Academic Press, London, 2020. 35, 44, 46, 49, 69, 193

[JIA 20b] Jiang X. J., Scott P. J.
Free-form surface filtering using wavelets and multiscale decomposition. *Advanced Metrology*, p. 195–246 Elsevier, 2020. 44

[JUN 21] Junet A.
Étude tridimensionnelle de la propagation en fatigue de fissures internes dans les matériaux métalliques. Doctoral thesis, Institut National des Sciences Appliquées de Lyon, 2021. 17

[KAH 17] Kahlin M., Ansell H., Moverare J.
Fatigue behaviour of notched additive manufactured Ti6Al4V with as-built surfaces. *International Journal of Fatigue*, vol. 101, 2017, p. 51–60. 16, 21, 22

[KAN 18] Kantzos C. A., Cunningham R. W., Tari V., Rollett A. D.
Characterization of metal additive manufacturing surfaces using synchrotron X-ray CT and

Cette thèse est accessible à l'adresse : https://theses.insa-lyon.fr/publication/2024ISAL0014/these.pdf
© [F. Steinhilber], [2024], INSA Lyon, tous droits réservés

micromechanical modeling. *Computational Mechanics*, vol. 61, n° 5, 2018, p. 575–580. 13, 54

[KAR 23] Karimialavijeh H., Ghasri-Khouzani M., Das A., Pröebstle M., Martin .
Effect of laser contour scan parameters on fatigue performance of A20X fabricated by laser powder bed fusion. *International Journal of Fatigue*, vol. 175, 2023. 12

[KAS 15] Kasperovich G., Hausmann J.
Improvement of fatigue resistance and ductility of TiAl6V4 processed by selective laser melting. *Journal of Materials Processing Technology*, vol. 220, 2015, p. 202–214. 16, 18, 21, 22, 82

[KAS 17] Kastner J., Salaberger D., Heinzl C., Gusenbauer C., Rao G.
High Resolution X-ray Computed Tomography for Non-destructive Characterization and In-situ Investigations. 2017. 4

[KER 12] Kerckhofs G., Pyka G., Moesen M., Schrooten J., Wevers M.
High-resolution micro-CT as a tool for 3D surface roughness measurement of 3D additive manufactured porous structures. *Proc iCT*, , 2012. 35

[KHA 21] Khan H. M., Karabulut Y., Kitay O., Kaynak Y., Jawahir I. S.
Influence of the post-processing operations on surface integrity of metal components produced by laser powder bed fusion additive manufacturing: a review. *Machining Science and Technology*, vol. 25, n° 1, 2021, p. 118–176. 131

[KHR 21] Khrapov D., Kozadayeva M., Manabaev K., Panin A., Sjöström W., Koptyug A., Mishurova T., Evsevleev S., Meinel D., Bruno G., Cheneler D., Surmenev R., Surmeneva M.
Different Approaches for Manufacturing Ti-6Al-4V Alloy with Triply Periodic Minimal Surface Sheet-Based Structures by Electron Beam Melting. *Materials*, vol. 14, n° 17, 2021. 52

[KNU 93] Knutsson H., Westin C.-F.
Normalized and differential convolution. *Proceedings of IEEE Conference on Computer Vision and Pattern Recognition*, New York, NY, USA, 1993 IEEE Comput. Soc. Press, p. 515–523. 47, 203

[LAC 17] Lachaud J.-O., Coeurjolly D., Levallois J.
Robust and Convergent Curvature and Normal Estimators with Digital Integral Invariants. Najman L., Romon P., Eds., *Modern Approaches to Discrete Curvature*, p. 293–348 Springer International Publishing, Cham, 2017. 51

[LAD 16] Ladewig A., Schlick G., Fisser M., Schulze V., Glatzel U.
Influence of the shielding gas flow on the removal of process by-products in the selective laser melting process. *Additive Manufacturing*, vol. 10, 2016, p. 1–9. 13

[LAR 18] Larrosa N., Wang W., Read N., Loretto M., Evans C., Carr J., Tradowsky U., Attallah M., Withers P.
Linking microstructure and processing defects to mechanical properties of selectively laser melted AlSi10Mg alloy. *Theoretical and Applied Fracture Mechanics*, vol. 98, 2018, p. 123–133. 18

[LAR 23] Larguier A.
Influence de l'alpha-case sur le comportement en fatigue de pièces en Ti-6Al-4V élaborées par fusion laser sur lit de poudre. Rapport de stage, 2023, INSA Lyon. 129

Cette thèse est accessible à l'adresse : https://theses.insa-lyon.fr/publication/2024ISAL0014/these.pdf
© [F. Steinhilber], [2024], INSA Lyon, tous droits réservés

[LE 21] Le V.-D., Pessard E., Morel F., Prigent S.
Effect of the surface roughness on the high cycle fatigue behaviour of Ti-6Al-4V alloy obtained by additive manufacturing process. *Engineering Integrity*, vol. 53, 2021. 33

[LEE 20] Lee S., Pegues J. W., Shamsaei N.
Fatigue behavior and modeling for additive manufactured 304L stainless steel: The effect of surface roughness. *International Journal of Fatigue*, vol. 141, 2020, Page 105856. 33

[LES 22] Lesseur J., Tranchand B., Mancier T., Montauzier A., Larignon C., Perusin S.
On the use of X-ray microtomography to control artificial defect geometries produced by metal additive manufacturing. *Nondestructive Testing and Evaluation*, vol. 37, n° 5, 2022, p. 611–630. 16

[LEU 13] Leuders S., Thöne M., Riemer A., Niendorf T., Tröster T., Richard H., Maier H.
On the mechanical behaviour of titanium alloy TiAl6V4 manufactured by selective laser melting: Fatigue resistance and crack growth performance. *International Journal of Fatigue*, vol. 48, 2013, p. 300–307. 22

[LEV 15] Levallois J., Coeurjolly D., Lachaud J.-O.
Scale-space feature extraction on digital surfaces. *Computers & Graphics*, vol. 51, 2015, p. 177–189. 69, 191, 193

[LI 19] Li P., Warner D., Pegues J., Roach M., Shamsaei N., Phan N.
Investigation of the mechanisms by which hot isostatic pressing improves the fatigue performance of powder bed fused Ti-6Al-4V. *International Journal of Fatigue*, vol. 120, 2019, p. 342–352. 19

[LI 22] Li Z., Li H., Yin J., Li Y., Nie Z., Li X., You D., Guan K., Duan W., Cao L., Wang D., Ke L., Liu Y., Zhao P., Wang L., Zhu K., Zhang Z., Gao L., Hao L.
A Review of Spatter in Laser Powder Bed Fusion Additive Manufacturing: In Situ Detection, Generation, Effects, and Countermeasures. *Micromachines*, vol. 13, n° 8, 2022, Page 1366. 13

[Lie 17] Liebherr
. Technologies for the future, 2017. 1

[LIF 21] Lifton J. J., Liu Y., Tan Z. J., Mutiargo B., Goh X. Q., Malcolm A. A.
Internal surface roughness measurement of metal additively manufactured samples via x-ray CT: the influence of surrounding material thickness. *Surface Topography: Metrology and Properties*, vol. 9, n° 3, 2021. 35

[LIN 23] Lin P., Wang M., Trofimov V. A., Yang Y., Song C.
Research on the Warping and Dross Formation of an Overhang Structure Manufactured by Laser Powder Bed Fusion. *Applied Sciences*, vol. 13, n° 6, 2023, Page 3460. 13

[LIU 14] Liu Q. C., Elambasseril J., Sun S. J., Leary M., Brandt M., Sharp P. K.
The Effect of Manufacturing Defects on the Fatigue Behaviour of Ti-6Al-4V Specimens Fabricated Using Selective Laser Melting. *Advanced Materials Research*, vol. 891-892, 2014, p. 1519–1524. 18

[LIU 17] Liu Y., Zhang J., Li S.-J., Hou W.-T., Wang H., Xu Q.-S., Hao Y.-L., Yang R.
Effect of HIP Treatment on Fatigue Crack Growth Behavior of Ti6Al4V Alloy Fabricated by

Cette thèse est accessible à l'adresse : https://theses.insa-lyon.fr/publication/2024ISAL0014/these.pdf
© [F. Steinhilber], [2024], INSA Lyon, tous droits réservés

Electron Beam Melting. *Acta Metallurgica Sinica (English Letters)*, vol. 30, n° 12, 2017, p. 1163–1168. 107

[LIU 19] Liu S., Shin Y. C.
Additive manufacturing of Ti6Al4V alloy: A review. *Materials & Design*, vol. 164, 2019. 107

[LIU 20] Liu W., Chen C., Shuai S., Zhao R., Liu L., Wang X., Hu T., Xuan W., Li C., Yu J., Wang J., Ren Z.
Study of pore defect and mechanical properties in selective laser melted Ti6Al4V alloy based on X-ray computed tomography. *Materials Science and Engineering: A*, vol. 797, 2020. 15

[LOR 87] Lorensen W. E., Cline H. E.
Marching cubes: A high resolution 3D surface construction algorithm. *ACM SIGGRAPH Computer Graphics*, vol. 21, n° 4, 1987, p. 163–169. 85

[LOU 13a] Lou S., Jiang X., Scott P. J.
Geometric computation theory for morphological filtering on freeform surfaces. *Proceedings of the Royal Society A: Mathematical, Physical and Engineering Sciences*, , 2013. 46

[LOU 13b] Lou S., Zeng W.-H., Jiang X.-Q., Scott P. J.
Robust Filtration Techniques in Geometrical Metrology and Their Comparison. *International Journal of Automation and Computing*, , 2013, p. 1–8. 44

[LOU 19a] Lou S., Jiang X., Sun W., Zeng W., Pagani L., Scott P.
Characterisation methods for powder bed fusion processed surface topography. *Precision Engineering*, vol. 57, 2019, p. 1–15. 46

[LOU 19b] Lou S., Pagani L., Zeng W., Ghori M. U., Jiang X., Scott P. J.
Surface texture evaluation of additively manufactured metallic cellular scaffolds for acetabular implants using X-ray computed tomography. *Bio-Design and Manufacturing*, vol. 2, n° 2, 2019, p. 55–64. 35, 44

[LOU 20] Lou S., Pagani L., Zeng W., Jiang X., Scott P.
Watershed segmentation of topographical features on freeform surfaces and its application to additively manufactured surfaces. *Precision Engineering*, vol. 63, 2020, p. 177–186. 191, 192

[MAH 22] Mahtabi M., Yadollahi A., Stokes R., Morgan-Barnes C., Doude H., Bian L.
Effect of Powder Reuse on Microstructural and Fatigue Properties of Ti-6Al-4V Fabricated via Directed Energy Deposition. *Proceedings of the 33rd Annual International Solid Freeform Fabrication Symposium*, , 2022. 72

[MAJ 10] Majzoobi G. H., Daemi N.
The effects of notch geometry on fatigue life using notch sensitivity factor. *Transactions of the Indian Institute of Metals*, vol. 63, n° 2-3, 2010, p. 547–552. 25

[MAL 21] Maleki E., Bagherifard S., Bandini M., Guagliano M.
Surface post-treatments for metal additive manufacturing: Progress, challenges, and opportunities. *Additive Manufacturing*, vol. 37, 2021, Page 101619. 131

[MAN 16] Mancisidor A. M.
Reduction of the Residual Porosity in Parts Manufactured by Selective Laser Melting Using Skywriting and High Focus Offset Strategies. *Physics Procedia*, , 2016, Page 10. 12

[MAR 19] Martin A. A., Calta N. P., Khairallah S. A., Wang J., Depond P. J., Fong A. Y., Thampy V., Guss G. M., Kiss A. M., Stone K. H., Tassone C. J., Nelson Weker J., Toney M. F., van Buuren T., Matthews M. J.

Cette thèse est accessible à l'adresse : https://theses.insa-lyon.fr/publication/2024ISAL0014/these.pdf
© [F. Steinhilber], [2024], INSA Lyon, tous droits réservés

Dynamics of pore formation during laser powder bed fusion additive manufacturing. *Nature Communications*, vol. 10, n° 1, 2019, Page 1987. 12

[MAS 18] Masuo H., Tanaka Y., Morokoshi S., Yagura H., Uchida T., Yamamoto Y., Murakami Y.
Influence of defects, surface roughness and HIP on the fatigue strength of Ti-6Al-4V manufactured by additive manufacturing. *International Journal of Fatigue*, vol. 117, 2018, p. 163–179. 19, 20, 22, 26, 27, 28, 29

[MAT 03] Matsunaga H., Murakami Y., Kubota M., Lee J.-H.
Fatigue Strength of Ti-6Al-4V Alloys Containing Small Artificial Defects. *Journal of the Society of Materials Science, Japan*, vol. 52, 2003, p. 263–269. 27

[MCB 20] McBride J. W., Cross K. J.
The surface area and localised 3D roughness of a highly structured surface using X-Ray Computed tomography (XCT). *Metrology Letters*, , 2020. 35

[MEA 17] Mearian L.
. Boeing turns to 3D-printed parts to save millions on its 787 Dreamliner, 2017. 1

[MIA 21] Mian M. J., Razmi J., Ladani L.
Defect Analysis and Fatigue Strength Prediction of As-built Ti6Al4V Parts, Produced Using Electron Beam Melting (EBM) AM Technology. *Materialia*, , 2021. 32

[MIL 22] Milhomme S.
Influence du procédé sur les propriétés mécaniques et microstructurales de pièces en Ti-6Al-4V issues de fabrication additive (LMD et SLM). Doctoral thesis, Université de Bordeaux, 2022. 16

[MIN 14] Mingareev I., Bonhoff T., El-Sherif A. F., Meiners W., Kelbassa I., Biermann T., Richardson M.
Femtosecond laser post-processing of metal parts produced by laser additive manufacturing. *J. Laser Appl.*, vol. 25, n° 5, 2014, Page 5. 35

[MUR 83] Murakami Y., Masahiro E.
Quantitative evaluation of fatigue strength of metals containing various small defects or cracks. *Engineering Fracture Mechanics*, vol. 17, n° 1, 1983, p. 1–15. 26

[MUR 02] Murakami Y.
Metal Fatigue - Effects of Small Defects and Nonmetallic Inclusions. Elsevier, 1st édition, 2002. 27, 31, 33, 64

[NAJ 19] Najmon J. C., Raeisi S., Tovar A.
Review of additive manufacturing technologies and applications in the aerospace industry. *Additive Manufacturing for the Aerospace Industry*, p. 7–31 Elsevier, 2019. 1

[NAK 19] Nakatani M., Masuo H., Tanaka Y., Murakami Y.
Effect of Surface Roughness on Fatigue Strength of Ti-6Al-4V Alloy Manufactured by Additive Manufacturing. *Procedia Structural Integrity*, vol. 19, 2019, p. 294–301. 2, 31

[NAV 22] Navickait K., Nestler K., Böttger-Hiller F., Matias C., Diskin A., Golan O., Garkun A., Strokin E., Biletskiy R., Safranchik D., Zeidler H.
Efficient polishing of additive manufactured titanium alloys. *Procedia CIRP*, vol. 108, 2022, p. 346–351. 131, 132, 133

[NGU 22] Nguyen H. D., Pramanik A., Basak A., Dong Y., Prakash C., Debnath S., Shankar S., Jawahir I., Dixit S., Buddhi D.

Cette thèse est accessible à l'adresse : https://theses.insa-lyon.fr/publication/2024ISAL0014/these.pdf
© [F. Steinhilber], [2024], INSA Lyon, tous droits réservés

A critical review on additive manufacturing of Ti-6Al-4V alloy: microstructure and mechanical properties. *Journal of Materials Research and Technology*, vol. 18, 2022. 82, 101

[NUT 19] Nutal N.
. Finition de surface de pièces produites par fabrication additive, 2019. 131

[OGD 55] Ogden H., Jaffee R.
The effect of carbon, oxygen, and nitrogen on the mechanical properties of titanium and titanium alloys. rapport n° TML-20, 4370612, 1955. 118

[OTS 79] Otsu N.
A Threshold Selection Method from Gray-Level Histograms. *IEEE Transactions on Systems, Man, and Cybernetics*, , 1979. 41

[PAG 18] Pagani L., Lou S., Zeng W., Jiang X., Scott P. J.
Effect of the form estimation on the areal texture parameters for X-ray computed tomography measurement. *Proc iCT 2018*, , 2018. 35, 44

[PAL 18] Pal S., Lojen G., Kokol V., Drstvensek I.
Evolution of metallurgical properties of Ti-6Al-4V alloy fabricated in different energy densities in the Selective Laser Melting technique. *Journal of Manufacturing Processes*, vol. 35, 2018, p. 538–546. 15

[PAR 61] Paris P., Gomez M., Anderson W.
A rational analytic theory of fatigue. *The Trend in Engineering*, , n° 13, 1961, p. 9–14. 26

[PAU 23] Pauzon C., Raza A., Hanif I., Dubiez-Le Goff S., Moverare J., Hryha E.
Effect of layer thickness on spatter properties during laser powder bed fusion of Ti6Al4V. *Powder Metallurgy*, vol. 66, n° 4, 2023, p. 333–342. 13

[PEG 18] Pegues J., Roach M., Scott Williamson R., Shamsaei N.
Surface roughness effects on the fatigue strength of additively manufactured Ti-6Al-4V. *International Journal of Fatigue*, vol. 116, 2018, p. 543–552. 108, 114

[PEG 19] Pegues J. W., Shamsaei N., Roach M. D., Williamson R. S.
Fatigue life estimation of additive manufactured parts in the as-built surface condition. *Material Design & Processing Communications*, vol. 1, n° 3, 2019. 23, 33

[PER 18] Persenot T.
Fatigue of Ti-6Al-4V thin parts made by electron beam melting. Doctoral thesis, Université de Lyon, Lyon, 2018. 21, 40

[PER 19] Persenot T., Burr A., Martin G., Buffiere J.-Y., Dendievel R., Maire E.
Effect of build orientation on the fatigue properties of as-built Electron Beam Melted Ti-6Al-4V alloy. *International Journal of Fatigue*, vol. 118, 2019, p. 65–76. 2, 13, 14, 34, 40, 54

[PER 20] Persenot T., Burr A., Dendievel R., Buère J.-Y., Maire E., Lachambre J., Martin G.
Fatigue performances of chemically etched thin struts built by selective electron beam melting: Experiments and predictions. *Materialia*, , 2020. 3, 12, 27, 29, 30, 62, 63, 64, 65, 67, 70

[PES 20] Pessard E.
Contribution à la prise en compte des effets du procédé de mise en forme sur la tenue en fatigue des matériaux métalliques. Habilitation à Diriger des Recherches, Université d'Angers, 2020. 13, 14

Cette thèse est accessible à l'adresse : https://theses.insa-lyon.fr/publication/2024ISAL0014/these.pdf
© [F. Steinhilber], [2024], INSA Lyon, tous droits réservés

[PET 59] Peterson R.
Notch sensitivity. *Metal Fatigue*, , 1959, p. 293–306. 25

[PLE 20a] du Plessis A., Beretta S.
Killer notches: The effect of as-built surface roughness on fatigue failure in AlSi10Mg produced by laser powder bed fusion. *Additive Manufacturing*, vol. 35, 2020. 2, 23

[PLE 20b] du Plessis A., Macdonald E.
Hot isostatic pressing in metal additive manufacturing_ X-ray tomography reveals details of pore closure. *Additive Manufacturing*, vol. 34, 2020. 19, 54, 62

[PLE 20c] du Plessis A., Yadroitsava I., Yadroitsev I.
Effects of defects on mechanical properties in metal additive manufacturing: A review focusing on X-ray tomography insights. *Materials & Design*, vol. 187, 2020. 18

[POL 14] Polasik A.
Presented in Partial Fulfillment of the Requirements for the Degree Doctor of Philosophy in the Graduate School of The Ohio State University. Doctoral thesis, The Ohio State University, OH, USA, 2014. 107

[POL 22] Polley C., Radlof W., Hauschulz F., Benz C., Sander M., Seitz H.
Morphological and mechanical characterisation of three-dimensional gyroid structures fabricated by electron beam melting for the use as a porous biomaterial. *Journal of the Mechanical Behavior of Biomedical Materials*, vol. 125, 2022. 52

[POM 19] Pomberger S., Stoschka M., Leitner M.
Cast surface texture characterisation via areal roughness. *Precision Engineering*, vol. 60, 2019, p. 465–481. 44

[POM 20] Pomberger S., Stoschka M., Aigner R., Leitner M., Ehart R.
Areal fatigue strength assessment of cast aluminium surface layers. *International Journal of Fatigue*, vol. 133, 2020. 33

[PYK 13] Pyka G., Kerckhofs G., Papantoniou I., Speirs M., Schrooten J., Wevers M.
Surface Roughness and Morphology Customization of Additive Manufactured Open Porous Ti6Al4V Structures. *Materials*, vol. 6, n° 10, 2013, p. 4737–4757. 13

[RA 13] Ra H. K., Karthik N. V., Gong H., Starr T. L., Stucker B. E.
Microstructures and Mechanical Properties of Ti6Al4V Parts Fabricated by Selective Laser Melting and Electron Beam Melting. *Journal of Materials Engineering and Performance*, , 2013, Page 13. 22

[REK 15] Rekedal K., Liu D.
Fatigue Life of Selective Laser Melted and Hot Isostatically Pressed Ti-6Al-4v Absent of Surface Machining. *56th AIAA/ASCE/AHS/ASC Structures, Structural Dynamics, and Materials Conference*, Kissimmee, Florida, 2015 American Institute of Aeronautics and Astronautics. 22

[ROM 17] Romano S., Brandão A., Gumpinger J., Gschweitl M., Beretta S.
Qualification of AM parts: Extreme value statistics applied to tomographic measurements. *Materials & Design*, vol. 131, 2017, p. 32–48. 27

[ROM 18] Romano S., Brückner-Foit A., Brandão A., Gumpinger J., Ghidini T., Beretta S.
Fatigue properties of AlSi10Mg obtained by additive manufacturing: Defect-based modelling

Cette thèse est accessible à l'adresse : https://theses.insa-lyon.fr/publication/2024ISAL0014/these.pdf
© [F. Steinhilber], [2024], INSA Lyon, tous droits réservés

and prediction of fatigue strength. *Engineering Fracture Mechanics*, vol. 187, 2018, p. 165–189. 23

[SAN 20] Sanaei N., Fatemi A.
Analysis of the effect of surface roughness on fatigue performance of powder bed fusion additive manufactured metals. *Theoretical and Applied Fracture Mechanics*, vol. 108, 2020. 18

[SAN 21] Sanaei N., Fatemi A.
Defects in additive manufactured metals and their effect on fatigue performance: A state-of-the-art review. *Progress in Materials Science*, vol. 117, 2021. 11, 34

[SAV 07] Savio E., De Chiffre L., Schmitt R.
Metrology of freeform shaped parts. *CIRP Annals*, vol. 56, n° 2, 2007, p. 810–835. 44

[SCH 70] Schoen A. H.
Infinite periodic minimal surfaces without self-intersections. rapport n° D-5541, 1970, NASA. 40

[SCH 09] Schijve J.
Fatigue of structures and materials. Springer, Dordrecht, 2nd édition, 2009. 10, 11, 23, 24, 27, 118, 130, 167

[SEI 17] Seifi M., Gorelik M., Waller J., Hrabe N., Shamsaei N., Daniewicz S., Lewandowski J. J.
Progress Towards Metal Additive Manufacturing Standardization to Support Qualification and Certification. *JOM*, vol. 69, n° 3, 2017, p. 439–455. 1

[SEO 21] Seo B., Park H.-K., Kim H. G., Kim W. R., Park K.
Corrosion behavior of additive manufactured CoCr parts polished with plasma electrolytic polishing. *Surface and Coatings Technology*, vol. 406, 2021. 131

[SHA 21] Shahpaski M., Sapaico L. R., Süsstrunk S.
Surface roughness estimation using structured light projection. *Electronic Imaging*, vol. 33, n° 5, 2021. 35

[SIL 98] Silverman B. W.
Density estimation for statistics and data analysis. N° 26 Monographs on statistics and applied probability Chapman & Hall/CRC, Boca Raton, 1998. 86

[SKR 19] Skrodzki M.
. The k-d tree data structure and a proof for neighborhood computation in expected logarithmic time, 2019. Preprint available at http://arxiv.org/abs/1903.04936. 197

[SOR 21] Soro N., Saintier N., Merzeau J., Veidt M., Dargusch M. S.
Quasi-static and fatigue properties of graded Ti6Al4V lattices produced by Laser Powder Bed Fusion (LPBF). *Additive Manufacturing*, vol. 37, 2021. 34, 40

[STE 23] Steinhilber F.
3D roughness computation from XCT data - Data and Python & ImageJ implementations. *Zenodo repository*, , 2023. Available at https://doi.org/10.5281/zenodo.10276253. 43, 45, 49, 185, 197

[STO 08] Stock S. R.
Recent advances in X-ray microtomography applied to materials. *International Materials Reviews*, vol. 53, n° 3, 2008, p. 129–181. 57

Cette thèse est accessible à l'adresse : https://theses.insa-lyon.fr/publication/2024ISAL0014/these.pdf
© [F. Steinhilber], [2024], INSA Lyon, tous droits réservés

[TAM 17] Tammas-Williams S., Withers P. J., Todd I., Prangnell P. B.
The Influence of Porosity on Fatigue Crack Initiation in Additively Manufactured Titanium Components. *Scientific Reports*, vol. 7, n° 1, 2017. 18, 23, 27, 62

[TAS 02] Tasdizen T., Whitaker R., Burchard P., Osher S.
Geometric surface smoothing via anisotropic diffusion of normals. Boston, MA, USA, 2002 IEEE, p. 125–132. 44, 60

[TAU 95] Taubin G.
Estimating the tensor of curvature of a surface from a polyhedral approximation. *Proceedings of IEEE International Conference on Computer Vision*, Cambridge, MA, USA, 1995 p. 902–907. 50

[TAY 91] Taylor D., Clancy O. M.
THE FATIGUE PERFORMANCE OF MACHINED SURFACES. *Fatigue & Fracture of Engineering Materials and Structures*, vol. 14, n° 2-3, 1991, p. 329–336. 32

[TAY 08] Taylor D.
The theory of critical distances. *Engineering Fracture Mechanics*, vol. 75, n° 7, 2008, p. 1696–1705. 25, 26

[THO 18] Thompson A.
Surface texture measurement of metal additively manufactured parts by X-ray computed tomography. Doctoral thesis, University of Nottingham, 2018. 35

[THO 19] Thomas M., Davoine C., Drawin S.
Fabrication additive en aéronautique et en spatial. *Techniques de l'ingénieur*, , 2019. 1, 2, 3

[TIL 23] Tilton M., Borjali A., Griffis J. C., Varadarajan K. M., Manogharan G. P.
Fatigue properties of Ti-6Al-4V TPMS scaffolds fabricated via laser powder bed fusion. *Manufacturing Letters*, vol. 37, 2023, p. 32–38. 52

[TOW 16] Townsend A.
Surface texture metrology for metal additive manufacturing: a review. *Precision Engineering*, vol. 46, 2016, p. 34–47. 35

[TUB 23] Tubei V., Toda H., Ketanond W., Fujihara H., Takakuwa O., Takeuchi A., Uesugi M.
Direct observation of three-dimensional short fatigue crack closure behavior in Ti-6Al-4V alloy using ultra-high-resolution X-ray microtomography. *International Journal of Fatigue*, vol. 168, 2023. 10

[VAF 21] Vafadar A., Guzzomi F., Rassau A., Hayward K.
Advances in Metal Additive Manufacturing: A Review of Common Processes, Industrial Applications, and Current Challenges. *Applied Sciences*, vol. 11, n° 3, 2021, Page 1213. 1

[Val 00] Vallellano, Navarro, Dominguez
Fatigue crack growth threshold conditions at notches. Part I: theory. *Fracture of Engineering Materials and Structures*, vol. 23, n° 2, 2000, p. 113–121. 25

[VAN 12] Van Hooreweder B., Boonen R., Moens D., Kruth J.-P., Sas P.
On the Determination of Fatigue Properties of Ti6Al4V Produced by Selective Laser Melting. Honolulu, Hawaii, 2012 American Institute of Aeronautics and Astronautics. 82

[VAN 22] Vanderesse N., Bocher P., Nuño N., Yánez A., Hof L. A.
On the characterization of roughness and geometrical irregularities of additively manufactured single titanium-alloy struts. *Additive Manufacturing*, vol. 54, 2022. 41

Cette thèse est accessible à l'adresse : https://theses.insa-lyon.fr/publication/2024ISAL0014/these.pdf
© [F. Steinhilber], [2024], INSA Lyon, tous droits réservés

[VAY 19] Vayssette B., Saintier N., Brugger C., El May M., Pessard E.
Numerical modelling of surface roughness effect on the fatigue behavior of Ti-6Al-4V obtained by additive manufacturing. *International Journal of Fatigue*, vol. 123, 2019, p. 180–195. 21, 22, 26

[VAY 20] Vayssette B.
Comportement en fatigue de pièces de Ti-6Al-4V obtenues par SLM et EBM: effet de la rugosité. Doctoral thesis, Ecole Nationale Supérieure d'Arts et Métiers, 2020. 15

[VET 14] Vetterli M., Schmid M., Wegener K.
Comprehensive investigation of surface characterization for laser sintered parts. *DDMC 2014 : Fraunhofer Direct Digital Manufacturing Conference : proceedings*, 2014. Artwork Size: 6 p. Medium: application/pdf Publisher: ETH Zurich. 46

[VIA 22] Viale V., Stavridis J., Salmi A., Bondioli F., Saboori A.
Optimisation of downskin parameters to produce metallic parts via laser powder bed fusion process: an overview. *The International Journal of Advanced Manufacturing Technology*, vol. 123, n° 7-8, 2022, p. 2159–2182. 13

[VIL 18a] Villarraga-Gómez H.
Studies of Dimensional Metrology with X-ray CAT Scan. Doctoral thesis, University of North Carolina, 2018. 3

[VIL 18b] Villarraga-Gómez H., Peitsch C. M., Ramsey A., Smith S. T.
THE ROLE OF COMPUTED TOMOGRAPHY IN ADDITIVE MANUFACTURING. vol. 69, 2018. 44

[VIL 19] Villarraga-Gómez H., Herazo E. L., Smith S. T.
X-ray computed tomography: from medical imaging to dimensional metrology. *Precision Engineering*, vol. 60, 2019, p. 544–569. 3, 190

[VI 23] Vié T., Deschanel S., Godin N., Normand B.
On the effect of coatings on the tensile and fatigue properties of 7075-T6 aluminum alloy monitored with acoustic Emission (AE): Towards lifetime estimation. *International Journal of Fatigue*, vol. 171, 2023, Page 107578. 126, 127, 130

[VUL 14] Vulliez M., Gleason M. A., Souto-Lebel A., Quinsat Y., Lartigue C., Kordell S. P., Lemoine A. C., Brown C. A.
Multi-scale Curvature Analysis and Correlations with the Fatigue Limit on Steel Surfaces after Milling. *Procedia CIRP*, vol. 13, 2014, p. 308–313. 193

[WAN 21] Wang R., Law A. C., Garcia D., Yang S., Kong Z.
Development of structured light 3D-scanner with high spatial resolution and its applications for additive manufacturing quality assurance. *The International Journal of Advanced Manufacturing Technology*, vol. 117, n° 3-4, 2021, p. 845–862. 35

[WAN 22] Wang Z., Yang S., Peng Z., Gao Z.
Effect of defects in laser selective melting of Ti-6Al-4V alloy on microstructure and mechanical properties after heat treatment. *Optics and Laser Technology*, vol. 156, 2022, Page 108522. 13, 15

[WAN 23] Wang F., Lei L., Fu X., Shi L., Luo X., Song Z., Zhang G.
Toward developing Ti alloys with high fatigue crack growth resistance by additive manufacturing. *Journal of Materials Science and Technology*, vol. 132, 2023, p. 166–178. 107

Cette thèse est accessible à l'adresse : https://theses.insa-lyon.fr/publication/2024ISAL0014/these.pdf
© [F. Steinhilber], [2024], INSA Lyon, tous droits réservés

[WEI 95] Weixing Y., Kaiquan X., Yi G.
On the fatigue notch factor, Kf. *International Journal of Fatigue*, vol. 17, n° 4, 1995, p. 245–251. 25

[WU 23] Wu M.-W., Ni K., Yen H.-W., Chen J.-K., Wang P., Tseng Y.-J., Tsai M.-K., Wang S.-H., Lai P.-H., Ku M.-H.
Revealing the intensified preferred orientation and factors dominating the anisotropic mechanical properties of laser powder bed fusion Ti6Al4V alloy after heat treatment. *Journal of Alloys and Compounds*, vol. 949, 2023, Page 169494. 10

[WYC 13] Wycisk E., Emmelmann C., Siddique S., Walther F.
High Cycle Fatigue (HCF) Performance of Ti-6Al-4V Alloy Processed by Selective Laser Melting. *Advanced Materials Research*, vol. 816-817, 2013, p. 134–139. 20, 21, 22

[XU 21] Xu Z., Liu A., Wang X., Liu B., Guo M.
Fatigue limit prediction model and fatigue crack growth mechanism for selective laser melting Ti6Al4V samples with inherent defects. *International Journal of Fatigue*, vol. 143, 2021. 17, 23

[YAN 19] Yang L., Yan C., Cao W., Liu Z., Song B., Wen S., Zhang C., Shi Y., Yang S.
Compressioncompression fatigue behaviour of gyroid-type triply periodic minimal surface porous structures fabricated by selective laser melting. *Acta Materialia*, vol. 181, 2019, p. 49–66. 40

[YIN 23] Yin H., Li P.
Micropore-propagation-based model of fatigue life analysis of SLM manufactured Ti-6Al-4V. *International Journal of Fatigue*, vol. 167, 2023. 26

[YU 19] Yu H., Li F., Wang Z., Zeng X.
Fatigue performances of selective laser melted Ti-6Al-4V alloy: Influence of surface finishing, hot isostatic pressing and heat treatments. *International Journal of Fatigue*, vol. 120, 2019, p. 175–183. 16, 18

[YUA 19] Yuan L., Ding S., Wen C.
Additive manufacturing technology for porous metal implant applications and triple minimal surface structures: A review. *Bioactive Materials*, vol. 4, 2019, p. 56–70. 52

[ZAB 18] Zabala A., Blunt L., Tato W., Aginagalde A., Gomez X., Llavori I.
The use of areal surface topography characterisation in relationto fatigue performance. *MATEC Web of Conferences*, vol. 165, 2018. 32

[ZAC 77] Zack G. W., Rogers W. E., Latt S. A.
Automatic measurement of sister chromatid exchange frequency. *Journal of Histochemistry & Cytochemistry*, vol. 25, n° 7, 1977, p. 741–753. 43

[ZAN 19] Zanini F., Pagani L., Savio E., Carmignato S.
Characterisation of additively manufactured metal surfaces by means of X-ray computed tomography and generalised surface texture parameters. *CIRP Annals*, vol. 68, n° 1, 2019, p. 515–518. 35

[ZEI 22] Zeidler H., Böttger-Hiller F.
Plasma-Electrolytic Polishing as a Post-Processing Technology for Additively Manufactured Parts. *Chemie Ingenieur Technik*, vol. 94, n° 7, 2022, p. 1024–1029. 131, 133

Cette thèse est accessible à l'adresse : https://theses.insa-lyon.fr/publication/2024ISAL0014/these.pdf
© [F. Steinhilber], [2024], INSA Lyon, tous droits réservés

[ZER 19] Zerbst U., Madia M., Klinger C., Bettge D., Murakami Y.
Defects as a root cause of fatigue failure of metallic components. I: Basic aspects. *Engineering Failure Analysis*, vol. 97, 2019, p. 777–792. 10

[ZHA 17] Zhao C., Fezzaa K., Cunningham R. W., Wen H., De Carlo F., Chen L., Rollett A. D., Sun T.
Real-time monitoring of laser powder bed fusion process using high-speed X-ray imaging and diffraction. *Scientific Reports*, vol. 7, n° 1, 2017, Page 3602. 13

[ZHA 18] Zhang L., Feih S., Daynes S., Chang S., Wang M. Y., Wei J., Lu W. F.
Energy absorption characteristics of metallic triply periodic minimal surface sheet structures under compressive loading. *Additive Manufacturing*, vol. 23, 2018, p. 505–515. 52

[ZHA 19] Zhang J., Chaudhari A., Wang H.
Surface quality and material removal in magnetic abrasive finishing of selective laser melted 316L stainless steel. *Journal of Manufacturing Processes*, vol. 45, 2019, p. 710–719. 13

[ZHA 21] Zhao C., Qu N., Tang X.
Removal of adhesive powders from additive-manufactured internal surface via electrochemical machining with flexible cathode. *Precision Engineering*, vol. 67, 2021, p. 438–452. 13

Cette thèse est accessible à l'adresse : https://theses.insa-lyon.fr/publication/2024ISAL0014/these.pdf
© [F. Steinhilber], [2024], INSA Lyon, tous droits réservés

Cette thèse est accessible à l'adresse : https://theses.insa-lyon.fr/publication/2024ISAL0014/these.pdf
© [F. Steinhilber], [2024], INSA Lyon, tous droits réservés

FOLIO ADMINISTRATIF

THÈSE DE L'INSA LYON, MEMBRE DE L'UNIVERSITÉ DE LYON

NOM : Steinhilber

Prénom : Florian

Date de soutenance : 01/02/2024

TITRE : On the use of X-ray computed tomography to investigate the influence of surface integrity on the fatigue properties of additively manufactured Ti64

NATURE : Doctorat

Numéro d'ordre : 2024ISAL0014

École doctorale : ED 34 - Matériaux de Lyon

Spécialité : Matériaux

RÉSUMÉ :

Manufacturing defects are known to significantly impact the fatigue properties of additively manufactured (AM) components. Notably, the large surface roughness, typical of AM processes, leads to increased stress concentrations that promote crack initiation, thereby reducing fatigue resistance.

Traditionally, surface roughness and related defects are evaluated using tools like white light interferometers. However, these instruments offer a limited, single-perspective and only partially three-dimensional analysis. Those limitations do not enable the thorough characterization of the complex surfaces and hidden defects typical in AM components.

This study describes a methodology for performing a 3D surface analysis using X-ray Computed Tomography (XCT) data. The method is illustrated on various samples, ranging from simple cylinders to more intricate architected structures. It turns out to be very efficient at detecting critical surface defects, such as notches hidden by partially melted powder particles.

The methodology is then applied to examine the effect of surface defects on the fatigue properties of Ti64 produced by Laser Powder Bed Fusion (L-PBF). This analysis includes both as-built surfaces and those subjected to post-treatments, specifically investigating the impact of Plasma electrolytic Polishing (PeP) and surface oxygen contamination (presence of an α-case layer) resulting from high-temperature heat treatment (860 °C).

Using XCT for 3D characterization, defects responsible for fatigue failure are identified, the latter being predominantly surface valleys. The method's ability to predict crack initiation locations is also evaluated, as well as its potential to estimate the fatigue resistance of a specimen before testing.

MOTS-CLÉS: 3D surface analysis, Fatigue, Additive Manufacturing, X-ray Computed Tomography, Ti64, Plasma electolytic Polishing, Alpha-case.

Laboratoires de recherche : MatéIS – UMR CNRS 5510 | SIMaP – UMR CNRS 5266

Président du jury : Stefano Beretta (Professeur)

Composition du jury : Fabien Szmytka, ENSTA Paris (Professeur associé, Rapporteur)
Sabine Rolland du Roscoat 3SR (Maître de Conférences, Rapporteur)
Stefano Beretta, PoliMI (Professeur, Examinateur)
Jean-Yves Buffière, INSA LYON (Professeur, Directeur de thèse)
Rémy Dendievel, Grenoble INP (Professeur, Co-encadrant)
Guilhem Martin, Grenoble INP (Maître de Conférences, Co-encadrant)
Victor Chastand, Dassault Aviation (Ingénieur, Invité)

Cette thèse est accessible à l'adresse : https://theses.insa-lyon.fr/publication/2024ISAL0014/these.pdf
© [F. Steinhilber], [2024], INSA Lyon, tous droits réservés